UNIVERSITÀ DEGLI STUDI DI PADOVA

SEDE AMMINISTRATIVA:

UNIVERSITÀ DEGLI STUDI DI PADOVA

Dipartimento di Scienze Chimiche

Scuola di Dottorato in Scienze Molecolari
Indirizzo: Scienze Chimiche

XXV ciclo

Functional molecular hybrids based on polyoxometalates: catalytic and biological studies

Coordinatore: Ch.mo Prof. Antonino Polimeno

Supervisore: Dott. Mauro Carraro

Dottoranda: Gloria Modugno

31 gennaio 2013

Ho attraversato i continenti

Per vedere il più alto dei mondi

Ho speso una fortuna

Per navigare sui sette mari

E non avevo avuto il tempo di notare

A due passi dalla porta di casa

Una goccia di rugiada su un filo d'erba

Rabindranath Tagore

A Elena ...

Functional molecular hybrids based on polyoxometalates: catalytic and biological studies

Ph. D. Thesis by Gloria Modugno, University of Padova, Italy.

Polyoxometalates (POMs) are molecular and nano-dimensional, multi-metal oxides, which have found applications in catalysis, materials science, and nano-medicine. Their general formula are: a) $[M_mO_y]^{p-}$; b) $[X_xM_mOy]^{q-}$, where M is the main transition metal constituent of the POM (M = Mo, V, W), O is the oxygen atom and X can be a non-metal atom, such as P, Si, As, Sb, another element of the p block, or a different transition metal. These species are characterized by a remarkable variety, since their properties depend on elemental composition, structure, and associated counterion. In addition, it is possible to synthesize "vacant" POMs derivatives, with surface defects. These last structures feature coordinatively unsaturated, terminal oxygen atoms, whose nucleophilicity can be exploited to foster reactions with electrophilic organic moieties to give O-X-R bonds, where X = As, P, Si, Sn, and R = organic residue. In this way, several organic-inorganic hybrid complexes can be obtained. Thus, the merging of organic domains with POM nano-scaffolds can be exploited to design new functional molecules and materials. In particular, POM-appended organic/organometallic moieties are instrumental for advanced catalytic applications and can direct the supramolecular organization of the hybrid molecules towards extended functional nanostructures. Among recent examples, the interplay of organic chromophores and POMs by covalent linkage and ionic assembly has been proposed for the development of photosensitized catalytic processes.

In this thesis, we report the synthesis of hybrid POM derivatives containing luminescent chromophores (dansyl, pyrene and fluorescein), grafted as silane (with general formula $(n\text{Bu}_4\text{N})_4[(\text{R-Si})_2\text{O}(\gamma\text{-SiW}_{10}\text{O}_{36})]$) or chiral phosphonate (with general formula $(n\text{Bu}_4\text{N})_3\text{Na}_2[(\text{R*PO})_2(\alpha\text{-A-PW}_9\text{O}_{34})]$) derivatives, with unique spectroscopic features. The use of tetrabutylammonium ($n\text{Bu}_4\text{N}^+$) as counterion promotes the solubilization of the POM in CH_3CN. The resulting hybrids have been characterized at the solid state and in solution by a combination of techniques (multinuclear NMR, FT-IR, ESI-MS). The characterization suggested a bis-substitution: the inorganic POM framework provides a molecular nanosurface where two molecules of the same fluorophore are anchored in a tweezer-type arrangement. Optical and chiroptical properties of the hybrid derivatives have been investigated. In particular, the fluorescence spectroscopy of the fluorophore-tagged POMs has been exploited for sensing applications towards metal ions and organic molecules:

(i) The bis-dansylated complex can selectively coordinate bivalent metal ions (Cu and Pb ions), which can be detected in micromolar concentration. In the presence of Cu^{2+}, a fluorescence quenching has been observed, whereas with Pb^{2+} an increase of luminescence has been obtained.

(ii) The extended π system of the pyrene derivative has been exploited to bind [60]fullerene. The luminescence quenching has highlighted the interaction of the POM with fullerene molecules in the micromolar range.

A promising potential for applications in many different fields such as sensing, catalysis, nanoelectronics, and photochemical conversion of solar energy is foreseen for these luminescent systems.

Moreover, due to the potential applications of POMs in medicine (many POMs exhibit antiviral, antitumoral and antibiotic activity), their association with organic domains may be also of interest to improve targeting and delivery strategies. In this scenario, the exploitation of hybrid complexes can allow: (i) to enhance stability and biocompatibility; (ii) to increment the affinity of derivatives towards carriers and biological targets; (iii) to incorporate imaging probes for cellular tracking/trafficking. Luminescent hybrid POMs, in particular, may couple the bio-imaging diagnostic potential with innovative therapy protocols. Thus, the assembly behavior and the stability of the luminescent hybrid POMs in physiological conditions have been investigated by means of dynamic light scattering (DLS), scanning electron microscopy (SEM) and transmission electron microscopy (TEM). The analysis showed the formation of spherical aggregates with a broad size distribution for these derivatives. The formation of such aggregates is expected to be driven by the hindered organic chromophores, bearing aromatic residues, whereas the tetrabutylammonium cations may assist the assembly, minimizing repulsion between adjacent inorganic polyanions. Moreover, since the fluorescence of these compounds is maintained under physiological conditions, they were tracked in the cells, showing their localization in different subcellular regions. An unprecedented uptake into nucleosomes and mitochondria has been highlighted. The cytotoxicity of hybrid POMs has also been determined, showing a reduced toxicity at low doses. These results are expected to pave the way to the use of suitable POMs both as drugs and as nanodimensional scaffolds for organic drugs.

Furthermore, since the preparation of hybrid derivatives could be a powerful strategy for the introduction of molecular recognition sites and the enhancement of biocompatibility, studies

on the interaction between POM and hybrid POMs with important biological macromolecules (ferritin and avidin) were explored.

The binding of two different kind of inorganic POMs ($[Ru^{IV}_4(\mu\text{-}OH)_2(\mu\text{-}O)_4(H_2O)_4(\mu\text{-}SiW_{10}O_{36})_2]^{10-}$ and $[EuW_{10}O_{36}]^{9-}$) on the ferritin (Ftn) has been indeed higlighted by a combined investigation, involving DLS, ζ-potential measurements, ITC (isothermal titration calorimetry), fluorimetry, CD (circular dichroism) and TEM. In particular, (i) the shift of Ftn ζ-potential towards more negative potentials (by 8-13 mV), in the presence of the POM and (ii) the complete quenching of the Trp luminescence (λ_{exc} = 290 nm, λ_{em} = 327 nm), upon addition of >24 eqs of POM, likely due to energy transfer between the two domains, have shown that the POM can be successfully attached to the Ftn by means of ionic interactions. In addition, the integrity of the protein has been estabilished by DLS and CD analysis.

Moreover, a biological hybrid POM containing biotin moieties was synthesized and its interaction capability with avidin was investigated. Such study allowed to investigate the confinement of hybrid POMs in correspondence of specific protein binding sites and to design bioconjugated systems with molecular recognition properties, to be exploited in targeting therapies.

A last work, developed during a short scientific mission in Dublin, in collaboration with the research group of Prof. Martin Albrecht, is also presented. We have studied a strategy for the synthesis of a POM-appended N-heterocyclic carbene (NHC) iridium complex. To this end, imidazolium moieties have been successfully grafted on the defect site of a divacant Keggin polyanion. The hybrid POM synthesized was tested in catalyzing hydrogen transfer reactions (HT). The reduction of benzophenone to diphenyl methanol in *i*PrOH as solvent and hydrogen donor was used as a model reaction for probing the catalytic activity of the iridium(I) complex. In particular, full conversion after 120 min has been obtained using *t*BuOK as base.

Ibridi molecolari funzionali basati su poliossometallati: studi catalitici e biologici

Tesi di Dottorato di Gloria Modugno, Università degli Studi di Padova, Italia.

I poliossometallati (POMs) sono una classe di composti a base di ossidi polianionici discreti che presentano potenzialità di utilizzo in campi diversi, quali la catalisi, la scienza dei materiali e la medicina. Tali composti possono essere rappresentati da due formule generali: (a) $[M_mO_y]^{p-}$ isopolianioni; (b)$[X_xM_mO_y]^{q-}$ eteropolianioni, dove M è un metallo delle serie di transizione (solitamente V, Mo o W nel più alto stato d'ossidazione (d^0)) mentre X può essere un non metallo (P, Si, Ge, As, Sb, Te, etc.), o un diverso metallo di transizione (Co, Fe, Mn, Cu, etc.).

La diversità strutturale e di composizione che caratterizza i POMs, si riflette in un ampio spettro di proprietà, controllabili a livello molecolare, che coinvolgono forma, potenziale redox, distribuzione della carica superficiale, acidità e solubilità. In particolare, una delle possibili modificazioni della struttura di un poliossometallato consiste nella preparazione di un complesso "vacante". Poichè tali derivati presentano dei difetti strutturali sulla loro superficie, caratterizzati dalla presenza di atomi di ossigeno con reattività nucleofila, possono essere sfruttati per preparare *complessi ibridi organici-inorganici.* Infatti, gli atomi di ossigeno che si trovano in prossimità della lacuna vengono funzionalizzati mediante reazioni con reagenti elettrofili per dare legami O-X-R, dove X = As, P, Si, Sn, e R = residuo organico. In questo modo, la funzionalizzazione di POMs con residui organici consente lo sviluppo di molecole e materiali ibridi che possono presentare diverse funzionalità. Per esempio, l'associazione di residui organici/organometallici ai poliossoanioni ha consentito lo sviluppo di aggregati supramolecolari estesi e di sistemi innovativi con applicazioni catalitiche bifunzionali e avanzate. Inoltre, l' ancoraggio di cromofori organici è stato recentemente proposto per lo sviluppo di processi fotoattivati.

Sulla base di queste premesse, in questo lavoro di tesi, sono state quindi studiate nuove strategie di sintesi, per la preparazione di derivati ibridi luminescenti basati su poliossometallati contenenti cromofori, quali dansile, pirene e fluoresceina e legati covalentemente al POM come organosilani (con formula generale $(n\text{Bu}_4\text{N})_4[(\text{R-Si})_2\text{O}(\gamma\text{-SiW}_{10}\text{O}_{36})]$) o come fosfonati chirali (con formula generale $(n\text{Bu}_4\text{N})_3\text{Na}_2[(\text{R*PO})_2(\alpha\text{-A-PW}_9\text{O}_{34})]$). Nella strategia di funzionalizzazione, l'uso di un sale di tetrabutilammonio ($n\text{Bu}_4\text{NBr}$) promuove la solubilizzazione del POM in CH_3CN.

I derivati ibridi ottenuti sono stati caratterizzati allo stato solido ed in soluzione utilizzando una combinazione di tecniche diverse (NMR multinucleare, FT-IR, ESI-MS). La caratterizzazione ha suggerito una bis-funzionalizzazione dello *scaffold* inorganico: due

molecole dello stesso fluoroforo organico sono ancorate sulla superficie del POM secondo un arrangiamento a *tweezer*. Sono state, quindi, studiate le proprietà ottiche e chiroottiche dei derivati ibridi luminescenti preparati e, in particolare, mediante indagini di fluorescenza, è stato possibile studiare la loro capacità come sensori verso ioni metallici e molecole organiche:

(i) Il derivato bis-dansilato coordina selettivamente ioni metallici bivalenti, come il rame e il piombo, i quali possono essere, così, rilevati in concentrazione micromolare in soluzione organica. In seguito alla presenza di Cu^{2+} e Pb^{2+}, in soluzione, sono stato stati osservati, rispettivamente, uno spegnimento e un aumento della fluorescenza del derivato.
(ii) Il sistema esteso π del POM ibrido contenente pirene è stato, invece, sfruttato per legare il fullerene. In particolare, misure di luminescenza hanno evidenziato l'interazione del POM con molecole di fullerene nell'intervallo micromolare.

I sistemi luminescenti proposti potranno essere utilizzati in diversi ambiti applicativi: sensoristica, catalisi, nanoelettronica, e fotochimica.
Inoltre, considerando il potenziale utilizzo dei POMs in ambito biomedico, che include possibile attività antibatterica, antivirale e antitumorale, la loro associazione con domini organici e leganti è di interesse anche per disegnare nuove strategie di *delivery* e di *targeting*. A questo proposito, l' utilizzo di POMs ibridi potrebbe consentire: (i) l'uso di derivati con maggiore stabilità e biocompatibilità; (ii) l'incremento dell'affinità dei derivati nei confronti di vettori cellulari e di bersagli biologici; (iii) l' associazione di sonde luminescenti per il rilevamento di POMs nelle cellule. In particolare, POMs ibridi luminescenti, possono essere utilizzati per il *bio-imaging*, consentendo anche lo sviluppo di protocolli terapeutici innovativi. A tale proposito, quindi, sono stati investigati i fenomeni di aggregazione e la stabilità dei poliossanioni in soluzione fisiologica mediante indagini di *dynamic light scattering* (DLS), microscopia a scansione elettronica (SEM) e microscopia a trasmissione elettronica (TEM). Le analisi hanno permesso di evidenziare, per tali derivati, la formazione di aggregati sferici con un' amplia distribuzione delle dimensioni. La formazione di questi aggregati è probabilmente dovuta alle interazioni idrofobiche che coinvolgono i residui aromatici, mentre i cationi tetrabutilammonio possono minimizzare la repulsione tra gruppi polianionici adiacenti. Inoltre, poichè la luminescenza di questi sistemi viene mantenuta anche in condizioni fisiologiche, essi sono stati veicolati all'interno delle cellule, e localizzati in diverse regioni subcellulari, come nei nucleosomi e nei mitocondri. Studi dell' attività

biologica dei POMs ibridi hanno, in seguito, mostrato una ridotta tossicità a basse dosi. Questi risultati sono molto promettenti in quanto potrebbero aprire la strada all' utilizzo di POM ibridi, come farmaci o supporti biologici per molecole bioattive, in nanomedicina.

Poichè, inoltre, la preparazione di derivati ibridi potrebbe essere una potente strategia per l'introduzione di siti di riconoscimento molecolare e il miglioramento della biocompatibilità del derivato stesso, sono stati condotti anche studi di interazione tra POMs e POMs ibridi con importanti macromolecole biologiche, come la ferritina e l'avidina.

Ad esempio, abbiamo studiato l' interazione ionica fra due diversi tipi di POM ($[Ru^{IV}_4(\mu\text{-}OH)_2(\mu\text{-}O)_4(H_2O)_4(\mu\text{-}SiW_{10}O_{36})_2]^{10-}$ e $[EuW_{10}O_{36}]^{9-}$) con la proteina ferritina (Ftn) mediante l' ausilio della combinazione di diverse tecniche che hanno incluso: DLS, *ζ-potential*, ITC (calorimetria isotermica di titolazione), fluorimetria, CD (dicroismo circolare) e TEM. In particolare, abbiamo osservato (i) lo spostamento del potenziale ζ di Ftn verso valori più negativi, in presenza del POM e (ii) il completo *quenching* della luminescenza di Ftn (Trp: λ_{ex} = 290 nm, λ_{em} = 327 nm), in seguito all' aggiunta di > 24 equivalenti di POM, dovuto, probabilmente, a trasferimenti energetici tra il POM e la macromolecola. Infine, l'integrità della proteina è stata verificata mediante analisi DLS e CD.

Inoltre, è stato preparato un POM ibrido biologico contenente due molecole di biotina, al fine di valutare la sua capacità di interazione con la proteina avidina. In particolare, questo tipo di studio ha permesso di investigare la possibilità di confinare POM ibridi in corrispondenza di siti specifici di legame delle proteina e di esplorare la progettazione di nuovi sistemi bioconiugati con proprietà di riconoscimento molecolare, sfruttabili in terapie di *targeting*.

Infine, è stata studiata una strategia di sintesi di un complesso di iridio, contenente come legante un poliossoanione ibrido funzionalizzato con un gruppo imidazolico. Questo lavoro è stato svolto nel laboratori di ricerca del Prof. Martin Albrecht presso University College of Dublin, Dublino, Irlanda. In questo caso, Il POM ibrido, preparato è stato sperimentato nella riduzione di gruppi carbonilici, mediante trasferimento di atomi di idrogeno da agenti riducenti sacrificali (*i*PrOH). La riduzione di benzofenone a difenil metanolo in *i*PrOH è stata, quindi, utilizzata come reazione modello per investigare l'attività catalitica del complesso. In particolare, è stato possibile ottenere una conversione completa dopo 120 min, utilizzando *t*BuOK come base.

Contents

Chapter 1

General introduction

1.1 Polyoxometalates: a general presentation

The history of polyoxometalates (POMs) goes back to early XIX century[1] when the discovery that metals belonging to early transition series, such as niobium, vanadium, tantalum, molybdenum, and tungsten in their higher oxidation states (configuration d^0 or d^1) can form in aqueous solution (at suitable pH, concentration and temperature) discrete polynuclear oxoanions with variable dimensions, ranging from few Angstrom and tens of nanometers.[2, 3, 4, 5,6] A first classification of these complexes is based on their chemical composition, essentially represented by two types of general formula.[2, 3, 4, 5, 6]:

a) $[M_mO_y]^{p-}$

b) $[X_xM_mOy]^{q-}$

where M is the main transition metal constituent of the polyoxometalate, O is the oxygen atom and X can be a non-metal atom as P, Si, As, Sb, another element of the p block, or a different transition metal. In the first case (a), polyoxometalates are called *isopolyanions*; while in the second case (b), they are called *heteropolyanions*.

There are many types of polyoxometalate structures (Lindqvist, Keggin, Wells-Dawson, Kreb), obtained by a careful tuning of the synthetic parameters: concentration, stoichiometric ratio of the reactants, temperature, acidity. Some examples of polyoxometalate structures are reported in figure 1.1.

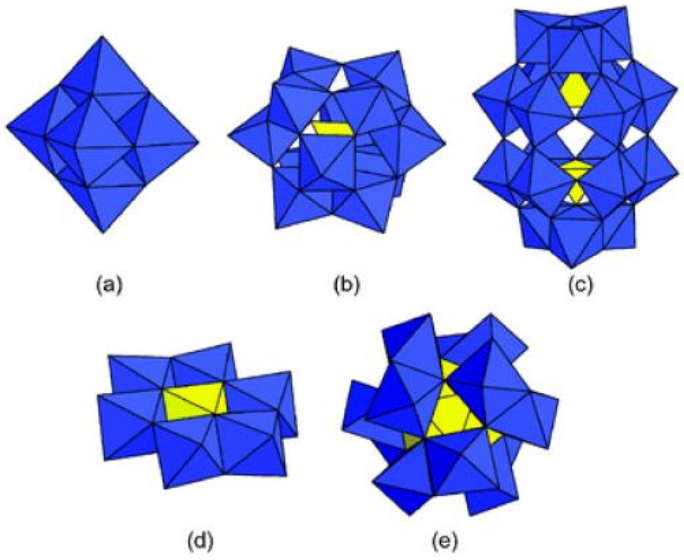

Figure 1.1 *Polyhedral* representation of polyoxometalates, in which blue octahedra are centred on tungsten atoms, while the yellow tetrahedra are centered on the central hetroatom.
a) *Lindqvist* structure $[M_6O_{19}]^{2-}$ (M = Mo, W); b) *α-Keggin* structure $[XW_{12}O_{40}]^{n-}$ (X = P, Si, B, Al, Ge; M = Mo, W); c) *α-Well Dawson* structure $[X_2M_{18}O_{82}]^{n-}$; d) Anderson-Evans heteropolyanion $[XMo_6O_{24}]^{m-}$ (X = P, As, Mn); e) *Dexter* structure $X_2M_{12}O_{42}^{n-}$.

The accessibility to such structural and compositional diversity is reflected in a broad range of properties that involve shape, redox potential, surface charge, acidity and solubility. Noteworthy, isostructural polyoxometalates may also display different properties depending on the heteroatom X, whereas the associated countercation is pivotal to foster solubility in different solvents. Properties and reactivity of POMs can thus be tuned and controlled at molecular level.

In most cases, the structure of the polyoxometalates is derived from the aggregation of octahedral units MO_6 with a central metal atom M and the oxygen atoms placed on their corners. In such octahedra, oxygen atoms exhibiting simple bonds with the metal allow the condensation between two octahedral units, while one oxygen atom- or a maximum of two – present a double bond character with the central metal atom and they are not shared with other metal atoms within the complex (terminal oxygens, Lipscom' s law[7]). In the following Figure 1.2, two kinds of octahedra constituting POM structures are represented[2]: the first one is a terminal mono-oxo type presenting only one terminal oxygen atom, while the other five oxygens are shared with other atoms of the polyoxometalate; the second one is a terminal *cis*-di-oxo type and it presents two terminal oxygens, in *cis* position, while the remaining four oxygens are shared by other metals in the whole polyoxometalate structure.

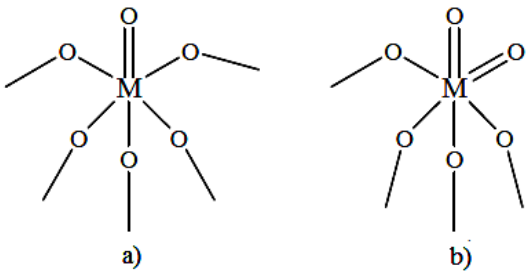

Figure 1.2 Octahedra constituting the most common structures of the polyoxometalates.

Two are the main characteristic features that a metal must possess to originate polyoxometalate complexes[2]:

i) dimensions (cationic radius) compatible with a octahedral coordination;

ii) presence of empty and available d orbitals, to allow the formation of terminal metal–oxygen double bond.

The first feature explains, for example, the absence of a polyoxoanionic chemistry for Cr (VI): indeed, its smaller dimensions (ionic radius = 0.58 Å) allow only up to four coordinating oxygens.

The octahedra condensation takes place through shared oxygen atoms, with the formation of μ - oxo bridged bonds between two metals ions, by the following three different ways[3,8]:

i) corner sharing;
ii) edge sharing;
iii) face sharing (less frequent).

These sharing modes are represented in figure 1.3. The presence of terminal oxygen atoms is essential for the aggregation to take place in discrete structures and not in an extended material (as for most common metal oxides, silicates, germanates, tellurates). Since terminal oxygens are less basic, they are not suitable for the condensation with other monomeric units, thus providing a barrier towards the linear polymerization and finally favouring discrete molecular units. [2]

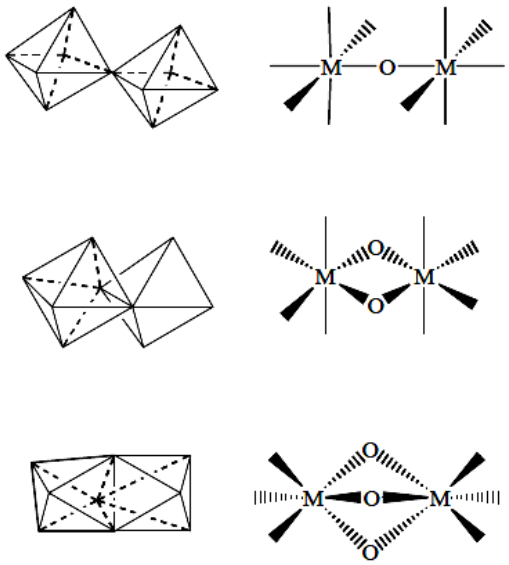

Figure 1.3 Condensation of the octahedral units in polyoxometalates.

1.1.1 α-Keggin structure

One of the most important class of polyoxometalates, is that of Keggin heteropolyanions. Their general formula is $[XM_{12}O_{40}]^{n-}$, with M = Mo (VI) or W (VI). Keggin obtained the structure of the hexahydrated dodecatungstophosphoric acid for the first time in 1934, by X-ray investigations[9]. This structure is called α-Keggin and consists of a central PO_4 tetrahedron surrounded by 12 octahedra WO_6 belonging to the mono-oxo terminal type.

Such octahedra are disposed in four groups (triplets M_3O_{13}), each of them constituted by the aggregation of three octahedral units by edge-sharing. The four different triplets are condensed each other by corner-sharing.

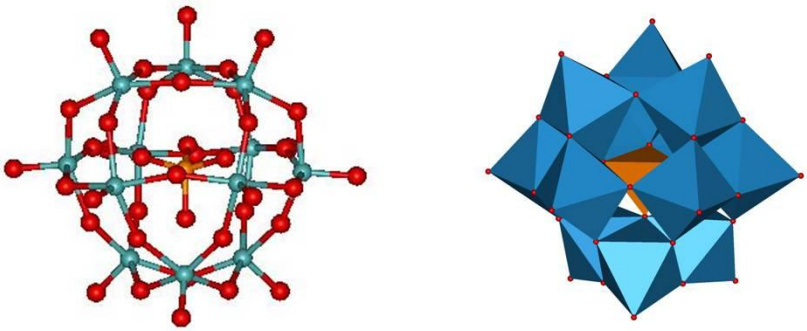

Figure 1.4 Two representation of the same α-Keggin structure of the $[\alpha\text{-}PW_{12}O_{40}]^{3-}$ heteropolyanion. On the left side a *ball-and-stick* model is represented: the red spheres are oxygen atoms, the blue ones are tungsten atoms and the orange one is the central phosphorous atom. On the right side a *polyhedral* model is represented: blue octahedra are centred on tungsten atoms, while the orange tetrahedron is centered on the phosphorous atom.

Structure and symmetry of α-Keggin polyanions have also been confirmed in solution by ^{29}Si, ^{31}P and ^{183}W NMR spectroscopies. [10, 11, 12,13] NMR characterizations of $[\alpha\text{-}PW_{12}O_{40}]^{3-}$ and $[\alpha\text{-}SiW_{12}O_{40}]^{4-}$ are reported in Table 1.1. The chemical equivalence of the 12 tungsten atoms leads to a single signal in both the ^{183}W NMR spectra,[10] while one signal is observed for the central atom (Si or P).[11, 12]

Keggin polyoxometalates can also present structural isomers, which are formally obtained from the α structure by 60° rotation of one (β isomer), two (γ isomer), three (δ isomer) or four (ε isomer) triplets M_3O_{13}.[2,3] These isomers are characterized by lower symmetry and by a decreased thermodynamic stability with respect to the α structure.

Table 1.1 Heteronuclear NMR characterizations of heteropolyanions with α-Keggin structure.

Polyoxoanion	^{183}W NMR[a] δ, ppm	^{31}P NMR[b] δ, ppm	^{29}Si NMR[c] δ, ppm
$[\alpha\text{-}PW_{12}O_{40}]^{3-}$	-99.4	-14.9	---
$[\alpha\text{-}SiW_{12}O_{40}]^{4-}$	-103.8	---	-85.3

[a] ref.: 1 M WO_4^{2-} in D_2O; [b] ref.: 85% H_3PO_4; [c] ref.: $Si(CH_3)_4$; [d] ref.: H_2O.

1.1.2 Vacant structures

Heteropolyoxotungstates described above are also called "saturated" structures, due to the high symmetry, the low anionic charge and the stability of the structure itself. Starting from them, it is also possible to synthesize derivatives with defects in the structure, the so called "vacant" (or "lacunary") polyoxometalates. Such complexes derives from the saturated original polyoxometalate, through the formal loss of one or more MO_6 tetrahedral units, thus affording vacancies on the surface. Synthetic procedures and experimental conditions to yield these species are strictly related to the thermodynamic and kinetic stability of the lacunary complexes themselves, which can be obtained from the precursors in suitable conditions of temperature, concentration and pH.

As an example, the synthetic procedure and the structure of a monovacant tungsten complex $[XW_{11}O_{39}]^{n-}$ (X = Si^{IV}, P^{V}, …), derived from the α-Keggin structure is reported below.[14]

The vacant complex $[XW_{11}O_{39}]^{n-}$ is stable and it can be isolated. Its synthesis can be obtained starting from $[\alpha\text{-}XW_{12}O_{40}]^{(n-4)-}$, as well as by mixing stoichiometric amounts of mononuclear metal salts and adjusting the pH to a specific acidic value.

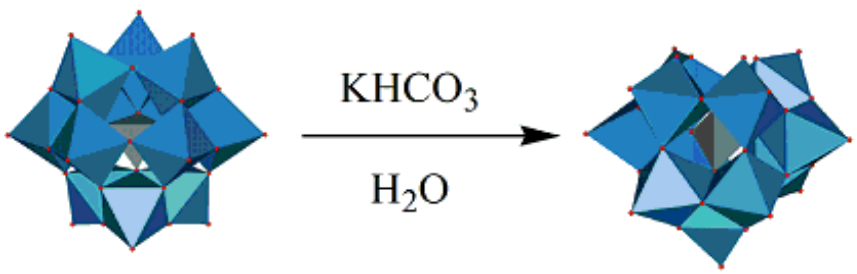

Scheme 1.1 Synthetic procedure of the monovacant α-Keggin $[XW_{11}O_{39}]^{n-}$.

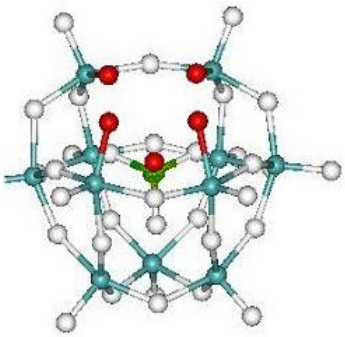

Figure 1.5 *Ball-and-stick* representation of the structure of the monovacant α-Keggin $[XW_{11}O_{39}]^{n-}$. The blue spheres are tungsten atoms, the white ones are oxygens and the green one is the central heteroatom X. The red spheres are the nucleophilic oxygen atoms bordering the vacant site.

The same considerations applies to di- ($[XW_{10}O_{36}]^{m-}$) and tri-vacant species ($[XW_9O_{33}]^{p-}$), resulting from the formal loss of two or three octahedra, respectively.[15]

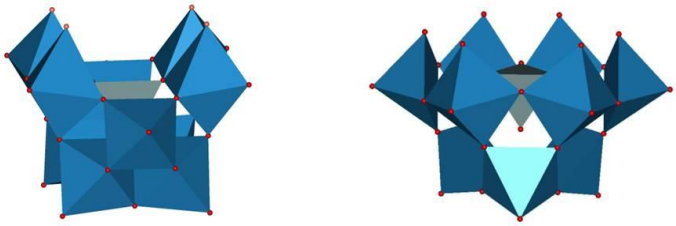

Figure 1.6 Polyhedral structures of di- (left) and tri-vacant Keggin polyoxotungstates (right).

Since these vacant polyanionic complexes feature reactive terminal, coordinatively unsaturated, oxygen atoms around the vacant sites, their nucleophilicity can be exploited to prepare the following derivatives:

i) Transition metals-substituted polyoxometalates (TMSPs) complexes

The reaction between a vacant polyoxometalate with a suitable transition metal precursor (M = Cr, Fe, Mn, Co e Ru) allows the incorporation of such metal on the POM structure, giving *Transition Metals-Substituted Polyoxometalates* (TMSPs) complexes (see Figure 1.7 A). In several cases, a "out-of-pocket" coordination of transition metals yields *sandwich-like* dimeric structures, whereby the metal ions bridge the subunits (Figure 1.7 B).[16,17]

TMSPs show high stability, since the transition metal becomes an effective constituent of the whole polyanion structure.

ii) Organic inorganic hybrid polyoxometalates (hybrid POMs)

The vacant polyoxometalates can react with electrophilic organic moieties to give O-X-R bonds, where X = As, P, Si, Sn, and R = organic residue. In this way organic - inorganic hybrid POM complexes are formed (see Figure 1.7 C).[18,19,20]

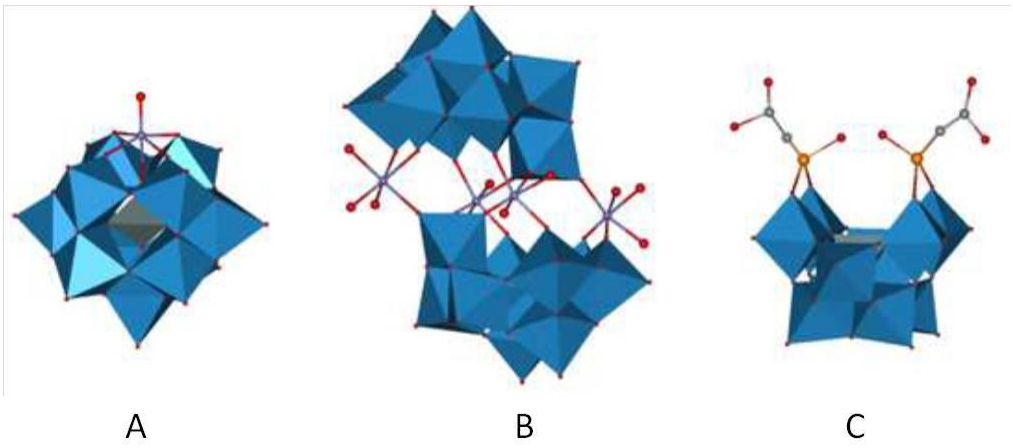

Figure 1.7 Examples of derivatives obtained from vacant POMs: **A** $[\alpha\text{-Fe}(H_2O)SiW_{11}O_{39}]^{5-}$; **B** $[Fe_4(H_2O)_{10}(\beta\text{-}AsW_9O_{33})_2]_6$; **C** $[(HO_2CCH_2PO)_2(\gamma\text{-}SiW_{10}O_{36})]^{4-}$.

1.1.3 Proprieties of POMs

Different properties make polyoxometalates very interesting in different scientific fields such as catalysis, material science and medicine[4]:

(i) In catalysis, their use as Brönsted acids and homogeneous oxidation catalysts has been firmly established since the late 70s and 80s, respectively.[21] Polyoxometalates in their protonated forms are called *heteropolyacids* (HPAs) and show a very strong Brönsted acidity, approaching the superacidic behavior; on the other hand, they are efficient oxidants, exhibiting fast reversible multielectron redox transformations under rather mild conditions. Furthermore, their acid-base and redox properties can be varied over a wide range by changing the chemical composition. On top of that, POMs exhibit a fairly high thermal stability in the solid state and they can be easily solubilized in a wide range of solvents, by choosing a suitable counterion. Of particular interest is the structural analogy between molecular POMs and extended solid oxides, as they may provide soluble models

to investigate reactions and surface properties of such related materials.[2,22] The intriguing prospect is to use the well-defined and discrete POM based systems as molecular probes to trace new mechanistic pathways at the heterogeneous interface of metal oxide surfaces.[21,23]

(ii) The anchoring of organic substituents on the POMs surface offers the possibility to tune the stereoelectronic features of the resulting complexes, and to affect their solubility, reactivity, and hydrolytic stability.[19,21,23] This strategy was successfully employed to obtain polymerizable,[24] dendrimeric[25], and supramolecular derivatives[26]. Indeed, the merging of organic and inorganic domains is a developing field of investigation, mainly focusing on the design of new hybrid materials.[27] *The concept of hybrid polyoxometalates will be developed in the paragraph 1.2: Hybrid POMs: synthesis and applications.*

(iv) More recently, an increasing number of potential medical properties for polyoxometalates have been reported in the literature. Several papers deal with their bioactivity as antibacterial, antiviral, antitumoral agents or focused on their interactions with proteins.[28] *The application of POMs in medicine will be developed in detail in the paragraph 1.3: Polyoxometalates in Medicine.*

1.2 Hybrid POMs: synthesis and applications

1.2.1 Synthetic strategies to obtain hybrid POMs

In relation to the synthetic strategy adopted for their construction, POM hybrids can be classified on the basis of of interaction type between their organic and inorganic subunits. In particular, *Class I* is made up of all the species in which only non-covalent interactions (i.e., hydrogen bonds, electrostatic, or van der Waals interactions) occur between the two domains, while in *Class II* the organic and inorganic moieties are linked via covalent bonds.[21,23]

1.2.1.1 *Class I* hybrids

The polyanionic nature of POMs offers a unique advantage in order to generate structural and function diversity, simply by counterion exchange.[19c] Moreover, due to the cooperative effect of multiple ionic interactions, polycharged species can be assembled in highly stable structures and evolve to persistent nano-architectures. This category includes all POM derivatives associated with organic cations (tetraalkylammonium or phosphonium), polycationic polymers, dendrimers and dendrons, and organometallic complexes with a positive charge.

As an example, following this approach, in our research group, a tetraruthenium substituted POM complex $[Ru_4(\mu\text{-}OH)_2(\mu\text{-}O)_4(H_2O)_4(\gamma\text{-}SiW_{10}O_{36})_2]^{10-}$ (RuPOM) has been associated to cationic polyaniline (PANI), polydiallyldimethyammonium charged polymers (PDDA) or on carbon nanotubes decorated with positively charged dendrons. This POM is known as a highly robust and efficient water oxidation catalyst. In particular, the unique mechanistic and stability features of RuPOM have been exploited to prepare innovative nano-structured oxygen-evolving anodes, upon assembly of the POM cluster on the functionalized nanotubes.[29]

.

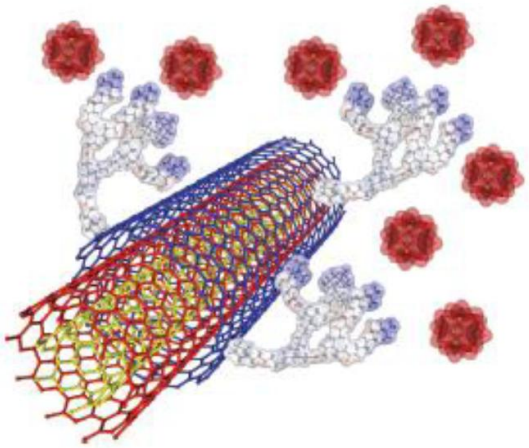

Figure 1.8 Electrostatic immobilization of the RuPOM on the surface of nanotubes functionalized with positively charged dendrons.

1.2.1.2 *Class II* hybrids

Organic derivatization of polyoxometalates is mainly achieved from lacunary heteropolyoxometalates (paragraph 1.1.2), since the nucleophilic vacant oxygen atoms can react with electrophilic groups such as organophosponates, organoarsonates, organotin, etc.[18,19] In particular, the variety of electrophilic groups available, combined with the various topologies observed in lacunary heteropolyoxometalate realm, explains the recent development of such organic/inorganic hybrids. The structure of the vacancy and the structural organization of the functionalizing agents are key parameters that need to be considered for the synthesis of functionalized heteropolyoxometalates. Furthermore, it has to be noticed that, aside from few exceptions, the functionalization of heteropolyoxometalates of Keggin and Dawson families is mainly observed with vacant tungsten species.

In 1978, Klemperer first synthesized a functionalized polyoxometalate from a lacunary structure: $[PW_{11}O_{39}]^{7-}$ was reacted with $CpTiCl_3$ in CH_2Cl_2 to give $[PW_{11}O_{39}(TiCp)]^{4-}$.[30] This approach was soon extended to the reactions of other hydrolyzable compounds such as

$RSiCl_3$, $RGeCl_3$, $RAsCl_2$, $RP(O)Cl_2$ and $RSnCl_3$ with monovacant Keggin and Dawson POM structures (Schemes 1.2 and 1.3).[31]

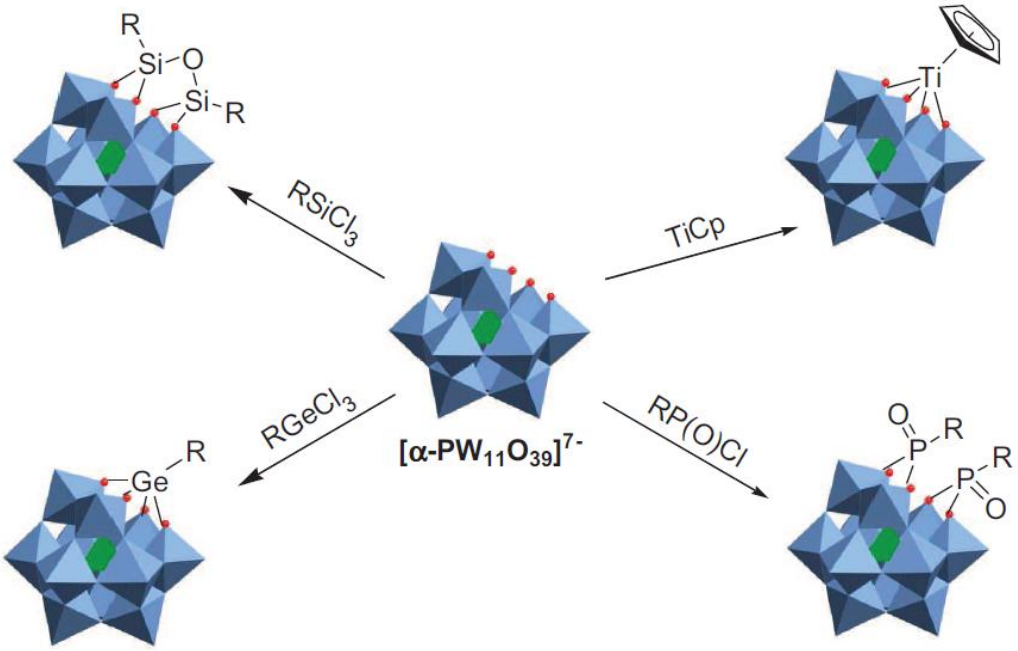

Scheme 1.2 Functionalization of monovacant Keggin $[\alpha\text{-}PW_{11}O_{39}]^{7-}$ POM with organic moieties to yield hybrid POMs.

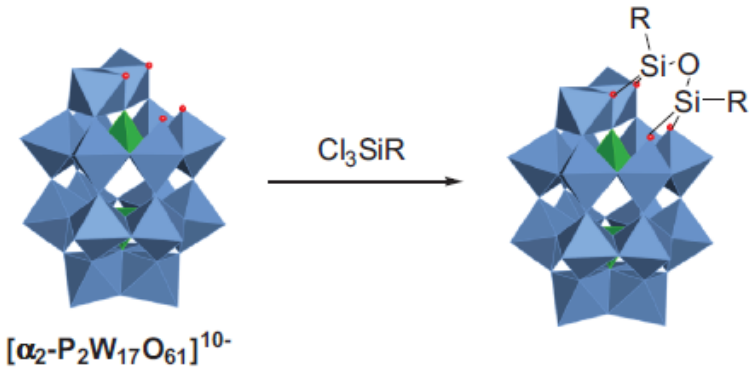

Scheme 1.3 Functionalization of monvacant Dawson $[\alpha_2\text{-}P_2W_{17}O_{61}]^{10}$ POM with organic moieties to yield an hybrid POM.

In our Research Group, different procedures have been optimized in order to synthesize organic–inorganic POM-based hybrid complexes, starting from both organosilyl (SiX_3, X = Cl, OMe) and organophosphonyl (POX_2, X = Cl, OH) compounds as electrophilic reagents. The covalent functionalization of different lacunary POMs has been achieved with yields ranging from 65 up to 90%.[32] The use of the bivacant complex $[\gamma\text{-}SiW_{10}O_{36}]^{8-}$ has shown to be convenient for these reactions, since it is characterized by a higher hydrolytic stability, than other vacant complexes, in the acidic environment required for these reactions. As in the case of the monovacant precursor (see Figure 1.5) it presents four equivalent nucleophilic vacant oxygen atoms. These features allow to obtain bis-functionalized products with high selectivity. The reaction occurs readily in acetonitrile under phase-transfer conditions, by addition of nBu$_4$NBr, that guarantee the solubility of the product.[33]

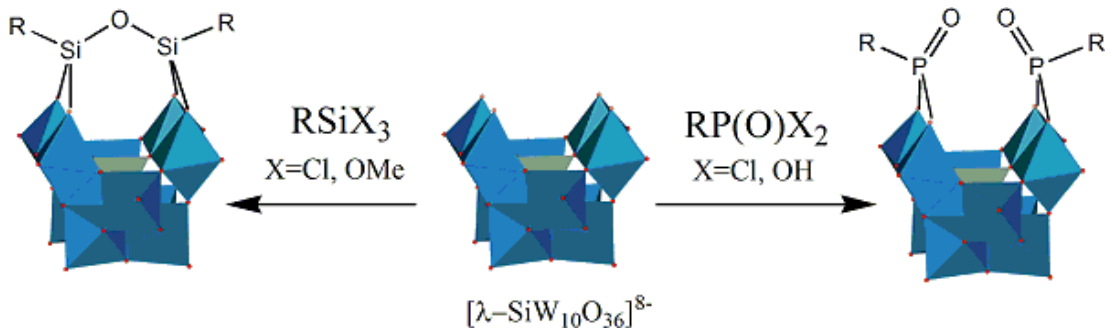

Scheme 1.4 Functionalization of divacant Keggin $[\gamma\text{-}SiW_{10}O_{36}]^{8-}$ POM with organic moieties to yield hybrid POMs.

Furthermore, to increase the complexity and diversity of these molecular structures, it is possible to chemically modify the organic arms grafted onto the polyoxometalate in post-functionalization reactions. In this respect, for example, in our research group, amino acid methyl esters were covalently linked to the phosphonoacetic-substituted POM $[(HOC(O)CH_2PO)_2(\gamma\text{-}SiW_{10}O_{36})]^{4-}$ by means of classic condensation reactions.[34] The synthetic scheme of the reaction is the following:

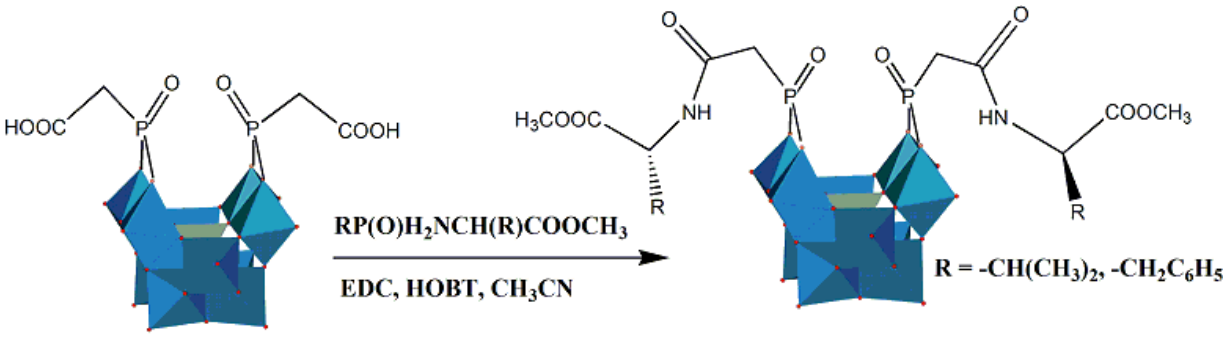

Scheme 1.5 Functionalization of the phosphonoacetic-substituted POM $[(HOC(O)CH_2PO)_2(\gamma\text{-}SiW_{10}O_{36})]^{4-}$ with amino acid methyl esters by means of classic condensation reactions.
EDC=Ethyl-γ-dimethylaminopropylcarbodimmide; HOBT =1-hydroxy-1,2,3-benzotriazole.

1.2.2 Hybrid POMs: molecules and materials with targeted properties and functions

One of the aims of this Thesis is to explore and broad the use of hybrid POMs towards different application fields. For a better contextualization of the results obtained, some examples of hybrid POM structures and their applications have been collected and discussed within this paragraph.

In general, the covalent functionalization of the POMs surface with organic residues can be exploited to:

(i) stabilize molecular inorganic structures, by preventing structure collapsing;[35]

(ii) tune the stereo-electronic features of the POMs surface, thus shaping their catalytic functions;

(iii) support organic residues and organometallic catalysts;[19(d),36,37]

(iv) provide solubilizing tags, suitable for a wide range of media, either aqueous or organic solvents, fluorinated phases, and non-conventional solvents, like ionic liquids;

(v) introduce polyfunctional groups to be used as spacers between polyoxometalates, so to obtain dimers, polymers and dendrimers;[20,33]

(vi) provide an efficient tool for the self-organization of POMs in various phases, their immobilization on surfaces and their embedding in polymer matrices.

In our research group, hybrids POMs obtained by functionalization of $[\gamma\text{-}SiW_{10}O_{36}]^{8-}$ POM scaffold with phenylphosphonic acid were used as catalysts in CH_3CN or in ionic liquids to perform oxidations of alcohols, olefins, sulfides and sulfoxides in the presence of H_2O_2, even under microwave irradiation (scheme 1.6).

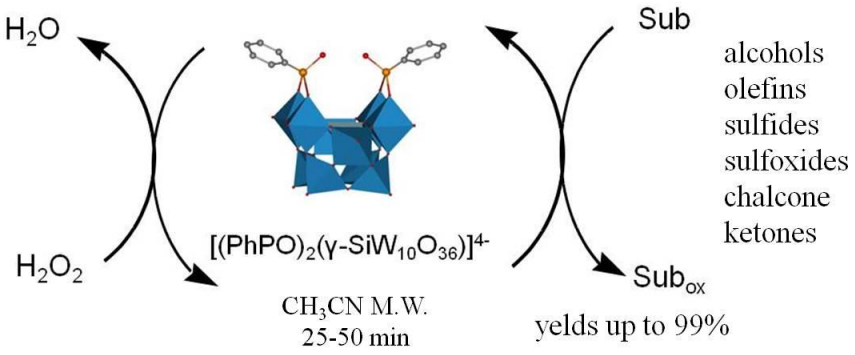

Scheme 1.6 POM-based catalysts for microwave-assisted H_2O_2 activation.

These hybrid derivatives presented superior performance and stability compared to the total inorganic POM precursors.[38] In addition, (i) functionalization of the vacant site prevents the thermal rearrangement of the POM structure, so to allow the use of harsher conditions, including microwave (MW) irradiation (Scheme 1.6); (ii) the catalyst activity is strongly dependent on the nature of the organic moieties decorating the POM surface.[19,39] The functionalization with chiral phosphonyl groups was also achieved, with the aim of performing enantioselective oxygen transfer.[34,39]

Furthermore, in our research group, a fullerene-based hybrid POM found application in photocatalytic oxygenations. The reactivity of the hybrid photocatalyst toward hydrosoluble organic substrates has been assessed in water at 25°C, irradiating with λ >375 nm, in the presence of dioxygen (1 atm) (Scheme 1.7).

Combining photoactive groups with POMs is a key strategy to access innovative photosensitized processes, with application in the field of photocatalysis and solar energy conversion.[19(d),40]

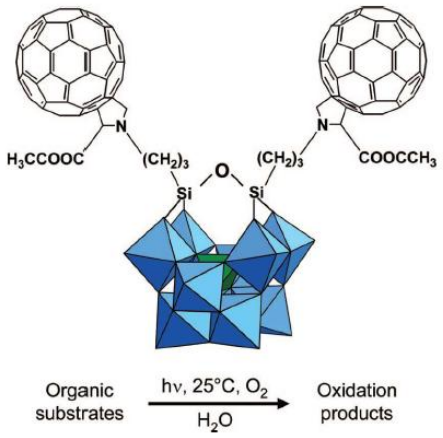

Scheme 1.7 Schematic representation of the structure of a photoactive fullerene-based hybrid POM, able to perform the photo-oxidation of organic substrates, as phenol and L-methionine, in water.

In particular, considering POMs ability to store several electrons with only minor structural reorganization, the association of organic sensitizers, as fullerene derivatives or different residues: pirene[41] and perilene[42], on the polyanionic scaffolds can be used to promote electron transfer phenomena between the two domains.

This behavior is of interest to access new systems capable of combining the three functions necessary to photosynthetic activity: (i) collection of light; (ii) charge separation; (iii) accumulation of charge.

As an example, a multi-porphyrin cluster has been covalently attached to a polyoxometalate catalyst in order to form an advanced model for the photosynthetic reaction complex. This bio-inspired mimic system, reported in Figure 1.9, displays efficient energy transfer from the peripheral zinc porphyrins (ZnP) to the central free-base porphyrin (FbP). The latter species participate in a light-induced electron transfer with the POM.[43]

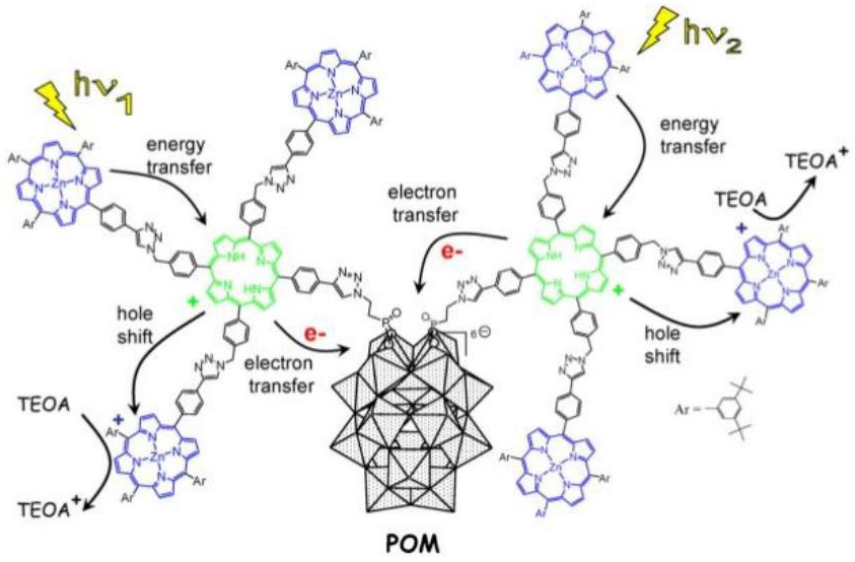

Figure 1.9 Schematic representation of the structure and of the light-induced electron transfer for the POM-based multi-porphyrin cluster.

Unprecedented functionalization strategies of lacunary POMs with different luminescent probes, as well as their optical and sensing properties will be presented in Chapter 2: paragraph 2.2.3. In addition, they have been delivered into model human cells (see Chapter 3: paragraph 3.2.1).

Polyanionic inorganic scaffolds were also functionalized with organometallic complexes, examples include metallo-salen,[36(a)] Wilkinson-type rhodium ligands[36(b)]. These hybrids were, generally, described as being more active and/or selective than the related organometallic precursor complexes. The main role of the POM scaffold is to tune the steric and electronic properties of the catalyst. Another expected role of the POM is to enhance the robustness to the whole hybrid (see also *Chapter 4*, paragraph 4.1.1). In our research group, POM-appended N-heterocyclic carbene (NHC) palladium complexes, capable to promote C-C cross coupling reactions were also synthesized.[37]

In Chapter 4, the design of a novel POM-appended N-heterocyclic carbene (NHC) iridium organometallic complex and its catalytic activity in hydrogen transfer reactions will be discussed.

Finally, POMs serve also as building blocks for the bottom-up assembly of organic–inorganic hybrid 3D structures with applications in materials science, surface chemistry, electrochemistry and photochemistry.[19c),29,44,45]

In this research group, Strandberg-type polyoxomolybdates[$(R^*PO_3)_2Mo_5O_{15}]^{4-}$ where R* is a chiral amino-phosphonate, were prepared. Due to the formation of a hydrogen bonded network, these hybrid units self-assembleand evolve to a hierarchical architecture of entangled fibers, showing solvent gelation capability, and amplification of chirality (Figure 1.10).[27(b)]

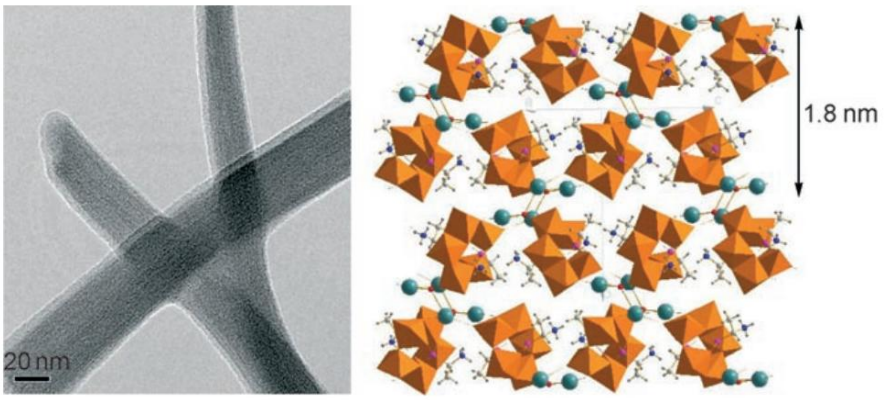

Figure 1.10 Left: TEM analysis of Na-(R,R)-$[(R^*PO_3)_2Mo_5O_{15}]^{2-}$. Right: crystal packing diagram for Rb-(R,R)-$[(R^*PO_3)_2Mo_5O_{15}]^{2-}$. MoO_6 octahedra orange, O red, P magenta, C gray, N blue, H white, Rb azure.

Moreover, considering the redox activity of POMs, numerous electronic devices based on the interaction between POMs and electrically active materials (eg carbon nanotubes, graphene, semiconductors, etc..) have been developed (Figure 1.11). In these devices, POMs play the role of mediators for electron transfers. Indeed, they can act as electron reservoirs after photochemical or electrochemical reduction, to their corresponding colored mixed-valence species with no significant structural changes.

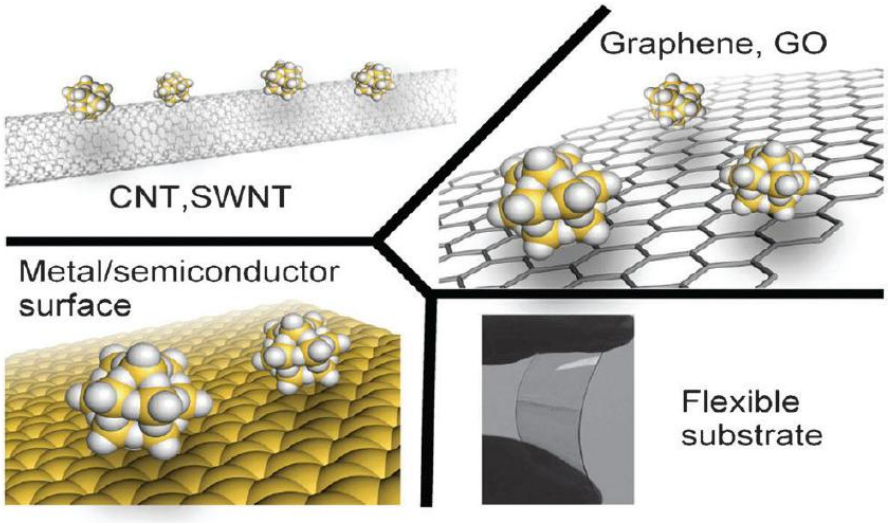

Figure 1.11 Hybrids based on POMs and electrically active materials.

In the field of Li-ion battery, for example, different electrodes based on POMs hybridized with polyaniline,[46] carbon[47] or single-wall nanotubes (SWNTs)[48] were built; the resulting batteries show an increased capacity, due to the high storage electronic ability of POMs, based on reversible multi-step reduction processes.

1.3 Polyoxometalates in medicine

An increasing number of potential applications for polyoxometalates in human medicine have been reported in the literature. Several papers deal with their bioactivity as antibacterial, antiviral, antitumoral agents.[28]

The main advantageous feature of POMs is that nearly every molecular property that impacts the recognition and reactivity of POMs with target biological macromolecules can be controlled. These include polarity, redox potentials, surface charge distribution, shape, and acidity. As already introduced above, another attractive feature is that rational and reproducible synthetic methods are now available (i) for the replacement of one or more of the skeletal d^0 early transition metal cations in POMs with d- or p-block ions and also (ii) for the covalent attachment of organic groups to POMs via linkages that are compatible with physiological conditions (long half-lives in H_2O or buffers at pH~7). Both metal substitution and organic derivatization extend considerably the number of POMs that are potentially bioactive. In particular, organic/biological pendant groups could be used to improve bioavailability and drug formulation, or to introduce recognition functions of target

biomacromolecules. To date, there are only few papers involving the biological behavior of POMs derivatized with organic groups, so this is a largely uncharted technical territory.

The main disadvantage of POMs medicine is that they are not organic species. Low molecular weight, organic species dominate in the pharmaceutical industry (drug discovery, synthesis and development). An intrinsic counterpoint is that POM-based pharmaceuticals are much less expensive and more amenable to scale-ujp than the great majority of organic pharmaceuticals, so their successful application might positively impact large and growing markets in the emerging world.

Two types of POM activity, antiviral and antitumoral, have dominated the medicinal chemistry of these compounds to date. Moreover, the antibiotic activity of some POMs has been demonstrated recently. These topics will be presented in the next paragraphs.

1.3.1 Bioactivity of POMs

1.3.1.1 Antiviral activities

In 1970, Chermann and coworkers noticed an inhibitory effect of "silicotungstic acid supernatants (STAS)", a cell culture supernatant obtained in a procedure where silicotungstic acid was employed.[49] They subsequently recognized that the inhibitor was the silicotungstate ion,[50] and this led to a systematic study of the antiviral activities of this and other polyanions.[51] Prior to 1990, in *vitro* studies conducted by various groups showed the efficacy of these POMs against several viruses: murine leukemia sarcoma (MLSV), vesicular stomatitis (VSV), polio, rubella, Rauscher leukemia (RLV), Rabies (RV), Rhabdovirus, and Epstein-Barr (EBV). Most of these POMs showed good inhibitory activity with low cytotoxicity, in a variety of cell lines. A particular effective compound was the tungstoantimonate $(NH_4)_{19}[Sb_9W_{21}O_{86}]$ (HPA-23). This POM was shown to be an effective antiviral agent against MLSV, RV, rhabdovirus and EBV, at nontoxic doses for the cells.[52]

The advent of AIDS has increased the search for antiviral agents, and encouraged many studies that included polyoxometalates. In particular the groups of Hill and Yamase were very active in this area.[28(a)]

More recently, many different POMs have been shown to selectively inhibit in *vitro* the replication of retro-, toga-, paramyxo-, flavi-, and several herpes viruses and cytomegalovirus (CMV). Of significance was the finding that most POMs are highly effective against HIV-1, HIV-2, and simian immunodeficiency virus (SIV) in culture. Their activity is primarily antiviral and not virucidal (i.e., they do not interact directly with the virus in cell-free systems).

As for instance, the activities of cesium and tetramethylammonium (TMA) salts of polyoxotungstate anions with covalently attached organosilyl groups against human immunodeficiency virus in primary human lymphocytes were evaluated (Figure 1.12).[53]

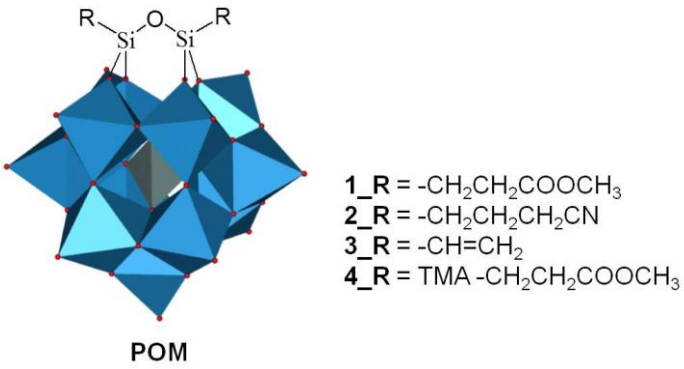

Figure 1.12 Structure of the hybrid POM $[(RSi)_2O(\gamma\text{-}SiW_{11}O_{39})]^{4-}$. **1-3_R**: cesium (Cs) salts, **4_R**: tetramethylammonium (TMA) salt.

Table 1.2 lists the median effective concentration (EC_{50}), and the median inhibitory concentration (IC_{50}) of compounds **1-4_R** compared to phosphonoformate (PFA), an antiviral agent used as a positive control, tested on human peripheral blood mononuclear cells (PBMC).

Table 1.2 Anti-HIV-1 activity and toxicity of organosilyl functionalized polytungstosilicate complexes (**1-4_R**) in Human PBM cells.

#	R	**HIV-1 in PBMC: EC_{50}[a]**	**toxicity in PBMC: IC_{50}[b]**
1_R	$CH_2CH_2COOCH_3$	3.3	>100
2_R	$CH_2CH_2CH_2CN$	19.8	>100
3_R	$CH{=}CH_2$	35.3	>100
4_R	TMA $CH_2CH_2COOCH_3$	39.0	>100
	Phosphonoformate	21.0	>100

[a]EC_{50} = median effective (antiviral) concentration in µM. [b]IC_{50} = median inhibitory (toxicity) concentration in µM.

The activities (EC_{50}) of these compounds against human immunodeficiency virus in primary human lymphocytes range from 3.3 µM to 39.0 µM. Their IC_{50} values are all greater than 100

μM. Compound **1_R**, was the most potent in the series with an EC_{50} of 3.3 μM and no toxicity to the uninfected host human lymphocytes when tested up to 100 μM.[53]

While the inhibition of viruses by POMs has been well documented, the primary mechanism for antiviral action has remained elusive. Both data and physical properties of POMs outlined in literature are consistent with multiple modes of action. The most likely of these are inhibition of viral enzymes (reverse transcriptase, RT, and/or protease in retroviruses).[53] The polyanionic POM was proposed to bind electrostatically to the viral enzymes. Consequently, the charge and size of the POM was postulated to be a factor in viral inhibition. Nearly all the early experimental work on POM antiviral activity addressed inhibition of RT.[28(b)]

Another possible antiviral mechanism is the inhibition of surface viral proteins (such as gp120 for HIV).[54] Indeed, a strong interaction between a chemotherapeutic agent and viral surface proteins can lead to inhibition of virus-cell recognition and viral penetration into the cell (viral infectivity).

POM antiviral activity varies considerably, not only with the structural class, composition, size, and charge of the POM, but also with the virus and viral strain and the cell line at parity of virus strain. Moreover, countercations of the polyanion and the organic functions of the POM play a significant role in biological activity and selectivity.

As a final remark, while the antiviral effectiveness of over 200 POMs has been documented *in vitro*, the efficacy of fewer than 20 POMs has been documented *in vivo*.

1.3.1.2 Antitumoral activities

Antitumor activities of a variety of polyoxotungstates are mentioned in the scientific literature or in patents. In the last few years, Liu, Pope and their co-workers have investigated the cytotoxic properties of many heteropolyoxotungstates against cancer cell lines *in vitro*.[55]

The authors focused mainly on hybrid derivatives of heteropolyoxotungstates containing RSn or CpTi (Cp = cyclopentadienyl) groups. Attempts have been made to correlate the cytotoxicity of the compounds with the potential of the first reduction process. Within several series of closely related compounds, it was found that the sequence of IC_{50} values is consistent with the order of the reduction potential: the higher the reduction potential, the higher their cytotoxicity.[56] However, this correlation cannot be generalized: structure and composition clearly also play an important role in determining the activity.

The IC_{50} values of some hybrid heteropolyoxotungstates derivatives are reported in μM in Table 1.3.[28(b)]

Table 1.3 IC_{50} values in µM for different heteropolyoxotungstates on tumor cells *in vitro.*

Compound	Cancer Cell Line	
	SSMC-7721	**HeLa**
α-$[(CpTi)_3Si_3W_9O_{37}]^{7-}$	7.8	14.0
α-$[(CpTi)_3Ge_3W_9O_{37}]^{7-}$	4.0	7.6
β-$[(CpTi)_3Si_3W_9O_{37}]^{7-}$	6.7	12.1
γ-$[(CH_3OOCCH_2CH_2Sn)_2SiW_{10}O_{38}]^{6-}$	20.2	24.5
γ-$[(CH_3OOCCH(CH_3)CH_2Sn)_2SiW_{10}O_{38}]^{6-}$	19.0	23.2
γ-$[(C_5H_5Ti)_2SiW_{10}O_{38}]^{6-}$	4.4	8.8
$[(CH_3OOCCH_2CH_2Sn)_2PW_{10}O_{38}]^{5-}$	17.2	21.7
$[(CH_3OOCCH(CH_3)CH_2Sn)_2PW_{10}O_{38}]^{5-}$	16.7	21.1
$[(CH_3OOCCH_2CH_2Sn)_3(PW_9O_{34})_2]^{9-}$	8.7	9.1
$[(CH_3OOCCH(CH_3)CH_2Sn)P_2W_{17}O_{61}]^{7-}$	16.7	18.3
α-$[(CH_3OOCCH_2CH_2Sn)_3SiW_9O_{37}]^{7-}$	28.1	28.8
β-$[(CH_3OOCCH_2CH_2Sn)_3SiW_9O_{37}]^{7-}$	19.1	24.9
α-$[(CH_3OOCCH_2CH_2Sn)_3(SiW_9O_{34})_2]^{11-}$	10.8	15.6
$[(C_5H_5Ti)CoW_{11}O_{39}]^{7-}$	3.2	11.5
$[(C_5H_5Ti)BW_{11}O_{39}]^{6-}$	12.9	14.6

Furthermore, the encapsulation of $[CoW_{11}TiO_{40}]^{8-}$ in starch nanoparticles increases the cell penetration of $[CoW_{11}TiO_{40}]^{8-}$: the higher efficiency observed for this system is likely due to a higher concentration of the heteropolytungstate inside the cell (see also paragraph 1.3.3.1). Organic substituents on the polyoxometalate core might have the same effect (see paragraph 1.3.3.2) but this hypothesis still needs to be verified. Obviously, further investigations are necessary to elucidate the mechanism of the cytotoxicity of polyoxotungstates *in vitro*, and to establish a structure-activity relationship.

Few data are available on the antitumor activity of polyoxotungstates *in vivo*. Yamase reported, in his patent applications, the growth inhibition of Meth A tumors in mice by rare earth-containing decatungstates.[28] Yamase and his coworkers also recognized the antitumor

activities of Anderson-type polyoxomolybdates and of heptamolybdates *in vivo*.[28(a)] They found, in particular, that the compound $(NH_3iPr)_6[Mo_7O_{24}]$ significantly suppressed the tumor growth in mice bearing subcutaneously or intraperitoneally implanted methylcholanthrene-induced tumor (Meth A sarcoma) or MM-46 adenocarcinoma. Promising antitumor activity of $(NH_3iPr)_6[Mo_7O_{24}]$ was also reported against CO-4 human colon cancer and OAT human lung cancer xenografts. The antitumoral activity of POMs was found to compare favorably with that of commercial drugs. Based on the strong toxic effect of reduced heptamolybdate, the authors have proposed a mechanism for the antitumor action of $(NH_3iPr)_6[Mo_7O_{24}]$: the $[Mo_7O_{24}]^{6-}$ species would be reduced to $[H_xMo_7O_{24}]^{6-}$ after thermal activation of a oxygen-to-molybdenum-charge-transfer. The reduced species would then be reoxidized by reduction of the tumor cell, causing cell lysis.

1.3.1.3 Antibacterial activities

In 1993, Tajima reported that the lacunary Keggin polyoxotungstate $[PW_{11}O_{39}]^{7-}$, when used in combination with β-lactam antibiotics, greatly enhanced antibiotic effectiveness against otherwise resistant strains of bacteria.[28(b)] Thus, an extended investigation on the synergistic effect of more than 70 polyoxometalates in combination with β-lactam antibiotics followed the initial studies.[28(b)] However, there are too few studies of isostructural polyoxometalates to draw conclusions about the relationship between composition and activity.

1.3.1.4 Cellular penetration of POMs

POMs are large (in the nanometer size range) and highly negatively charged species. These two factors certainly do not facilitate their penetration into cells. One might therefore conclude that the observed activities result from the interaction of the POMs with the cell surface. Some studies however indicate that, under certain circumstances, POMs can cross the barrier and penetrate inside a cell.[28] In particular, some polyoxotungstates have been found into the cells by means of high energy techniques, such as X-fluorescence microscopy, raman laser microscopy or scanning electron microscopy (see also *Chapter 3*, paragraph 3.1.1). Since these techniques are destructive for the cells, they cannot be used for imaging and cell tracking modalities.

In this respect, in this Thesis hybrid POMs containing chromophores on their surface have been designed and exploited to study specific interactions of POMs with the cells. All this topics will be presented in the Chapter 3 of this Thesis.

On the other hand, as wjue have previously described (see paragraph 1.3.1.1), most of the biological, *in vivo* effects of POMs may be explained by interactions with target proteins accessible from the extracellular site. For this reason, the next paragraph will be focused on the POM-biomolecules interactions.

1.3.2 Interaction of POMs with biological macromolecules

Their promising biological activities make POMs attractive candidates for novel, innovative and cheap therapeutic strategies for various human diseases. However, the mechanisms of these phenomena at a molecular level remain unclear. As a consequence, preliminary studies of interactions, in a broad sense, between POMs and several target proteins, are one of the necessary steps toward an understanding their bio-functions. Furthermore, research on the interaction between POMs and proteins may open new paths for finding novel bio-function compounds.

First, investigations of POMs in the presence of viral enzymes (e.g., HIV-1 reverse transcriptase -HIV-1 RT- and HIV-1 protease -HIV-1 P-) and proteins (e.g., gp120 and CD4) have indeed provided additional information into their mode of action.

Initially, the structural and electronic complexity of POMs interacting with biological macromolecules has limited the collective efforts to probe these interactions theoretically. In this respect, as for instance, Hill and co-workers conducted theoretical studies on interaction(s) of different POMs (α_1-$K_7[P_2W_{17}(NbO_2)O_{61}]$ and α_2-$K_7[P_2W_{17}(NbO_2)O_{61}]$; α_1-$K_7[P_2W_{17}NbO_{62}]$ and α_2-$K_7[P_2W_{17}NbO_{62}]$) with HIV-1 P. These computational studies strongly suggest that the POMs bind to a cationic pocket on the "hinge" region of the flaps covering the active site and not to the active site directly (the mode of inhibition of all other HIV-1 P protease inhibitors). The kinetics and binding studies, conducted after the molecular modelling, were in remarkable agreement with the modeling results.[57]

Furthermore, several classic POMs (such as the Keggin $K_6SiNiW_{11}O_{39}$, the Wells–Dawson α-$K_8P_2NiW_{17}O_{61}$, and the trivacant Keggin-derived sandwich $K_{10}P_2Zn_4(H_2O)_2W_{18}O_{68}$ bind to the cationic pocket of basic fibroblast growth factor (bFGF).[58] The inhibition of angiogenesis-promoting factors such as fibroblast growth factor is considered to be a potential treatment for cancers.

More recently, the molecular interaction between HSA and two different polyoxometalates with Keggin $[H_2W_{12}O_{40}]^{6-}$ (H_2W_{12}) and wheel-shaped $[NaP_5W_{30}O_{11}0]^{14-}$ (P_5W_{30}) structures were studied by isothermal titration calorimetry (ITC), complemented by fluorescence and

circular dichroism (CD) experiments.[59] Both polyoxometalates H_2W_{12} and P_5W_{30} strongly bind to the protein, mainly by electrostatic interactions.

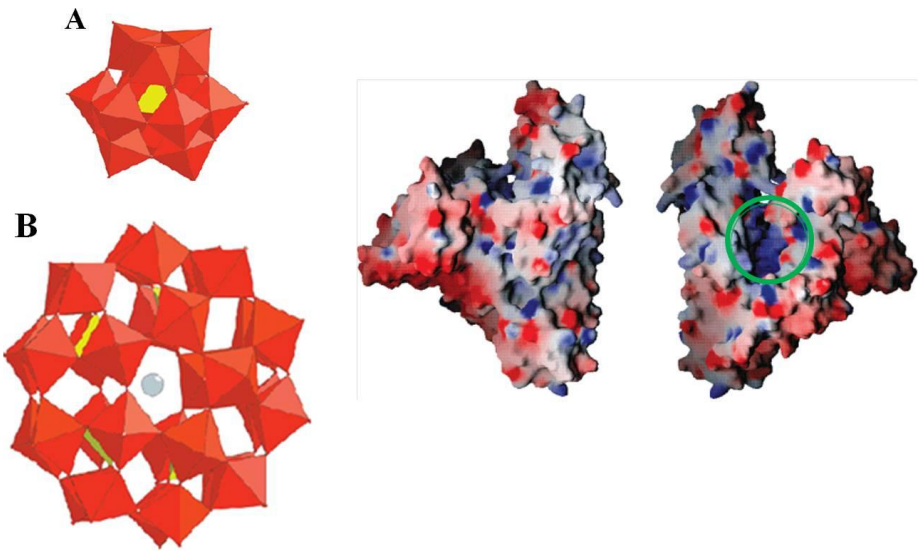

Figure 1.13 Left: POM structures: **A** the Keggin structure $[H_2W_{12}O_{40}]^{6-}$ (H_2W_{12}), **B** the wheel-shaped structure $[NaP_5W_{30}O_{110}]^{14-}$ (P_5W_{30}); Right: surface potential of HSA calculated with the GRASP software. The protein is in its N conformation. The two views are related by a 180° rotation about the vertical axis of the sheet. The region in the green circle is the most likely the unique (for H_2W_{12}) or initial (for P_5W_{30}) binding site for POMs (blue for positively and red for negatively charged areas).

It was suggested that both size and charges of the polyoxometalates play key roles in the molecular interaction process. The surface map of the protein is shown in Figure 1.13: upon close examination, it appears that a cavity with a positively charged inner wall is located roughly in the center of the protein. The width of this cavity is about 1 nm length, which would fit to the diameter of H_2W_{12}. In particular, the results have suggested that the POM H_2W_{12} specifically binds on this cavity of the protein and forms a 1:1 protein-POM complex, whereas the wheel shaped P_5W_{30} binds to more than five sites and forms a complicated complex with the protein. The binding of H_2W_{12} has almost no effect on the protein structure, in contrast with the binding of P_5W_{30}, which destabilizes the protein structure.

Furthermore, the binding with HSA of three POMs with the Wells-Dawson structure, α_2-$[P_2W_{17}O_{61}]^{10-}$ and two of its metal-substituted derivatives, α_2-$[NiP_2W_{17}O_{61}]^{8-}$ and α_2-$[CuP_2W_{17}O_{61}]^{8-}$ suggested the importance of the atomic composition in the interaction event.[60] The interaction between lanthanide containing decatungstate $[EuW_{10}O_{36}]^{9-}$ (EuW_{10}) and HSA was also studied. Fluorescence analysis showed the existence of a strong 1:1 interaction between the POM and HSA (Scheme 1.8).

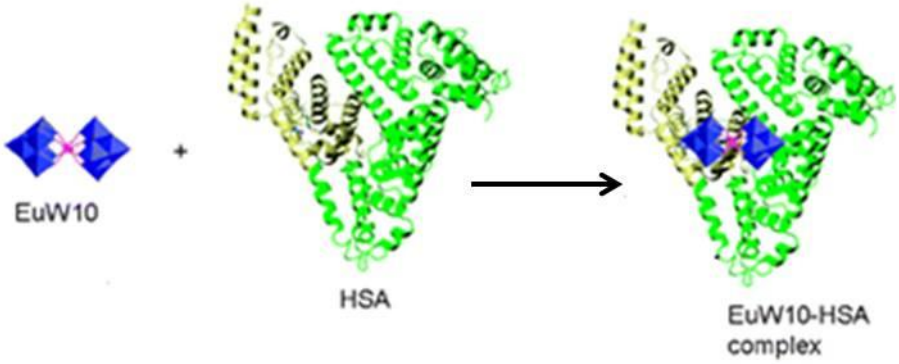

Scheme 1.8 Interaction between EuW_{10} and HSA.

This interaction has key effects both on luminescence of the POM and on the behaviour of HSA: an enhancement of the POM luminescence is observed upon interaction, while an increasing concentrations of the POM results in the progressive quenching of the fluorescence of the single tryptophan of HSA. Circular dichroism evidenced that the binding of EuW_{10} did not significantly alter the secondary structure of the protein[61] (see also *Chapter 3*, paragraph 3.1.2).

Finally, four POMs capable of inhibiting amyloid β-peptides (Aβ) aggregation have been identified. The polymerization of Aβ into amyloid fibrils is crucial for the Alzheimer's disease (AD). Therefore, the development of Aβ inhibitors has received much attention. The highest inhibition was observed for $K_8[P_2CoW_{17}O_{61}]$, a phosphotungstate with a Wells Dawson structure. POMs with a Keggin structure showed moderate to high inhibition of Aβ aggregation. Smaller POMs, such as $Na_5[IMo_6O_{24}]$ with an Anderson structure were inactive. Indeed, the size of POMs might play a key role in Aβ recognition. In particular, an electrostatic effect is the main factor in the interactions between POMs and Aβ. Experiments based on enzyme digestion, competitive binding, fluorescence quenching, and the use of a different Aβ fragment indicated that POMs bind to the positively charged His13–Lys16 cluster region of Aβ.[62]

1.3.3 Strategies for the biofunctionalization of POMs

Since the main part of POMs derivatives present little or no hydrolytic stability at physiologically relevant pH values and some of them exhibit toxicity, many efforts have been made to modify POMs through altering their structure, polarity, charge, and composition in order to obtain compounds featuring low toxicity, high stability, and high activity.[57,63] In this respect, a number of new POMs with hydrolytic stability at physiologically relevant pH values have been synthesized recently, and the toxicity problems exhibited by some POMs are considerably smaller or nonexistent in the second generation of POM-based chemotherapeutic agents.

Moreover, an organic modification of POMs can be used to achieve higher stability under physiological conditions, together with a lower toxicity and a tunable biodistribution. In particular, two strategies for the biofunctionalization of POMs can be individuated:

(i) non-covalent encapsulation of POMs by biopolymers, dendritic ligands and surfactants;
(ii) covalent grafting of organic ligand or biomolecule on POMs.

in the next sections these two strategies will be examined.

1.3.3.1 Encapsulation of bioactive POMs into macromolecular matrices

Different studies investigated the possibility of using nanocarriers for POM delivery, showing that the preparation of hybrid composite materials, through encapsulation of bioactive POMs into no toxic macromolecular matrices is a flexible and straightforward approach that should provide direct access to a wide spectrum of POM composites, improving their cellular uptake. The same strategy may be also useful to enhance hydrolytic stability of POMs and to decrease their toxicity.

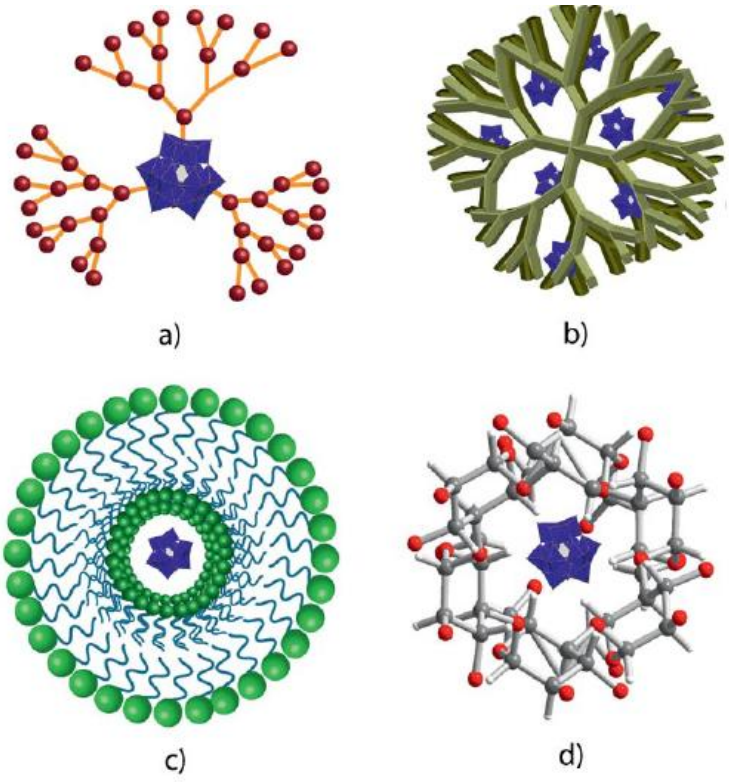

Figure 1.14 Strategies for the non-covalent bio-functionalization of POMs. (a) encapsulation using dendrons, (b) encapsulation in dendrimers, (c) encapsulation in liposomes and (d) encapsulation in biopolymers (starch, chitosan).

For instance, sugar-capped poly(propylene amine) (POPAM) dendrimers (Figure 1.14 (b)) are well suited for encapsulating and slowly releasing polyanions such as $[Re_6S_8(OH)_6]^{4-}$. The loading capacity of nanosized dendritic hosts with anionic guests and the pharmacokinetic properties of the host–guest complexes can be tuned by variation of the generation, the type of branching unit and the moieties grafted on to the periphery of the dendrimers.[64]

Moreover, the synthesis of liposome-encapsulated polyoxometalate (LEP) nanoparticles of size 15-60 nm containing $K_6[SiW_{11}TiO_{40}]\cdot 16H_2O$ ($SiW_{11}Ti$) is reported in the literature (Figure 1.14 (c)). Based on *in vitro* measurements with KB and HeLa cancer cells, the liposome encapsulation enhances cell-membrane penetration, the stability and antitumoral activity of the POM. The toxicity of the POM was also reduced when LEPs were employed against HL-60 tumors *in vivo*.[65]

The combination of chitosan and its derivatives with different drug types into core-shell nanoparticles (preferably in the 100 nm size range) offers manifold therapeutic advantages, such as reductions of side effects, prolonged drug circulation times or passive drug targeting.[66] In the case of POMs, the mechanism of interaction with chitosan (Figure 1.14 (d)) is likely to be electrostatic. It is expected that the terminal/bridging oxygen on the surface of

POM interacts with the NH_3^+ protonated groups of chitosan to form intermolecular cross-linking which thereby results in the formation of the nanocomposite (Figure 1.15).

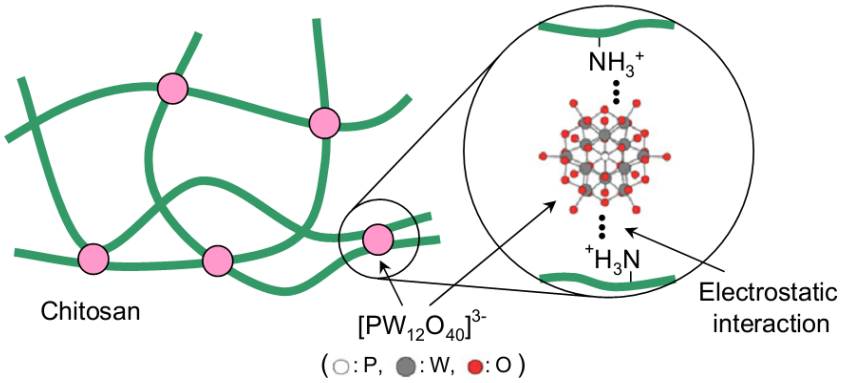

Figure 1.15 Representation of the interaction mechanism between POM and chitosan.

As an example, the potential of a novel europium containing the polytungstoarsenate ($[Cs\subset Eu_6As_6W_{63}O_{218}(H_2O)_{14}(OH)_4]^{25-}$)[67] (EuWAs) trapped whitin biopolymer chitosan, was evaluated as a cancer nanomedicine. Highly stable, monodispersed nanoparticles of size about 200 nm, encapsulating EuWAs were prepared by ionotropic gelation technique. The aggregate showed a slow and sustained drug release profile when tested *in vitro* under physiological conditions. Its anticancer activity was found to be enhanced at lower doses. Flow cytometry studies revealed that reactive oxygen species (ROS) generation can be the plausible mechanism for the apoptosis induced by this material.[68]

Moreover, the disadvantage of chitosan only being soluble in acidic media, can be overcome by transforming it into the water-soluble carboxymethyl chitosan (CMC) through carboxymethylation of the primary alcohol group and the amino group.[69] The carboxymethylated chitosan has the ability to serve as a drug carrier for polyoxometalates. In this respect, the synthesis, characterization and cytotoxicities of POM/CMC-based composites has been investigated. Since $[Co_4(PW_9O_{34})_2]^{10-}$ is well known for its manifold properties, such as antiviral activity, it was selected as a model POM. The resulting composites were characterized with a wide range of analytical methods, such as UV-Vis, FT-IR spectroscopy, as well as solid-state ^{31}P NMR and EDX measurements, which pointed to quantitative encapsulation of intact POMs within the CMC matrix. The nanocomposites display a narrow size distribution ranging from 50–160 nm, which makes them ideal for cellular uptake. Thus the biocompatibility of the POM/CMC nanocomposites on HeLa cells was also evaluated through MTT and proliferation assays. Even after prolonged incubation times at high

concentrations, the composites did not display cytotoxicity, thereby drastically reducing the side effects of POMs.[70]

Finally, the use of fluorescein-tagged CMC as POMs carrier was applied to get insights about their localization, by means of confocal fluorescence microscopy.[71] Thus POM/CMC nanocomposites with an average diameter of 130 nm were synthesized and labeled with fluorescein isothiocyanate (FITC) for a combined drug-carrier and cellular-monitoring approach. In particular, cellular uptake of fluorescently labeled $\{EuSiW_{11}O_{39}\}$/FITC-CMC nanoparticles were monitored with confocal laser scanning microscopy. Nanoparticle uptake occurs after incubation times of about 1 h and no cyctotoxic effect was observed upon prolonged treatment. The preferential location of these nanocomposites in the perinuclear region was furthermore verified with transmission electron microscopy investigations on unlabeled nanopart,icles. Therefore, this approach is a promising dual strategy for the safe cellular transfer and monitoring of bioactive POMs.

1.3.3.2 Decoration of POMs with biological macromolecules

The presence of organic substituents anchored on the POM surface also offers the possibility to modulate essential features, such as stability, bioavailability, recognition and affinity towards suitable carriers, that need to be mastered for pharmaceutical purposes.[63(c),72,73] In particular, the introduction of chiral molecules on POMs surface is highly desirable for biomedical applications.[74]

In this respect, numerous different synthetic approaches have permitted the grafting of biomolecules like amino acids,[75] peptides[76] and carbohydrates[77] onto the polyoxometalate framework.

For instance, in the literature are known complexes of polyoxomolybdates with peptides or aminoacids. γ-Type octamolybdates with formula, $Na_4[Mo_8O_{26}(alaO)_2]\cdot 18H_2O$, $Na_4[Mo_8O_{26}(glyglyO)_2]\cdot 15H_2O$ and $Na_4[Mo_8O_{26}(glyglyO)_2]\cdot 12H_2O$ have been prepared from sodium molybdate in aqueous solution by adding DL-alanine or glycylglycine. Their crystal structures have been determined by X-ray structural analysis. DL-alanine and glycylglycine coordinate molybdenum atom in γ-octamolybdate $[Mo_8O_{26}]^{4-}$ anions via monodentate carboxylate-oxygen atom. These prepared octamolybdates were screened for the possible antiproliferative activity on a panel of five tumor cell lines and on a normal cell line. All tested compounds showed a differential cell-growth inhibition, in a dose-dependent manner, selectively on hepatocellular carcinoma cell line (HepG2) and breast cancer cell line.[78]

Moreover, hybrid organic-inorganic Wells-Dawson polyoxotungstates were prepared through addition of functionalized tricholorostannanes to lacunary α_2- and α_1-$[P_2W_{17}O_{61}]^{10-}$. The resulting products α_2- and α_1-$[P_2W_{17}O_{61}\{SnR\}]^{7-}$ with R = CH_2COOH, CH_2COOEt, CH_2CHO, $CH{=}CH_2$ were further functionalized with various molecules. Thus, coupling the polyoxotungstate platforms with amines and alcohols led to new structures in good yields.[79]

In particular, amino acids or chiral amines were covalently linked to the chiral scaffold α_1-$[P_2W_{17}O_{61}\{SnCH_2COOH\}]^{7-}$ by means of classic condensation reactions.

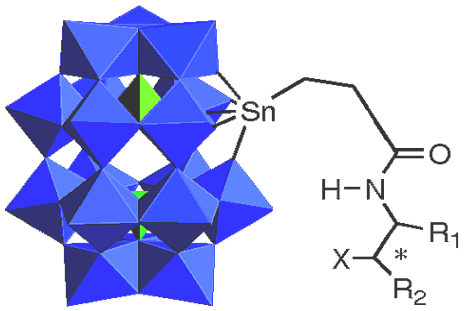

Figure 1.16 Structure of α_1-$[P_2W_{17}O_{61}(SnCH_2CH_2CONHR)]^{7-}$.

In particular, coupling of chiral amines with the previously organotin-substituted α_1 derivatives allowed the isolation of diastereomers, which feature in some cases splitted ^{1}H, ^{13}C, and ^{31}P NMR signals.

Furthermore, more recently, different kinds of molecules (lipophilic, hydrophilic and biologically relevant) were coupled to the platforms α_1- and α_2-$[P_2W_{17}O_{61}\{SnR\}]^{7-}$ with R = $CH_2CH{\equiv}CH$ or $CH_2CH_2CH_2N_3$ to generate hybrids by means of the copper-catalyzed azide/alkyne cycloaddition (click chemistry).[77]

Finally, in our research group, lacunary Keggin POMs have been also functionalized with enantiopure phosphonates (see also Scheme 1.5). These optically active hybrid complexes were characterized by FT-IR, heteronuclear NMR spectroscopy, mass spectrometry, and UV/Vis experiments. In such complexes, the merging of the organic and inorganic domains induces intense and multiple CD features up to 400 nm.

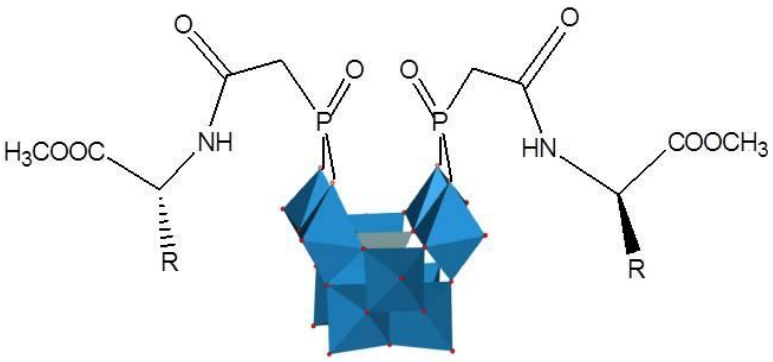

Figure 1.17 Stucture of α_2-$[P_2W_{17}O_{61}(SnCH_2CH_2CONHR)]^{7-}$.

1.4 Aim of Ph.D Thesis

The work described in this Thesis mainly deals with the synthesis of functional molecular hybrids based on polyoxometalates for sensing, biological and catalytic applications. In particular, considering the great potential of hybrid organic-inorganic POMs derivatives, for improving recognition capabilities and selectivity towards organic/biological substrates, the use of different organic domains grafted on the POMs surface has been explored for imaging, targeting and catalytic purposes.

The work is divided in three parts, involving synthesis, characterization and properties of different POMs:

- *Chapter 2* describes the functionalization and characterization of lacunary POMs with luminescent probes, that exhibit interesting opto-electronic properties and sensing applications. Fluorescence experiments have been performed to investigate the chemo-sensing capabilities of the luminescent hybrid systems towards metal cations and hydrophobic molecules.

- *Chapter 3* is dedicated to the exploitation of POM-based hybrid systems for biological studies.

  In particular, the work has been dedicated to fill the lack of experimental data about POMs cellular uptake/ mechanism of action/ localization. In this scenario, the exploitation of stable hybrid luminescent complexes is suggested as a method to unravel their cellular localization. Furthermore, since the preparation of hybrid derivatives could be a powerful strategy for the introduction of molecular recognition sites and the enhancement of biocompatibility, studies of interaction between POMs and hybrid POMs with important

biological macromolecules (ferritin and avidin) has been explored. For this purpose, a hybrid POM containing biotin moieties has been synthesized and its interaction with avidin has also been investigated.

- *Chapter 4*. In this chapter a strategy for the synthesis of a POM-appended N-heterocyclic carbene (NHC) iridium complex is presented. To this end, imidazolium moieties have been successfully grafted on the defect site of a divacant Keggin polyanion. The resulting hybrid POM has been tested for catalyzing hydrogen transfer reactions (HT). This last project was developed during a short scientific mission in Dublin, in collaboration with the research group of Prof. Martin Albrecht.

1.5 References and notes

[1] A. Hiskia, A. Mylonas, E. Papaconstantinou, *Chem. Soc. Rev.* **2001** *30*, 62.

[2] M. T. Pope, A. Müller in *Heteropoly and Isopoly Oxometalates,* SPRINGER VERLAG, New York, **1983**.

[3] M. T. Pope, A. Müller, *Angew. Chem. Int. Ed.* **1991**, *30*, 34.

[4] C. L. Hill, *Polyoxometalates, Chem. Rev.* (Special Issue), **1998**, *98*, 1.

[5] D. L. Kepert in: *The Early Transition Metals,* ACADEMIC PRESS Inc., London, **1972**.

[6] Y. P. Jeannin, *Chem. Rev.* **1998**, *98*, 51.

[7] W. N. Lipscomb, *Inorg. Chem.* **1965**, *4*, 132.

[8] O. Chen, J. Zubieta, *Coord. Chem. Rev.* **1992**, *114*, 107.

[9] J. F. Keggin, *Proc. R. Soc. London Scr. A.* **1934**, *144*, 75.

[10] R. Acerete, C. F. Hammer, L. C. W. Baher *J. Am. Chem. Soc.* **1982**, *104*, 5384.

[11] R. Massart, R. Contant, J. M. Fruchart, J. P. Ciabrini *Inorg. Chem.* **1977**, *11*, 2916.

[12] P. Judeinstein, C. Deprum, L. Nadjo *J. Chem. Soc. Dalton Trans.* **1991**, 1991.

[13] M. Filowitz, R. K. C. Ho, W. G. Klemperer, W. Shum *Inorg. Chem.* **1979**, *18*, 93.

[14] F. Zonnevijlle, C. M. Tournè, G. F. Tournè *Inorg. Chem.* **1982**, *21*, 2742.

[15] J. Canny, A. Tézé, R. Thouvenot, G. Hervé *Inorg. Chem.* **1986**, *25*, 2114.

[16] M. Misono, M. Mizuno, T. Watanabe, *J. Phys. Chem.***1985**, *89*, 80.

[17] C.L. Hill, M. Kadkhodayan, M. Pasquali, R.F. Renneke, *J. Am. Chem. Soc.* **1991**, *113*, 8357.

[18] A. Müller, P. Kögerler, *Coord. Chem. Rev.* **1999**, *182*, 3.

[19] a) M. Carraro, L. Sandei, A. Sartorel, G. Scorrano, M. Bonchio, *Org. Lett.* **2006**, *8*, 3671; b) S. Berardi, M. Bonchio, M. Carraro, V. Conte, A. Sartorel, G. Scorrano, *J. Org. Chem.* **2007**, *72*, 8954; c) M. Bonchio, M. Carraro, G. Scorrano, E. Fontananova, E. Drioli, *Adv. Synth. Catal.* **2003**, *345*, 1119; d) M. Bonchio, M. Carraro, G. Scorrano, A. Bagno, *Adv. Synth. Catal.* **2004**, *346*, 648.

[20] H. Zeng, G. R. Newkome, C. L. Hill, *Angew. Chem., Int. Ed.* **2000**, *39*, 1772.

[21] P. Gouzerh, A. Proust *Chem. Rev.* **1998,** *98*, 77.

[22] a) L. C.W. Baker in Advances in the Chemistry of Coordination Compounds (Ed.: S. Kirschner), Macmillan: New York, **1961**, 604; b) V.W. Day, W. G. Klemperer, *Science* **1985**, *228*, 533.

[23] A. Dolbecq, E. Dumas, C. R. Mayer, P. Mialane, *Chem. Rev*. **2010**, *110*, 6009.

[24] C. R. Mayer, R. Thouvenot, *Chem. Mater*. **2000**, *12*, 257.

[25] S. Nlate, L. Plault, D. Astruc, *Chem. Eur. J.* **2006**, *12*, 903.

[26] a) S. Favette, B. Hasenknopf, J. Vaissermann, P. Gouzerh, C. Roux, *Chem. Commun.* **2003**, 2664; b) Z. H. Peng, *Angew. Chem. Int. Ed.* **2004**, *43*, 930.

[27] a) D. L. Long, E. Burkholder, L. Cronin, *Chem. Soc. Rev.* **2007**, *36*, 105; b) M. Carraro, A. Sartorel, G. Scorrano, C. Maccato, M. H. Dickman, U. Kortz, M. Bonchio, *Angew. Chem.* **2008**, *120*, 7385; *Angew. Chem. Int. Ed.* **2008**, *47*, 7275.

c) D.-L. Long, R. Tsunashima, L. Cronin, *Angew. Chem.* **2010**, *122*, 1780; *Angew. Chem. Int. Ed.* **2010**, *49*, 1736.

[28] a) J. T. Rhule, C. L. Hill, D. A. Judd, R. F. Schinazi *Chem. Rev.* **1998**, *98*, 327.b) B. Hasenknopf *Frontiers in Bioscience* **2005**, *10*, 275.

[29] F. M. Toma, A. Sartorel, M. Iurlo, M. Carraro, P. Parisse, C. Maccato, S. Rapino, B. Rodriguez Gonzalez, H. Amenitsch, T. Da Ros, L. Casalis, A. Goldoni, M. Marcaccio, G. Scorrano, G. Scoles, F. Paolucci, M. Prato, M. Bonchio, *Nat. Chem.* **2010**, *2*, 826.

[30] R. K. C Ho, W. G. Klemperer, *J. Am. Chem. Soc.* **1978**, *100*, 6772.

[31] a) W. H. Knoth *J. Am. Chem. Soc.* **1979**, *101*, 759; b) F. Zonnevijlle, M.T. Pope *J. Am. Chem. Soc.* **1979**, *101*, 2731; c) G.-S. Kim; K. S. Hagen; C.L. Hill *Inorg Chem.* **1992**, *31*, 5316; d) C. R. Mayer, C. Roch- Marchal, H. Lavanant R. Thouvenot, N. Sellier, J.-C. Blais, F. Sécheresse, *Chem. Eur. J.* **2004**, *10*, 5517; e) C. N. Kato, Y. Kasahara, K. Hayashi, A. Yamaguchi, T. Hasegawa, K. Nomiya *Eur. J. Inorg. Chem.* **2006**, 4834.

[32] P. Mason *Master degree thesis,* Università degli studi di Padova, a.a. **1998/1999.**

[33] C. R. Mayer, I. Fournier, R. Thouvenot *Chem Eur. J.* **2000**, *6*, 105.

[34] M. Carraro, G. Modugno, A. Sartorel, G. Scorrano, M. Bonchio *Eur. J. Inorg. Chem.* **2009**, 5164.

[35] A. Proust, P. Gouzerh, F. Robert, *Inorg. Chem.* **1993**, 32, 5291.

[36] (a) I. Bar-Nahum, H. Cohen, R. Neumann, *Inorg. Chem.* **2003**, *42*, 3677; b) I. Bar-Nahum, R. Neumann, *Chem. Commun*. **2003**, 2690.

[37] S. Berardi, M. Carraro, M. Iglesias, A. Sartorel, G. Scorrano, M. Albrecht , M. Bonchio, *Chem.–Eur. J.* **2010**, *16*, 10662.

[38] A. Sartorel, M. Carraro, A. Bagno, G. Scorrano, M. Bonchio. *Angew. Chem. Int. Ed.* **2007**, *46*, 3255.

[39] S. Berardi, M. Carraro, A. Sartorel, G. Modugno, M. Bonchio *Isr. J. Chem*. **2011**, *51*, 1.

[40] M. Carraro, A. Sartorel, F. M. Toma, F. Puntoriero, F. Scandola, S. Campagna, M. Prato, and M. Bonchio *Top. Curr. Chem.* **2011**, 1.

[41] B. Matt, S. Renaudineau, L.-M. Chamoreau, C. Afonso, G. Izzet, A. Proust, *J. Org. Chem.* **2011**, 76.

3107.

[42] F. Odobel, M. Severac, Y. Pellegrin, E. Blart, C. Fosse, C. Cannizzo, C. R. Mayer, K. J. Elliott, A. Harriman, *Chem. Eur. J.* **2009**, *15*, 3130.

[43] K, J. Elliott, A. Harriman, L. Le Pleux, Y. Pellegrin, E. Blart, C. R. Mayerc, F. Odobel *Phys. Chem. Chem. Phys.* **2009**, *11*, 8767.

[44] F. M. Toma, A. Sartorel, M. Iurlo, M. Carraro, S. Rapino, L. Hoober-Burkhardt, T. Da Ros, M. Marcaccio, G. Scorrano, F. Paolucci, M. Bonchio, M. Prato, *Chem-SusChem.* **2011**, *4*, 1447.

[45] a) M. Carraro, M. Gardan, G. Scorrano, E. Drioli, E. Fontananova, M. Bonchio, *Chem. Commun.* **2006**, 4533.

[46] M. Lira-Cantù and P. Gomez-Romero, *Chem. Mater.* **1998**, *10*, 698.

[47] B. M. Azumi, T. Ishiara, H. Nishiguchi and Y. Takita, *Electrochemistry*, **2002**, *70*, 869.

[48] N. Kawasaki, H. Wang, R. Nakanishi, S. Hamanaka, R. Kitaura, H. Shinohara, T. Yokoyama, H. Yoahikawa and K. Awaga, *Angew. Chem., Int. Ed.* **2011**, *50*, 3471.

[49] a) J. C. Chermann, M. Raynaud, C. Jasmin, G. Mathé *Nature* **1970**, *227*, 173 ; b) M. Raynaud, J.-C. Chermann, C. Jasmin and G. Mathé . *R. Acad. Sci. Hebd. Seances Acad. Sci. D* **1970**, *270*, 578.

[50] M. Raynaud, J.-C. Chermann, F. Plata, C. Jasmin, G. Mathé . *R. Acad. Sci. Hebd. Seances Acad. Sci. D* **1971**, *272*, 347.

[51] a) C. Bonissol, P. Kona, J. C. Chermann, C. Jasmin, M. Raynaud *C. R. Acad. Sci. Hebd. Seances Acad. Sci. D* **1972,** *274*, 3030; b) N. Raybaud, C. Jasmin, J. Huppert, J. C. Chermann, G. Mathé, M. Raynaud *Rev. Eur. Etud. Clin. Biol.* **1972**, *17*, 295; c) D. K. Haapala, C. Jasmin, F. Sinoussi, J. C. Chermann, M. Raynaud *Biomedicine* **1973**, *19*, 7 ; d) C. Jasmin, N. Raybaud, J. C. Chermann, D. Haapala, F. Sinoussi, C. B. Loustau, C. Bonissol, P. Kona, M. Raynaud *Biomedicine* **1973**, *18*, 319; e) C. Jasmin, J. C. Chermann, N. Raybaud, D. Bucchini, O. Jarrett, M. Raynaud, G. Mathé, F. Plata: *Bibl. Haematol.* **1973**, *39*, 381; f) N. Larnicol, Y. Augery, C. Le Bousse-Kerdiles, V. Degiorgis, J. C. Chermann, A. Tézé, C. Jasmin *J. Gen. Virol.* **1981**, *55*, 17.

[52] a) J.-C. Chermann, F. C. Sinoussi, C. Jasmin *Biochem. Biophys. Res. Commun.* **1975**, *65*, 1229; b) H. Tsiang, P. Atanasiu, J.-C. Chermann, C. Jasmin *J. Gen. Virol.* **1978**, *40*, 665 ; c) F. Bussereau, J. C. Chermann, E. De Clercq, C. Hannoun *Ann. Virol.* **1983**, *134E*, 127 ; d) F. Bussereau, A. Ermine *Ann. Virol. (Inst. Pasteur)* **1983**, *134E*, 487; e) M. Souyri-Caporale, G. Tovey, K. Ono, C. Jasmin, J.-C. Chermann, *J. Gen. Virol.* **1984**, *65*, 831.

[53] M. S. Weeks, C. L. Hill, R.F. Schinazi *J. Med. Chem.* **1992,** *35*, 1216.

[54] C. L Hill, M. Hartnup, M. Faraj, M. Weeks, C. M. Prosser- McCartha , R. B. Jr. Brown, M. Kadkhodayan, J.-P. Sommadossi, R. F. Schinazi, R. F. In *Advances in Chemotherapy of AIDS*; Diasio, R. B., Sommadossi, J.-P., Eds.; Pergamon Press, Inc.: New York, **1990**.

[55] a) T. Yamase *Molecular Engineering* **1993**, *3*, 241; b) T Yamase, H. Fujita, K. Fukushima, Y. Seto: In: *PCT Int. Appl* 68, Terumo Corp., Japan, Wo, (1988); c) T. Yamase, H. Fujita, K. Fukushima: *Inorg. Chim. Acta* **1988**, *151*, 15; d) H. Fujita, T. Fujita, T. Sakurai, T. Yamase, Y. Seto *Tohoku J.*

Exp. Med. **1992**, *168*, 421; e) K. Tomita, T. Yamase, K. Shishido *Inorg, Chim. Acta* **1989**, *157*, 167; f) J.-F. Liu, Y.-G. Chen, L. Meng, J. Guo, Y. Liu, M. T. Pope *Polyhedron* **1998** *17*, 1541.

[56] a) X. Wang, J. Liu, J. Li, Y. Yang, J. Liu, B. Li, M. T. Pope *J. Inorg. Biochem.* **2003** *94*, 279; b) X. H. Wang, J. F. Liu *J. Coord. Chem.* **2000**, *51*, 73.

[57] D. A. Judd, J. H. Nettles, N. Nevins, J. P. Snyder, D. C. Liotta, J. Tang, J. Ermolieff, R. F. Schinazi, C. L. Hill *J. Am. Chem. Soc.* **2001**, *123*, 886.

[58] Q. Wu, J. Wang, L. Zhang, A. Hong, J. Ren *Angew. Chem*. **2005**, 117, 4116.

[59] a) G. Zhang, B. Keita, B, J. C. Brochon, P. Oliveira, L. Nadjo, C.T. Craescu, S. Miron, *J. Phys. Chem. B* **2007**, *111*, 1809; b) G. Zhang, B. Keita, C.T. Craescu, S. Miron, P. Oliveira, L. Nadjo, *J. Phys. Chem. B* **2007**, *111*, 11253.

[60] G. Zhang, B. Keita, C. T. Craescu, S. Miron, P. de Oliveira, L. Nadjo *Biomacromolecules* **2008,** *9*, 812.

[61] L. Zheng, Y. Ma, G. Zhang, J. Yao, B. Keita, L. Nadjo *Phys.Chem.Chem.Phys.* **2010**, 12, 1299.

[62] J. Geng, M. Li, J. Ren, E. Wang, X. Qu *Angew. Chem. Int. Ed*. **2011**, 50, 4184.

[63] (a) J.T. Rhule, C.L. Hill, D.A. Judd *Chem. Rev*.**1998**, 98, 327; b) B. Moskovita, Antimicrob. Agents Chemother. **1988**, *32* (1988) 1300.

[64] M. Kubeil, H. Stephan, H. J. Pietzsch, G. Geipel, D. Appelhans, B. Voit, J. Hoffmann, B. Brutschy, Y. V. Mironov, K. A. Brylev, V. E. Fedorov, *Chem. Asian J.* **2010**, *5*, 2507.

[65] X. Wang, F. Li, S. Liu, M.T. Pope *J. Inorg. Biochem.* 2005, *99*, 452.

[66] M. N. V. Ravi Kumar, *React. Funct. Polym.* **2000**, *46*, 1.

[67] F. Hussain, B. Spingler, F. Conrad, M. Speldrich, P. Kogerler, C. Boskovic, G. R. Patzke *Dalton Trans*. **2009**, 4423.

[68] D. Menon, R. T. Thomas, S. Narayanan, S. Maya, R. Jayakumar, F. Hussain, V. K. Lakshmanan, S. V. Nair, *Carbohydr. Polym.* **2011**, *84*, 887

[69] a) X. G. Chen, H. J. Park, *Carbohydr. Polym.* **2003**, *53*, 355; b) M. Werle, H. Takeuchi, A. Bernkop-Schn_rch, *J. Pharm. Sci*. **2009**, *98*, 1643.

[70] G. Patzke, G. Geisberger, S. Paulus, M. Carraro, M. Bonchio *Chem. Eur. J.* **2011,** 2011, *17*, 4619.

[71] G. Geisberger, S. Paulus, E. Besic Gyenge, C. Maake, G. R. Patzke *Small* **2011**, *7*, 2808.

[72] a) S. Shigeta, S. Mori, E. Kodama, J. Kodama, K. Takahashi, T. Yamase, *Antiviral Res.* **2003**, *58*, 265; b) X. Wang, J. Liu, M. T. Pope, *Dalton Trans.* **2003**, 957; c) Y. Tajima, *Microbiol. Immunol.* **2003**, *47*, 207.

[73] K. Micoine, B. Hasenknopf, S. Thorimbert, E. Lacôte, M. Malacria, *Angew. Chem. Int. Ed.* **2009**, *48*, 3466.

[74] J. Schemberg, K. Schneider, U. Demmer, E. Warkentin, A. Müller, U. Ermler, *Angew. Chem. Int. Ed.* **2007**, *46*, 2408; corrigendum: *Angew. Chem. Int. Ed.* **2007**, *46*, 2970.

[75] a) U. Kortz, J. Vaissermann, R. Thouvenot, P. Gouzerh, *Inorg. Chem.* **2003**, *42*, 1135; b) J. Li, Y. F. Qi, J. Li, H. F. Wang, X. Y. Wu, L. Y. Duan, E. B. Wang, *J. Coord. Chem.* **2004**, *57*, 1309.

[76] C. Boglio, K. Micoine, E. Derat, R. Thouvenot, B. Hasenknopf, S. Thorimbert, E. Lacote, M. Malacria, *J. Am. Chem. Soc.* **2008**, *130*, 4553.

[77] K. Micoine, B. Hasenknopf, S. Thorimbert, E. Lacote, M. Malacria, *Org. Lett.* **2007**, *9*, 3981.

[78] M. Cindric, T. K. Novak, S. Kraljevic, M. Kralj, B. Kamenar, *Inorg. Chim. Acta,* **2006**, *359*, 1673.

[79] S. Bareyt, S. Piligkos, B. Hasenknopf, P. Gouzerh, E. Lacôte, S. Thorimbert, M. Malacria *J. Am. Chem. Soc.* **2005**, *127*, 6788.

Chapter 2

Luminescent hybrid polyoxometalates: synthesis, characterization, sensing and spectral features

In this chapter, we report the synthesis of hybrid polyoxometalate (POM) derivatives containing luminescent chromophores (dansyl, pyrene and fluorescein), grafted as organosilanes or chiral phosphonates, with unique spectroscopic features. The resulting hybrids have been characterized at the solid state and in solution by a combination of techniques (multinuclear NMR, FT-IR, ESI-MS). The characterization confirmed a bis-substitution: the inorganic POM framework provides a molecular nanosurface where two molecules of the same fluorophore are anchored in a tweezer-type arrangement. Optical and chiroptical properties of the hybrid derivatives have been investigated. In particular, the fluorescence of the fluorophore-tagged POMs has been exploited for sensing applications towards metal ions and organic molecules. A promising potential for applications in many different fields such as sensing, catalysis, nanoelectronics, and photochemical conversion of solar energy is foreseen for these luminescent systems.

2.1 Introduction

2.1.1 Hybrid polyoxometalates: synthesis and characterization

Polyoxometalates (POMs) are nano-dimensional molecular, multi-metal oxides, which have found applications in catalysis, materials science, and nano-medicine.[1,2,3,4] Tailored control of their properties is readily achieved by tuning the elemental composition, structure, and charge density of the inorganic scaffold.[1] Moreover, the introduction of surface bound organic arms is a valuable tool for modifying redox and spectroscopic behavior, as well as their solubility and hydrolytic stability in various media.[5,6] (see *Chapter 1* paragraph *1.2: Hybrid POMs: synthesis and applications*).

Covalent derivatization of POM surfaces occurs smoothly according to well-established synthetic strategies, in analogy to those applied for the functionalization of extended metal oxides surfaces. Two basic strategies which rely on direct functionalization of POMs or post functionalization of preformed hybrid POM platforms, can be distinguished.

2.1.1.1 Direct functionalization

As already introduced in *Chapter 1* (paragraph 1.1.2), vacant polyanionic complexes feature reactive terminal, coordinatively unsaturated, oxygen atoms. Their nucleophilicity can be exploited to foster a reaction with electrophilic organic moieties to give O-X-R bonds, where X = As, P, Si, Sn, Ge and R = organic residue. In this way organic-inorganic hybrid complexes can be obtained.[6,7,8]

In our research group, different procedures have been optimized in order to functionalize the POMs vacant site through the covalent grafting of organosilyl derivatives (SiX_3, X = Cl, OMe) as electrophilic reagents. The covalent functionalization of different vacant POMs has been achieved with yields ranging from 65 up to 90%. The use of the bivacant complex $[\gamma\text{-}SiW_{10}O_{36}]^{8-}$ has shown to be convenient for these reactions, since it is characterized by a higher hydrolytic stability than other vacant complexes in the acid environment required for these reactions. Thus the divacant complex $[\gamma\text{-}SiW_{10}O_{36}]^{8-}$ has been reacted with organosilyl clorides ($RSiCl_3$) and trialkoxysiloxanes ($RSi(OR)_3$), where R = Et, n-Pr, Ph.

The general mechanisms for the derivatization of vacant polyanions with organosilanes are reported in the following scheme.

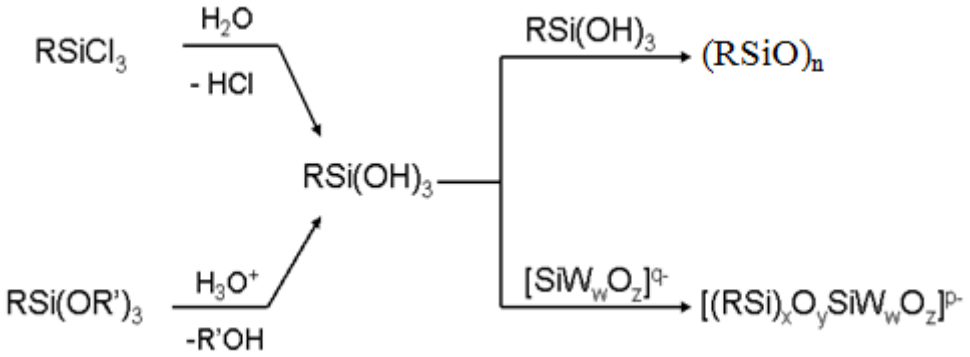

Scheme 2.1 General procedure for the preparation of organosilyl POM derivatives.

The process requires the hydrolysis of the Si-X bonds: although the silanols may give easy polymerization (to form RSiOn species), the condensation with oxygen atoms on POM defect sites, is preferred. Grafting strategies have been optimized in acetonitrile, where the presence of tetrabutylammonium bromide (nBu$_4$NBr) promotes the solubilization of the POM by counterion metathesis. Under these conditions, decoration of the vacant POM is known to yield hybrids with two surface-anchored organosilyl (RSi-) groups, each one linked to two oxygen atoms belonging to two edge-shared WO_6 octahedra.[4(a)]

By using a similar protocol, the divacant POM complex reacts with organophosphonyl (POX_2, X = Cl, OH) compounds in acetonitrile, under phase transfer conditions. In this case, the decoration of the divacant [γ-$SiW_{10}O_{36}$]$^{8-}$ unit provide hybrid POMs with two surface-anchored organophosphonyl (RPO^{2+}) groups facing each other while linked to two oxygen atoms of two edge-shared WO_6 octahedra. This structural arrangement was shown in the literature by solid-state X-ray characterization.[9] In the scheme below, are reported the synthetic strategies for both the functionalizations proposed (organosilyl and organophosphonyl derivatives) in the next paragraphs.

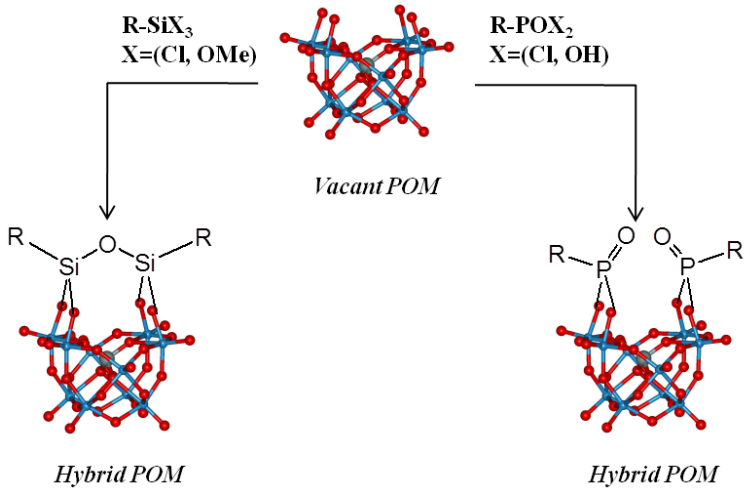

Scheme 2.2 Functionalization of vacant polyoxometalates with organic moieties to yield hybrid POMs.

The higher stability of hybrid structures in comparison to lacunary species, can be ascribed to the grafted organic functions, acting as protecting groups of the nucleophilic oxygenated sites on the POM lacuna. Thus, undesired parallel reactions, such as condensation or isomerisation of the vacant POMs, are inhibited, thus increasing their stability in different solvents and at higher temperatures.

2.1.1.2 Post-functionalization

Covalent functionalization of POMs provides – in principle – a robust link between the POM and the appended functional group. In this respect, as the complexity of the functional compond increases, the post-functionalization strategy is expected to be more attractive. Different hybrid POM platforms bearing functional groups have been involved in post functionalization reactions. The methodologies used to further derivatize preformed hybrid POM platforms can be classified according to the type of covalent bond formed: metal coordination, peptide and related bonds, imines as linkers, Huisgen 1,3-dipolar cycloaddition, carbon–carbon cross couplings. However, due to purification and stability issues, the number of reactions and related platforms are rather limited regarding the tremendous number of organic reactions available.[10]

Compared with direct functionalization of POMs which may involve alkaline salts of parent POMs, like in the preparation of silyl or phosphonyl derivatives, the post-functionalization reactions reported to date have all been carried out in organic solvents, starting generally with tetrabutylammonium salts of the hybrid POM platforms.

When the anchorage of electroactive groups has been considered, it is worth mentioning that the redox properties of both the POMs and the electroactive groups were not altered, thus

reflecting limited electronic interactions between the two domains. This is mainly due to the poor redox activity of vacant POMs.

2.1.1.3 Characterization

Different techniques can be combined to obtain information from both the inorganic and organic part of the molecule. In particular, the analysis which result most useful for monitoring the grafting of organic pendants on POM scaffold are the FT-IR and heteronuclear NMR spectroscopies.

In the FT-IR analysis, a region between 1000 and 600 cm^{-1} (vibrations of the bonds W-O and X-O), results particular diagnostic to verify the modification and functionalization of the inorganic domain. In particular, narrow and intense bands are consistent with the presence of stable and highly symmetrical structures for the complexes of Keggin, while for vacant complexes spectra with lower absorption frequencies are observed, in agreement with the partial weakening of the vacant polyoxotungstate structure. Furthermore, since in the vacant complex the simmetry is reduced from *Td* to *Cs* or C_{2v} due to the loss of WO^{4+} units, the bands result large and more numerous. The same region is also affected by the covalent linkage of the vacancy with organic compounds, with the occurrence of new signals due to XO bonds (with X = P, Si) above 1000 cm^{-1}. Finally, a partial symmetrization of the complex, lead again to a general reduction of the number of signals and to an increase of the absorption frequencies.

Information about the structure of the polyanion can be also derived from ^{183}W NMR where typical signals patterns demonstrate the symmetry of the complex. The understanding of the electronic factors that influence the chemical shifts of the tungsten nuclei in mono and polynuclear complexes is still an open and complex topic, discussed in the literature mainly on the basis of empirical observations. However, in the case of new structures for which X-ray diffraction is known, homonuclear ^{2}J (W, W) and heteronuclear ^{2}J (P, W) scalar couplings in 1 and 2-D techniques allowed the peaks assignment. In this way, characteristic patterns of signals allow to trace the exact symmetry of the complexes upon comparison with that of known structures.

Finally, ^{1}H NMR, ^{13}C NMR, ^{29}Si or ^{31}P NMR spectroscopies and mass spectrometries (ESI-MS, MALDI), are indispensable tolls to verify the introduction of organic residues.

2.1.2 Functionalization of POMs with fluorescent organic probes

Fluorescence plays a key role in a growing number of disciplines, from molecular biology, to analytical chemistry, to optoelectronics and material science. Its high spatial, temporal resolution and excellent signal-to-noise ratio make fluorescence an ideal tool for studying the structure and dynamics of matter and living systems on a molecular and nanometric scale.

The organic fluorophores may form covalent or noncovalent linkages with POMs, producing the respective conjugates or complexes, that can show fluorescence from short to very long wavelengths, depending on the marker used.[11]

In addition, the interplay of organic fluorophores and POMs by covalent and ionic linkage has been recently proposed to promote charge separation states, being instrumental for solar energy conversion and storage, as well as for the development of molecular capacitors and photosensitized catalytic processes.[12,13] Indeed the grafting of an organic pendant on POM nano-scaffold is a developing field of investigation focusing on the design of new functional molecules and materials (see also *Chapter 1*: paragraph 1.2.2). Furthermore, considering the interdisciplinary frontier of inorganic nano-clusters in medicinal chemistry (see *Chapter 1* paragraph 1.3), the introduction of luminescent probes on POMs can be also proposed for bio-imaging/sensors and could eventually couple the diagnostic potential with innovative therapy protocols.[14]

On these basis and perspectives, to exploit and combine the ability of organic luminescent molecules with the use of polyoxometalate scaffolds, fluorescent-tagged hybrids have been prepared, starting from vacant Keggin polyoxotungstates. To this aim, the organic reagents reported in Figure 2.1. have been selected.

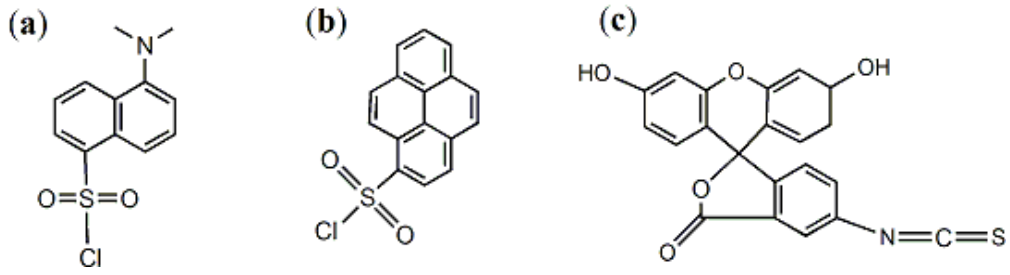

Figure 2.1 Organic reagents selected for the functionalization of POM scaffolds: (**a**) dansyl chloride (Dans-Cl); (**b**) pyrene sulphonyl chloride (Pyr-SO_2Cl); (**c**) fluorescein isothiocyanate (FITC).

In particular, the grafting of the molecules (**a**), (**b**), (**c**) on polyanionic scaffolds has allowed to obtain four different luminescent hybrid derivatives:

(a) a dansyl-functionalized POM with emission in the range 500-600 nm,
(b) a pyrene sulfonyl-functionalized POM with emission up to 500 nm,
(c) two fluoresceine isothiocyanate-functionalized POMs with emission beyond 500 nm.

The synthesis and the sensing applications of these complexes will be presented in this chapter, while the biological properties will be described in depth in the next chapter.

2.2 Results and discussion

The introductions of fluorescent probes have been achieved following two different synthetic strategies:

(i) Synthesis of the lacunary POM.

(ii) Functionalization of the lacunary POM with an organic spacer containing a suitable functional group.

(iii) Derivatization with the fluorophore in a post-functionalization reaction.

In a different synthetic strategy, the steps (ii) and (iii) may be replaced by:

(ii)* Derivatization of the organic fluorophore with an appropriate organic spacer.

(iii)* Direct functionalization of the fluorescent organic derivative on the POM.

In the following sections the synthetic procedures developed to prepare new functional hybrid derivatives will be described.

2.2.1 Preparation and characterization of vacant polyoxotungstate precursors

In this work, two different polyoxotungstates containing structural defects have been prepared as convenient precursors for the covalent functionalization with organic residues:

(i) $K_8[\gamma\text{-}SiW_{10}O_{36}]$: divacant decatungstate complex. It presents 4 unsaturated oxygen atoms on its surface. Beside the stability under functionalization conditions, it has been chosen because it can be produced with high selectivity, with no need to crystallize it;
(ii) $\beta\text{-A-}Na_8[HPW_9O_{34}]$: trivacant nonatungstate complex. It presents 6 unsaturated oxygen atoms on the surface. It can be functionalized with two or three organic groups, using, respectively, organophosphonates or organosilanes.[15]

^{183}W NMR has been used to confirm the structure of the POM precursors: the structure and the spectra are briefly described below.

(i) $K_8[\gamma\text{-}SiW_{10}O_{36}]$ *(SiW_{10})*

The divacant precursor has been synthesized through a two steps procedure. First, the monovacant precursor $[\beta_2\text{-}SiW_{11}O_{39}]^{8-}$ is obtained as potassium salt, starting from sodium silicate and tungstate, then this complex is converted to the divacant derivative in the presence of K_2CO_3 at pH = 9.1.[16]
The ^{183}W NMR spectrum, recorded for the potassium salt of $[\gamma\text{-}SiW_{10}O_{36}]^{8-}$, is reported in Figure 2.2: the corresponding spin-system, consisting of three signals with integration ratio 2:2:1, is in agreement with the anion symmetry (C_{2v}).[16]

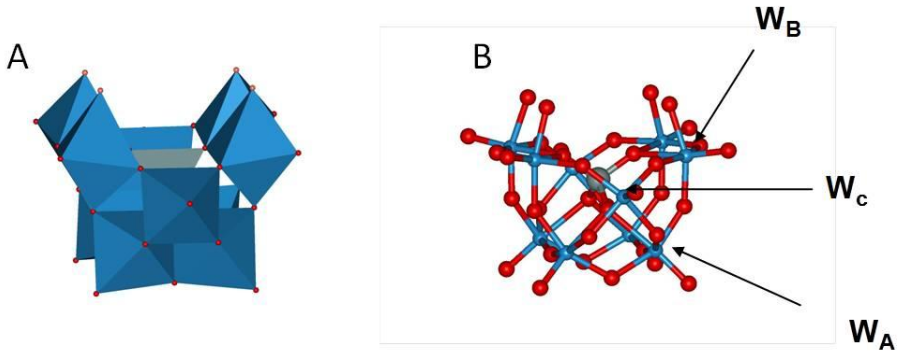

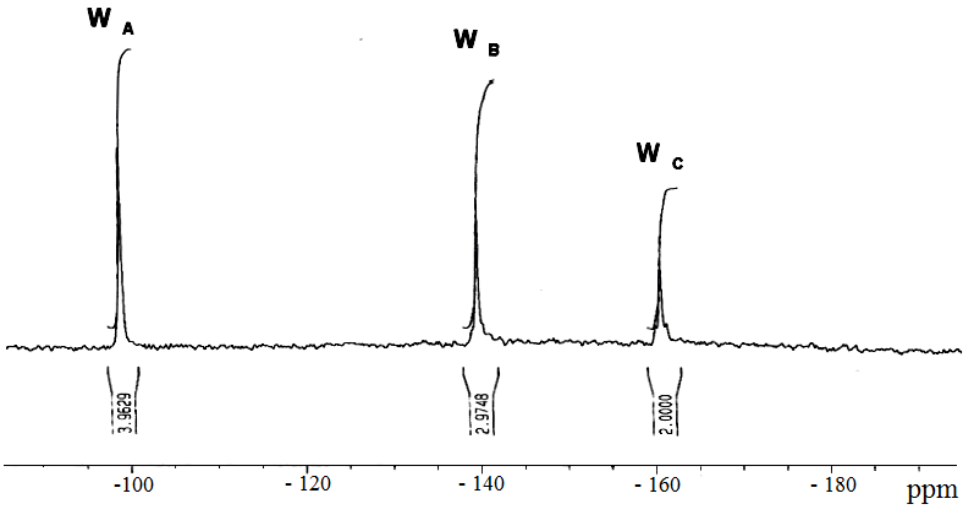

Figure 2.2 *Polyhedral* (**A**) and *Ball-and-stick* representation (**B)** of the divacant precursor **SiW_{10}** and ^{183}W-NMR spectrum for the potassium salt. A difference in integral ratio is due to spin relaxations. W_C (two tungsten side atoms), W_A (four bottom tungsten atoms), and W_B (four vacant tungsten atoms).

(ii) β-A-$Na_8[HPW_9O_{34}]$ *(PW_9)*

The trivacant precursor is obtained, according to the the literature,[17] from the dissolution of sodium tungstate in water, followed by addition of orthophosphoric acid, H_3PO_4 and concentrated acetic acid. The purity of the complex isolated was analyzed by ^{31}P NMR and FT-IR. In particular, FT-IR evidences diagnostic bands at 1056, 1014, 931, 821 and 737 cm^{-1} are in agreement with a *Cs* simmetry. [15,17] The trivacant structure is reported in Figure 2.3.

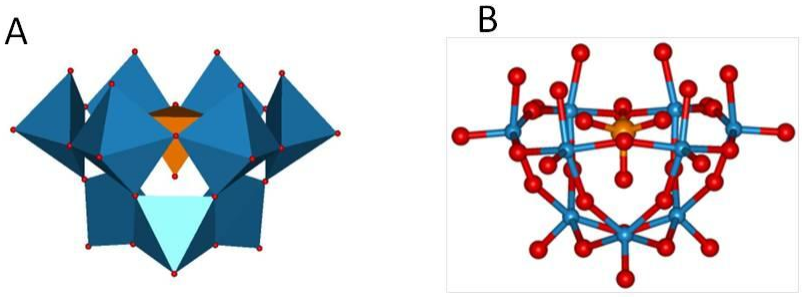

Figure 2.3 *Polyhedral* (**A**) and *Ball-and-stick* representation (**B)** of the trivacant precursor **PW_9**.

2.2.2 Synthesis and characterization of a bis-dansylated polyoxotungstate

Naphthalene-based fluorophores have been extensively investigated, for example, as labels for amino acids, peptides, and proteins. The 5-dimethylamino-1 naphthalenesulfonyl label (generally indicated as dansyl; see Figure 2.1) carries some key optical properties, such as: (i) intense fluorescence in the visible region; (ii) relatively long emission wavelength; (iii) high Stokes shift behavior preventing self quenching; (iii) solvatochromism, by effect of a twisted intramolecular charge-transfer (TICT) excited state, and (iv) antenna-effects of polydansylated arrays.[18,19] These unique features have been successfully exploited for the momolecular design of fluorescent chemosensors in which the dansyl chromophore is used in combination with receptor domains, including multi-dentate ligands, supramolecular hosts such as calix[4]arenes, cyclodextrins, crown ethers, and also silica surfaces.[20,21,22,23,24] Depending on the dansyl environment, selective fluoroionophores have been obtained with interesting sensitivity towards ions such as Pb^{2+},[25] Hg^{2+},[20,26] and Cu^{2+}.[21,27] Moreover, a strong signal amplification results from multi-cooperative fluorescence quenching involving a dansylated surface-array attached to tailored nanosens hors.[19,28]

2.2.2.1 Synthesis of $(n\mathrm{Bu_4N})_4[\{((CH_3)_2N)C_{10}H_6SO_2NH(CH_2)_3Si\}_2O(\gamma\text{-}SiW_{10}O_{36})]$ *(Dans-SiW_{10})*

Selective dansylation of the divacant polyoxotungstate $[\gamma\text{-}SiW_{10}O_{36}]^{8-}$ has been achieved after introduction of an aminopropyl trialkoxysilane spacer (step 1).

The synthetic strategy is reported in scheme 2.3. The reaction entails a double functionalization of the POM precursor at the tetra-oxygenated nucleophilic site, which occurs readily in acetonitrile under phase-transfer conditions, by addition of $n\mathrm{Bu_4NBr}$ (step 1).[6(a),29] The resulting intermediate $[\{NH_2(CH_2)_3Si\}_2O(\gamma\ SiW_{10}O_{36})]^{4-}$ (**APTES-SiW_{10}**)[12(a)], reacts in a post-functionalization (step 2) with dansyl chloride (3.5 equiv.) in the presence of triethylamine (TEA, 3.5 equiv.), in acetonitrile at 50 °C for 2.5 h. The final product $(n\mathrm{Bu_4N})_4[\{((CH_3)_2N)C_{10}H_6SO_2NH(CH_2)_3Si\}_2O(\gamma\text{-}SiW_{10}O_{36})]$ (**1**) was isolated in 69% yield, after precipitation with water and purification by extensive washing/extraction cycles with diethyl ether and acetone.

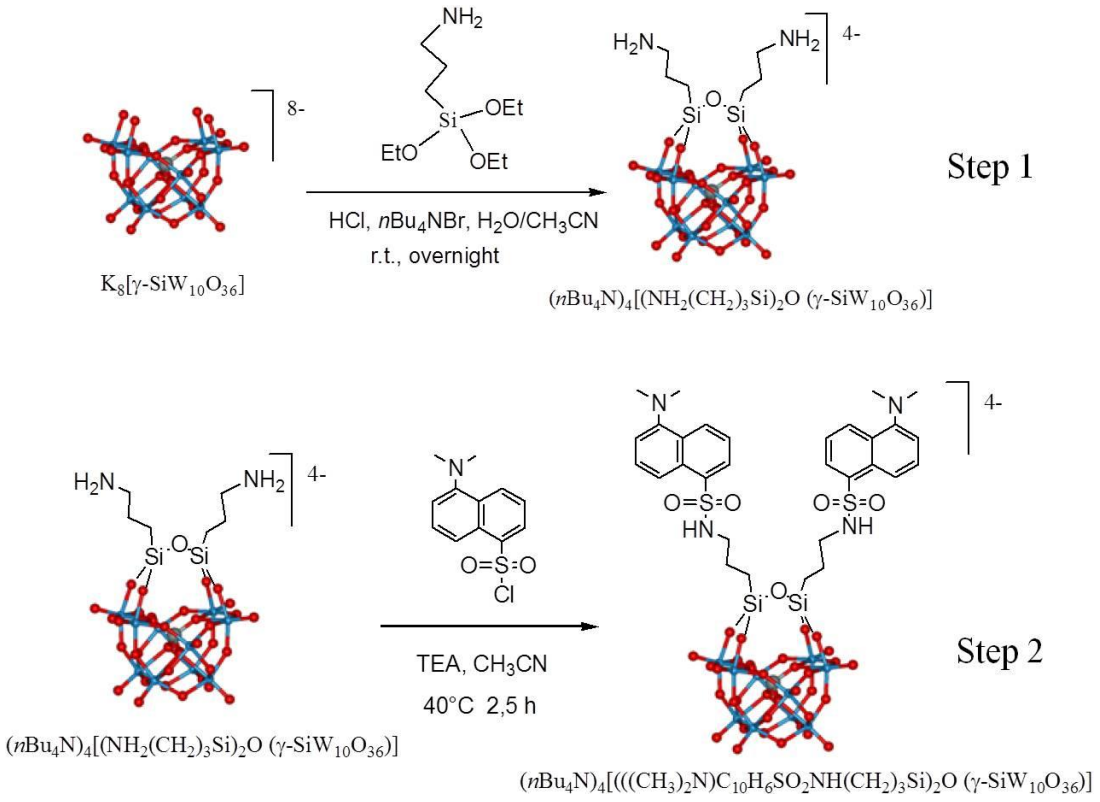

Scheme 2.3 Synthetic routes to a Keggin-type decatungstate functionalized with the dansyl chromophore. Step 1: grafting of $NH_2(CH_2)_3SiCl_3$; Step 2: grafting of the dansyl chromophore.

2.2.2.2 Characterization

Grafting of $NH_2(CH_2)_3SiCl_3$ (Step 1)

The hybrid POM **APTES-SiW$_{10}$** isolated in the first step (Scheme 2.3) display spectroscopic data (^{1}H, ^{13}C, ^{29}Si and ^{183}W NMR, FT-IR) that are in agreement with the expected bis-functionalized structure.[6(a)] In particular, as already introduced, among the characterization techniques, the spin-systems observed by mean of ^{183}W NMR spectrum, is particularly diagnostic because it allow to recognize the expected signal patterns, in agreement with the structural hypothesis, and with different chemical shifts with respect to the corresponding POM precursors **SiW$_{10}$** (see paragraph 2.2.1). In particular, the ^{183}W NMR spectrum of **APTES-SiW$_{10}$** shows three resonances at -107.8, -135.3 and -141.9 ppm in 2:1:2 ratio, confirming the retention of the C_{2v} symmetry of the vacant precursor (Figure 2.4). In comparison with the inorganic precursor, a major downfield shift is observed for the signals corresponding to W_c (two side W atoms), whereas the atoms W_B (four vacant W atoms) in proximity of the vacancy are now the most shielded.[30]

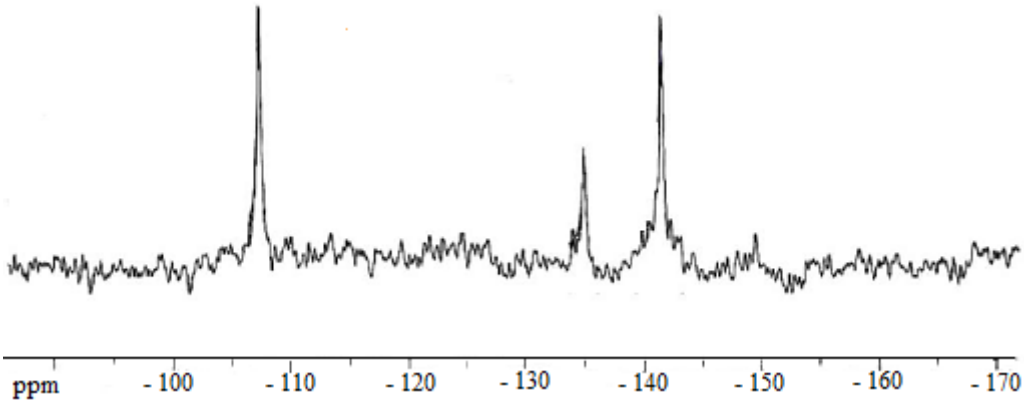

Figure 2.4 ^{183}W NMR spectrum of **APTES-SiW$_{10}$**.

The identification of a new signal ^{29}Si NMR (at - 62.45 ppm) for the POM hybrid derivative, in addition to that observed at - 88.36 ppm for the silicon atom inside the polyanion (integration ratio of 2:1), is a further evidence of the introduction of two RSiO-equivalent groups (Figure 2.5).

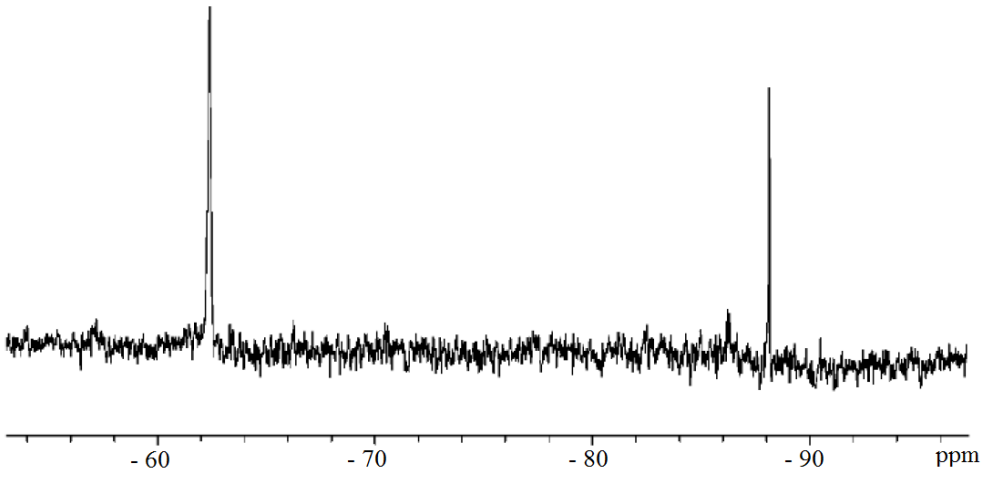

Figure 2.5 ^{29}Si NMR spectrum of **APTES-SiW$_{10}$**.

The FT-IR spectrum differs from that of the precursor POM **SiW$_{10}$** and shows intense absorption bands due to the organic counterion (2960-2874 cm^{-1}) and to the hybrid polyanion; the intense band at 1100 cm^{-1} is assignable to the stretching of the group Si-O-Si linked to the polyoxometalate scaffold and consistent with the bis-functionalization (Figure 2.6).

As expected, the bands are narrower and shifted to higher frequencies than those of the divacant precursor (see paragraph 2.1.1.3).

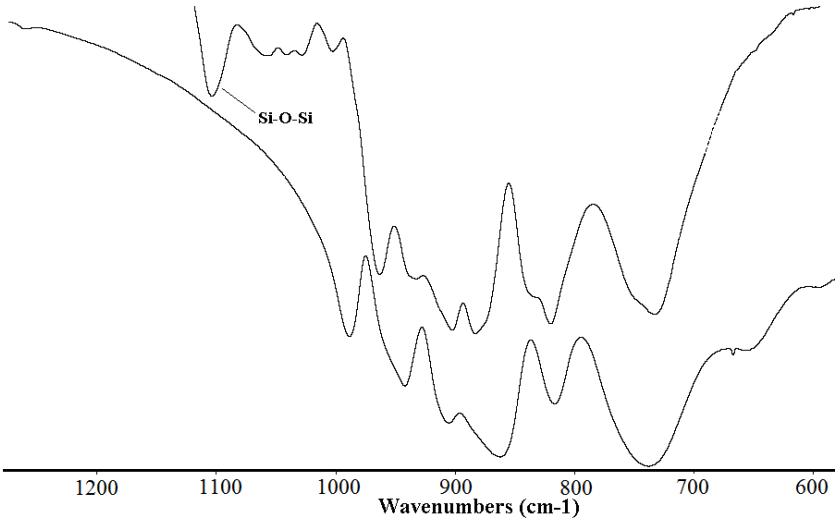

Figure 2.6 FT-IR (KBr) spectrum of **APTES-SiW$_{10}$** (up) in comparison with FT-IR (KBr) spectrum of $K_8[\gamma\text{-}SiW_{10}O_{36}]$ (bottom).

Finally ^{1}H NMR and ^{13}C NMR analysis confirm the presence of the aminopropyl group (Appendix, A1 and A2).

Grafting of the dansyl chromophore (Step 2)

The novel hybrid POM **Dans-SiW$_{10}$** (**1**) exhibits ^{29}Si and ^{183}W NMR spectral patterns confirming, respectively, the maintenance of the bis-organosilane anchoring (^{29}Si NMR: δ = – 62.5 ppm, 2Si), in addition to the central tetrahedral SiO_4 group (^{29}Si NMR: δ = – 88.4 ppm, 1Si), and the overall C_{2v} symmetry of the POM structure with a 2:1:2 intensity ratio of the three expected ^{183}W NMR signals (^{183}W NMR: δ = –107.9, –136.2, –142.1) (Appendix, A4 and A5).

The FT-IR spectrum features diagnostic bands between 982 and 737 cm^{-1} (W–O bonds) and weak absorptions at 1101 and 1045 cm^{-1} (Si–O); furthermore, comparison with the spectrum of **APTES-SiW$_{10}$** confirms the integrity of the hybrid POM network upon dansylation. The new absorption bands observed at 1318 and 1143 cm^{-1} result from the sulfonamidic substituents (Appendix, A3).

The ESI-MS spectrum of (**1**), recorded in the negative mode, shows a dominant cluster centered at *m*/*z* = 773.9 that can be ascribed to $[\{((CH_3)_2N)C_{10}H_6SO_2NH(CH_2)_3Si\}_2O(\gamma\text{-}SiW_{10}O_{36})]^{4-}$, confirming the introduction of two dansyl units through a bis-sulfonamide linkage involving both amino pendants on the POM surface (Figure 2.7).

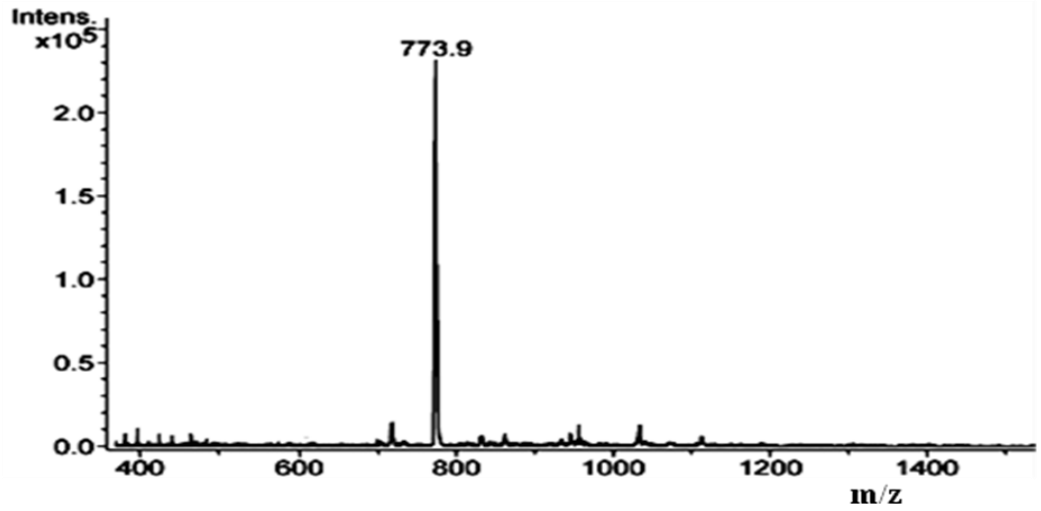

Figure 2.7 ESI-MS ((-),CH_3CN) spectrum of (**1**).

Finally, the ^{1}H and ^{13}C NMR spectra are also consistent with a covalent conjugation and, in particular, the signals of the aromatic carbons of (**1**) are sensibly deshielded (115–153 ppm), with respect to the dansyl chloride precursor (115–135 ppm) (Figure 2.9), the α methylene protons resonate at δ = 2.84 ppm ($\Delta\delta$ = –0.7 ppm with respect to the dansyl-free **APTES-SiW$_{10}$**), and the amidic (SO_2NH) proton resonates at δ = 5.95 ppm (Figure 2.8).

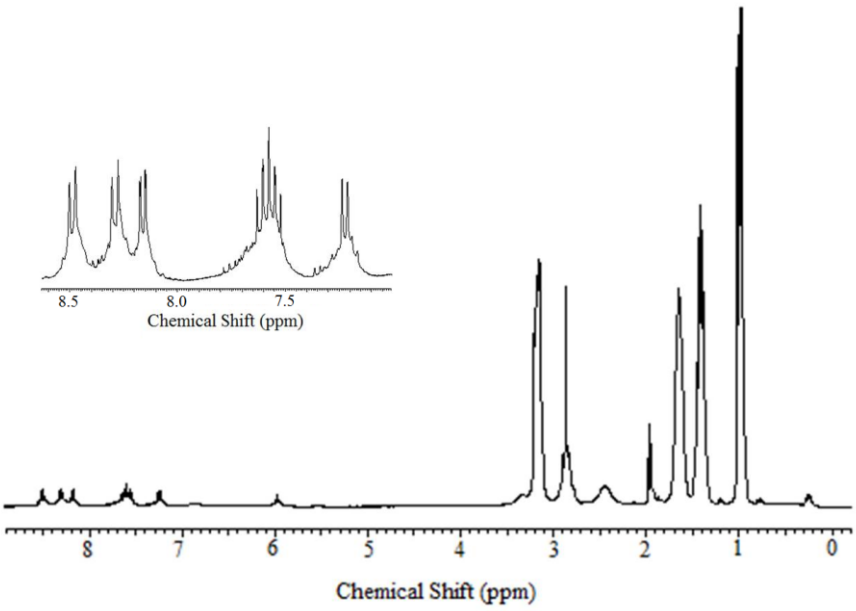

Figure 2.8 ^{1}H NMR spectrum of (**1**) in CD_3CN.

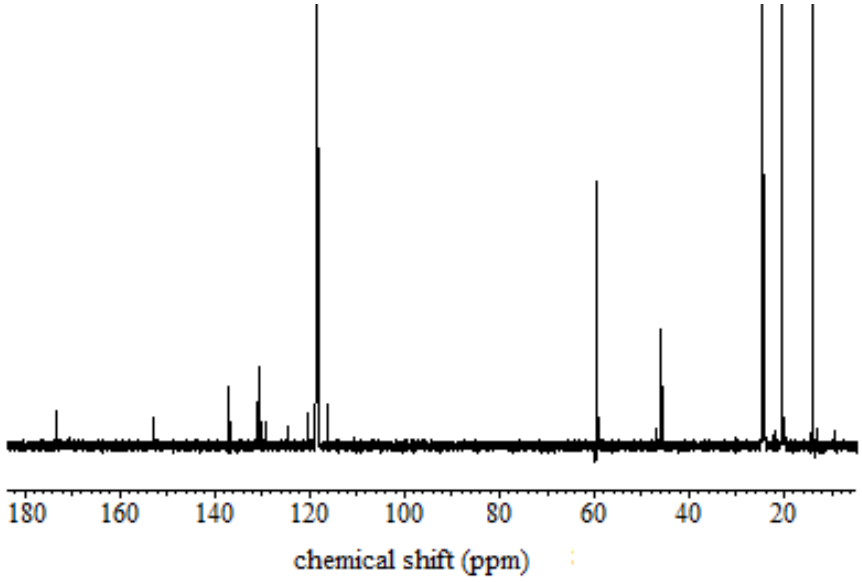

Figure 2.9 ^{13}C NMR spectrum of (**1**) in CD_3CN.

2.2.2.3 Study of optical and sensing properties

The UV-Vis spectrum of (**1**) (>200 nm) displays a shoulder at 218 and a maximum at 250 nm, together with a broad absorbance tail extending up to 450 nm. This spectral behavior is the result of the POM oxygen-to-tungsten charge transfer bands, overlapping with the typical absorption features of the fluorophore moiety, as can be seen from the superimposed spectra of dansyl-free **APTES-SiW$_{10}$** and of 3-(dansylamido)propyl(triethoxy)silane (reference dansylated silane). In particular, the three absorption bands at 218, 252, and 338 nm can be ascribed to the appended dansyl tweezer (Figure 2.10).

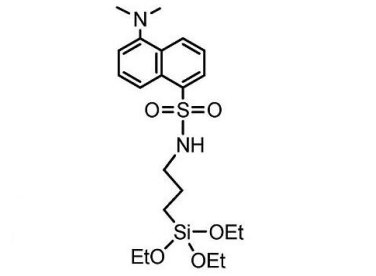

$(Me_2N)C_{10}H_6SO_2NH(CH_2)_3Si(OEt)_3$

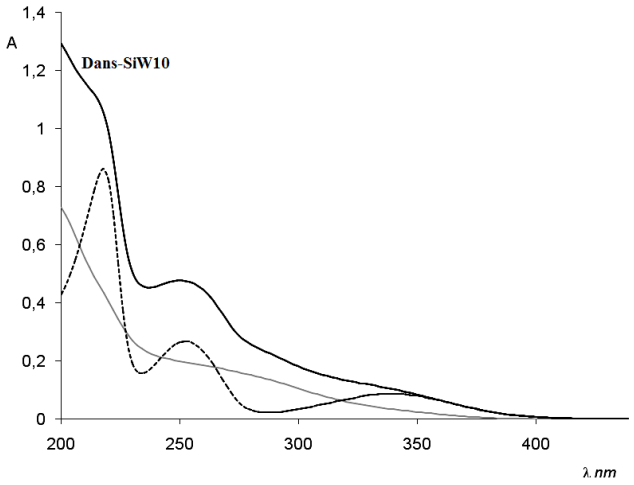

Figure 2.10. Left: structure of the reference dansylated silane[31]; Right: UV-Vis spectra of the dansyl reference (20 μM, dashed line), **APTES-SiW$_{10}$** (10 μM, gray solid line), and **Dans-SiW$_{10}$** (**1**) (10 μM, black solid line) in CH_3CN..

The fluorescence spectra of (**1**) (Figure 2.11) retain the typical pattern expected for the dansyl fluorophore with one emission band centered at 449 nm (λ_{exc} = 324 nm), albeit somewhat blue-shifted and with diminished intensity (20-fold) when compared to the emission observed for the singlet n,π* excited state of the dansylated silane, upon excitation at 336 nm. As verified for **APTES-SiW$_{10}$**, the polyoxotungstate component shows only negligible fluorescence so that the excitation spectrum of (**1**) (λ_{em} = 450 nm) is dominated by the dansyl contribution, exhibiting well-resolved bands at 223, 245, and 329 nm.

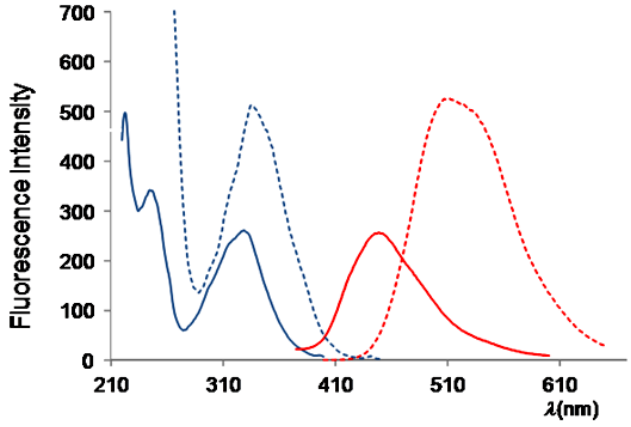

Figure 2.11 Fluorescence spectra of the reference dansylated silane [20 μM, dashed lines: excitation (λ_{em} = 551 nm) and emission (λ_{exc} = 336 nm)] and **Dans-SiW$_{10}$ (1)** [10 μM, solid lines: excitation (λ_{em} = 450 nm) and emission (λ_{exc} = 324 nm)], in CH_3CN.

The quenching effect can be due to the electron acceptor properties of the POM network: a charge transfer state dansyl^{+}-POM^{-} is likely occurring at lower energy in comparison to the dansyl emission state, so to provide an inactivation route by means of an electron-transfer mechanism. Moreover, the blue-shift phenomenon is probably due to destabilization of the dansyl emission state by inter-electronic repulsions with electrons on the POM network, inducing an increase of its energy.

Protonation equilibria

Hybrid (**1**) (10 μM) undergoes protonation equilibria in acetonitrile/water (97.5:2.5 v/v) upon addition of acid (HCl, 1.6x10^{-3} M). The spectrophotometric titration shows major modifications in the spectral range 210–410 nm, whereby a gradual decrease of the bands at 342 and 250 nm is accompanied by a progressive increase of a new absorption at 293 nm, giving rise to four isosbestic points at 222, 236, 274, and 308 nm (Figure 2.12 a).

A parallel modification is registered in the emission and excitation spectra (Figure 2.12, b), where a progressive decrease of the dansyl-centered bands is observed respectively at 450 (λ_{exc} = 324 nm) and at 247 and 330 nm (λ_{em} = 450 nm). This behavior is consistent with the protonation of both dansyl amino groups, and is responsible for a gradual disappearance of the

electronic transition bands involving the nitrogen lone-pair, as experimentally observed in both the absorption and fluorescence spectra.[19]

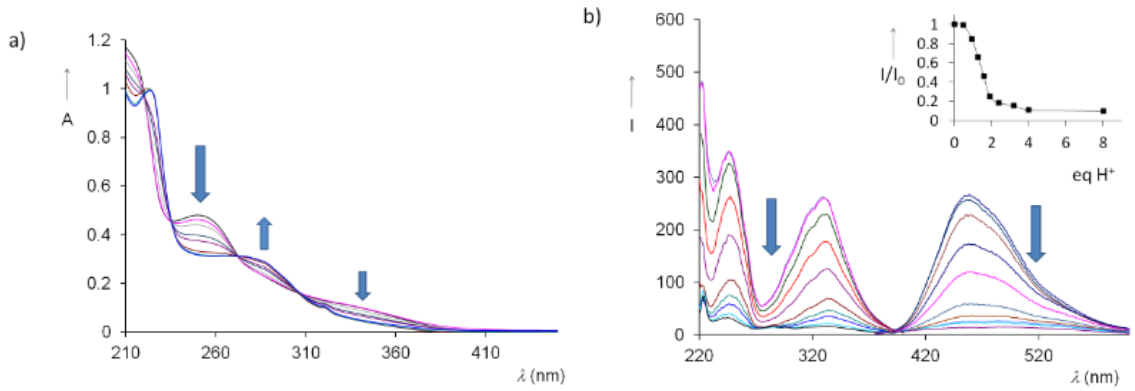

Figure 2.12 Titration of **Dans-SiW$_{10}$** (**1**) (10 μM in CH_3CN) with aqueous HCl ($1.6x10^{-3}$ M). (**a**) UV/Vis spectra; (**b**) Excitation (λ_{em} = 450 nm) and emission (λ_{exc} = 324 nm) spectra. Inset: relative emission intensity at 450 nm upon excitation at 236 nm (one of the isosobestic points).

The spectrophotometric titrations determined either in absorption, emission, or excitation modes, display similar profiles, as a function of the added acid equivalents, and highlight the independent behavior of the dansyl units (Figure 2.13).

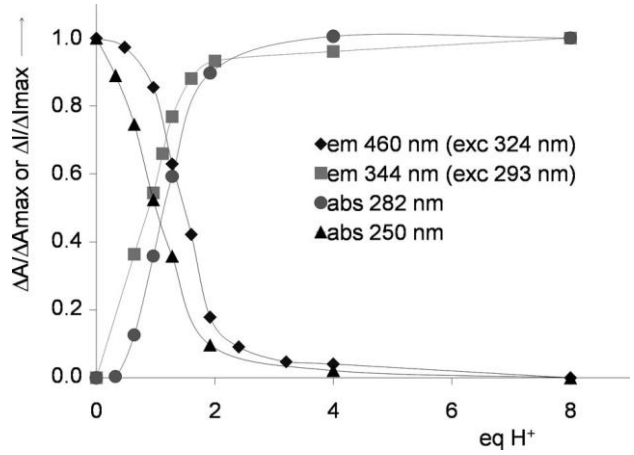

Figure 2.13 Spectrophotometric titration of **Dans-SiW$_{10}$ (1)** (10 μM in CH_3CN) by stepwise addition of aqueous HCl (1.6 mM). Normalized values of absorbance (A) and fluorescence intensity (I) variations monitored at different wavelengths.

In all cases, the observed spectral variations can mainly be ascribed to the dansyl probe, and they follow a sigmoidal behavior, with an initial "silent" phase, which was clearly determined in the fluorescence titration, followed by a linear behavior to a plateau value reached at two

equivalents. This is likely explained by an initial buffering effect of the inorganic polyanion, which acts as a competing proton scavenger in the system.[32]

This hypothesis has been addressed by DFT calculations by using the ZORA-BP86 functional with the TZ2P basis set, including solvent and relativistic effects. Due to the large size of the molecules and to the high number of heavy metals, the internal or core electrons were kept frozen (see *Chapter 5*; paragraph: 5.3.2). These methods provide the optimized geometry for (**1**), together with the molecular electrostatic potential (MEP), and frontier molecular orbital (FMO) analysis (Figure 2.14). MEP analysis allowed the relative basicity of the different sites in the molecular hybrid to be estimated and indicated that a significant and extended electron density was localized at the oxygen centers of the polyoxometalate framework (Figure 2.14 A). Moreover, inspection of the calculated FMO distribution showed that the filled orbitals were delocalized on the oxygen POM centers (oxo band) with energy levels close to the dansyl HOMO and $HOMO^{-1}$, mostly identified by the π orbitals of the naphthalenic units with approximately 30% contribution of the p orbital of the nitrogen atoms of the dimethylamino functions (Figure 2.14 B). These findings support the involvement of the POM scaffold in protonation equilibria.

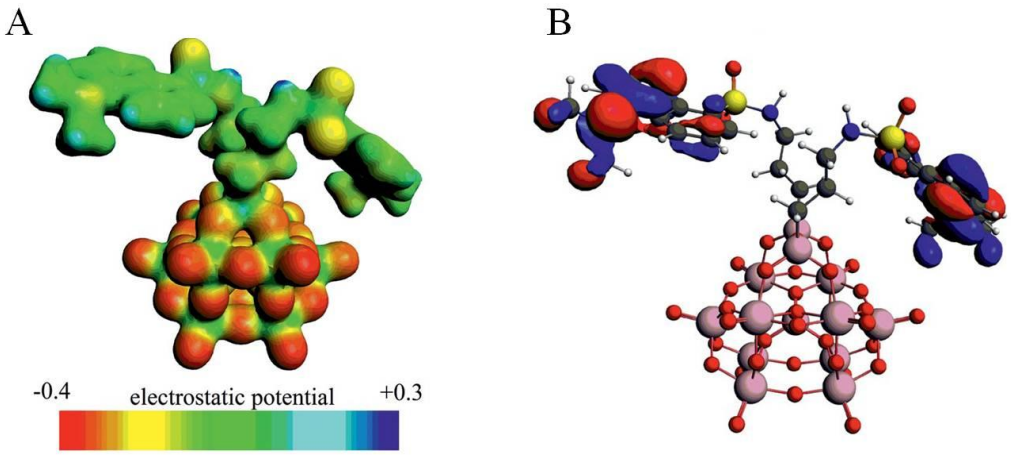

Figure 2.14 A Map of the electrostatic potential and **B** representation of the HOMO and $HOMO^{-1}$ orbitals of **Dans-SiW$_{10}$** (**1**), delocalized in the dansyl moieties.

Fluoroionophore properties

To evaluate the optical response of hybrid **DansSiW$_{10}$** (**1**) towards other cationic analytes and its potential as a fluorescent chemosensor for metal ions, emission quenching experiments were performed in the presence of Cu^{2+} Fe^{2+}, Ni^{2+}, Hg^{2+}, Co^{2+}, Cd^{2+}, Zn^{2+}, and Pb^{2+} by addition of an aqueous analyte solution (1.6 mM) to (**1**) (10 μM in CH_3CN). The bar-graph in

Figure 2.15 highlights the dependence of the fluorescence intensity ratio I/I_0 determined at λ_{em} = 457 (λ_{exc} = 324 nm) as a function of the metal ion added in the system.

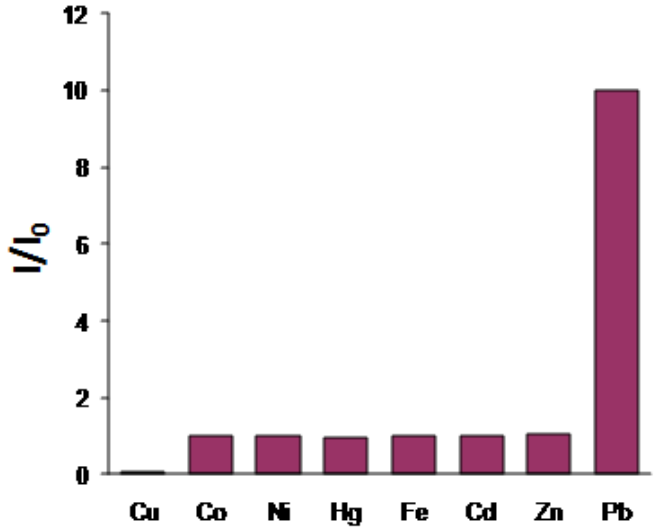

Figure 2.15 Optical sensing screening determined as the ratio between the fluorescence intensity observed for **Dans-SiW$_{10}$ (1)** (10 μM in CH_3CN with 2.5% v/v H_2O) in the absence of any metal ion (I_0) and in the presence of 40 μM metal ions (I) (λ_{exc} = 324 nm; λ_{em} = 457 nm, for Pb^{2+} λ_{em} = 525).

In most cases, no appreciable change in the emission intensity occurred ($I/I_0 \approx 1$), with the remarkable exceptions of Cu^{2+} and Pb^{2+}, which are two ions that are typically recognized as hazardous contaminants for drinking water.[33] The optical sensing by (**1**) clearly entails diverse recognition mechanisms, because opposite effects are induced in the fluorescence emission upon addition of either Cu^{2+} or Pb^{2+} analyte.

In particular, sensing of aqueous $PbSO_4$ (40 μM), was determined by a red shift (68 nm) of the maximum emission wavelength (λ = 525 nm), together with a progressive tenfold increase of luminescence at that wavelength (Appendix, A6). Fluorescence enhancement has been previously reported for dansyl-based Pb^{2+} ionophores, and it was ascribed to metal ligation upon deprotonation of the NH amide function.[27] In this specific case, however, Pb^{2+} ions may trigger a change either in the electronic structure or in the interactions between the chromophoric units, such as a decreased stacking of paired naphthalenic moieties. The similar emission of the Pb^{2+} adduct and of reference dansylated silane may also suggest a reduced interaction between the dansyl units and the polyanionic domain.

On the other hand, stepwise addition of $CuSO_4$ ($1.6x10^{-3}$ M, ca. 4 μL aliquots) induced a progressive quenching of the emission band, monitored at 457 and at 525 nm (λ_{exc} = 324 nm), down to a plateau value of about 5–14% with respect to the initial conditions (Figure 2.16).

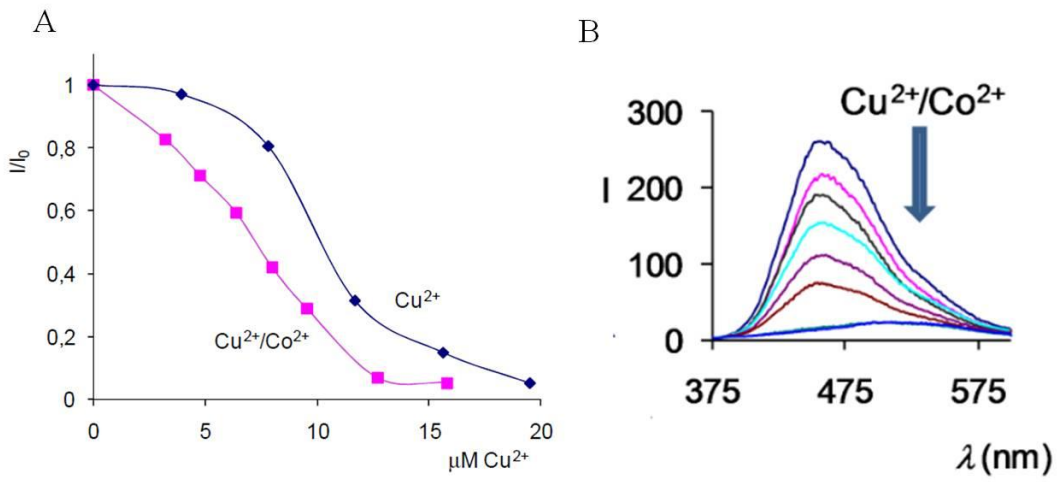

Figure 2.16 A Normalized values of fluorescence intensity (I) obtained for the titration of hybrid **DansSiW$_{10}$** (**1**) (10 µM in CH_3CN) with an aqueous $CuSO_4$ solution (0–20 µM), in the presence and in the absence of 40 µM $CoSO_4$. **B** Emission (λ_{exc} = 324 nm) spectra.

The Cu^{2+} titration profile resembles the protonation curve, determined for (**1**) with a similar procedure, again showing a sigmoidal shape, with a turning point at about 1:1 equiv. ratio. Moreover, the UV/Vis spectrum registered for (**1**) in the presence of the cuprous salt retains isosbestic points (albeit with a lower absolute ΔAbs) similar to those ascribed to the protonation equilibria (Figure 2.12 and 2.13). Accordingly, a plausible trigger for the Cu^{2+}-induced emission quenching could originate from its binding at the electron rich amine sites of the luminophore moiety. For comparison, the fluorescence response of reference compound was evaluated with respect to Cu^{2+}, which showed negligible activity. This observation highlights the interplay between the two domains in the sensing mechanisms.

Indeed, at variance with the majority of previously reported Cu-chemosensors, (**1**) does not contain any additional binding site tailored for a specific transition metal.[34] Selective sensing by (**1**) and the tuning of its optical response stems from its multi-functional molecular nature integrating a dansyl-based optical transducer with the tungsten-oxide polyanionic surface. These latter features are instrumental for the geometrical constrains/spacing of the bis-fluorophore tweezer, and the occurrence of competing cation scavenging equilibria that can be exploited in the analysis of complex mixtures. Indeed, the selective recognition of Cu^{2+} by (**1**) has also been validated in the presence of potentially interfering bivalent metal ions such as Fe^{2+}, Ni^{2+}, Co^{2+}, and Zn^{2+}. The presence of these latter ions did not result in any detrimental effects in the system, even when added in large excess (40 µM). On the other hand, the combined presence of "dansyl silent" metal cations, for instance Co^{2+}, turns out to improve the optical signaling of Cu^{2+}, resulting in a linearization of the sigmoidal fluorescence titration

curve (Figure 2.16). This can be explained by a preferential electrostatic interaction between Co^{2+} and the POM surface, thus overriding the initial lag-response of the dansyl fluorophore.[35] Under such optimized conditions, a linear correlation is obtained, featuring a micromolar detection limit with maximum quenching at [Cu^{2+}] above 12 μM, pointing to a 1:1 interaction with (**1**).

2.2.3 Synthesis and characterization of a pyrene-functionalized polyoxotungstate

Pyrene is a rigid polyaromatic hydrocarbon fluorophore. It is a good probe as it presents a strong absorption and luminescence in the visible region (350-450 nm). One important application of the pyrene fluorescence stems from its ability to probe the polarity of the local microenvironment, either in a hydrophobic or hydrophilic media, from the change of specific emission spectrum.

The extended π-system of the pyrene derivatives can be also exploited to bind hydrophobic molecules, such as [60]fullerene.[36] Furthermore, the use of pyrene molecules as donors has been reported for a range of molecular systems exhibiting photo-induced electron transfer (PET). In this respect, many POMs are able to store several electrons with only minor structural reorganization and their reduced forms display efficient electrocatalytic properties,[37] notably for the hydrogen evolution reaction.[38] As a consequence, POMs are attractive candidates for the development of functional artificial photosynthetic devices and, in particular, their association to a light-harvesting antenna, such as pyrene derivatives, is yet necessary, since POMs themselves are only photoactive in the UV part of the solar spectrum.[39]

Moreover, amphiphilic hybrid POM clusters with pendent pyrene fluorescent probes are of potential interest for the construction of smart supramolecular assemblies.[40]

Finally, planar aromatic moiety, as pyrene, can intercalate into neighboring base pairs of double-stranded DNA.[41] This intercalation can results from collective interactions of different forces depending on the structure of intercalators, including π-π interactions, the van der Waals force, hydrophobic interactions, and so forth. Considering the potential applications of POMs in medicine, the grafting of an intercalator containing aromatic rings on POMs surface, could be a focus of interest to researchers in different fields, referring to molecular recognition and nanomedicine.

2.2.3.1 Synthesis of $(n\mathrm{Bu_4N})_4[\{C_{16}H_9SO_2NH(CH_2)_3Si\}_2O(\gamma\text{-}SiW_{10}O_{36})]$ *(Pyr-SiW$_{10}$)*

Synthesis of the reactive ligand: pyrene sulfonyl chloride

First, in order to obtain a chromophore reactive in the reaction with the hybrid **APTES-SiW$_{10}$** (see previous paragraph), we have functionalized the pyrene with the sulfonyl chloride group. The synthetic scheme reaction is reported below.

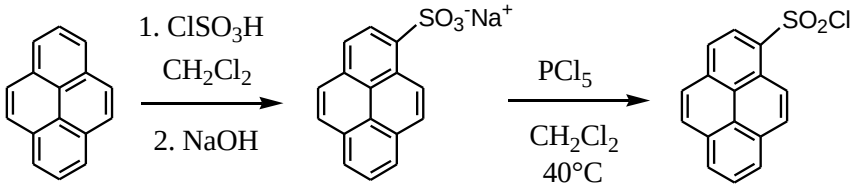

Scheme 2.4 Synthetic routes to 1-pyrensulfonyl chloride.

The first synthetic step (Scheme 2.4), chlorosulfonation of pyrene, proceeded smoothly. The isolated intermediate, sodium l-pyrenesulfonate contains hydration water and NaOH, but it can be used without further purification. Transformation to pyrenesulfonyl chloride was performed in CH_2Cl_2 at 40°C in the presence of phosphorus pentachloride. Pyrene sulfonyl chloride was purified by silica gel column chromatography using CH_2Cl_2:hexane (2:3) as eluent. The yield of the orange product was 92.7%.[42]

Grafting of the ligand on the POM scaffold

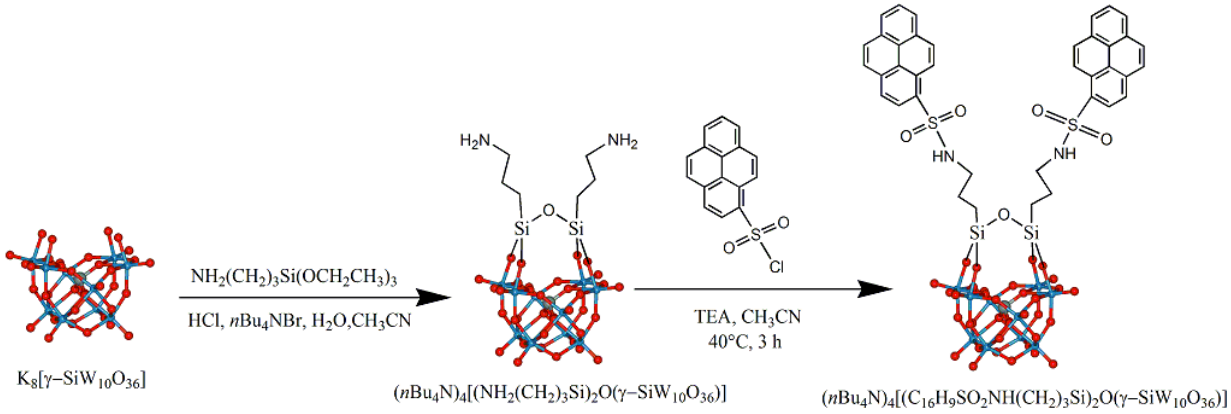

Scheme 2.5 Synthetic routes to a Keggin-type decatungstate functionalized with the pyrene chromophore.

Selective introduction of pyrene on the divacant polyoxotungstate $[\gamma\text{-}SiW_{10}O_{36}]^{8-}$ was achieved after introduction of an aminopropyl silane spacer, as reported for the bis-dansylated

polyoxotungstate $(n\text{Bu}_4\text{N})_4[\{((\text{CH}_3)_2\text{N})\text{C}_{10}\text{H}_6\text{SO}_2\text{NH}(\text{CH}_2)_3\text{Si}\}_2\text{O}(\gamma\text{-SiW}_{10}\text{O}_{36})]$ (**1**). The first intermediate $[\{\text{NH}_2(\text{CH}_2)_3\text{Si}\}_2\text{O}(\gamma\text{-SiW}_{10}\text{O}_{36})]^{4-}$ reacts in a post-functionalization reaction in acetonitrile at 50°C, in the presence of 1-pyrensulfonyl chloride (Pyr-SO_2Cl) (2.5 equiv.) and triethylamine (TEA, 2.5 equiv.) for 3 h. Finally, the mixture was centrifuged to remove insoluble reagents and byproducts. The volume of the solution was reduced to 1 mL, upon evaporation under vacuum, than diethylether was added to precipitate the product. $(n\text{Bu}_4\text{N})_4[\{\text{C}_{16}\text{H}_9\text{SO}_2\text{NH}(\text{CH}_2)_3\text{Si}\}_2\text{O}(\gamma\text{-SiW}_{10}\text{O}_{36})]$ **Pyr-SiW$_{10}$** (**2**) was isolated in 71% after washing/extraction with water, diethyl ether, and a small amount of CH_2Cl_2 on a fritted funnel and drying several hours under vacuum.

The solution characterization of the resulting hybrid POM was performed by the following techniques: ^{183}W, ^{29}Si, ^{13}C, ^{1}H NMR spectroscopy and ESI-MS.

The hybrid (**2**) exhibits a ^{183}W NMR spectral pattern in agreement with the expected bis-functionalized, C_{2v}-symmetric structure, with three multiple resonances at -107.51, -136.03, -141.52 ppm in relative ratio 2:1:2 respectively, corresponding to W_A (four bottom W atoms), W_C (two side W atoms), and W_B (four vacant W atoms).

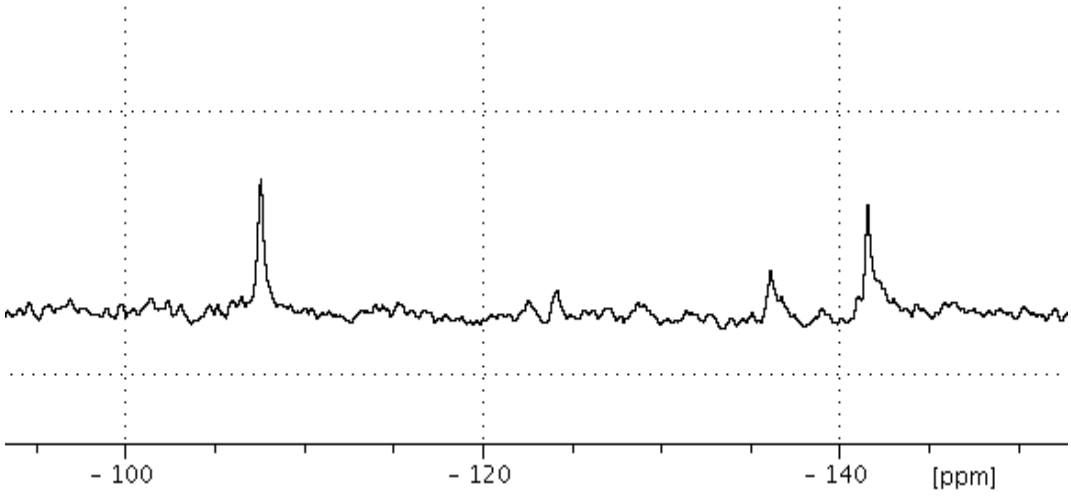

Figure 2.17 ^{183}W NMR of (**2**) in $\text{CD}_3\text{CN}/\text{CH}_3\text{CN}$.

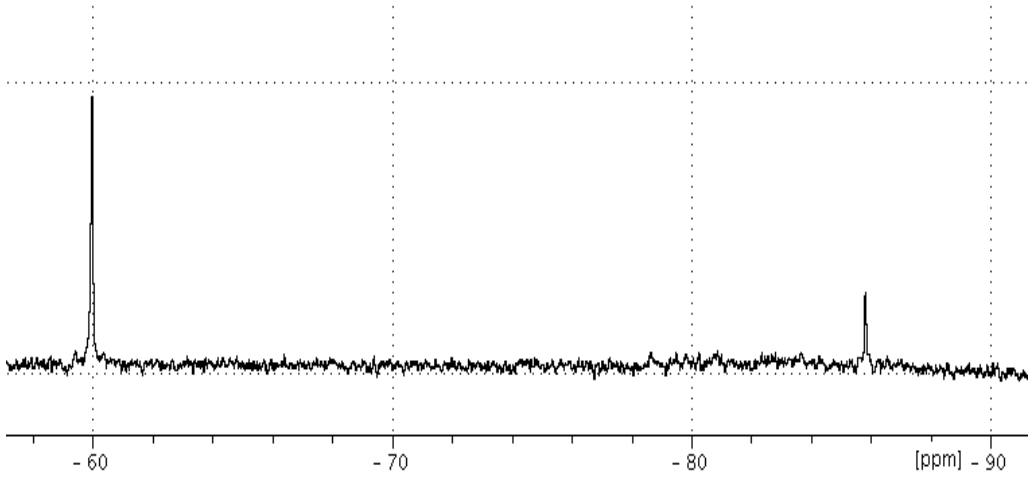

Figure 2.18 ^{29}Si NMR of (**2**) in CD_3CN/CH_3CN.

The ^{29}Si NMR spectrum reveals two signals at - 62.61 and - 88.34 ppm with integration ratio 2:1 respectively. These results are consistent with a double functionalization.

FT-IR evidences diagnostic bands at 964, 950, 903, 886, 840, 821 cm^{-1} for ν_{as}(W–O–W), weak bands at 1050 cm^{-1} for ν_{as}(Si–O-Si) and 1102 cm^{-1} for ν_{as}(Si–C), confirming the maintenance of the POM structure (Appendix, A7).

^{1}H NMR and ^{13}C NMR spectroscopies confirm the introduction of the pyrene groups, since expected resonances for the aromatic pyrene protons and carbons are observed between 8.86 - 8.02 and 135.21–124.66 ppm respectively (Figure 2.19 and Appendix, A8).

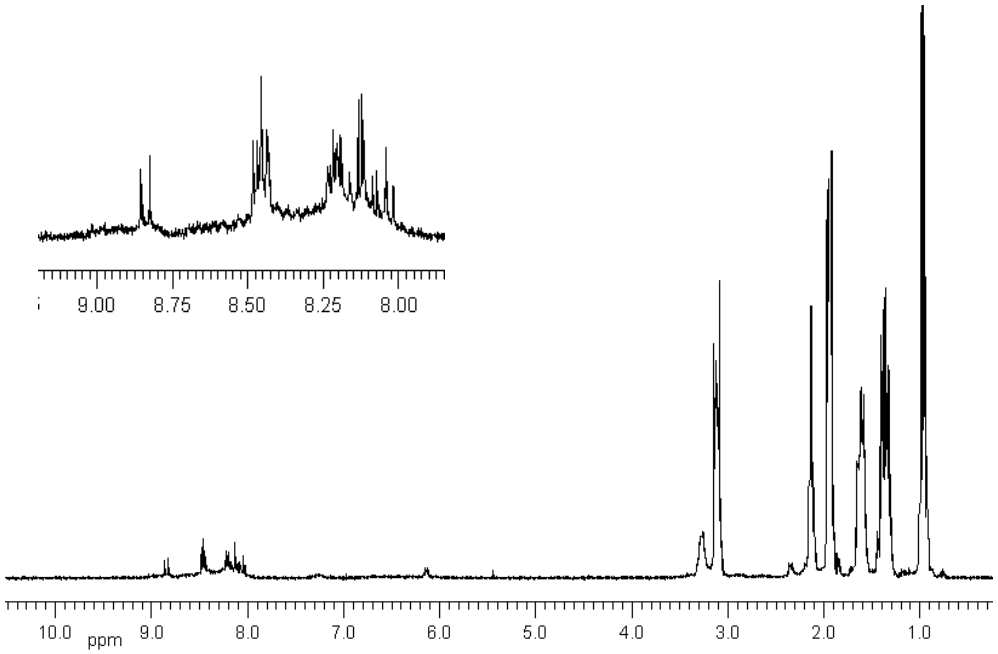

Figure 2.19 ^{1}H-NMR of (**2**) in CD_3CN.

The ESI-MS of hybrid (**2**), registered in negative mode, show cluster signals centered at *m*/*z* = 789.5; 1053.1 attributed, respectively, to the ions $[C_{38}H_{32}N_2O_{41}S_2Si_3W_{10}]^{4-}$ = 789.9 and $[C_{38}H_{33}N_2O_{41}S_2Si_3W_{10}]^{3-}$ = 1053.5 (Appendix, A9).

2.2.3.2 Study of optical, sensing and interaction properties

The UV-Vis spectrum of (**2**) (>200 nm) display seven absorption bands at 233, 242, 269, 279, 336, 351 and 358 nm that can be ascribed to the appended pyrene tweezer.

This spectral behavior is the result of the POM oxygen-to-tungsten charge transfer bands overlapping with the typical absorption features of the pyrene moiety, as can be seen from the comparison with the spectrum of the pyrene (Figure 2.20).

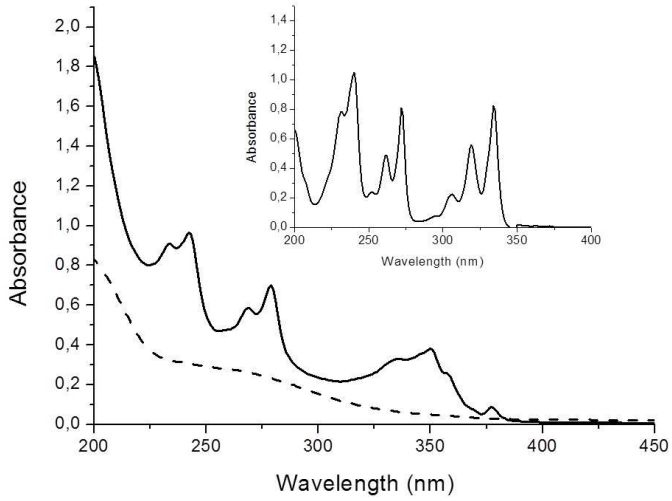

Figure 2.20 UV-Vis spectra of **Pyr-SiW$_{10}$** (**2**) (10 μM, black solid line) and **APTES-SiW$_{10}$** (10 μM, dashed line) in CH_3CN; Inset: UV/Vis spectrum of pyrene (20 μM) in CH_3CN.

The fluorescence spectrum of (**2**) (Figure 2.21) maintains the typical pattern expected for the pyrene fluorophore with two emission bands centered at 379 and 397 nm (λ_{exc} = 338 nm), albeit somewhat red-shifted in excitation and with diminished intensity (~ 3-fold) when compared to the reference compound fluorescence (pyrene).

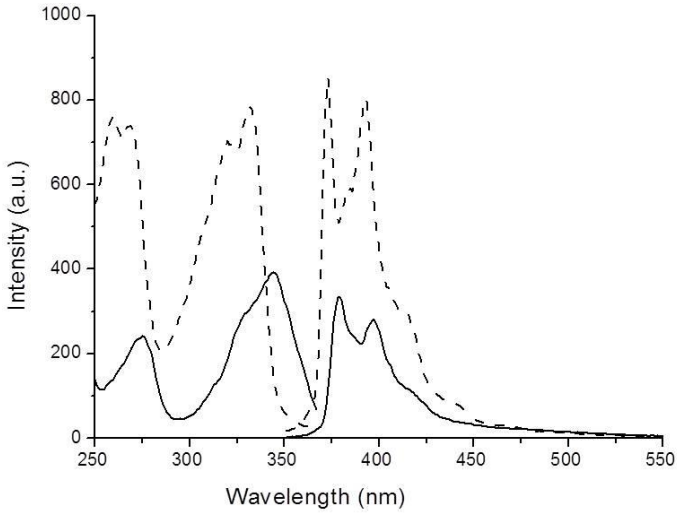

Figure 2.21 Fluorescence spectra of (**2**) [10 μM, solid lines: excitation (λ_{em} = 380 nm) and emission (λ_{exc} = 338 nm)] and pyrene [20 μM, dashed lines: excitation (λ_{em} = 389 nm) and emission (λ_{exc} = 338 nm)], in CH_3CN.

To evaluate the molecular interaction capability of the pyrene-functionalized decatungstosilicate towards hydrophobic molecules we have performed luminescence quenching experiments in the presence of different neutral molecules. To promote π-π stacking interactions, we included derivatives with extended π-system: 1,4-dinitrobenzene (DNB),[43] adenin (ADN), adenosin (ADS), caffeine[44] and fullerene (C_{60})[45].

The bar-graph in Figure 2.22 highlights the dependence of the fluorescence intensity ratio as a function of the molecules added in the system.

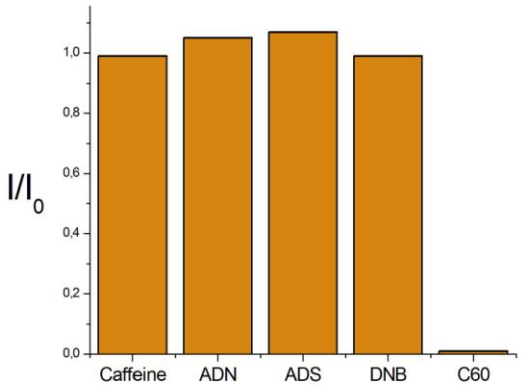

Figure 2.22 Optical sensing screening determined as the ratio between the fluorescence intensity observed for (**2**) (1 μM in DMF) in the absence of any molecules (I_0) and in the presence of 100 equivalents of aromatic molecules (I).

In most cases, no appreciable change in the emission intensity occurred ($I/I_0 \approx 1$), with the remarkable exceptions of C_{60}.

The nature of the interaction between the hybrid system containing pyrene moieties and fullerene molecules was further investigated. Stepwise addition of C_{60} in *ortho*-dichlorobenzene (*o*-DCB) ($5x10^{-3}$ M, 4µL aliquots) induced a progressive quenching of the emission band, detected at 379 and at 397 nm (λ_{exc} = 330 nm) of the hybrid (**2**) dissolved in DMF.

The luminescence quenching (Figure 2.23 A) has highlighted the interaction of the POM with fullerene molecules in the micromolar range. The fluorescence intensity ratio, $(I^0/I)-1$, of POM (**2**) at 400 nm was measured as a function of the C_{60} concentration at room temperature. As shown in Figure 2.23 B, the slope of the Stern-Volmer (S-V) plot is higher in the presence of a little percentage of H_2O, confirming the π-π stacking contribute in the interaction.

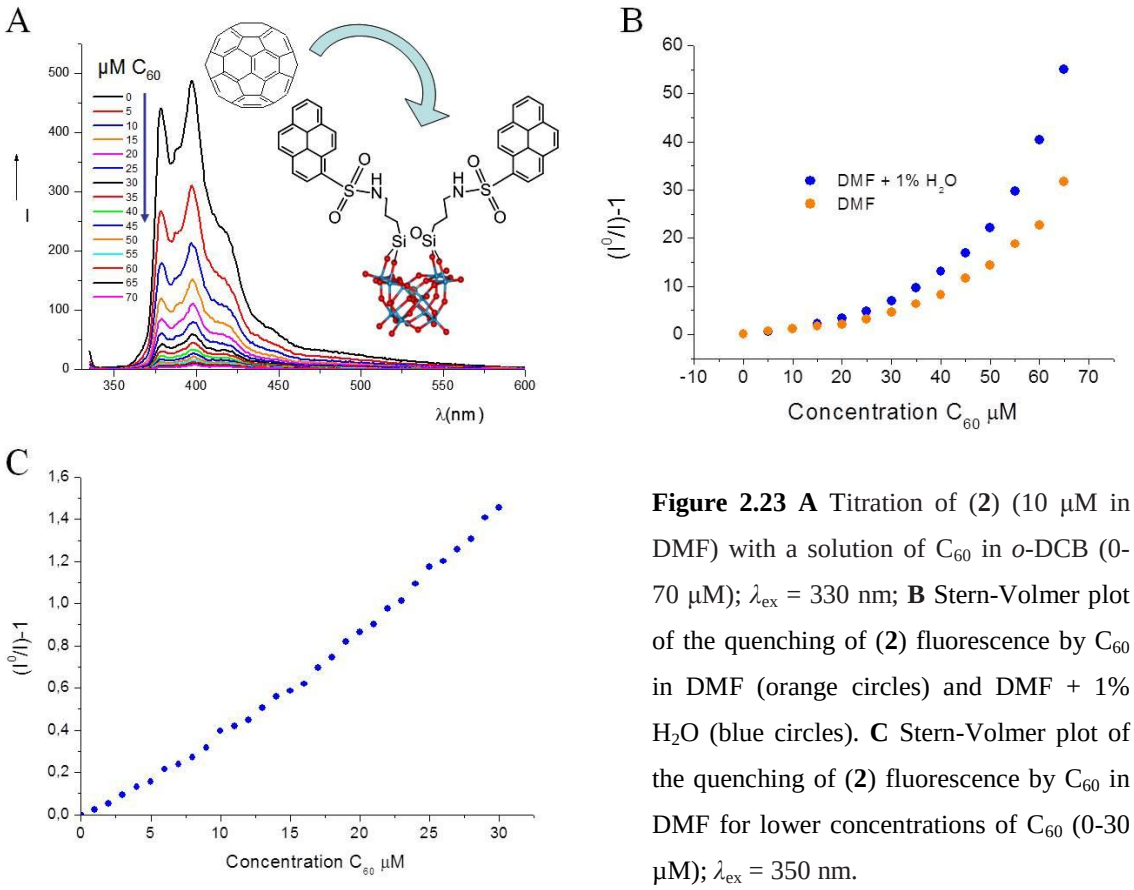

Figure 2.23 A Titration of (**2**) (10 µM in DMF) with a solution of C_{60} in *o*-DCB (0-70 µM); λ_{ex} = 330 nm; **B** Stern-Volmer plot of the quenching of (**2**) fluorescence by C_{60} in DMF (orange circles) and DMF + 1% H_2O (blue circles). **C** Stern-Volmer plot of the quenching of (**2**) fluorescence by C_{60} in DMF for lower concentrations of C_{60} (0-30 µM); λ_{ex} = 350 nm.

The Stern-Volmer plot show a linear profile up to 1 equivalent of C_{60} added (10 µM of C_{60} in solution). After 1 equivalent the plot became highly curved, upward, and non linearly proportional to the fullerene concentration. In particular, the competition for light absorption

by C_{60} can explain the observed upward deviation. To minimize this effect, a further titration was performed at low C_{60} concentration region (0-30 μM), choosing an excitation wavelength (λ_{ex} = 350 nm) where the light absorption of the quencher is weaker in comparison to the absorption of pyrene groups. In such conditions, a linear S-V behavior can be observed (Figure 2.23 C). The data were thus corrected for the inner filter absorption effects of the C_{60} (see *Chapter 5*: paragraph 5.3.1) and the Stem Volmer constant results Ksv = (9.40 ± 0.22) $x10^3$ M^{-1}. Such weak binding constant is likely ascribed to the non-planar structure of C_{60}.[46]
Hence, experiments with nanotubes (SWNTs) have been performed to yield an enhanced bonding. In particular, SWNTs contain a vast mixture of diameters and chiralities defining their electronic structure as being metallic or semiconducting. Among the efforts to increase the processability of this unique materials, noncovalent functionalization of these systems represents a corner stone, as it is nondestructive and does not alter the intrinsic properties of nanotubes. In this respect, a strong and specific interaction with the SWNTs can be ensured through π–π stacking.
Thus, 3 mg of carbon nanotubes (CNTs) were added to 3 mg of **Pyr-SiW$_{10}$** dispersed in 3 mL of a DMF/MeOH 1:1 solution. Fluorescence experiments show a quenching of the **Pyr-SiW$_{10}$** luminescence upon addition of CNTs (3 mg/$7.27x10^{-7}$ mol POM) (peaks at 379 nm and 398 nm), confirming that the pyrene units are involved in an electron transfer with the carbon nanostructures. Furthermore, upon the interaction of **Pyr-SiW$_{10}$** with different kind of CNTs, changes in the NIR-semiconducting region can be observed: red shift and reduction of absorption intensity for HiPCO (SWNTs diameter distribution 0.8–1.4 nm; Figure 2.24 C), blue shift for CoMoCAT (SWNTs diameter distribution 0.7–0.9 nm; Figure 2.24 D) respectively. This suggest the capability of **Pyr-SiW$_{10}$** to interact and recognize carbon nanotubes according to their helicity and diameter. This behaviour will be studied in detail in collaboration with the group of Prof. M. Prato (University of Trieste).

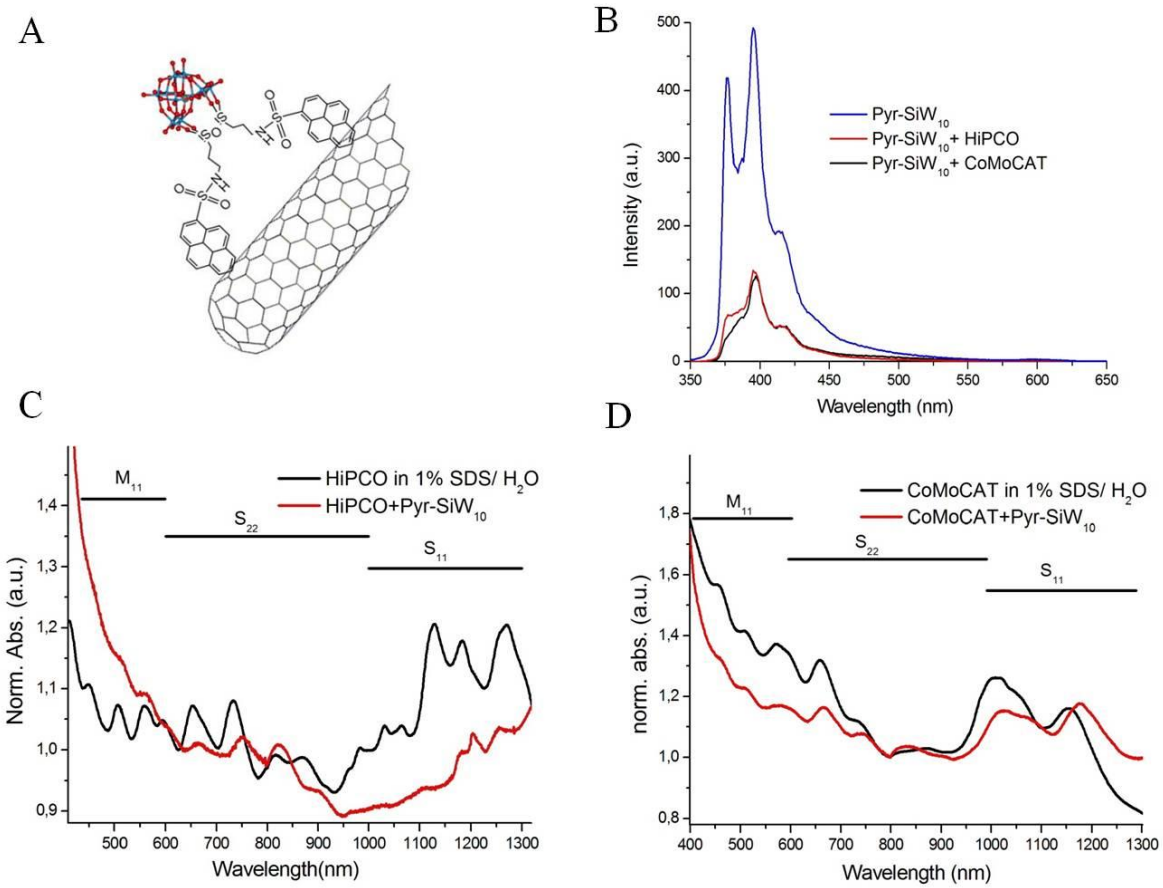

Figure 2.24 A Representation of interaction of (**2**) with a nanotube. **B** Fluorescence spectra of (**2**) (λ_{exc}=335 nm) in the absence (blue line) and in the presence of CNTs (HiPCO: red line, CoMoCAT: black line). **C** UV/Vis/NIR spectra of HiPCO nanotubes in the absence (black line) and in the presence of (**2**) (red line). **D** UV/Vis/NIR spectra of CoMoCAT nanotubes in the absence (black line) and in the presence of (**2**) (red line). (3 mg/ 7.27x10^{-7} mol POM); SDS: sodium dodecyl sulfate.u

2.2.4 Synthesis and characterization of two fluoresceine-appended polyoxotungstates

Fluorescein is a synthetic organic compound soluble in water and alcohol. It is widely used as a fluorescent tracer for many applications. In particular, in cellular biology, the isothiocyanate derivative of fluorescein is often used to label and track labeled compounds within cells by fluorescence microscopy. The fluorescence of this molecule is very intense at 521 nm, and excitation occurs at 494 nm. Fluorescein has a pK_a of 6.4, and its ionization equilibrium leads to pH-dependent absorption and emission over the pH range from 5 to 9.

In this paragraph, the introduction of fluoresceine on two different POM scaffolds (K_8[γ-$SiW_{10}O_{36}$] and β-A-Na_8[HPW_9O_{34}]) will be described.

2.2.4.1 Synthesis of $(n\mathrm{Bu_4N})_4[\{(C_{20}H_{11}O_5)NHCSNH(CH_2)_3Si\}_2O(\gamma\text{-}SiW_{10}O_{36})]$ *(FITC-SiW_{10})*

The introduction of fluoresceine probe on the polyanionic scaffold $[\gamma\text{-}SiW_{10}O_{36}]^{8-}$ was achieved by a synthetic procedure that also involves the amino-functionalized POM (**APTES-SiW_{10}**), and its reaction with fluoresceine isothiocyanate (FITC), to obtain a thioureido group. The scheme of reaction is reported below.

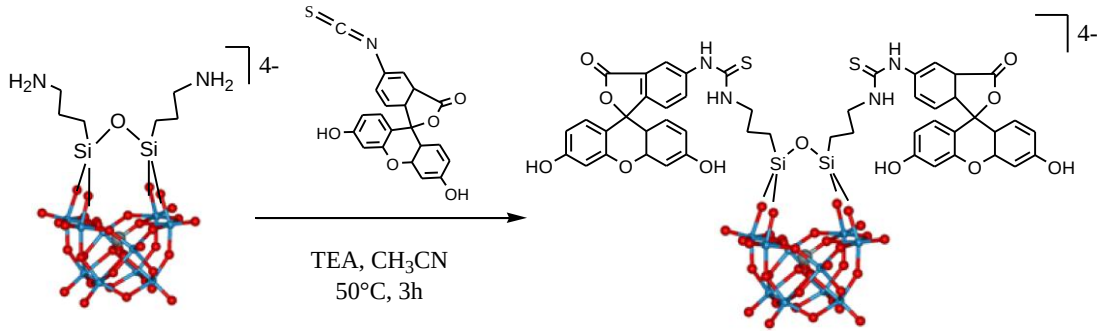

$(n\mathrm{Bu_4N})_4[(NH_2(CH_2)_3Si)_2O\ (\gamma\text{-}SiW_{10}O_{36})]$

$(n\mathrm{Bu_4N})_4[(C_{20}H_{11}O_5)NHCSNH(CH_2)_3Si)_2O\ (\gamma\text{-}SiW_{10}O_{36})]$

Scheme 2.6 Synthetic routes to a Keggin-type decatungstate functionalized with the fluoresceine chromophore.

The hybrid POM $[\{NH_2(CH_2)_3Si\}_2O(\gamma\text{-}SiW_{10}O_{36})]^{4-}$ reacts with 2.5 equivalents of FITC in the presence of 2.5 equivalents of triethylamine (TEA). As in the previous cases, the product $(n\mathrm{Bu_4N})_4[\{(C_{20}H_{11}O_5)NHCSNH(CH_2)_3Si\}_2O(\gamma\text{-}SiW_{10}O_{36})]$ (FITC-SiW_{10}) (**3**) was isolated by precipitation with water and then washed with water and various organic solvents (diethyl ether, methanol), obtaining a yield of 56%.

The bis-decorated molecular hybrid was characterized by FT-IR, multinuclear NMR, ESI-MS, UV-Vis and luminescence spectroscopy. The complete characterization has highlighted several features shared with the previously described POMs.

^{1}H NMR and ^{13}C NMR spectroscopies confirm the introduction of the fluoresceine groups, since the expected resonances for the aromatic fluoresceine protons and carbons are observed between 9.14 -6.56 ppm and 181.78 and 84.25 ppm respectively.

Finally, relevant spectral features, in agreement with the bis-substitution, are reported in Table 2.1 (see also *Chapter 5* and Appendix, A10 - A15):

Table 2.1 Relevant spectral features of **FITC-SiW$_{10}$** (**3**).

Solvent	m/z	^{29}Si NMR (ppm)	^{183}W NMR (ppm)
CH_3CN	852.5[a] 1217.5[b]	-61.34 (2Si), -88.26 (1Si)	- 108.32 (4W) - 132.87 (2W) - 143.32 (4W)

(a) expected for $[C_{48}H_{38}N_4O_{47}S_2Si_3W_{10}]^{4-}$ = 852.4, (b) expected for $[C_{64}H_{74}N_5O_{47}S_2Si_3W_{10}]^{3-}$ = 1217.3; polyanion without (a) and with (b) a single nBu$_4$N$^+$ countercation.

2.2.4.2 Study of optical properties

Generally, the absorption and the luminescence analysis of free fluorescein are conducted in aqueous solution at buffered pH. In our case, since the hybrids are not water-soluble, the optical measures were performed in EtOH with added DMSO (1.8 % v/v). EtOH does not affect fluoresceine luminescence, whereas the small percentage of DMSO, required to dissolve the hybrid POM in solution, is responsible for a minor emission quenching.

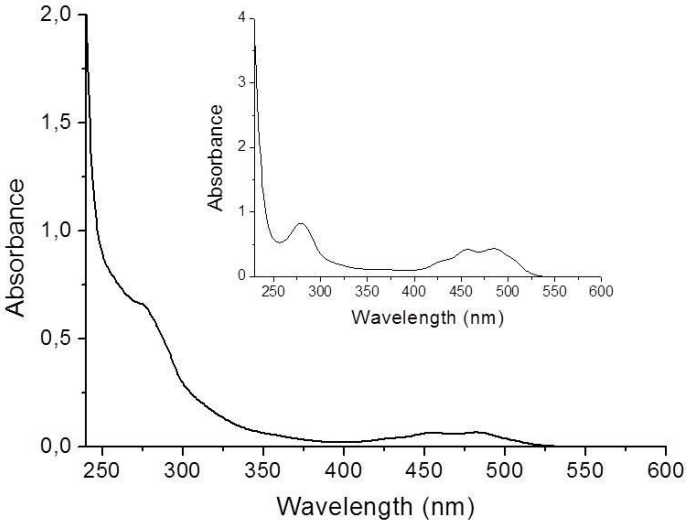

Figure 2.25 UV-Vis spectrum of **FITC-SiW$_{10}$** (**3**) (10 μM) in EtOH with added DMSO (1.8 % v/v); Inset: UV/Vis spectrum of FITC (20 μM) in EtOH with added DMSO (1.8 % v/v) .

The UV-Vis spectrum of (**3**) display a shoulder at 275 nm and three absorption bands at 428, 454 and 482 nm. These can be ascribed to the appended fluoresceine moieties. Upon

introduction of the fluoresceine groups on the polyanion, a hypochromic effect, in comparison with FITC, can be observed for the UV-Vis absorption (Figure 2.25).

The fluorescence spectrum of (**3**) (Figure 2.26 A) maintains the typical pattern of the fluoresceine fluorophore, with a large emission band centered at 528 nm (λ_{exc} = 480 nm), albeit somewhat blue-shifted and with diminished intensity (~ 10-folds) when compared to the reference emission (FITC) (Figure 2.26 B).

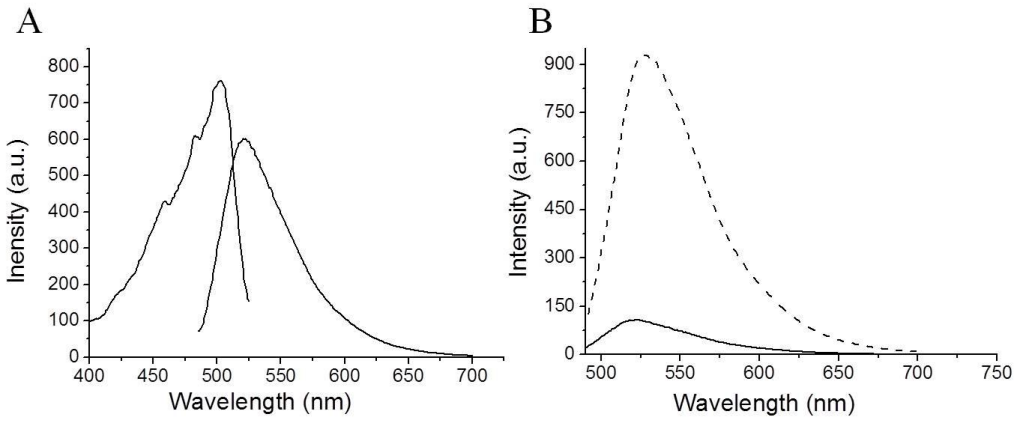

Figure 2.26 A Fluorescence spectra of (**3**) [10 μM, excitation (λ_{em} = 528 nm) and emission (λ_{exc} = 480 nm)] **B** Comparison between emission spectrum of FITC (20 μM, dashed lines) with (**3**) (10 μM, solid lines) (λ_{em} = 528 nm) in DMSO/EtOH (2% v/v).

To evaluate the effect of POM scaffold on fluoresceine luminescence, the same probe was also introduced on β-A-$Na_8[HPW_9O_{34}]$ (see Figure 2.3). The synthetic strategy is described in the next paragraph.

2.2.4.3 Synthesis of $(n\mathbf{Bu_4N})_3\mathbf{Na_2}[\{(C_{20}H_{11}O_5)NHCSNHCH(CH_3)PO\}_2(\alpha\text{-A-}PW_9O_{34})]$ *(FITC-PW_9)*

The fluorescein probe has been also introduced on the trivacant β-A-$Na_8[HPW_9O_{34}]$ (**PW_9**) scaffold with a different synthetic strategy, exploiting phosphonic acid units.

Synthesis of the reactive ligand: $(C_{20}H_{11}O_5)NHCSNHCH(CH_3)PO(OH)_2$ (FITC-AEPA)

In this case, the fluorescein isothiocyanate (FITC) has been first functionalized with a chiral residue: 1-aminoethyl phosphonic acid (AEPA), by means of a reaction carried out in water and DMSO (9:1) at pH 9.

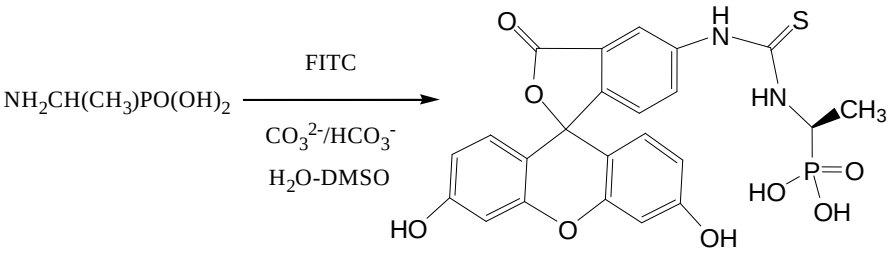

Scheme 2.7 Synthetic route to **FITC-AEPA**.

The synthetic procedure and the characterization are reported in the *Chapter 5* (Appendix, A28-A33).

Grafting of the ligand on the POM scaffold

The trivacant POM **PW_9** was reacted with two equivalents of 1-aminoethyl phosphonic acid derivatized with fluorescein in CH_3CN, in the presence of four equivalents of hydrochloric acid, using a tetrabutylammonium salt (nBu$_4$NBr). The final product (nBu$_4$N)$_3$Na$_2$[($C_{20}H_{11}O_5$)NHCSNHCH(CH_3)PO)$_2$(α-A-PW_9O_{34})] **(FITC-PW_9)** (**4**) was isolated with 50% yield, upon precipitation with water and purification by extensive washing/extraction cycles with ethanol and Et_2O/MeOH (5:1).

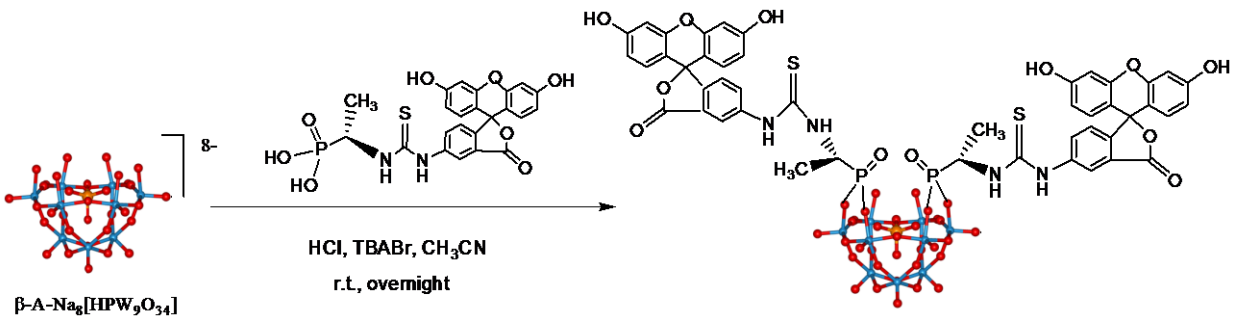

Scheme 2.8 Synthetic routes to a Keggin-type nonaoxotungstate functionalized with fluoresceine chromophore.

The spectroscopic characterization confirms an bis-functionalization, in agreement with the data in literature.[15]

In the FT-IR the low-wavenumber part (ν< 1000 cm^{-1}) is characteristic of the polyoxometalate framework.[47] The stretching vibrational bands [ν_{asym} (W-O_b-W) and ν_{asym} (W=O_{ter})] are shifted to higher frequency, compared to those of the starting trivacant [PW_9O_{34}]$^{9-}$ anion (Figure 2.27 and Table 2.2). This effect, previously observed for organosilyl derivatives of trivacant polyoxotungstates, is attributed to a partial saturation of the polyoxometallic moiety. The stretching vibration bands of the PO_4 and RPO_3 groups are observed between 1000 and

1100 cm^{-1}. Finally, vibrational bands relative to the counterion (2850-3000 cm^{-1}) and minor bands attributable to fluorescein (1100-1650 cm^{-1}) can be observed.

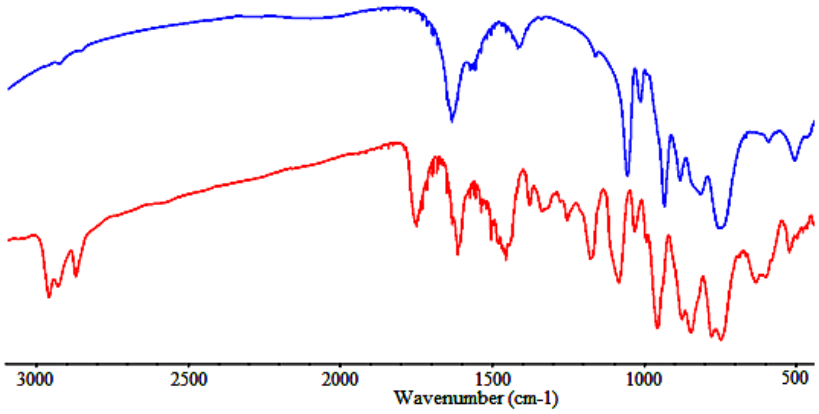

Figure 2.27 FT-IR (KBr) spectrum of (**4**) (red) in comparison with FT-IR (KBr) spectrum of **PW_9** (blue).

Table 2.2 Infrared data (cm^{-1}) for (**4**) and β-A-$Na_8H[PW_9O_{34}]*24H_2O$

Assignment[47]	**$FIPW_9$**	**β-PW_9**
ν(P-C)	1179m	
ν_{asym}(P-O) (PO_4)	1090s; 1036m	1056s; 1014w
ν_{asym}(P-O) (PO)	998m	
$\nu_{asym}(W=O_{ter})$	959vs	931vs
$\nu_{asym}(W-O_b-W)$	879vs; 850vs; 782vs; 752vs	821vs; 737vs

m: medium; s: strong; vs: very strong

The ^{31}P NMR spectrum presents two lines with a relative intensity of 2:1 (Figure 2.28). Integration was carried out on proton coupled spectra: the high-frequency resonance (19.32 ppm) is attributed to the RPO group. The low-frequency singlet of relative intensity 1 (-12.59 ppm) is assigned to the central PO_4 unit of the polyoxotungstate. The value of literature for compounds bis-functionalized is $\delta = -11.46 \pm 0.2$[17].

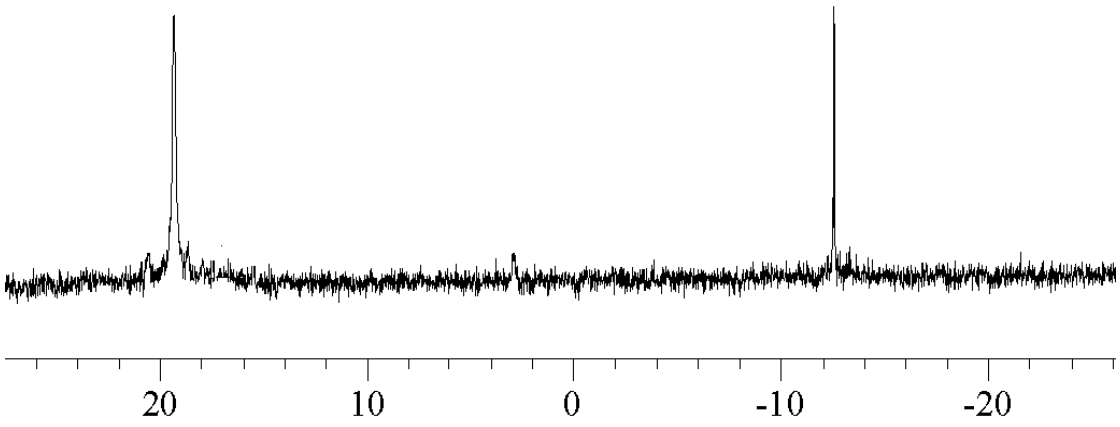

Figure 2.28 ^{31}P NMR ([D_6]DMSO, 28 °C) of (**4**).

Studies of ^{1}H NMR and ^{31}P NMR, performed at different temperatures, have shown the presence of different equilibria in solution: a splitting of the signals that still maintain an integration ratio 2:1 is observed at temperature under 18° C (Appendix, A16) . This is probably due to the fact that the fluorescein has several forms in equilibrium in solution (cationic, neutral, anionic and dianionic) dependent on the pH and temperature.[48] These forms probably affect the electron density of the polyanion in different ways.

2.2.4.4 Study of optical and chiroptical properties

Since, the conjugation with AEPA does not affect the spectral properties of FITC, we used this latter as reference. Optical features were studied by using solutions of EtOH with a little percentage of DMSO.

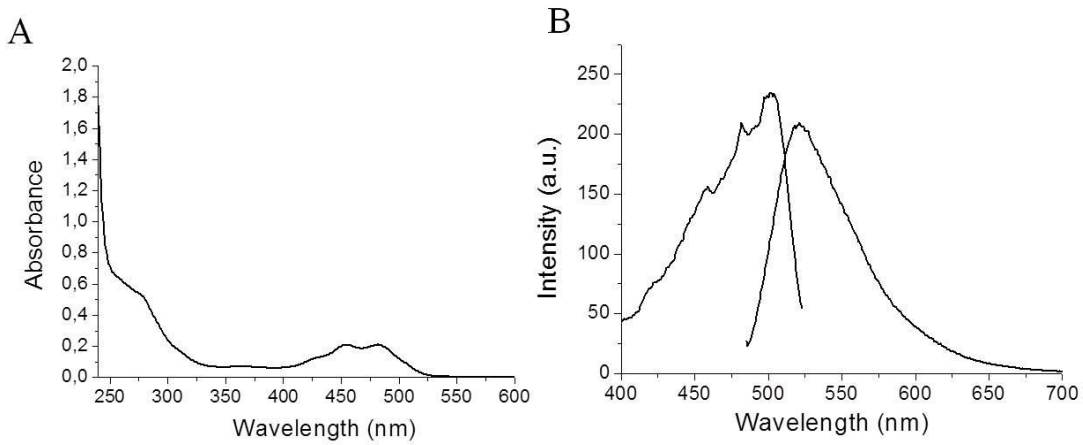

Figure 2.29 A UV-Vis spectrum of (**4**) (10 μM) in EtOH with added DMSO (1.8 % v/v) **B** Fluorescence spectra of (**4**) [10 μM, excitation (λ_{em} = 528 nm) and emission (λ_{exc} = 480 nm)].

Also in this case, we observed a depletion of fluorophore absorption and fluorescence when the FITC is grafted on the polyanion, as reported for the hybrid polyoxotungstate **FITC-SiW$_{10}$** (**3**).

In particular, a comparison of fluorescence spectra (reported in Figure 2.30), shows that the divacant polyanion [γ-$SiW_{10}O_{36}$]$^{8-}$ induces a stronger quenching of the fluoresceine luminescence with respect to the trivacant [A-β-PW_9O_{34}]$^{9-}$, suggesting that the interaction with the divacant POM is stronger. This can be explained by the fact that the divacant POM (**SiW$_{10}$**) does not show equilibria involving the ligand, as in the case for the trivacant one (**PW$_9$**).

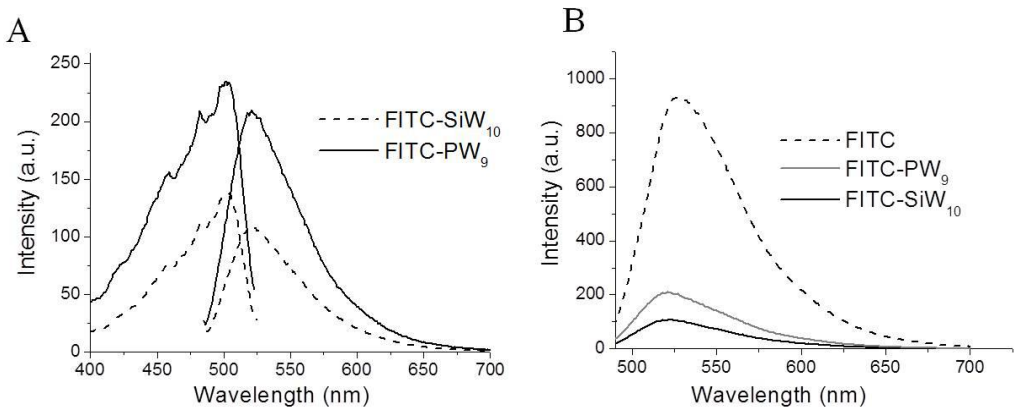

Figure 2.30 A Fluorescence spectra of (**3**) [10 μM, dashed line: excitation (λ_{em} = 528 nm) and emission (λ_{exc} = 480 nm)] and fluorescence spectra of (**4**) [10 μM, solid line: excitation (λ_{em} = 528 nm) and emission (λ_{exc} = 480 nm)]. **B** Comparison between emission spectra of (**3**) (black solid line) and (**4**) (gray solid line) with emission spectra of fluoresceine isothiocyanate (dashed line). (λ_{exc} = 480 nm); solvent: DMSO/EtOH (2% v/v).

Finally, both (*R*,*R*) and (*S*,*S*) enantiomers of (**4**) were prepared upon functionalization of **PW$_9$** with the two enantiomers of the aminoethylphosphonic acid, functionalized with fluoresceine isothiocyanate. As expected, the two enantiomers of hybrid (**4**) show mirror-symmetric CD spectra (θ_{max} = 8.3×10^4 deg cm^2 dmol^{-1} at 274 nm) (Figure 2.31). In addition, the lower optical activity observed for the **FITC-AEPA** (a single positive Cotton effect at 253 nm with θ_{max} = 7.30×10^3deg cm^2 dmol^{-1}) in the spectral region where the characteristic oxygen-to-tungsten charge-transfer bands of the polyanion absorbs (Appendix, A33) suggests that the optical activity is induced through chirality transfer.[49]

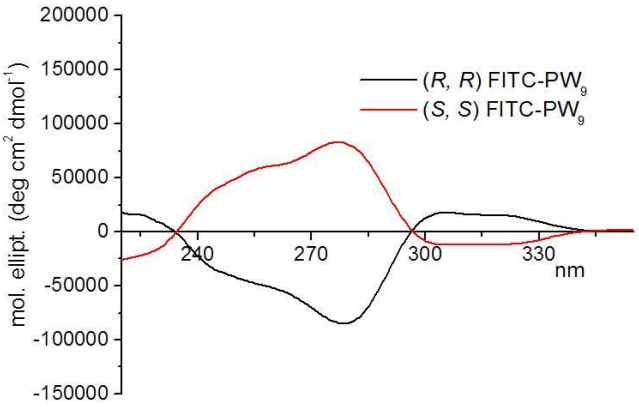

Figure 2.31 Circular dichroic spectra of (*R, R*) and (*S,S*)-(**4**) in CH_3CN (10 μM).

2.3 Conclusions and future perspectives

In conclusion, we have presented a family of novel POMs featuring different luminescent behaviour. In particular, an innovative polyoxometalate-based molecular chemosensor displaying recognition and luminescent signalling functions has been described. The POM-based bis-dansyl tweezer (**1**) acts as selective fluorescence sensor for Cu^{2+} and Pb^{2+} ions, in quenching and enhancing mode, respectively, with tunable intensity depending on the emission wavelength, POM-aided scavenging of potentially interfering cations, detection limit in the micromolar range. In addition, a remarkable benefit, with respect to previously known nano-colloid analogs, is that the tweezer arrangement does not require the integrating of a multi-dentate ligand fragment for the Cu^{2+}/Pb^{2+} capture.

Moreover, the present study reports the synthesis of a pyrene-functionalized POM (**2**), and its interaction with C_{60} and SWCNTs in DMF and DMF/MeOH 1:1 medium respectively. The bidimensional ordering of [60]fullerene and its derivatives with organic counterparts, self-assembled on suitable metal or semiconductor single-crystal surfaces, is a interesting perspective to develop photoactive materials. A promising potential for applications in many different fields such as sensing, catalysis, nanoelectronics, and photochemical conversion of solar energy is foreseen.

Finally, considering the medical applications of POMs (see *Chapter 1* paragraph 1.3) compounds (**1**)-(**4**) can be exploited for the cellular tracking by means of fluorescence microscopy. In the next Chapter, the biological properties and the exploitation of the organic domain for imaging or targeting purposes will be described. In particular, POM (**3**) and (**4**) are specifically designed for cellular trafficking studies, and their behavoir will be presented in the next chapter.

2.4 References and notes

[1] a) *Polyoxometalate Chemistry from Topology via Self-Assembly to Applications* (Eds.: M. T. Pope, A. Müller), Kluwer Academic Publishers, Dordrecht, The Netherlands, **2001**; b) *Polyoxometalate Molecular Science* (Eds.: J. J. Borrás-Almenar, E. Coronado, A. Müller, M. T. Pope), Kluwer Academic Publishers, Dordrecht, The Netherlands, **2003**; c) D. L. Long, E. Burkholder, L. Cronin, *Chem. Soc. Rev.* **2007**, *36*, 105.

[2] a) M. Bonchio, M. Carraro, G. Scorrano, U. Kortz, *Adv. Synth. Catal.* **2005**, *347*, 1909; b) M. Bonchio, M. Carraro, A. Farinazzo, A. Sartorel, G. Scorrano, U. Kortz, *J. Mol. Catal. A* **2007**, *262*, 36; c) A. Sartorel, M. Carraro, R. De Zorzi, S. Geremia, N. D. McDaniel, S. Bernhard, G. Scorrano, M. Bonchio, *J. Am. Chem. Soc.* **2008**, *130*, 5006.

[3] a) D. A. Judd, J. H. Nettles, N. Nevins, J. P. Snyder, D. C. Liotta, J. Tang, J. Ermolieff, R. F. Schinazi, C. L. Hill, *J. Am. Chem. Soc.* **2001**, *123*, 886; b) S. Shigeta, S. Mori, E. Kodama, J. Kodama, K. Takahashi, T. Yamase, *AntiViral Res.* **2003**, *58*, 265; c) X. Wang, J. Liu, M. T. Pope, *Dalton Trans.* **2003**, 957; d) B. Hasenknopf, *Front. Biosci.* **2005**, *10*, 275; e) J. Geng, M. Li, J. Ren, E. Wang, X. Qu, *Angew. Chem. Int. Ed.* **2011**, *50*, 4184; f) G. Geisberger, S. Paulus, M. Carraro, M. Bonchio, G. R. Patzke, *Chem. Eur. J.* **2011**, *17*, 4619.

[4] a) A. Proust, R. Thouvenot, P. Gouzerh, *Chem. Commun.* **2008**, 1837; b) W. Qi, L. Wu, *Polym. Int.* **2009**, *58*, 1217.

[5] a) P. Gouzerh, A. Proust, *Chem. Rev.* **1998**, *98*, 77; b) A. Dolbecq, E. Dumas, C. R. Mayer, P. Mialane, *Chem. Rev.* **2010**, *110*, 6009; c) S. Berardi, M. Carraro, A. Sartorel, G. Modugno, M. Bonchio, *Isr. J. Chem.* **2011**, *51*, 259; d) S. Thorimbert, B. Hasenknopf, E. Lacôte, *Isr. J. Chem.* **2011**, *51*, 275.

[6] a) M. Carraro, L. Sandei, A. Sartorel, G. Scorrano, M. Bonchio, *Org. Lett.* **2006**, *8*, 3671; b) S. Berardi, M. Bonchio, M. Carraro, V. Conte, A. Sartorel, G. Scorrano, *J. Org. Chem.* **2007**, *72*, 8954.

[7] A. Müller, P. Kögerler, *Coord. Chem. Rev.* **1999**, *182*, 3.

[8] H. Zeng, G. R. Newkome, C. L. Hill, *Angew. Chem., Int. Ed.* **2000**, *39*, 1772.

[9] C. R. Mayer, P. Herson, R. Thouvenot, *Inorg. Chem.* **1999**, *38*, 6152.

[10] A. Proust, B. Matt, R. Villanneau, G. Guillemot, P. Gouzerha, G. Izzeta *Chem. Soc. Rev.* **2012**, *41*, 7605.

[11] M. Sameiro, T. Gonçalves *Chem. Rev.* **2009**, *109*, 190.

[12] a) M. Bonchio, M. Carraro, A. Bagno, G. Scorrano, *Adv. Synth. Catal.* **2004**, *346*, 648; b) C. Allain, S. Favette, L.- M. Chamoreau, J. Vaissermann, L. Ruhlmann, B. Hasenknopf, *Eur. J. Inorg. Chem.* **2008**, 3433; c) F. Odobel, M. Séverac, Y. Pellegrin, E. Blart, C. Fosse, C. Cannizzo, C. R. Mayer, K. J. Elliott, A. Harriman, *Chem. Eur. J.* **2009**, *15*, 3130; d) K. J. Elliott, A. Harriman, L. Le Pleux, Y. Pellegrin, E. Blart, C. R. Mayer, F. Odobel, *Phys. Chem. Chem. Phys.* **2009**, *11*, 8767; e) B. Matt, S.

Renaudineau, L.-M. Chamoreau, C. Afonso, G. Izzet, A. Proust, *J. Org. Chem.* **2011**, *76*, 3107; f) B. Matt, C. Coudret, C. Viala, D. Jouvenot, F. Loiseau, G. Izzet, A. Proust, *Inorg. Chem.* **2011**, *50*, 7761.

[13] a) F. Puntoriero, G. La Ganga, A. Sartorel, M. Carraro, G. Scorrano, M. Bonchio, S. Campagna, *Chem. Commun.* **2010**, *46*, 4725–4727; b) M. Orlandi, R. Argazzi, A. Sartorel, M. Carraro, G. Scorrano, M. Bonchio, F. Scandola, *Chem. Commun.* **2010**, *46*, 3152.

[14] a) C. Minelli, S. B. Lowe, M. M. Stevens, *Small* **2010**, *6*, 2336; b) J. Xie, S. Lee, X. Chen, *Adv. Drug Delivery Rev.* **2010**, *62*, 1064.

[15] C. R. Mayer, R. Thouvenot *J. Chem. Soc*., *Dalton Trans*. **1998**, *1*, 7.

[16] a) J. Canny, A. Tézé, R. Thouvenot, G. Hervé, *Inorg. Chem.* **1986**, *25*, 2114; b) A. Tézé, G. Hervé, *Inorg. Synth.* **1990**, *27*, 85; b) A. Tezè, G. Hervè, *J. Inorg. Nucl. Chem*. **1977**, *39*, 999; c) see also M. Carraro, Ph. D. Thesis, Università degli studi di Padova, 2001 and A. Sartorel, Ph. D. Thesis, Università degli Studi di Padova, 2002 in the Experimental Parts.

[17] R. Massart, R. Contant, J.-M. Fruchart, J.-P. Ciabrini. M. Fournier, *Inorg. Chem.* **1977**, *16*, 2916.

[18] a) P. Ceroni, I. Laghi, M. Maestri, V. Balzani, S. Gestermann, M. Gorka, F. Vogtle, *New J. Chem.* **2002**, *26*, 66; b) Y. Zheng, J. Orbulescu, X. Ji, F. M. Andreopoulos, S. M. Pham, R. M. Leblanc, *J. Am. Chem. Soc.* **2003**, *125*, 2680; c) J. R. Lakowicz, in: *Principles of Fluorescence Spectroscopy*, Kluwer Academics/PlenumPublishers, NewYork, 3rd ed., **2006**.

[19] a) M. Montalti, L. Prodi, N. Zaccheroni, G. Falini, *J. Am. Chem. Soc.* **2002**, *124*, 13540; b) F. Vögtle, S. Gestermann, C. Kauffmann, P. Ceroni, V. Vicinelli, L. De Cola, V. Balzani, *J. Am. Chem. Soc.* **1999**, *121*, 12161.

[20] N. Wanichacheva, S. Watpathomsub, V. S. Lee, K. Grudpan, *Molecules* **2010**, *15*, 1798.

[21] a) R. Métivier, I. Leray, B. Lebeau, B. Valeur, *J. Mater. Chem.* **2005**, *15*, 2965; b) T. Gruber, C. Fischer, M. Felsmann, W. Seichter, E. Weber, *Org. Biomol. Chem.* **2009**, *7*, 4904.

[22] M. Xu, S. Wu, F. Zeng, C. Yu, *Langmuir* **2010**, *26*, 4529.

[23] E. D. Roper, V. S. Talanov, M. G. Gorbunova, R. A. Bartsch, G. G. Talanova, *Anal. Chem.* **2007**, *79*, 1983.

[24] a) M. Montalti, L. Prodi, N. Zaccheroni, G. Battistini, S. Marcuz, F. Mancin, E. Rampazzo, U. Tonellato, *Langmuir* **2006**, *22*, 5877.

[25] R. Métivier, I. Leray, B. Valeur, *Chem. Commun.* **2003**, 996.

[26] S. Pandey, A. Azam, S. Pandey, H. M. Chawla, *Org. Biomol. Chem.* **2009**, *7*, 269.

[27] K. Kaur, S. Kumar, *Dalton Trans.* **2011**, *40*, 2451.

[28] P. Passaniti, M. Maestri, P. Ceroni, G. Bergamini, F. Vögtle, H. Fakhrnabavi, O. Lukin, *Photochem. Photobiol. Sci.* **2007**, *6*, 471.

[29] C. R. Mayer, I. Fournier, R. Thouvenot, *Chem. Eur. J.* **2000**, *6*, 105.

[30] A. Bagno , M. Bonchio, J. Autschbach *Chem. Eur. J.* **2006**, *12*, 8460.

[31] E. Rampazzo, E. Brasola, S. Marcuz, F. Mancin, P. Tecilla, U. Tonellato, *J. Mater. Chem.* **2005**, *15*, 2687.

[32] A. Sartorel, M. Carraro, A. Bagno, G. Scorrano, M. Bonchio, *Angew. Chem.* **2007**, *119*, 3319; *Angew. Chem. Int. Ed.* **2007**, *46*, 3255.

[33] a) World Health Organization (WHO), Guidelines for drinking-water quality, Geneva, 2nd ed., **1996**; b) L. Järup, *Br. Med. Bull.* **2003**, *68*, 167; c) D. L. Sparks, B. G. Schreurs, *Proc. Natl. Acad. Sci. USA* **2003**, *100*, 11065.

[34] a) Y. Q. Lan, S. L. Li, Z. M. Su, K. Z. Shao, J. F. Ma, X. L.Wang, E. B. Wang, *Chem. Commun.* **2008**, 58; b) Y. Q. Lan, S. L. Li, X. L. Wang, K. Z. Shao, D. Y. Du, Z. M. Su, E. B. Wang, *Chem. Eur. J.* **2008**, *14*, 9999.

[35] a) N. Avarvari, J. D. Wallis, *J. Mater. Chem.* **2009**, *19*, 4061; b) E. Coronado, J. R. Galan-Mascaros, *J. Mater. Chem.* **2005**, *15*, 66; c) P. Gerbier, N. Domingo, J. Gómez-Segura, D. Ruiz-Molina, D. B. Amabilino, J. Tejada, B. E. Williamson, J. Veciana, *J. Mater. Chem.* **2004**, *14*, 2455.

[36] Y. L. Hwang, K. C. Hwang *Full. Sci. Technol.* **1999**, *7*, 437.

[37] M. Sadakane, E. Steckhan, *Chem. Rev*. **1998**, *98*, 219.

[38] (a) B. Keita, L. Nadjo, *J. Mol. Catal. A: Chem*. **2007**, *262*, 190; (b) B. Keita, U. Kortz, L.R.B. Holzle, S. Brown, L. Nadjo, *Langmuir* **2007**, *23*, 9531.

[39] (a) E. Papaconstantinou, *Chem. Soc. Rev.* **1989**, *18*, 1; (b) A. Troupis, E. Gkika, T. Triantis, A. Hiskia, E. Papaconstantinou, *Photochem. Photobiol., A* **2007**, *188*, 272. (c) C. L- Hill, D. A Bouchard, M. Kadkhodayan, M. M. Williamson, J. A. Schmidt, E. F. Hilinski, *J. Am. Chem. Soc*. **1988**, *110*, 5471; (d) R. F. Renneke, M. Pasquali, C. L. Hill *J. Am. Chem. Soc.* **1990**, *112*, 6585: (e) D. C. Duncan, T. L. Netzel, C. L. Hill, *Inorg. Chem.* **1995**, *34*, 4640; (f) T. Ruther, V. M. Hultgren, B. P. Timko, A. M. Bond, W. R. Jackson, A. G. Wedd, *J. Am. Chem. Soc.* **2003**, *125*, 10133; (g) T. Yamase, X. O. Cao, S. J. Yazaki *Mol. Catal. A: Chem*. **2007**, *262*, 119.

[40] D. Li, J. Song, P. Yin, S. Simotwo, A. J. Bassler, Y. Y. Aung, J. E. Roberts, K. I. Hardcastle, C. L. Hill, T. Liu *J. Am. Chem. Soc.* **2011**, *133*, 14010.

[41] Z. Jiang, Y. Zhang, Y. Yu, Z. Wang, X. Zhang *Langmuir* **2010**, *26*, 13773.

[42] J. B. Issa, A. S. Salameh, E. W. Castner, Jr. J. F. Wishart, S. S. Isied, *J. Phys. Chem. B* **2007**, *111*, 6878.

[43] (a) R. Vaiyapuri, B. W. Greenland, J. M. Elliott, W. Hayes, R. A. Bennett, C. J. Cardin, H. M. Colquhoun, H. Etman, C. A. Murray *Anal. Chem*. **2011**, *83*, 6208; (b) Y. H. Lee, H. Liu, J. Y. Lee, S. H. Kim, S. K. Kim, J. L. Sessler, Y. Kim, J. S. Kim *Chem. Eur. J*. **2010**, *16*, 5895.

[44] (a) S. Rochat, S. N. Steinmann, C. Corminboeuf, K. Severin *Chem. Commun.*, **2011**, *47*, 1058; (b) N. Luisier, A. Ruggi, S. N. Steinmann, L. Favre, N. Gaeng, C. Corminboeuf, K. Severin *Org. Biomol. Chem.***2012**, *10*, 7487.

[45] Y. L. Hwang, K. C. Hwang *Fullerene Science and Technology* **1999**, *7*, 437.

[46] S. Mukherjeea, A. K. Bauria, S. Bhattacharyaa, *Spectrochimica Acta Part A* **2010**, *77*, 64.

[47] C. Rocchiccioli-Deltcheff, R. Thouvenot, R. Franck *Spectrochim. Acta*, *Part A*, **1975**, *32*, 587.

[48] (a) D. M. Togashi, B. Szczupak, A. G. Ryder, A. Calvet, M. O'Loughlin, *J. Phys. Chem. A* **2009**, 113, 2757; (b) S. Das, A. P. Chattopadhyay, S. De *J. Photochem. and Photobiol. A: Chem.*, *197*, **2008**, 402.

[49] M. Carraro, G. Modugno, A. Sartorel, G. Scorrano, M. Bonchio *Eur. J. Inorg. Chem.* **2009**, 5164.

Chapter 3

Interaction of polyoxometalates with biological targets

Due to the potential applications of polyoxometalates (POMs) in medicine (many POMs exhibit antiviral, antitumoral and antibiotic activity), their association with organic domains and ligands is of interest to improve targeting and delivery strategies. In particular, the fluorescence of POMs functionalized with luminescent probes is maintained under physiological conditions and, due to the overall low toxicity of POMs, they can be exploited for *in vitro* cellular imaging, whereby the luminescent moieties is useful to track POMs towards different regions of the cells. Furthermore, since the preparation of hybrid derivatives could be a powerful strategy for the introduction of molecular recognition sites and the enhancement of biocompatibility, studies on the interaction between POM and hybrid POMs with important biological macromolecules (ferritin and avidin) has been explored.

3.1 Introduction

Among small inorganic systems, polyoxometalates (POMs) are multi metallic and polyanionic oxides which have shown interesting potential applications in nanomedicine (see *Chapter 1* paragraph 1.3). Several papers deal with their bioactivity as antibacterial,[1] antiviral,[2] antitumoral[3] agents, suggesting their possible use as drugs. Such activity mainly stems from their redox behaviour and their capability to interact with biological macromolecules through electrostatic bonds. Some paper, indeed, focuses on their interactions with cation pockets of proteins and enzymes.[4] In this respect, systematic studies, performed particularly by the groups of Yamase, Hill and Pope, indicated that the biological activities of polyoxometalates, in many cases, are closely associated with enzyme inhibition. However, fundamental questions concerning the mechanisms responsible for many of the observed biological effects remain essentially unanswered. In particular, although most of the *in vivo* effects of POMs may be explained by interactions with extracellular target proteins, different POMs, despite their size and charge density, can cross cell membranes and interact with intracellular targets. The interaction capability of POMs with intracellular and biological targets will be presented in the next paragraphs.

3.1.1 Interactions of POMs with intracellular targets

Few details are known about POMs cellular localization. In this regard, POMs can be used as electron-dense imaging agents when exposed to high energy radiations. Different electronic microscopies may give information on the molecular shape, orientation and assembly of the cluster compounds.[5] Thus, the distribution of POMs in cells can be determined with high spatial resolution.

For example, an increased number of vacuoles was observed by fluorescence into macrophages cell line J774 incubated with different POMs: $[P_2W_{12}O_{48}]^{14-}$, $[P_2W_{18}Zn_4(H_2O)_2O_{68}]^{10-}$, $[Si_2W_{18}Nb_6O_{77}]^{8-}$. In particular, exploiting transmission electron microscopy (TEM) and scanning electron X-ray -wavelength dispersive spectroscopy (SEM-WDS), it was possible to detected the tungsten.[6] The results confirmed that the POMs were taken up by the macrophages and concentrated in the cytoplasma. Furthermore, X-ray fluorescence microscopy and raman laser microscopy were used to detect a POM into a cytoplasmic precipitate obtained after incubation of C3HBi fibroblasts with the tugstoantimonate $[NaSb_9W_{21}O_{86}]^{18-}$.[7] By using electron probe microanalysis, this tungstoantimonate was localized in the lysosomes of different macrophages after intravenous administration in rats. Moreover, a scanning proton microprobe was used to analyse the metal

content of individual peripheral blood mononuclear cells treated with the cobalt substituted polyoxotungstate $[Co_4(H_2O)_2(PW_9O_{34})_2]^{10-}$,[8] showing its subcellular distribution: this trivacant Keggin-derived sandwich structure was found on the surface of the cell nucleus in peripheral blood lymphocytes.

The studies reported above have allowed to establish that POMs are able to penetrate into scavenger cells such as macrophages. However, they were carried out by means of invasive techniques, that cause the destruction of cells. To avoid damage at cellular level, luminescent lanthanide-substituted POMs were also used as model probes, but their emission is readily quenched by water oscillators, thus hampering imaging studies under physiological conditions, unless they are completely encapsulated and protected from the aqueous environment.[9]

A promising alternative to study POMs cellular tracking, could stem from decoration of the POM scaffolds with resident luminophores (see *Chapter 2*), whereby covalent bonds guarantee long-term performance under physiological conditions. In particular, in this chapter we will see the utilization of the luminescent hybrid POMs described in the *Chapter 2*, to investigate the interactions of POMs with cells by means of fluorescence microscopy.

3.1.2 Interactions of POMs with extracellular targets

The pharmacological POMs effects observed in *vivo* could be mainly due to the interaction between POMs with extracellular target proteins as well as proteins integrated into the cell membrane. In particular, enzyme inhibition has been demonstrated for several different enzyme families (e.g., *ecto*-nucleotidases, *ecto*-kinases, sulfo- and sialyltransferases) and for a variety of POMs with inhibitory potencies from micro- to nanomolar concentrations.

As for instance, inactivation of reverse transcriptases and DNA polymerases by POMs may contribute to the protection against viral infection.[10] The synergistic effect of POMs with β-lactam antibiotics against the pathogenic Gram-positive bacteria *Staphylococcus aureus* appears to be due to the reduced expression of the penicillin binding protein and β-lactamase, but additional, yet unknown, mechanisms of actions are likely involved.[3,11] The activity of the decavanadate against leishmania (a genus of Trypanosomatid protozoa, parasite responsible for the disease leishmaniasis) may be due to the inhibition of phosphoglycerate mutase and various phosphatases.[12] It has been speculated that the antidiabetic activities of oxometalates might be a result of the inhibition of regulatory protein phosphates or glucose-6-phosphatase.[13] Recently, *ecto*-nucleotidase and protein kinase inhibition by POMs have been

identified as possible modes of actions contributing to their antibiotic and/or anticancer activities.[4e),14]

However, systematic structure–activity relationship studies of POMs using various enzymes are still difficult because of the very limited number of compounds, often with large structural variations and different stabilities.

In this scenario, the research on POM–protein interactions (structural and energetic aspects) is an active field of interest due to the perspective of understanding POM action mechanisms and the possibility of designing novel drugs (see also *Chapter 1*, paragraph 1.3.2). In particular molecular recognition and binding of POMs by the target proteins constitute the first step in the complex mechanism of their biological action. In this respect, the interaction capability of different classes of POMs with various proteins was investigated in the literature.

For example, the direct interaction between human serum albumin (HSA)[4a),15] or basic fibroblast growth factor (bFGF)[16] and POMs was demonstrated by the combination of several techniques: fluorescence, ultraviolet absorption, circular dichroism and isothermal titration measurements. In the case of HSA a complex forms upon selective binding of POM in a site containing positively charged residues. In figure 3.1, HSA intrinsic fluorescence quenching by a selected polyoxometalate $[EuW_{10}O_{36}]^{9-}$ is reported.[17]

The fluorescence of HSA, which is due to the single tryptophan residue in the protein, Trp214, can efficiently be quenched by POM. A Stern–Volmer analysis was applied to the fluorescence quenching data and the Stern–Volmer plot shows a linear relationship (Figure 3.1 B). The quenching stopped when the molar ratio between EuW_{10} and HSA reached 1, indicating the stoichiometry of the interaction between EuW_{10} and HSA.[15,17]

Furthermore, as shown in Figure 3.1 C, binding of EuW_{10} has no significant effect on the secondary structure content of the protein, which is characterized by a high helical proportion.[15,17]

In this chapter, preliminary interaction studies of POMs and hybrid POMs with different proteins (ferritine and avidin) will be described.

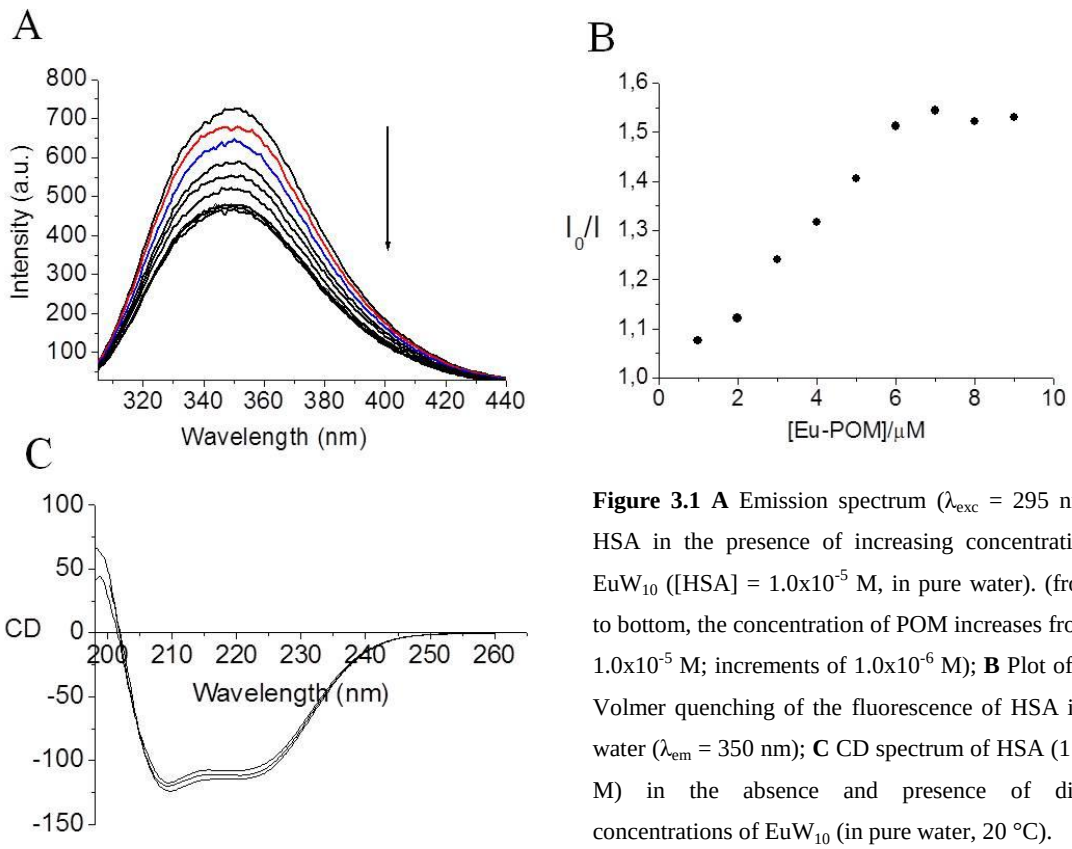

Figure 3.1 A Emission spectrum (λ_{exc} = 295 nm) of HSA in the presence of increasing concentrations of EuW_{10} ([HSA] = $1.0x10^{-5}$ M, in pure water). (from top to bottom, the concentration of POM increases from 0 to $1.0x10^{-5}$ M; increments of $1.0x10^{-6}$ M); **B** Plot of Stern-Volmer quenching of the fluorescence of HSA in pure water (λ_{em} = 350 nm); **C** CD spectrum of HSA ($1.0x10^{-6}$ M) in the absence and presence of different concentrations of EuW_{10} (in pure water, 20 °C).

3.1.3 Bioactive POMs: strategies for imaging, delivery and targeting

Despite the great potential of hybrid organic-inorganic POMs derivatives,[18] for improving recognition capabilities and selectivity, no report deal with the exploitation of the organic domain for imaging or targeting purposes.

New POM based systems have thus been designed to overcome the main obstacles to POMs medical exploitation. In particular we will present:

(i) The use of POM luminescent derivatives for **cellular imaging**. The introduction of organic probes on the polyanionic scaffolds can help to study the POMs cellular uptake and to reveal their specific interactions with intracellular portions, by means of fluorescence microscopy. The utilization of organic probes on the polyanionic scaffolds can allow to investigate POM cellular tracking, without inducing any cellular change or damage.

(ii) The study of interaction between an hollow protein (apoferritin) with totally inorganic POMs. Interaction studies between POMs and macromolecules can be useful to clarify POM biological effects (paragraph 3.1.2) as well as to design novel **drug delivery**

systems, capable to limit the toxicity of POMs. In this respect, different literature studies investigated the possibility of using nanocarriers for POM delivery, showing that the encapsulation of POMs by dendritic ligands, surfactants and biopolymers leads to an increase in both the stability and cellular uptake of POMs (see *Chapter 1* paragraph 1.3.3).[19]

(iii) The design of a hybrid POM containing a bioactive molecule (biotin) capable of biomolecular recognition for **targeting** purposes. The goal of a selective POM-based bioconjugate is to increase its concentration in the vicinity of the cells responsible for disease thus decreasing unwanted side effects on healthy cells.

3.2 Results and discussion

3.2.1 Interaction studies of luminescent POMs with cells

In this chapter, we describe the biological activity and the use of the organic chromophore-appended POMs described in *Chapter 2* to unravel their cellular localization by means of fluorescence microscopy. The following POMs were prepared (see *Chapter 2*, paragraph 2.2):

three derivatives of the divacant decatungstosilicate $[\gamma\text{-}SiW_{10}O_{36}]^{8-}$:

(i) a dansyl-tagged POM $(n Bu_4N)_4[\{((CH_3)_2N)C_{10}H_6SO_2NH(CH_2)_3Si\}_2O(\gamma\text{-}SiW_{10}O_{36})]$ ***(Dans-SiW$_{10}$)*** (**1**),

(ii) a pyrene-tagged POM $(n Bu_4N)_4[\{(C_{16}H_9)SO_2NH(CH_2)_3Si\}_2O(\gamma\text{-}SiW_{10}O_{36})]$ ***(Pyr-SiW$_{10}$)*** (**2**),

(iii) a fluorescein-tagged $(n Bu_4N)_4[\{(C_{20}H_{11}O_5)NHCSNH(CH_2)_3Si\}_2O(\gamma\text{-}SiW_{10}O_{36})]$ ***(FITC-SiW$_{10}$)*** (**3**).

In addition, a fluoresceine-tagged chiral derivative of the trivacant nonatungstophosphate β-A-$Na_8[HPW_9O_{34}]$ was also prepared, to explore the effect of a different inorganic scaffold:

(iv) a fluorescein-tagged (*R,R*) and (*S,S*)-$(n Bu_4N)_4[\{(C_{20}H_{11}O_5)NHCSNHCH(CH_3)PO\}_2(\alpha\text{-}A\text{-}PW_9O_{34})]$ ***(FITC-PW$_9$)*** (**4**).

They were characterized by several techniques (see *Chapter 2*) and delivered into HEK293 cells, showing their different localization, which depends on both the chromophore and on the inorganic scaffold.

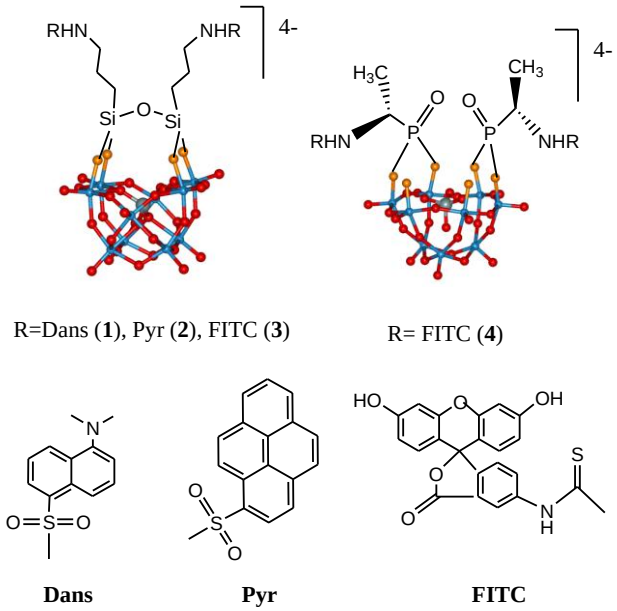

Scheme 3.1. Chemical structures of luminescent polyoxotungstate derivatives: (**1**): **Dans-SiW$_{10}$**; (**2**): **Pyr-SiW$_{10}$**; (**3**): **FITC-SiW$_{10}$** ; (**4**): **FITC-PW$_9$**.

The emission of the luminescent POMs cover different spectral regions, as shown in Figure 3.2.

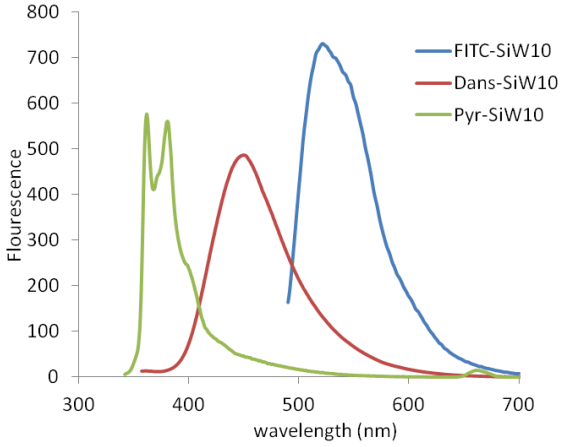

Figure 3.2 Fluorescence spectra of **Dans-SiW$_{10}$** (10 µM), **Pyr-SiW$_{10}$** (10 µM) in CH_3CN and of **FITC-SiW$_{10}$** (5 µM) in EtOH with added DMSO (2% v/v)**.**

3.2.1.1 Structural investigation of luminescent hybrid POMs in aqueous and physiological conditions

The hybrid **POMs** (**1-4**) are very soluble in polar organic solvents (acetonitrile, dimethylformamide (DMF), dimethylsulfoxide (DMSO). To test their behaviour in water, spectroscopic and structural features of **POMs** have been monitored in aqueous and physiological conditions. A first attempt to obtain a water soluble hybrid POM, involving the exchange of tetrabutylammonium (nBu$_4$N$^+$) with sodium countercations, has also been performed (see *Chapter 5*: paragraph 5.2.2).

The resulting hybrid POM Na$_x$(nBu$_4$N)$_{4-x}$[{(N(CH$_3$)$_2$)C$_{10}$H$_6$SO$_2$NH(CH$_2$)$_3$Si}$_2$O(γ-SiW$_{10}$O$_{36}$)] ***(Na$^+$_Dans-SiW$_{10}$)*** has been isolated and characterized by FT-IR, UV-VIS and fluorescence analysis.

The FT-IR spectrum is consistent with the exchange of the countercation; whereby particularly diagnostic regions are:

(i) 3000-2875 cm^{-1}: the C-H stretching of nBu$_4$N$^+$ are significantly reduced;

(ii) 1700 cm^{-1}: appearance of a strong band relative to coordinated H$_2$O (H-O-H bending);

(iii) 1000-600 cm^{-1}: the variation of the characteristic stretching of the inorganic framework (vibrations of the bonds W-O and Si-O) suggests a variation of the electron density of the structure due to the introduction of sodium as countercation.

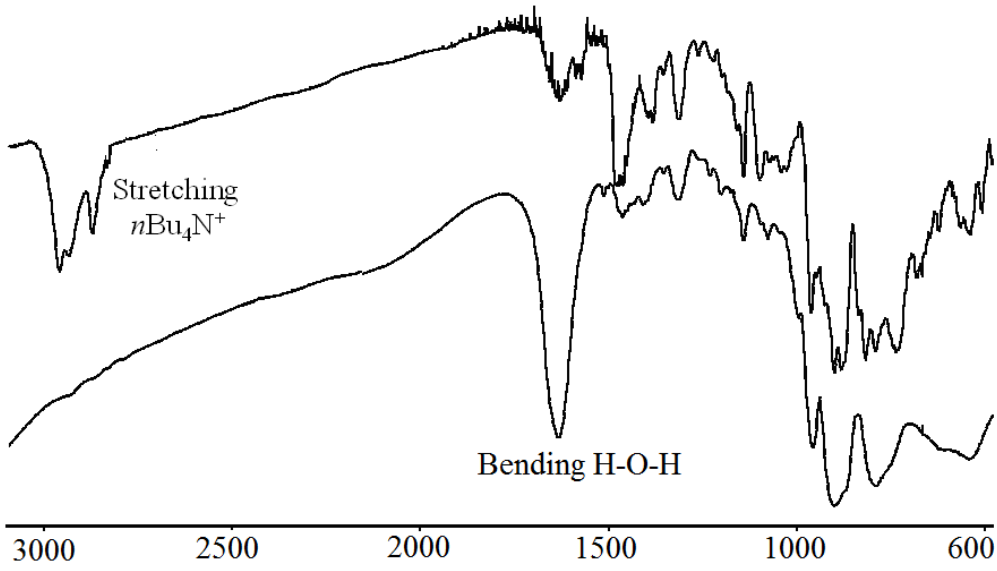

Figure 3.3 FT-IR spectrum of Na$_x$(nBu$_4$N)$_4$-x[{(N(CH$_3$)$_2$)C$_{10}$H$_6$SO$_2$N(CH$_2$)$_3$Si}$_2$O(γ-SiW$_{10}$O$_{36}$)] (below) compared with the FT-IR spectrum of (nBu$_4$N)$_4$[{(N(CH$_3$)$_2$) C$_{10}$H$_6$SO$_2$NH(CH$_2$)$_3$Si}$_2$O (γ-SiW$_{10}$O$_{36}$)] (above).

The UV-Vis spectral features of the water soluble hybrid **Na^+_Dans-SiW_{10}** are kept in H_2O: the shoulder at 250 nm can be attributed to the dansyl fluorophore (Figure 3.4 A). The fluorescence spectrum presents an emission band centered at 495 nm (λ_{exc} = 330 nm) and an excitation band centered at 332 nm (λ_{em} = 510 nm). The emission band of the water soluble POM exhibits a red-shift ($\Delta\lambda$ = 46 nm) and a reduced intensity (about 20 times less) in comparison with the corresponding emission band observed for the acetonitrile soluble-hybrid derivative **Dans-SiW_{10}** (Figure 3.4 B).

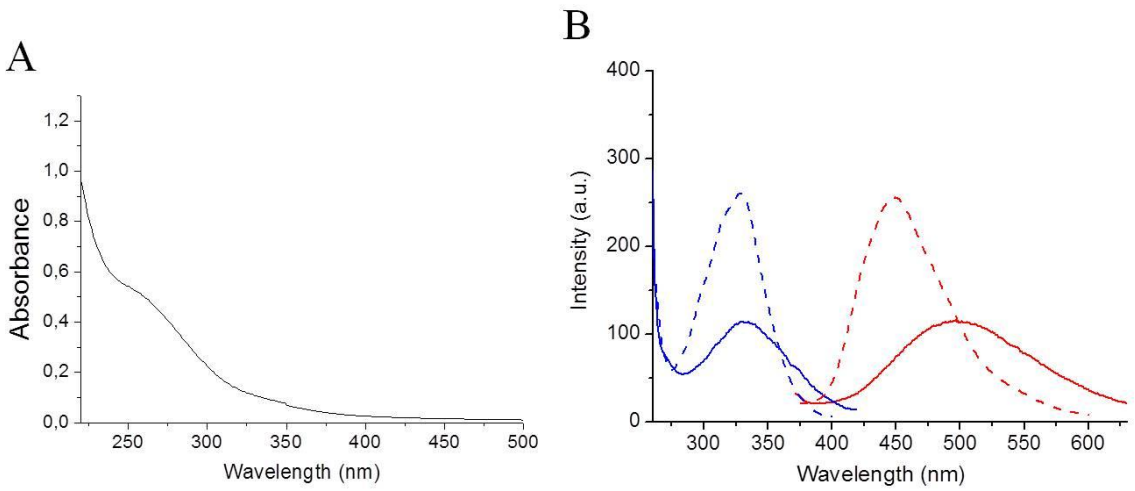

Figure 3.4 A UV-Vis spectrum of **Na^+_Dans-SiW_{10}** ($2.4x10^{-5}$ M), **B** Emission (λ_{exc} = 330 nm) and excitation (λ_{em} = 510 nm) spectra of **Na^+_Dans-SiW_{10}** (solid line, $2.4x10^{-5}$ M) in H_2O in comparison with emission (λ_{exc} = 336 nm) and excitation (λ_{em} = 551 nm) spectra of **Dans-SiW_{10}** (dashed line, $2.4x10^{-5}$ M) in CH_3CN.

Despite partial water-induced fluorescence quenching, POM (**1**) still maintains its luminescence features into aqueous conditions even after countercation exchange.

However, the solubility of hybrid **POMs** (**1-4**) in H_2O is strongly affected by the apolar organic compound grafted on the surface of the polyanion. In particular the POM **Na^+_Pyr-SiW_{10}** (**2**) only gives an emulsion in water.

Due to the generally low metathesis yield, we found more convenient to dissolve hybrid **POMs** (**1-4**) in water (or in physiological conditions) at low concentration, upon dilution of a concentrated DMSO solution.

Dynamic Light Scattering (DLS) measurements show the formation of nanoparticles characterized by a large polydispersion, with minor peaks around 150-250 nm and higher peaks between 500 nm-1.05 µm for **Dans-SiW_{10}**, 400-900 nm for **Pyr-SiW_{10}**, 300-800 nm for **FITC-SiW_{10}**. **FITC-PW_9** forms smaller aggregates, with 25-105 nm diameter. (Appendix, A37). ζ–potential investigations highlighted the polyanionic nature of the assemblies: **SiW_{10}**

derivatives are more negatively charged, with potentials between -25 and -30 mV, whereas **FITC-PW$_9$** displays a less negative potential (-17 mV) (Appendix, A36).

Transmission electronic microscopy (TEM) confirms the formation of spherical aggregates with a broad size distribution. Coalescence of the nanoparticles towards the formation of worm-like aggregates has been frequently observed. The formation of such aggregates is expected to be driven by the hindered organic chromophores, bearing aromatic residues, whereas the tetrabutylammonium cations may assist the assembly, avoiding repulsion between adjacent inorganic polyanions.[20]

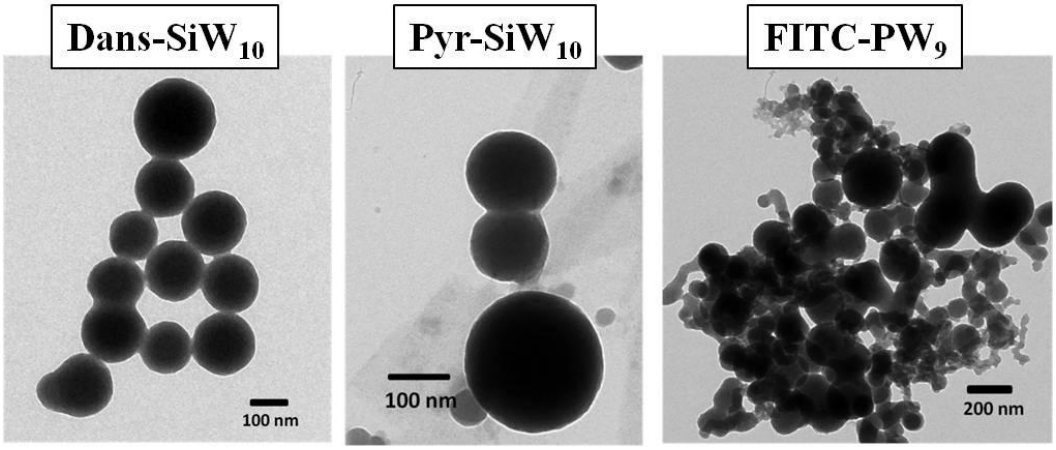

Figure 3.5 Transmission electronic microscopy (TEM) images of POMs in H_2O/0.05 % DMSO.

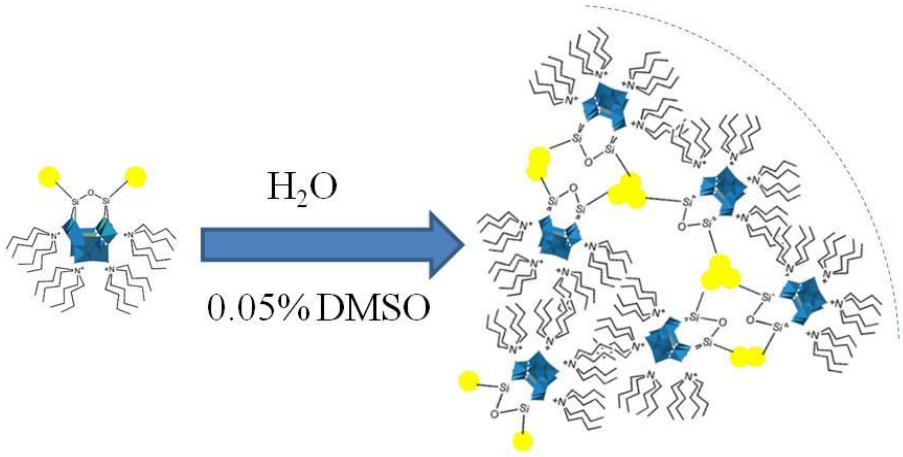

Scheme 3.2 Assembly of the hybrid POMs in H_2O/0.05 % DMSO; (circular sector representing a portion of a spherical vesicle with exposed anionic scaffolds).

To evaluate the use of the POMs (**1-4**) under physiological conditions, we have performed further investigations in a extra cellular-mimicking solution. DLS and ζ-potential measurements were not reproducible, thus suggesting that the aggregates are less stable.

Indeed, different inorganic cations may efficiently neutralize the surface charges. However, the formation of nanoparticles has been confirmed by SEM and TEM measures, which show the formation of vesicles with diameter of 80-100 nm (**Dans-SiW$_{10}$**; Figure 3.6), 150 nm (**Pyr-SiW$_{10}$**; appendix A38) or 200-220 nm (**FTIC-PW$_9$**; appendix A39).

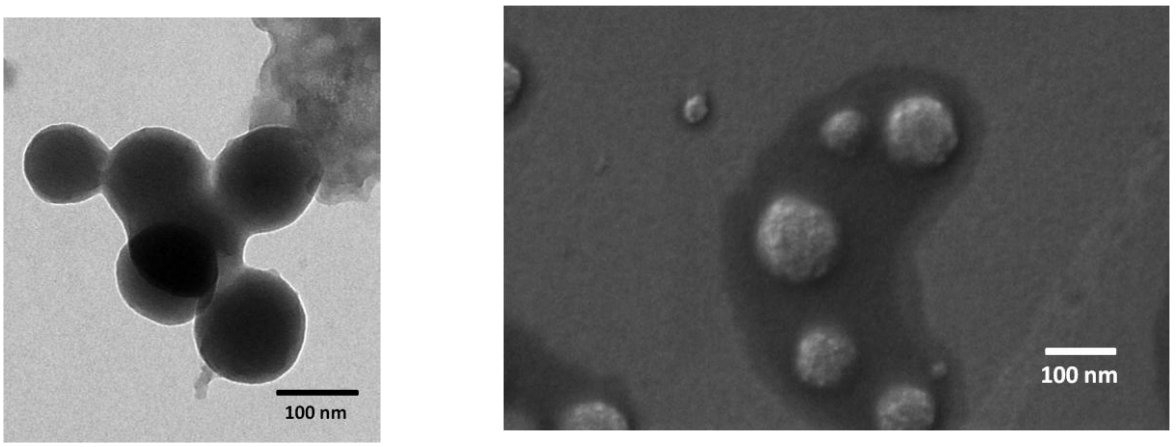

Figure 3.6 Left: transmission electronic microscopy (TEM) images of POM **Dans-SiW$_{10}$** (**1**) in physiological-like solution containing 0.05% v/v of DMSO. Right: scanning electronic microscopy (SEM) images of POM **Dans-SiW$_{10}$** (**1**) in physiological-like solution containing 0.05% v/v of DMSO.

Partially coalesced aggregates can be observed also in these conditions. In particular, TEM analysis show nanoparticles consisting in an denser inner part, surrounded by a shell featuring lower contrast, likely rich in solvent.[21] This kind of assembly is expected to reduce repulsion with the negatively charged cellular membrane, while increasing the affinity toward lipid bilayers.

3.2.1.2 Biological activity of luminescent hybrids POMs

Cytotoxic tests were carried out with MTT[22] assays based on the quantification of cell mitochondrial metabolism of (3-(4,5-dimethylthiazol-2-yl)-2,5-diphenyltetrazolium bromide. Viability MTT test were performed after an exposure of 24 h with different POM concentrations (up to 500 µM), upon comparison of the metabolic activity of the treated cell with the control ones (Figure 3.7).

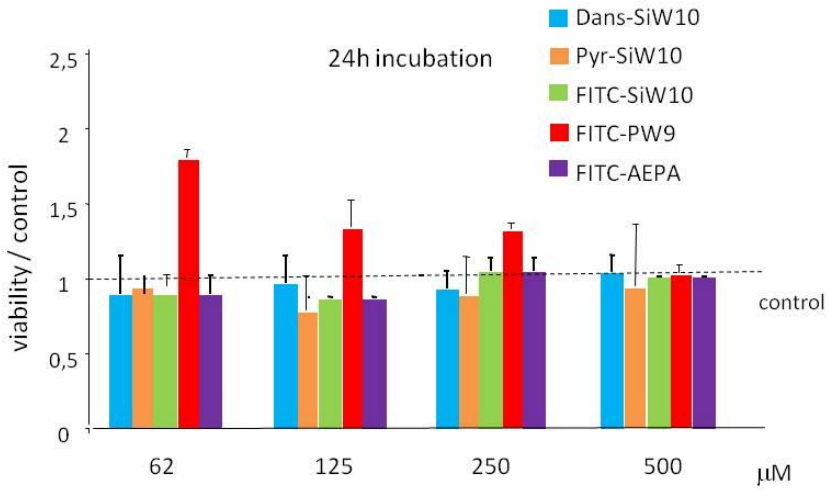

Figure 3.7 Cells viability studies of HEK cells incubated with different concentrations of **POMs** (**1-4**) and **FITC-AEPA** at 37°C for 24 h.

After 24 h, very low toxicity was observed for all compounds. In addition, a even larger MTT metabolic activity was found in cells exposed to 62-250 µm of **FITC-PW$_9$**.

IC_{50} (median inhibitory (toxicity) concentration in µM) assessed at ca. 0.5 mM. This value has been extrapolated from the MTT test at 48 h, in correspondence of 500 µM (Appendix, A42).

This value is 1-2 orders of magnitude higher in comparison with other polyoxotungstates.[23]

To test if 24 h exposure with **POMs** (**1-4**) altered cell basic functions, cell proliferation was tested using a dedicated assay (Cell proliferation WST-1 assay, Roche)[24] at different concentrations (18 µM and 250 µM).

After removing the medium containing the POMs, the proliferation curve was monitored up to 6 hours (Figure 3.8). The data show that at higher concentration all POMs except **Pyr-SiW$_{10}$** have a significant delay in the proliferation rate with respect to control (Figure 3.8 B). This effect is less important at lower concentrations (18 µM), although **SiW$_{10}$**-based samples show a higher toxicity (Figure 3.8 A). Proliferation rate of samples exposed with **FITC-AEPA** was comparable with that of the control.

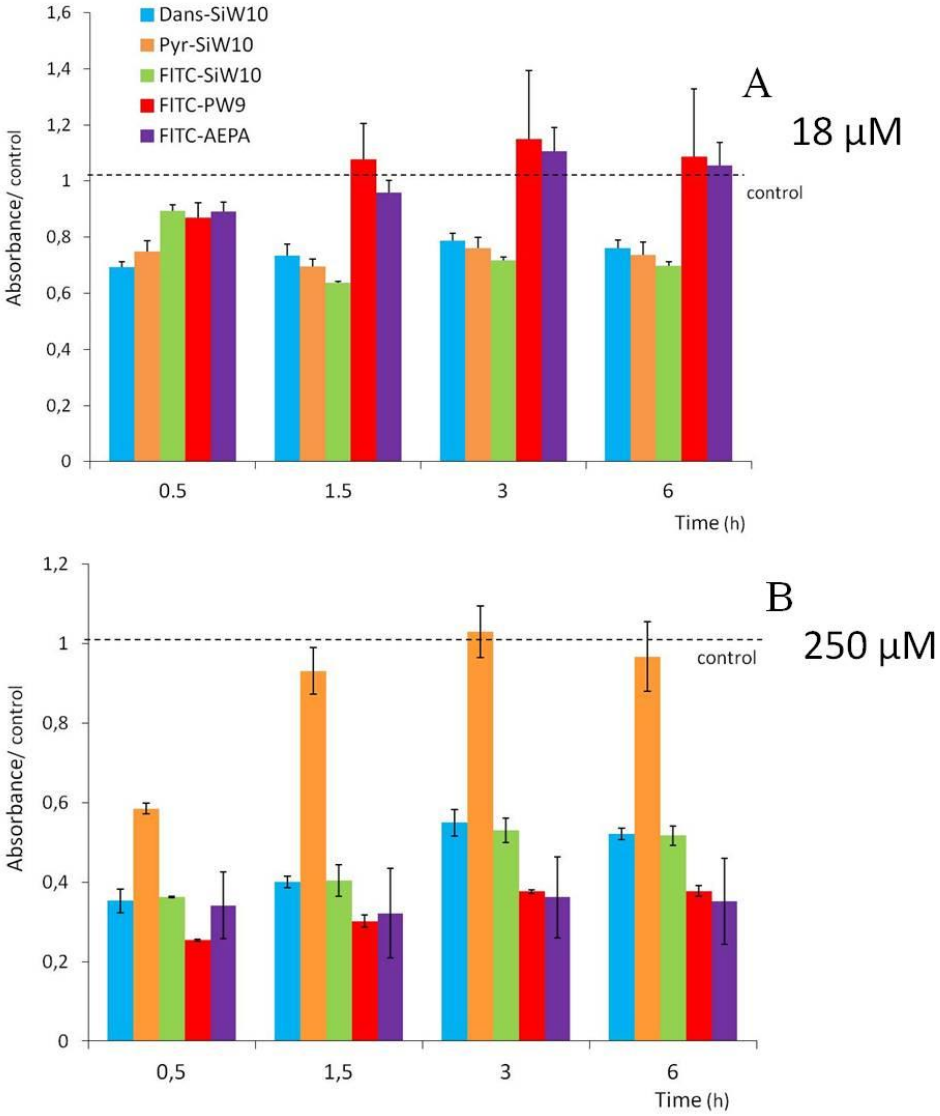

Figure 3.8 Proliferation assay in HEK cells treated for 24 h with **POMs** (**1-4**) at 18 µM (**A**) and 250 µM (**B**). The analyses were performed at time 0.5, 1.5, 3 and 6 h after removal of the POM containing medium. Proliferation of non-treated cells (control) is also shown.

Considering the minor alteration of cell viability at low POM concentrations, we performed cell uptake and distribution studies on HEK293 culture cells at 18 µM.

3.2.1.3 Cell tracking of luminescent hybrids POMs

Thank to their intrinsic emission properties, luminescent hybrid **POMs** (**1-4**) can be observed by fluorescence microscopy. In particular **Dans-SiW$_{10}$** and **Pyr-SiW$_{10}$** were observed with a selective 305 nm filter (EX G 365, BS FT 395, EM BP 445/50), while fluorescein-based compounds were observed with a selective 488 nm filter (EX BP 470/40, BS FT 495, EM BP

525/50). Despite a very fast quenching of the luminescence (Δt = 20-30 sec), the **POMs** can be easily observed in specific subcellular regions, showing a strong dependence with the organic domain itself. Their uptake was more efficient after a prolonged time (>12 h).
Transmitted light microscopy allowed to monitor cell morphology after the uptake, and showed that POMs do not induces major morphology changes or damages (Figure 3.9).

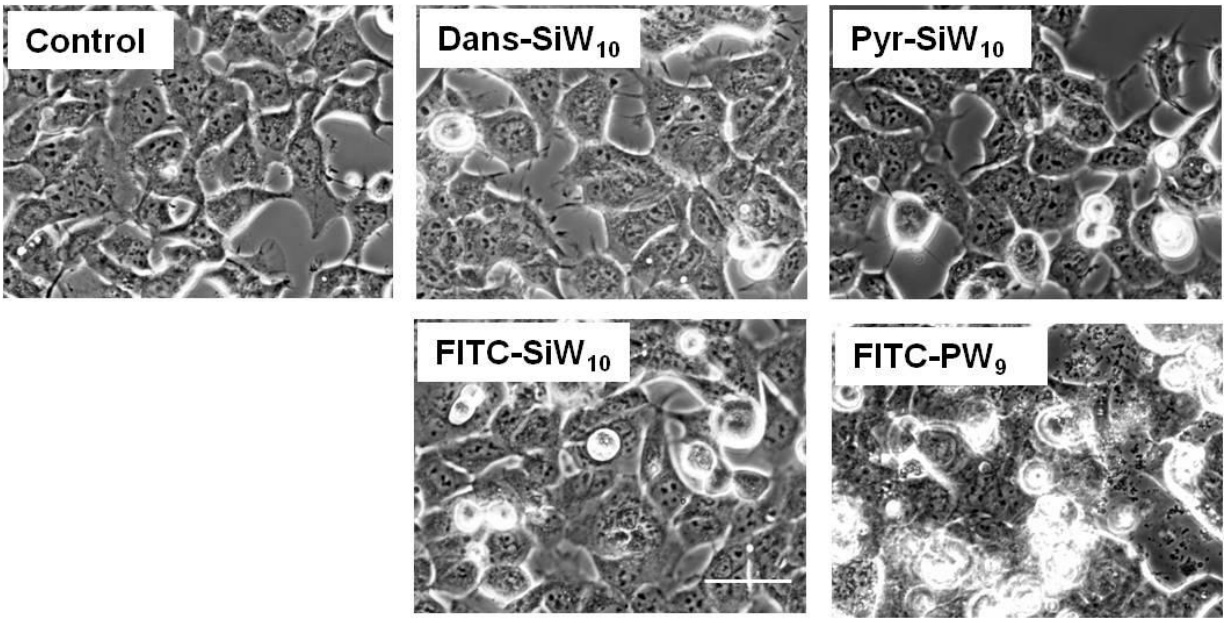

Figure 3.9 Effect on cell survival and proliferation. Representative microscopy images of cells in control conditions and after exposure with different POMs (18 µM, 15 h, 37°C), visualized with transmitted light. Note limited effects of exposed compounds on cell morphology, limited overall toxicity. Bar = 50 µm.

Compounds **Dans-SiW$_{10}$** (**1**) and **Pyr-SiW$_{10}$** (**2**) were mainly detected as spots in the cytoplasmatic and in the perinuclear regions. To identify the cellular localization of POMs (**1**) and (**2**), colocalization experiments using mitochondria and nuclei-selective staining reagents were also performed.
The cells have been also incubated with carbocyanine-based MitoTracker Red FM Probe: both POMs show a signal in spots, and a partial co-localisation with mitocondria.

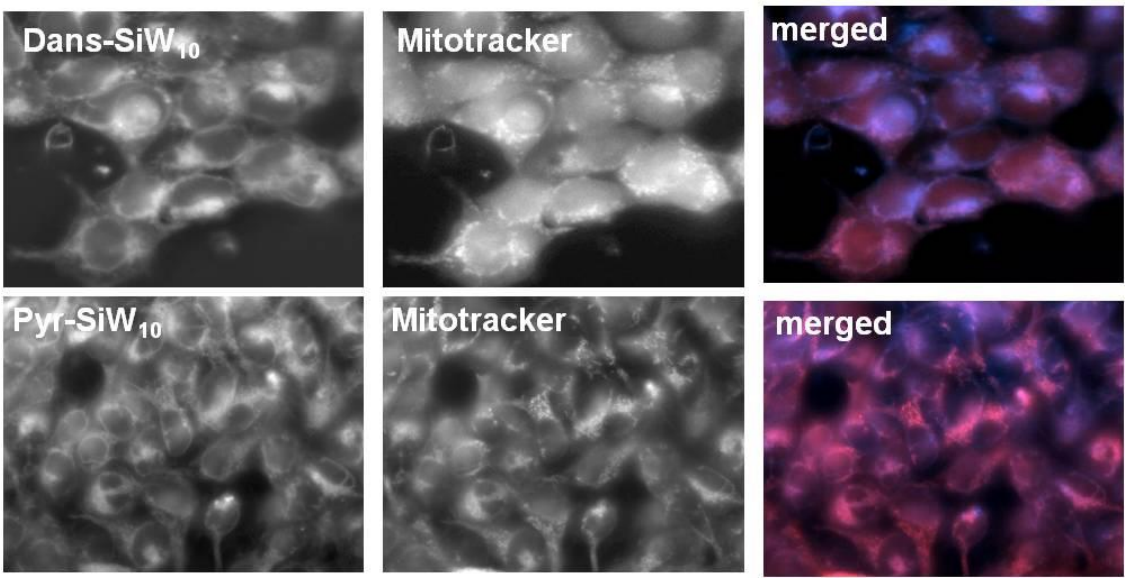

Figure 3.10 Subcellular localization of **Dans-SiW$_{10}$** and **Pyr-SiW$_{10}$** compounds. In *vitro* fluorescence imaging of HEK cells treated with POMs (18 µM, 16h at 37°C) and counterstained with mitochondrial probe (Mitotracker, red) [25] suggesting preferential mitochondrial localization of the compounds.

Fluorescein-based compounds **FITC-SiW$_{10}$** and **FITC-PW$_9$** were able to penetrate the nuclear membrane and to accumulate into the nuclei. Furthermore, a different fluorescence efficiency, depending on the inorganic domain was observed. **FITC-PW$_9$** shows a better uptake, with preferential nuclear localization (Figure 3.11). The brillant aggregates seems to be co-localised with inner nuclear structures. **FITC-SiW$_{10}$**, was scarcely and not evenly uptaken, with bright aggregates on cell surface. The POM-free **FITC-AEPA** was also detected in the nuclear regions, even if only at low intensity, highlighting a major role of the organic tag (Appendix, A41).

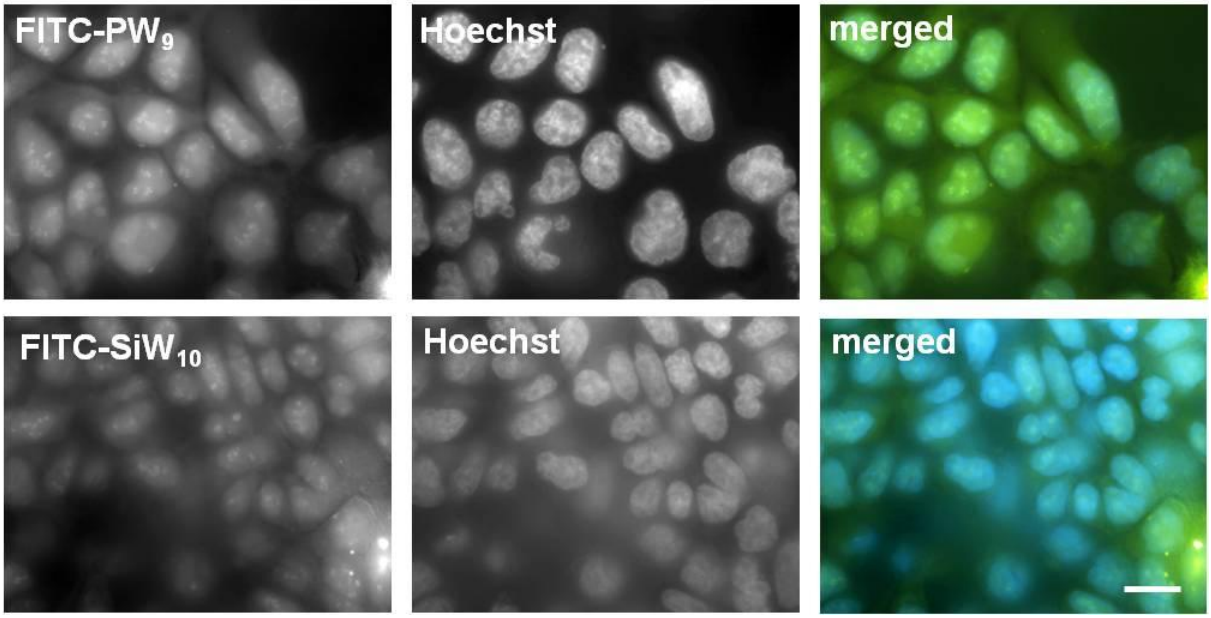

Figure 3.11 Subcellular localization of **FITC-POMs**. Fluorescent microscopy imaging of HEK cells treated with **FITC-PW$_9$** and **FITC-SiW$_{10}$** (18 µM, 16h at 37°C) and counterstained with nuclear dye (Hoechst blue)[26] confirm nuclear localization of these compounds. Scale bar: 10 µm.

Cell fixation with 2% paraformaldehyde in phosphate buffer increased consistently membrane permeability of POMs, that retained the subcellular preferential colocalisation, towards the cytoplasmatic region (**Dans-SiW$_{10}$** and **Pyr-SiW$_{10}$**) or nuclei (**FITC**-based compounds).

3.2.1.4 Conclusions and future perspectives

In conclusion, we have shown that the luminescent hybrid **POMs**(**1-4**) are hydrophobic and self-assemble into nanoparticles: in such form, they can be delivered into HEK cells without any carrier, likely using the intrinsic surface membrane recycling activity of the cells.[27] We have indeed proven that the these luminescent POMs can be tracked in the cells, showing their localization in different subcellular regions. An unprecedented uptake into nuclei and mitochondria has been highlighted. Biological effects and biocompatibility of hybrid POMs have been determined, showing a reduced toxicity at low doses. These results are expected to pave the way to the use of suitable POMs both as drugs and as nanodimensional scaffolds.

In the next paragraphs we will consider the design and the possible delivery of POMs functionalized with small biochemical molecules[28] and POM-based bioconjugates.

3.2.2 Interaction studies between POMs and apoferritin protein (aFtn)

As we have mentioned in the *Introduction* of this chapter (paragraph 3.1), the mechanisms of POMs biological activity at a molecular level remain unclear. As a consequence, preliminary studies on the interactions, in a broad sense, between POMs and several proteins is an important field of interest with the aim of unravel biological effects and the possibility of designing novel POMs-based drugs.

Furthermore, such kind of interaction studies between POMs and macromolecules can be also useful to design drug delivery systems, capable to carry, protect and confine POMs, while decreasing their toxicity. In particular, the encapsulation of POMs within an organized protective protein environment represents a promising approach to overcome stability issues and can be used to generate functional nanodevices with potential medical applications. In this respect, in the literature, some types of nanocarriers have already been investigated to gather information about the stabilization, biocompatibility, cell permeability and interaction of these systems with healthy and tumour cells (see *Chapter 1*, paragraph 1.3.3).

Within this context, due to their well defined size and morphology, proteins can act as soluble templating agents with enhanced recognition capabilities, useful to increment the biocompatibilty of POMs into physiological conditions. In particular, POM polyanionic nature can be indeed exploited to drive electrostatic interactions with the cationic residues on the surface or into the pockets of the proteins.[15,17,29]

In this paragraph, a preliminary investigation to explore the use of apoferritin (aFtn) as a nano cage/scaffold for polyoxometalate complexes will be presented. Apoferritin is an hollow protein containing 24 subunits, with approximately 12 and 8 nm external and internal diameter (Figure 3.12). The protein, present in the intestinal mucosa, it is able to bind and store iron. Inside the apoferritin shell, Fe^{III} ions are incorporated in mineral ferrihydrite $[FeO(OH)]_8[FeO(H_2PO_4)]$, together with phosphate and hydroxide ions and form ferritin. To release iron when the body needs it, the iron must be changed from the Fe^{III} to the Fe^{II} oxidation state. Then, the iron leaves through channels in the spherical structure. In this way, Ftn molecules result ubiquitous proteins which are used by several organisms to temporarily store up to 4500 iron ions as hydrated Fe^{III} oxide, so to prevent the formation of free radicals that can be generated by an excess of Fe^{II} ions, through Haber-Weiss reaction mechanism.[30]

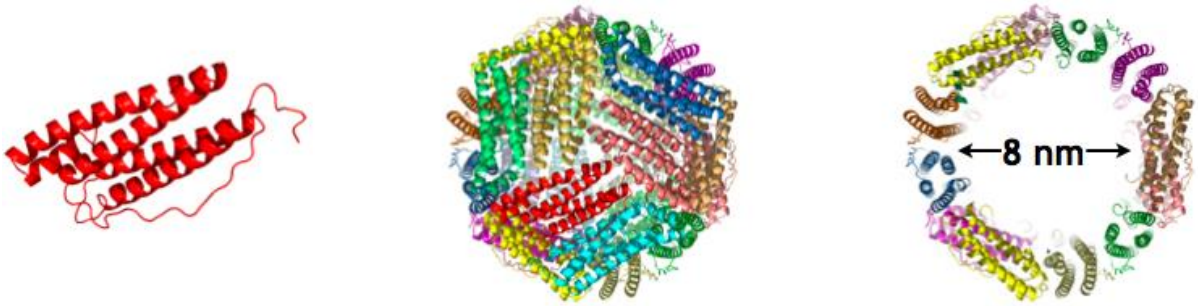

Figure 3.12 Drawing of aFtn: subunit(left), exterior (middle) and internal cavity (right).

Fe can be completely removed by dialysis against a reducing agent and aFtn can be used as a bio-template, to host inorganic nanoparticles and organometallic complexes with catalytic properties. In addition, aFtn is able to disassemble into subunits at pH<3.0 and reassemble as an almost intact sphere at pH>5.[31] This property has allowed the introduction of different molecules including drugs[32] and quantum dots[33] within the Ftn, to be used as delivery agents.
In this work, in particular, the POMs reported in Figure 3.13 have been chosen for the interaction studies with apoferritin:

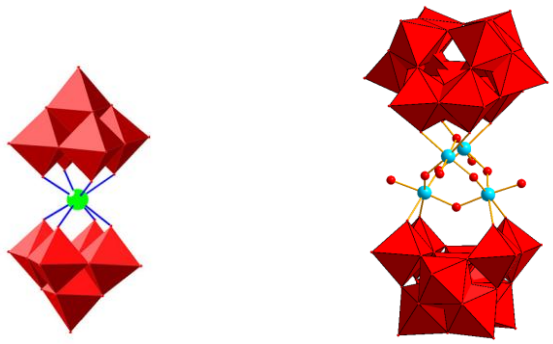

$[EuW_{10}O_{36}]^{9-}$ **EuPOM**

$[Ru^{IV}_4(\mu\text{-}OH)_2(\mu\text{-}O)_4(H_2O)_4(\gamma\text{-}SiW_{10}O_{36})_2]^{10-}$ **RuPOM**

Figure 3.13 *Polyhedral/ball and stick* representations of the two POMs used for the experiments. Red polyhedra contain tungsten atoms. **EuPOM**: green sphere is europium heteroatom (Eu^{III}); **RuPOM**: red spheres are oxygen atoms, blue spheres are ruthenium heteroatoms (Ru^{IV}).

(i) $[EuW_{10}O_{36}]^{9-}$ (**EuPOM**) is a fluorescent POM and it can be used as a fluorescent probe. Its emission spectrum exhibits three main emissions: 593 nm ($^5D_0 \rightarrow {}^7F_1$), 619 nm ($^5D_0 \rightarrow {}^7F_2$), and 700 nm ($^5D_0 \rightarrow {}^7F_4$), which are very sensitive to the environment.[34]

(ii) $[Ru^{IV}_4(\mu\text{-}OH)_2(\mu\text{-}O)_4(H_2O)_4(\gamma\text{-}SiW_{10}O_{36})_2]^{10-}$ (**RuPOM**) has been selected for its outstanding activity in mimicking the activity of photosystem II and of catalase enzymes.[35]

In particular, two strategies have thus been explored for the development of a novel nanocomposite material featuring noncovalent interactions between the POMs and the proteic scaffold:

(i) Electrostatic interaction between POMs and Ftn at pH 3.5, to reduce the overall negative charges on the Ftn surface upon protonation of acidic residues (Glu, Asp) and of amino groups (His, Arg, Lys).

(ii) Opening of the Ftn at pH 2.5, to exploit the internal sites of Ftn for POM binding, followed by reassembly at neutral pH.

3.2.2.1 Association through electrostatic interactions

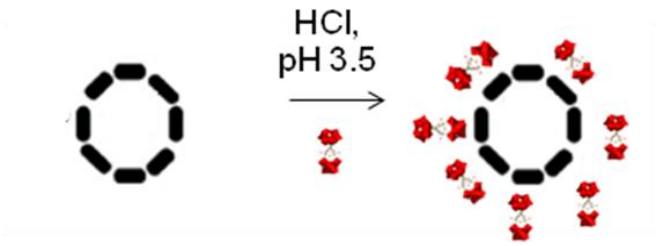

Scheme 3.3

Study of fluorescence, ζ-potential and DLS were performed to study the interaction of aFtn with **EuPOM** and **RuPOM**. Since the buffers may give a strong contribution to ζ-potential measurements, analyses were carried out in non buffered media.

As stated above, to favour the association with the polyanionic POM, the pH was decreased to 3.5 (with diluted HCl or in a 20 mM AcONa/AcOH buffer). At these values ζ-potential increases towards less negative values (from -21.3 to -9.8 mV). Addition of RuPOM resulted in a shift at -17.8 mV, suggesting an interaction with the polyanion (Appendix, A43).

Binding of the POM was thus followed by fluorescence spectroscopy in such pH conditions. The Trp residues present in the three-fold channels can be irradiated at 290 nm, while the emission can be monitored at 327 nm.

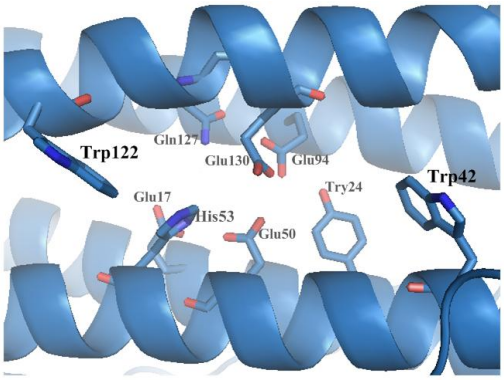

Figure 3.14 Schematic representation of a three fold channel of Ftn.

The **RuPOM** was dissolved in a buffered media (20 mM AcONa/AcOH) and added stepwise to a Ftn solution in the same buffer.

A complete quenching of the Trp fluorescence was observed when > 30 eqs of the **RuPOM** were added (Figure 3.15). Each subunit seems able to coordinate with a POM unit, without yielding a complete saturation of other accessible binding sites.

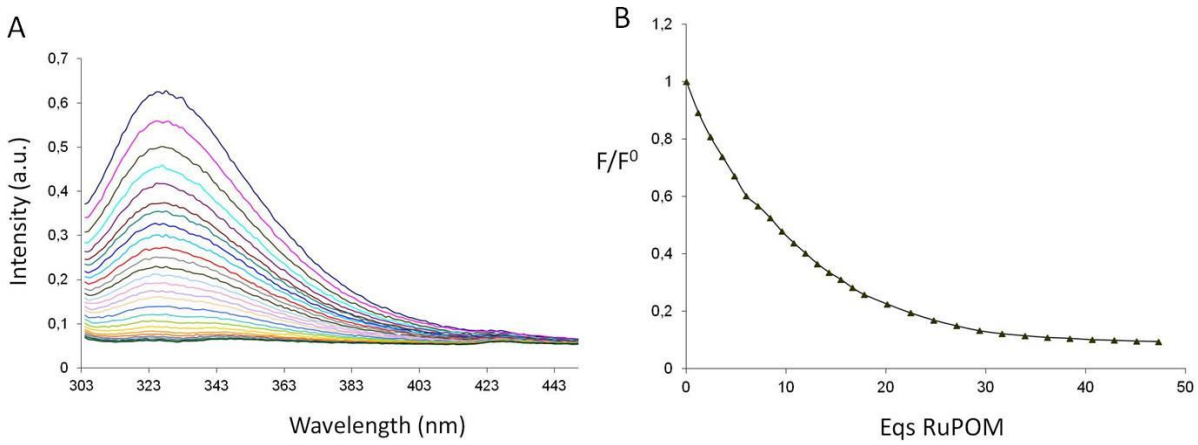

Figure 3.15 A Fluorescence quenching observed upon addition of **RuPOM** to a 0.5 µM Ftn solution in acetate buffer 20 mM, pH 3,5. **B** Monitoring of the emission at 327 nm (λ_{exc} = 290 nm).

At pH 3.5, quenching of the Trp fluorescence was also observed upon addition of 0-35 eqs of $[EuW_{10}O_{36}]^{9-}$ (**EuPOM**) (Figure 3.16). Since the luminescence of this POM is also completely quenched, we can state that the POM is not protected from the aqueous enviroment.[17]

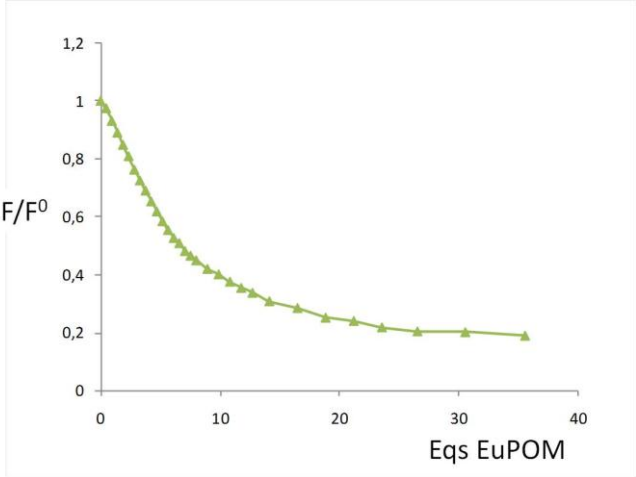

Figure 3.16 Fluorescence quenching observed during the addition of **EuPOM** to a solution of Ftn 0.5 μM in 20 mM AcONa/AcOH (pH 3.5); monitoring of the emission at 327 nm (λ_{exc} = 290 nm).

The minor differences in charge (-9 vs -10) and dimensions of this last POM (ca 1.6 vs 1.8 nm), in comparison with **RuPOM** does not strongly affect the binding process. This suggests that the binding could be readily obtained with different POMs featuring similar charge density.

Even if at pH 3.5, aFtn may start to loose some subunit, so to expose a fraction of Trp residues, the quenching is not expected to result from a direct interaction between these aminoacids and the POM. Indeed, the channels are too small to allow the introduction of the polyanion; moreover, Trp residues are close to Glu aminoacids, and no cationic side chain is present to favour the interaction (see Figure 3.14). As reported in the literature, for Eu-based POMs with HSA, a dynamic quenching, involving long range energy transfer may be considered.[15] As a further remark, the addition of POM do not seem to alter the tridimensional secondary structure of the protein, since the CD signal is only slightly decreased (Figure 3.17).

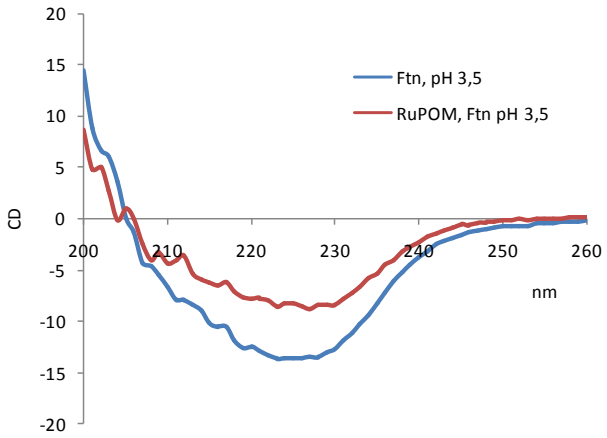

Figure 3.17 CD of a 0.5 µM aFtn solution in acetate buffer 2mM (pH 3,5), in the absence and in the presence of **RuPOM** (25µM).

Finally, the isothermal titration calorimetry (ITC) analyses show a saturation behaviour after addition of 20 (**EuPOM**) or 25 (**RuPOM**) eqs. The binding is an exothermic process with reaction enthalpies of about -15 (**RuPOM**) and -17 kcal/mol (**EuPOM**). This results are in agreement with an enthalpy driven electrostatic assembly.

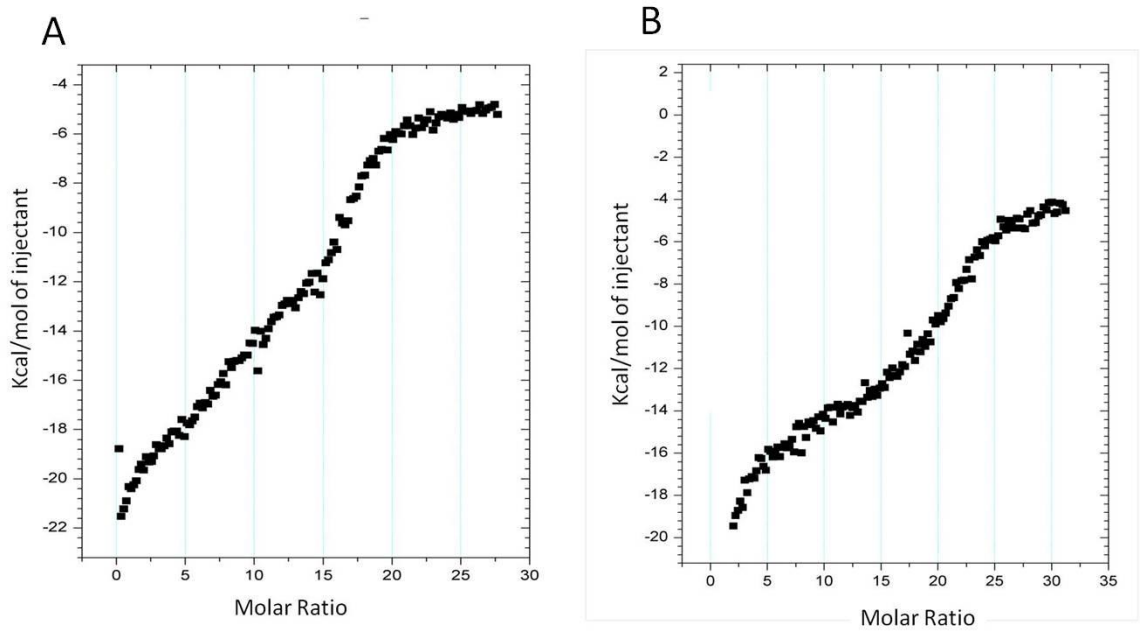

Figure 3.18 Isotherms recorded during the titration of aFtn (2.25 µM) with **A EuPOM** and **B RuPOM** (2 µl aliquots of a 0.315 mM solution) at pH 3.5 (20 mM AcONa/AcOH).

3.2.2.2 Opening the aFtn at pH 2.5

As already introduced, the aFtn can partially disassemble upon release of some subunits at pH<3.0, to be reassembled at neutral pH. Ftn has been opened at pH 2.5 by using a glycine-HCl buffer or diluted HCl, and POMs have been added (Scheme 3.4).

Scheme 3.4

Table 3.1: ζ-potential measurements of POMs (5.88 μM) and Ftn (0.245 μM) in different aqueous conditions.

#	Compound	pH	Peak 1 (mV)*	Peak 2 (mV)
1	Ftn	2.5 HCl	-7.0	-
2	Ftn	Back to 7,8 with NaOH	-26.8	
3	RuPOM@Ftn	2,5 (HCl)	-19.0 ÷ -15.4	
4	RuPOM@Ftn	Back to 7,8 with NaOH	-33.0	-14.6
5	RuPOM@Ftn	Back to 7.4 with tris/acetate	-21.6	-5.19
6	EuPOM@Ftn	Back to 7.4 with tris/acetate	-28.1	(1.72)

*Main peak.

At this pH, the ζ-potential exhibits a less negative value. A trend can thus be observed while going from pH 7.8 (-21.3 mV), pH 3.5 (-9.8 mV) and pH 2.5 (-7.0 mV), in non buffered media. The decreased stability of the particles featuring less negative potential is confirmed by the broader dispersion of the potential.

The addition of **RuPOM** decreases the negative charge to -20 mV. This values is, as expected, lower than those observed at pH 3.5 (-17.8 mV), confirming the possibility to host more POM complexes.

The fluorimetric analysis has been repeated in such conditions. A very similar behavior has been observed, even if with a decreased quenching efficiency.

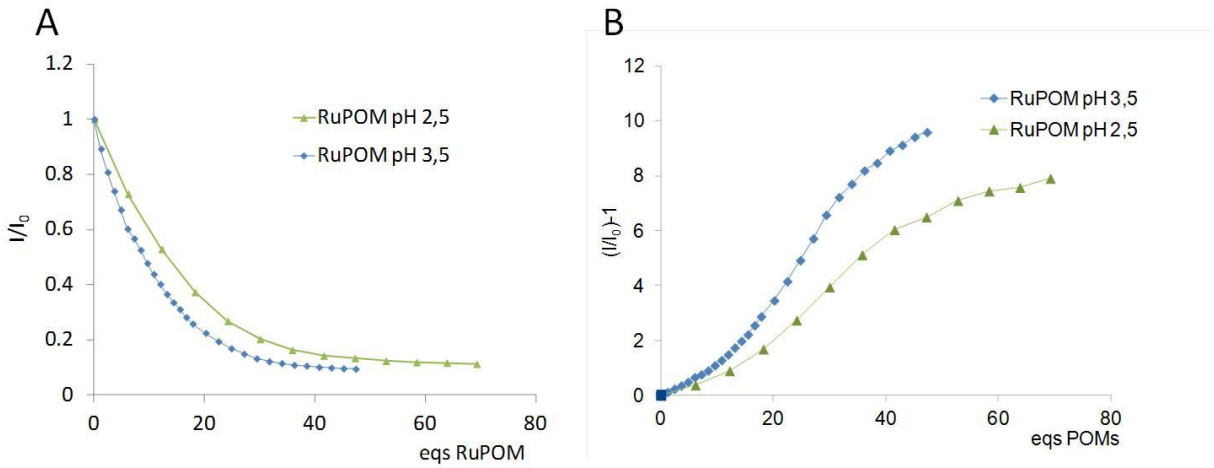

Figure 3.19 Fluorescence quenching observed during the addition of **RuPOM** to a 0.5 µM Ftn solution. **A** Comparison of titrations at pH 3.5 and 2.5 (20 mM Gly/HCl); **B** Ster-Volmer graphs.

A Stern-Volmer analysis was applied to the fluorescence quenching data in a range of POM concentrations where the plot remains linear (up to 10-15 eqs of quencher). The quenching constant calculated from the Stern-Volmer plot at 293 K are $K_{SV} = 2.78 \times 10^5\ M^{-1}$ at pH 3.5 and $K_{SV} = 1.59 \times 10^5\ M^{-1}$ at pH 2.5, respectively.[15(a)] The saturation occurs after the addition of > 35 eqs of POM. In such conditions, however, there is an extensive precipitation of the adduct. To avoid separation of the adducts from the solution, further experiments have been carried out in the presence of 24 eqs of POMs.

The addition of TRIS to restore the neutral pH resulted in a partial recovery of fluorescence (Figure 3.20 A). Closure of the Ftn and release of non trapped POM is indeed expected. This speaks in favour of a stable interaction.

The CD spectrum, recorded at pH 2.5, is slighty affected after addition of **RuPOM** (partial unfolding) but the spectral features can be recoverd at pH 7.8 (Figure 3.20 B). In addition, the CD spectrum show that at this pH apoferritin has a high proportion of ordered structures. Indeed protein undergo changes attributed to pH-dependent conformational transitions in the range 200-240 nm.[36]

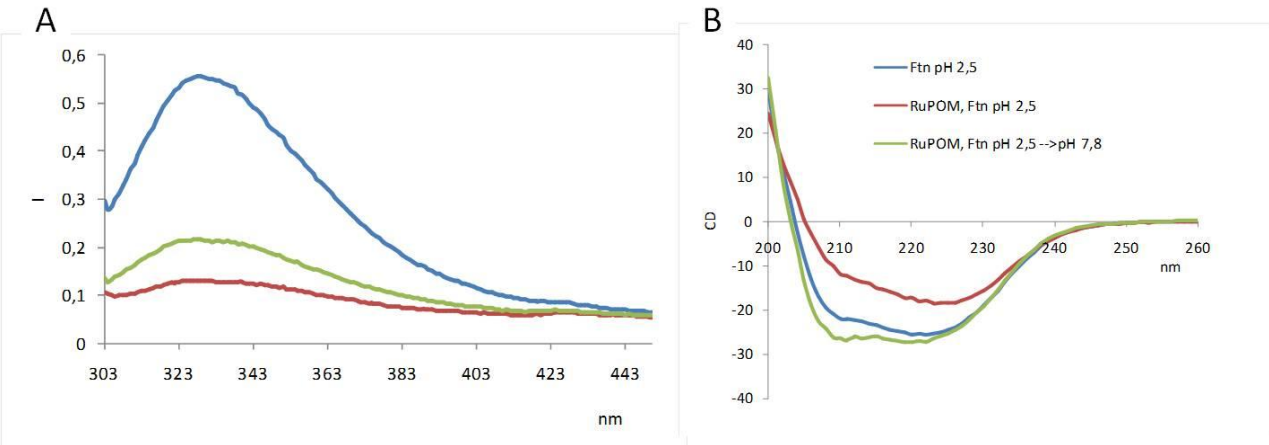

Figure 3.20 Ftn (0.5 µM) at pH 2.5 (blue), Ftn with **RuPOM** (12 µM) at pH 2.5 (red) and after addition of TRIS (green), up to pH 7.8.

Upon pH increase with NaOH, ζ-potential of aFtn get close to its initial value (-26.8 mV Vs -21.3 mV), whereas in the presence of **RuPOM**, the ζ-potential is still more negative, even if with an irregular distribution (Table 3.1, # 2 and 4; Appendix, A44).

The procedure has also been carried out in different conditions (Table 1, #5 and #6) with 0.245 µM aFtn and 50 eqs of POMs. The Ftn has been placed in the presence of a glycine buffer (pH 2.5), followed by addition of the POM and further modification of the pH by dialysis against a TRIS buffer (pH 7.8). The size of the particles containing POMs, after opening/closure is 10.8 nm, whereas a -28.1 mV of ζ-potential has been observed (with **EuPOM**), suggesting that there could still be POM on the spherical aFtn surface (Appendix, A45).

Interestingly, transmission electronic microscopy (TEM) images had shown further possible evidences relative the inner confinement of the **RuPOM** (Figure 3.21).

The darker regions into the ferritin core can be attributed to the POM: indeed, the reference aFtn does not display the same contrast.

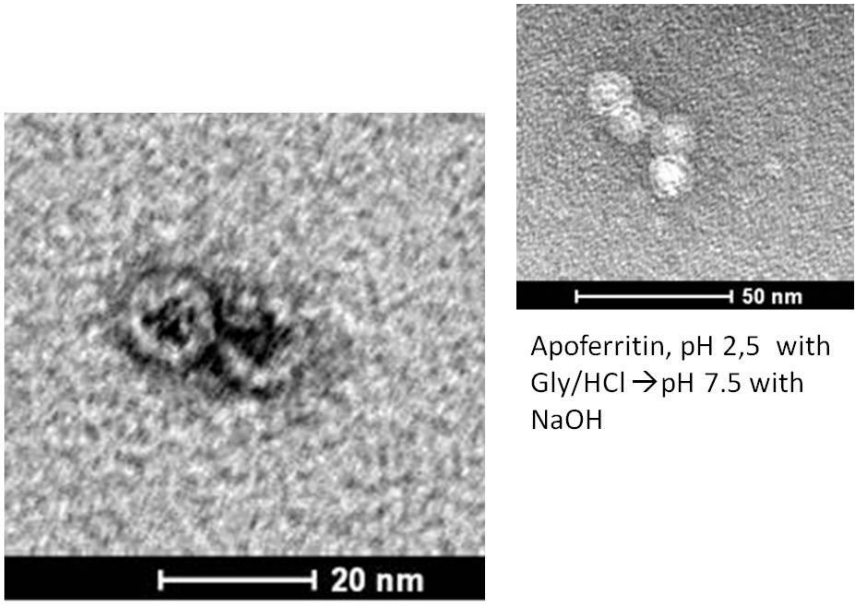

Figure 3.21 Transmission electron microscopy (TEM) image of aFtn containing **RuPOM,** upon opening with Gly/HCl buffer (pH = 2.5) and closing with NaOH (pH=7.5). Inset: aFtn in the same conditions and without **RuPOM**. Both images were obtained in the presence of uranyl acetate (5%) to provide a negative staining of the proteic structures.

Dialysis procedures were also used to remove non encapsulated POM, but the POMs do not cross the membrane (100KDa cut off). PAGE (Polyacrylamide gel electrophoresis) seems to be more promising for the separation of the Ftn and the free POMs and will be carefully investigated.

3.2.2.3 Conclusions and future perspectives

The bio-template approach has been studied by a combined investigation, involving DLS (dynamic light scattering), ζ-potential measurements, ITC (isothermal titration calorimetry), fluorimetry, CD (circular dichroism) and TEM (trasmission elctronic microscopy). The results have shown that the POM can be successfully attached to the Ftn by means of ionic interactions. The binding of the POMs ($[Ru^{IV}_4(\mu\text{-}OH)_2(\mu\text{-}O)_4(H_2O)_4(\mu\text{-}SiW_{10}O_{36})_2]^{10-}$ and $[EuW_{10}O_{36}]^{9-}$ on Ftn has been indeed higlighted by:

(i) the shift of Ftn ζ-potential towards more negative potentials (by 8-13 mV), in the presence of the POM;

(ii) complete quenching of the Trp luminescence (λ_{exc} = 290 nm, λ_{em} = 327 nm), upon addition of >24 eqs of POM, likely due to energy transfer between the two domains;

(iii) hexothermal heat tranfer during the titration of Ftn with POM.

In addition, the integrity of the Ftn has been estabilished by DLS and CD analysis showing, respectively, retention of the cage size (10 nm) as well as of its secondary structure (positive Cotton effect of β-sheets).

3.2.3 Synthesis of a biotin-conjugated POM and study of its interaction with avidin protein

In this paragraph the synthesis of a hybrid POM containing a bioactive molecule and a preliminary study of its capability to interact with a protein will be presented. This study allows to investigate the possibility to confine hybrid POMs in correspondence of specific protein binding sites and to design bio-conjugated systems with molecular recognition properties, to be exploited in targeted cancer therapy.

To this purpose, the polyanion $[\gamma\text{-}SiW_{10}O_{36}]^{8-}$ have been bis-functionalized with biotin molecule. In particular, biotin is able to bind avidin, a protein isolated from chicken eggs, and its bacterial analogue, streptavidin, (from Streptomyces avidinii) with an extremely high affinity, fast on-rate, and high specificity.

The biotin-avidin interaction system is extensively used in biotechnology and, more recently, in biomedical field in order to (i) isolate proteins, (ii) perform biochemical assays and, in particular, (iii) implement drug therapies.

Figure 3.22 avidin containing 4 molecules of biotin

In detail, avidin consist of 4 subunits, each capable of binding a molecule of biotin, with dissociation constants of the order of 10^{-15} M (Figure 3.22).

The specific characteristics of avidin have been shown to be of great advantage for selective drug design: the high positive charge of avidin augments the efficiency of cellular uptake of biotin-coated particles, whereas incubation of bio-conjugated avidin with biotinylated cells lines results in rapid surface attachment and endocytosis, with efficiencies approaching 100%. In addition, avidin has been demonstrated to accumulate in specific tissues, especially in tumors in *vivo*. Indeed the strong avidin-biotin interaction can be used to develop targeted therapies by the biotinylation of ligands or tissues in *vivo*.[37]

In the next paragraph the synthesis of a biotinylated POM and its interaction with avidin protein is described.

3.2.3.1 Synthesis of $(n\mathrm{Bu_4N})_4[\{(C_5H_7N_2OS)(CH_2)_4CONH(CH_2)_3Si\}_2O(\gamma\text{-}SiW_{10}O_{36})]$ *(Biot-SiW_{10})*

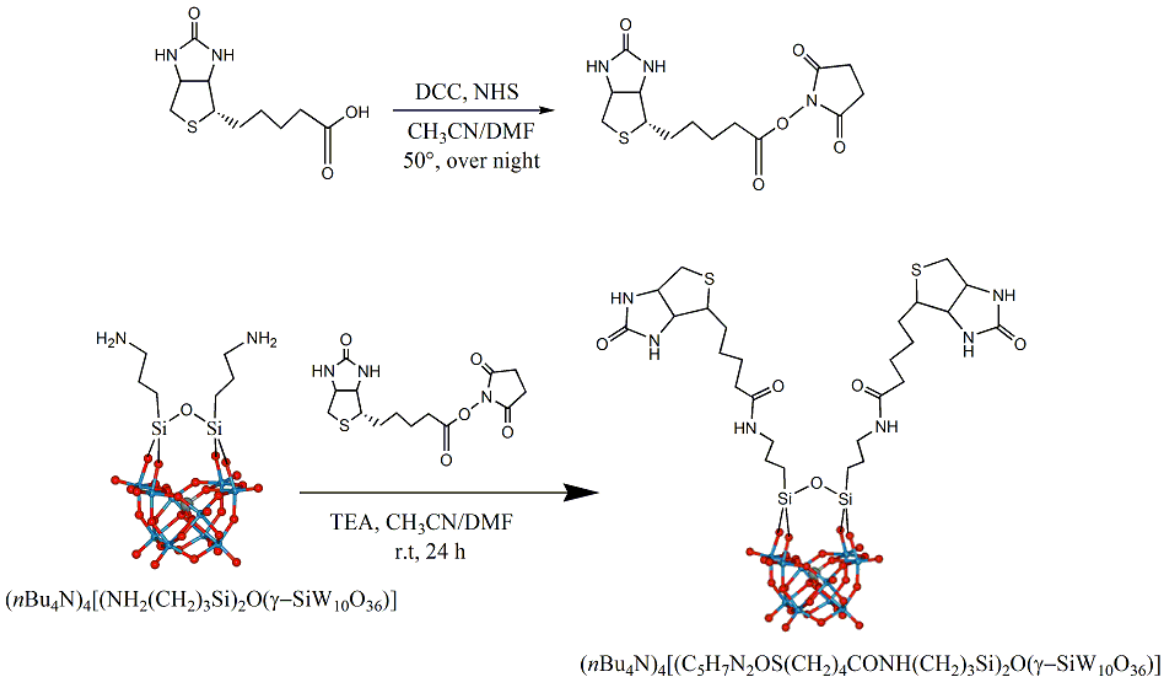

Scheme 3.5 Synthetic routes to a Keggin-type polyoxotungstate functionalized with biotin biomolecules.

The complex **Biot-SiW_{10}**, containing two molecules of biotin, was prepared by means of a classical coupling reaction in solution between the carboxylic acid function of the biotin and the amine function of the hybrid POM intermediate **APTES-SiW_{10}** (see *Chapter 2*, paragraph 2.2.2) in the presence of TEA (triethylamine).

In a first step (Scheme 3.5), the carboxyl group of biotin was activated with DCC (dicyclohexyl-carbodiimide, 2.5 eq) and NHS (N-hydroxy-succinimide, 2.5 eq) in CH_3CN/DMF for one night at 50°C. The resulting activated biotin was reacted, in a molar ratio 2:1, with the hybrid precursor **APTES-SiW$_{10}$** in CH_3CN, in the presence of TEA for 24 h, at room temperature.

Finally, the product, $(n\text{Bu}_4\text{N})_4[\{(C_5H_7N_2OS)(CH_2)_4CONH(CH_2)_3Si\}_2O(\gamma\text{-}SiW_{10}O_{36})]$ ***(Biot-SiW$_{10}$)*** **(5)** was isolated by precipitation with diethyl ether and extensively washed with water, obtaining a yield of 64%.

The bis-decorated molecular hybrid was characterized by FT-IR, multinuclear NMR, ESI-MS, UV-Vis and circular dichroism. The complete characterization has highlighted several features shared with the previously hybrid POMs (**1-4**) described in *Chapter 2*. In particular, relevant spectral features, reported in Table 3.2, are in agreement with a bis-substitution.

Table 3.2 Relevant spectral features of **Biot-SiW$_{10}$** (**5**)

Solvent	**m/z**	**^{29}Si NMR (ppm)**	**^{183}W NMR (ppm)**
CH_3CN	768.0*	-62.01 (2Si), -88.43 (1Si)	- 107.55 (4W) - 136.09 (2W) - 142.08 (4W)

* expected for $[C_{26}H_{44}N_6O_{41}S_2Si_3W_{10}]^{4-}$ = 770.5.

After the introduction of the biotin chiral centers, a C_2 symmetric complex is obtained. However, since the distance between the asymmetric centers and the POM is too long, ^{29}Si and ^{183}W NMR resonance values are very close to those of the precursor **APTES-SiW$_{10}$** and do not display any splitting (see *Chapter 2*, paragraph 2.2.2).[38]

Finally, the ^{1}H NMR spectrum is also consistent with the biotinylation, since resonances due to protons of the condensed rings of biotin can be recognized.

In this case, the signals of the biotin protons are not significantly shifted with respect to the free molecule, suggesting that also the organic moiety is not altered after attachment to the POM.

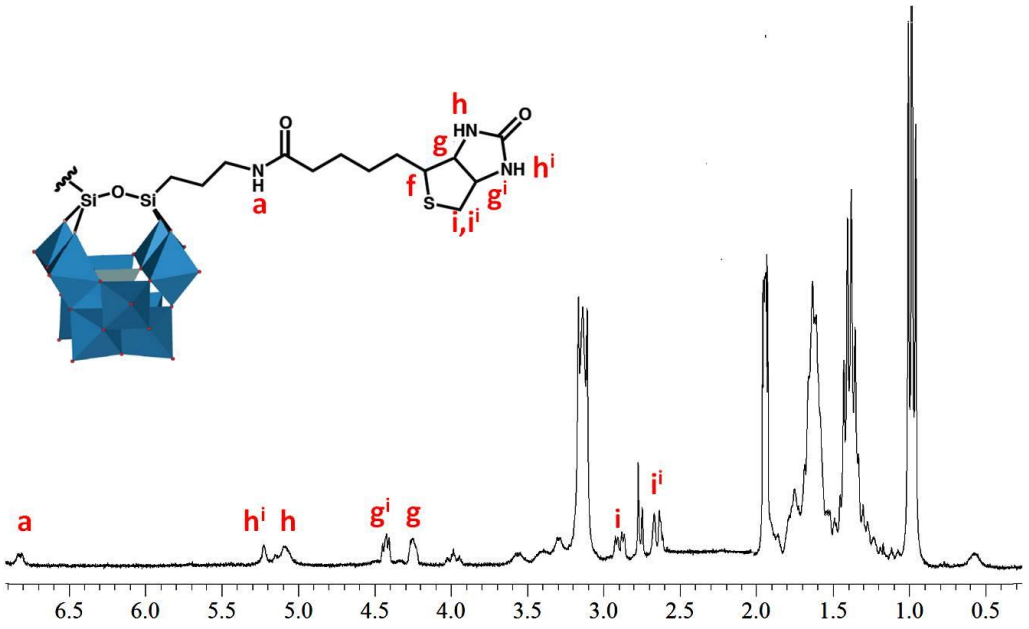

Figure 3.23 ^{1}H NMR (CD_3CN) of **Biot-SiW$_{10}$**.

3.2.3.2 Preliminary interaction studies of Biot-SiW$_{10}$ with avidin

Once synthesized the hybrid POM containing two molecules of biotin, we have evaluated its capability to bind avidin (see the introduction of the paragraph). To this aim, a known amounts of **Biot-SiW$_{10}$** has been added to a solution containing avidin and the 4'-hydroxyazobenzene-2-carboxylic acid (HABA). The HABA is a dye capable to weakly bind avidin and produce a yellow-orange colored complex. The interaction between biotin and avidin causes the release of HABA, with a consequent increase of its absorbance (monitored at 348 nm) in aqueous solution. The binding event can thus be followed by UV-Vis spectroscopy.

The UV-Vis titration show a saturation behaviour after addition of 1.28 equivalents of **Biot-SiW$_{10}$**, leading to a 64% saturation of the binding sites available in the protein. This important result suggests that biotin maintains its ability to bind avidin even when anchored to the polyanionic scaffold.

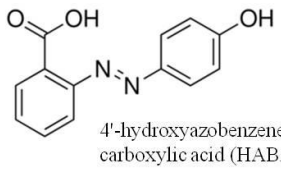

Figure 3.24 Structure of HABA.

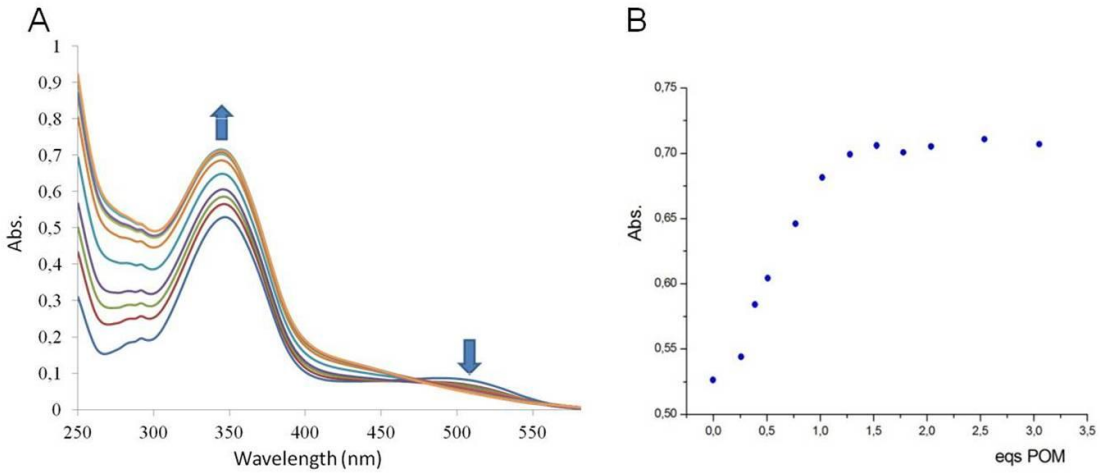

Figure 3.25 A UV-Vis titration of **Avidin/HABA** system (0.68 µM in H_2O) with **Biot-SiW$_{10}$** (0-3 eqs); **B** binding monitored at 348 nm; in y-axes is reported the absorption of HABA.

In figure 3.26 are reported the different binding models proposed for the Biot-SiW$_{10}$/avidin interaction.

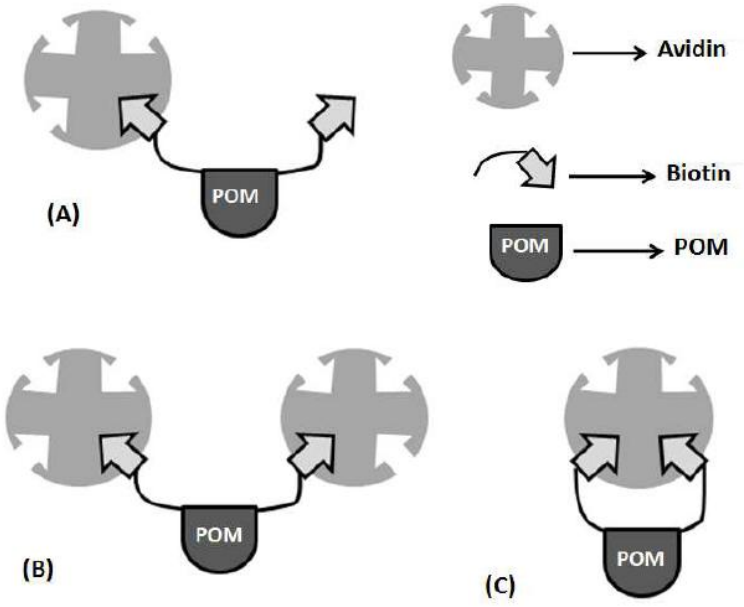

Figure 3.26 Possible binding models between **Biot-SiW$_{10}$** and avidin.

Considering the structural features of the hybrid complex, since the distance between the two biotin molecules on the polyanionic scaffold is not sufficient, a single **Biotin-SiW$_{10}$** molecule is not able to bind with both biotin units to a single avidin molecule (Figure 3.26, C).[39] Indeed, it is much more probable that the **Biotin-SiW$_{10}$** binds the protein according to the cases A and B illustrated in figure 3.26. The possibility that the POM may bridge two different molecules of avidin to yield a cross-linked polymeric structure, is suggested by the decreased solubility of the resulting adduct.

3.2.2.3 Conclusions and future perspectives

A POM-based bio-conjugate has been successfully prepared by the bis-functionalization of the [γ-SiW$_{10}$O$_{36}$]$^{8-}$ scaffold with biotin molecules. Furthermore, its interaction capability with avidin has been investigated by means of UV-Vis titration. The results suggested that the **Biot-SiW$_{10}$** is proximal to the biotin binding site of the protein. Such kind of interaction could be useful to protect and deliver POMs towards biological targets, increasing the bio-stability. The final goal is to obtain bio-conjugated systems that integrate POMs with molecular recognition properties. Although these are preliminary studies, these data demonstrate the potential of POM hybrid for targeting and delivery applications.

3.3 References and notes

[1] a) S. Chen, G. Wu, D. Long, Y. Liu *Carbohyd. Polym.* **2006**, *64*, 92; b) M. Inoue, T. Suzuki, Y. Fujita, M. Oda, N. Matsumoto, T. Yamase J. *Inorg. Biochem*. **2006**, *100*, 1225.

[2] a) B. L. Moskovitz, *Antimicrob. Agents Chemother*. **1988**, *32*, 1300; b) S. G. Sarafianos, U. Kortz, M. T. Pope, M. J. Modak *Biochem. J.* **1996**, *319*, 619; c) A. Flütsch, T. Schroeder, M. G. Grütter, G. R. Patzke *Bioorg. Med. Chem. Lett.* **2011**, *21*, 1162.

[3] a) T, J. Yamase *Mater. Chem*. **2005**, *15*, 4773; b) D. Menona, R. T. Thomas, S. Narayanan, S. Maya, R. Jayakumar, F. Hussain, V-K. Lakshmanan, S.V. Nair *Carb. Polym*. **2011**, *84*, 887.

[4] a) G. Zhang, B. Keita, C. T. Craescu, S. Miron, P. de Oliveira, L. Nadjo, *J. Phys. Chem. B* **2007**, *111*, 11253; b) G. Hungerford, K. Suhling, M. Green, *Photochem. Photobiol. Sci.* **2008**, *7*, 734; c) L. Zheng, Y. Ma, G. J. Zhang, J. N. Yao, B. S. Bassil, U. Kortz, B. Keita, P. de Oliveira, L. Nadjo, C. T. Craescu, S. Miron, *Eur. J. Inorg. Chem.* **2009**, *34*, 5189; d) G. Hungerford, F. Hussain, G. R. Patzke, M. Green, *Phys. Chem. Chem. Phys.* **2010**, *12*, 7266; e) R. Prudent, V. Moucadel, B. Laudet, C. Barette, L. Lafanechere, B. Hasenknopf, J. Li, S. Bareyt, E. Lacôte, S. Thorimbert, M. Malacria, P. Gouzerh, C. Cochet, *Chem. Biol.* **2008**, *15*, 683; d) J. Iqbal, M. Barsukova-Stuckart, M. Ibrahim, S.U. Ali, A.A Khan, U. Kortz *Med. Chem. Res*. **2012**, DOI 10.1007/s00044-012-0125-8.

[5] a) M. S. Kaba, I. K. Song, D. C. Duncan, C. L. Hill, M. A. Barteau, *Inorg. Chem.* **1998**, *37*, 398; b) M. Kinne, M. A. Barteau, *Surf. Sci.* **2000**, *447*, 105.

[6] L. Ni, P. Greenspan , R. Gutman , C. Kelloes , M. A. Farmer , F. D. Boudinot *Antiv. Res*. **1995**, *32*, 141.

[7] C. Cibert, C. Jasmin, *Biochem. Biophys. Res. Commun.* **1982**, *108*, 1424.

[8] M.Cholewa, G. J. F. Legge, H. Weigold, G. Holan, C. Birch, *J. Life Sci.* **1994**, *54*, 1607.

[9] a) L. Zheng, Z. J. Gu, Y. Ma, G. J. Zhang, J. N. Yao, B. Keita, L. Nadjo, *J. Biol. Inorg. Chem.* **2010**, *15*, 1079; b) L. Zheng, Y. Ma, G. Zhang, J. Yao, B. Keita, L. Nadjo, *Phys. Chem. Chem. Phys.* **2010**, *12*, 1299; c) C. Boglio, G. Lenoble, C. Duhayon, B. Hasenknopf, R. Thouvenot, C. Zhang, R. C. Howell, B. P. Burton-Pye, L. C. Francesconi, E. Lacôte, S. Thorimbert, M. Malacria, C. Afonso, J.-C. Tabet, *Inorg. Chem.* **2006**, *45*, 1389, and references therein.

[10] a) Y. Inouye, Y. Tokutake, J. Kunihara, T. Yoshida, T. Yamase, A. Nakata, S. Nakamura, *Chem. Pharm. Bull.* **1992**, *40*, 805; b) D. A. Judd, R. F. Schinazi, C. L. Hill, *Antiviral Chem. Chemother.* **1994**, *5*, 410; c) S. G. Sarafianos, U. Kortz, M. T. Pope, M. J. Modak, *Biochem. J.* **1996**, *319*, 619; d) C. Schoeberl, R. Boehner, B. Krebs, C. Mueller, A. Barnekow, *Int. J. Oncol.* **1998**, *12*, 153; e) M. Witvrouw, H. Weigold, C. Pannecouque, D. Schols, E. De Clercq, G. Holan, *J. Med. Chem.* **2000**, *43*, 778; f) D. A. Judd, J. H. Nettles, N. Nevins, J. P. Snyder, D. C. Liotta, J. Tang, J. Ermolieff, R. F. Schinazi, C. L. Hill, *J. Am. Chem. Soc.* **2001**, *123*, 886.

[11] a) T. Yamase, N. Fukuda, Y. Tajima, *Biol. Pharm. Bull.* **1996**, *19*, 459; b) M. Inoue, T. Suzuki, Y. Fujita, M. Oda, N. Matsumoto, J. Iijima, T. Yamase, *Biomed. Pharmacother.* **2006**, *60*, 220; c) N. Fukuda, T. Yamase, Y. Tajima, *Biol. Pharm. Bull.* **1999**, *22*, 463.

[12] T. L. Turner, V. H. Nguyen, C. C. McLauchlan, Z. Dymon, B. M. Dorsey, J. D. Hooker, M. A. Jones, *J. Inorg. Biochem.* **2012**, *108*, 96.

[13] a) K. Nomiya, H. Torii, T. Hasegawa, Y. Nemoto, K. Nomura, K. Hashino, M. Uchida, Y. Kato, K. Shimizu, M. Oda, *J. Inorg. Biochem.* **2001**, *86*, 657; b) a) J. D. Foster, S. E. Young, T. D. Brandt, R. C. Nordlie, *FASEB J.* **1998**, *12*, A1360; c) J. D. Foster, S. E. Young, T. D. Brandt, R. C. Nordlie, *Arch. Biochem. Biophys.* **1998**, *354*, 125.

[14] C. E. Müller, J. Iqbal, Y. Baqi, H. Zimmermann, A. Röllich, H. Stephan, *Bioorg. Med. Chem. Lett.* **2006**, *16*, 5943.

[15] a) G. Zhang, B. Keita, J.-C Brochon, P. de Oliveira, L. Nadjo, C. T. Craescu, S. Miron *J. Phys. Chem. B* **2007,** *111*, 1809; b) G. Zhang, B. Keita, C. T. Craescu, S. Miron, P. de Oliveira, L. Nadjo *Biomacromolecules* **2008,** *9*, 812.

[16] Q. Wu, J. Wang, L. Zhang, A. Hong, J. Ren *Angew. Chem. Int. Ed.* **2005**, *44*, 4048.

[17] L. Zheng, Y. Ma, G. Zhang, J. Yao, B. Keita, L. Nadjo *Phys.Chem.Chem.Phys.* **2010**, *12*, 1299.

[18] a) A. Dolbecq, E. Dumas, C. R. Mayer, P. Mialane, *Chem. Rev*. **2010**, *110*, 6009 ; b) E. Antonova, C. Näther, P. Kögerler, W. Bensch, *Angew. Chem. Int. Ed.* **2011**, *50*, 764 ; c) C. Boglio, K. Micoine, E. Derat, R. Thouvenot, B. Hasenknopf, S. Thorimbert, E. Lacôte, M. Malacria, *J. Am. Chem. Soc.*

2008, *130*, 4553 ; d) S. Berardi, M. Carraro, A. Sartorel, G. Modugno, M.Bonchio *Isr. J. Chem.* **2011,** *51*, 259.

[19] X. H. Wang, J. F. Liu, M. T. Pope, *Dalton Trans.* **2003**, *5*, 957.

[20] a) J. Zhang, Y.-F. Song, L. Cronin, T. Liu, *J. Am. Chem. Soc.*, **2008**, *130*, 14408; b) C. P. Pradeep, M. F. Misdrahi, F.-Y. Li, J. Zhang, L. Xu, D.-L. Long, T. Liu and L. Cronin *Angew. Chem. Int. Ed.***2009**, *48*, 8309; c) F. Xiao, M. F. Misdrahi, J. Zhang, P. Yin, J. Hao, C. Lv, Z. Xiao, T. Liu and Y. Wei *Chem. Eur. J.* **2011**, *17*, 12006 ; d) D. Li, J. Song, P. Yin, S. Simotwo, A. J. Bassler, Y. Aung, J. E. Roberts, K. I. Hardcastle, C. L. Hill and T Liu *J. Am. Chem. Soc.* **2011**, *133*, 14010.

[21] Y. Han, Y. Xiao, Z. Zhang, B. Liu, P. Zheng, S. He, W. Wang, Macromolecules **2009**, *42*, 6543.

[22] This is a colorimetric assay that measures the reduction of yellow 3-(4,5-dimethythiazol-2-yl)-2,5-diphenyl tetrazolium bromide (MTT) by mitochondrial succinate dehydrogenase. The MTT enters the cells and passes into the mitochondria where it is reduced to an insoluble, coloured (dark purple) formazan product. The cells are then solubilised with an organic solvent (eg. isopropanol) and the released, solubilised formazan reagent is measured spectrophotometrically. Since reduction of MTT can only occur in metabolically active cells the level of activity is a measure of the viability of the cells.

[23] B. Hasenknopf, *Front. Biosci.* **2005**, *10*, 275.

[24] WST-1 (Water soluble Tetrazolium salt) is a water soluble dye for MTT assays. Since WST-1 is reduced outside cells and yield a water-soluble formazan, it is advantageous over MTT. In particular, it give a more effective signal and decrease toxicity to cells (unlike cell-permeable MTT, and its insoluble formazan that accumulate inside cells).

[25] Note: molecular Probes MitoTracker probes are a series of novel mitochondrion-selective dyes that are well retained during cell fixation. The cell-permeant MitoTracker probes contain a thiol-reactive chloromethyl moiety. Once the MitoTracker probe accumulates in the mitochondria, it can react with accessible thiol groups on peptides and proteins to form an aldehyde-fixable conjugate. These reduced probes do not fluoresce until they enter live cells, where they are oxidized to the corresponding fluorescent mitochondrion-selective probe and then sequestered in the mitochondria.

[26] Note: the blue fluorescent Hoechst dyes are bisbenzimidazole derivatives. Hoechst 33342 nucleic acid stain is a popular cell-permeant nuclear counterstain that emits blue fluorescence when bound to dsDNA.

[27] R. M. Steinman, I. S. Mellman, W. A. Muller, Z. A. Cohn *J. Cell. Biol.* **1983**, *96*, 1.

[28] M. Carraro, G. Modugno, A. Sartorel G. Scorrano, M. Bonchio *Eur. J. Inorg. Chem.* **2009**, *34*, 5164.

[29] a) R. Prudent, C. F Sautel, C. Cochet *Biochim. Biophys. Acta* **2010**, *1804*, 493; b) J.Geng, M. Li, J. Ren, E. Wang, X. Qu *Angew. Chem. Int. Ed.* **2011**, 50, 4184.

[30] Liu, X. F.; Theil, E. C. *Acc. Chem. Res.* **2005**, *38*, 167.

[31] a) P. M. Harrison, D. W. Gregory, *Nature* **1968**, *220*, 78; b) M. Kim, Y. Rho, K. Sik Jin, B. Ahn, S. Jung, H. Kim, M. Ree *Biomacromolecules* **2011**, *12*, 1629; c) E. Simsek, M. Akif Kilic *J. Magn. Magn. Mat.* **2005**, *293*, 509.

[32] a) J. M. Domínguez-Vera, J. *Inorg. Biochem*. **2004**,*98*, 469; b) Z. Yang, X. Wang, H. Diao, J. Zhang, H. Li, H. Sun, Z. Guo, *Chem. Commun.* **2007**, 3453.

[33] B. Hennequin, L. Turyanska, T. Ben, A. M. Beltrán, S. I. Molina, M. Li, S. Mann, Amalia Patanè, N. R. Thomas *Adv*. *Mater*. **2008**, *20*, 3592.

[34] R. Ballardini, Q.G. Mulazzani, M. Venturi,F. Bolletta, V. Balzani *Inorg Chem* **1984**, *23*, 300.

[35] a) A. Sartorel, M. Carraro, R. De Zorzi, S. Geremia, N.D. McDaniel, S. Bernhard, G. Scorrano, M. Bonchio *J. Am. Chem. Soc.*; **2008,** *130*, 5006; b) A. Sartorel, M. Truccolo, S. Berardi, M. Gardan, M. Carraro, F. M. Toma, G. Scorrano, M. Prato, M. Bonchio *Chem Commun.* **2011**, *47*, 1716,

[36] G.C. Wood, R, R. Crichton *Biochimica et Biophysica Acta (BBA) - Protein Structure* **1971**, *229*, 83.

[37] H. P. Lesch, M. U.Kaikkonen, J. T. Pikkarainen, S. Yla-Herttuala *Expert Opin. Drug. Deliv.* **2010**, *7*, 551.

[38] M. Carraro, G. Modugno, A. Sartorel, G. Scorrano, M. Bonchio *Eur. J. Inorg. Chem.* **2009**, 5164.

[39] S. Geninatti Crich, A. Barge, E. Battistini, C. Cabella, S. Coluccia, D. Longo, V. Mainero, G. Tarone, S. Aime, *J. Biol. Inorg. Chem.*, **2005**, *10*, 78.

Chapter 4

Hybrid polyoxometalate as ligand for an iridium catalyst with hydrogen transfer activity

In this chapter, we report a strategy for the synthesis of a POM-appended N-heterocyclic carbene (NHC) iridium complex. To this end, imidazolium moieties have been successfully grafted on the defect site of a divacant Keggin polyanion. The hybrid POM synthesized has been tested for catalyzing hydrogen transfer reactions. The reduction of benzophenone to diphenyl methanol in *i*PrOH as solvent and hydrogen donor has been used as a model reaction for probing the catalytic activity of the iridium(I) complex. In particular, full conversion after 120 min has been obtained using *t*BuOK as base.*

***** This work has been developed during a short scientific mission in Dublin, in collaboration with the research group of Prof. Martin Albrecht.

4.1 Introduction

4.1.1 Organometallic catalysts tethered to POMs

The anchorage of an organometallic catalyst on a nanodimensional and molecular scaffold is a valuable tool to implement the catalytic strategy. This allows to introduce a bulky molecule which can be useful to tune the solubility, so to easily exploit removal by precipitation, or for the successful recovery through nanofiltration and dialysis techniques. Between the suitable molecular species, we can find dendrimers, POSS (polyhedral oligomeric silsesquioxane), fullerenes, polyoxometalates (POMs) and metallic clusters.

POMs, in particular, represent molecular models of extended oxide-based solid supports, with the advantage of a tuneable solubility, that mainly depend on the counterions. In this respect, polydentate salen-type ligands, thiols, phosphines, and N-heterocycles carbene ligands have already been immobilized on the POM surface to bind Mn, Pd or Rh ions, respectively.[1,2,3]

The resulting hybrid POMs may display a remarkable stability under harsh catalytic conditions, enabling a multi-turnover performance under both oxidative and reductive conditions.[2,4]

In particular, Neumann and co-workers, developed new catalytic systems based on the covalent linkage of well-established organometallic catalysts to POM scaffolds: examples include tethering of metallo-salen (SiW_{11}–Msalen, M = Mn, Co, Ni, Pd)[1] and Wilkinson-type rhodium (SiW_{11}–Rh)[2].

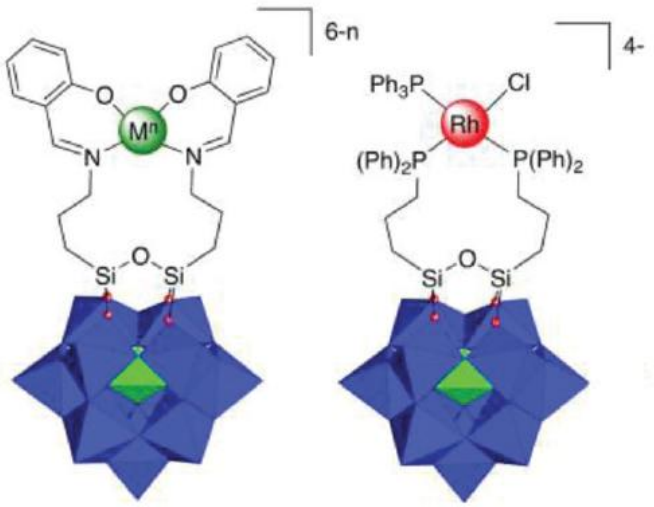

Figure. 4.1 Representation of the SiW_{11}–Msalen (left), and SiW_{11}–Rh (right) hybrids. Blue octahedra, $\{WO_6\}$; green tetrahedral, $\{SiO_4\}$.

At first, $[SiW_{11}O_{39}]^{8-}$ scaffolds were functionalized with silyl groups, than the metalation was achieved in a post-functionalization reaction.

These hybrids have been described as being more active and/or selective than the related organometallic precursor complexes. The main role of the POM is to tune the steric and electronic properties of the catalyst. In the case of the SiW_{11}–Msalen complexes, a charge transfer between the metallo-salen donor and the POM acceptor has been observed, with stabilization of unusual oxidation state of the appended metal M and/or oxidation of the salen ligand. Interestingly, this is an intramolecular phenomenon, not observed for mechanical mixtures of the parent POM and metallo-salen complexes. This underlines the beneficial effect of covalent tethering, compared to an electrostatic association. Improved stabilization of an intermediate Rh(III) was also proposed to account for the increased reactivity of the SiW_{11}–Rh hybrid.

4.1.2 Polyoxometalate-based N-heterocyclic carbene (NHC) complexes

N-heterocyclic carbenes (NHC) behave like typical σ-donor ligands able to form robust metal-carbene bonds with a variety of transition metals M, leading to M-NHC metal complexes with extraordinary stability toward temperature, oxidation and hydrolysis.[5,6]

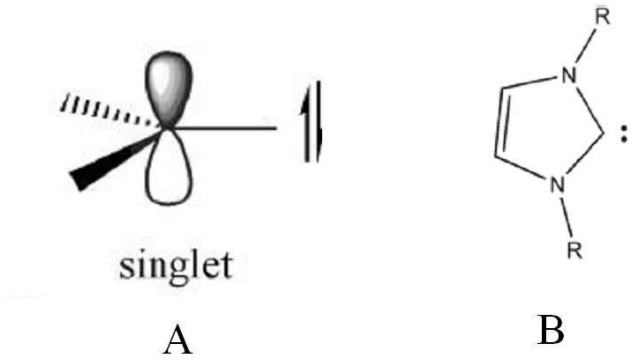

Figure 4.2 Singlet state of a carbene (**A**) and structure of an imidazol-2-ylidene (**B**) (the most widely used NHC in catalysis).

Electronic features of the NHC ligands may be optimized in order to improve the catalytic performance of the resulting M-NHC complexes, which are often reported to overcome the activity of phosphine analogues, in different catalytic reactions (e.g. cross-coupling reactions, metathesis).[6(a),7,8] Thus, several NHCs incorporating bulky substituents, donor groups, rigid systems and chiral functionalities have been developed. Recently, a series of homo- and

hetero-dimetallic complexes of 9th and 10th group metal ions have been obtained using Y-shaped tris-NHC ligands, to perform tandem process including a transfer hydrogenation (TH) step.[9]

In our research group, a hybrid POM containing Pd-NHC units has been prepared. In this case, the organometallic hybrid derivative (SiW_{10}–Pd(NHC)) results from the direct functionalization of the [γ-$SiW_{10}O_{36}$]$^{8-}$ scaffold with the preformed organometallic silane.[3]

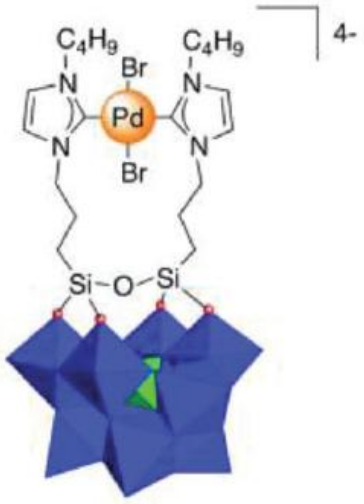

Figure 4.3 Representation of SiW_{10}–Pd(NHC). Blue octahedra, {WO_6}; green tetrahedral, {SiO_4}.

In particular, the complex SiW_{10}–Pd(NHC) displays outstanding catalytic activity in Suzuki Miyaura C–C cross coupling in harsh catalytic conditions, i.e. under microwave (MW) irradiation. In this case, the polyanionic domain represent an efficient MW-absorber, and provides for repulsive interactions between the catalytic units, so to prevent formation of inactive Pd-black upon aggregation of Pd^0 centers during catalytic turnover. Furthermore, the POM, due to its charge, presents high affinity towards ionic liquid media.[4] The POM-based system was also effective in coupling aryl chlorides. The particular role of the POM in these catalytic systems is to bring robustness to the whole hybrid and thus to increase its stability and performance.[4]

In this chapter, we present the synthesis of a hybrid POM, with anchored Ir-NHC moieties. This kind of complex has been tested as catalysts for the transfer hydrogenation of ketones.

4.1.3 Metal-catalyzed hydrogen transfer reactions

During transfer hydrogenation (TH), a hydrogen is transferred from an alcohol to an unsaturated bond. With respect to hydrogenation reaction using the hydrogen, TH is a safer and environmentally benign method, in which the alcohol acts as both the reaction solvent and the source of hydrogen. There is a continuous demand in developing new active catalysts that can perform such reactions under mild conditions and by simple methodologies. Many recent reports have also focused on the mechanistic aspects of the reaction. A common feature of these reactions is that they involve metal hydride (monohydride or dihydride) intermediates, and a base is generally required in order to promote their formation.

Two general reaction pathways can thus be envisaged for hydrogen transfer: a step-wise process, called "*hydridic route*", and a concert process, called "*direct hydrogen transfer*" (Scheme 4.1).

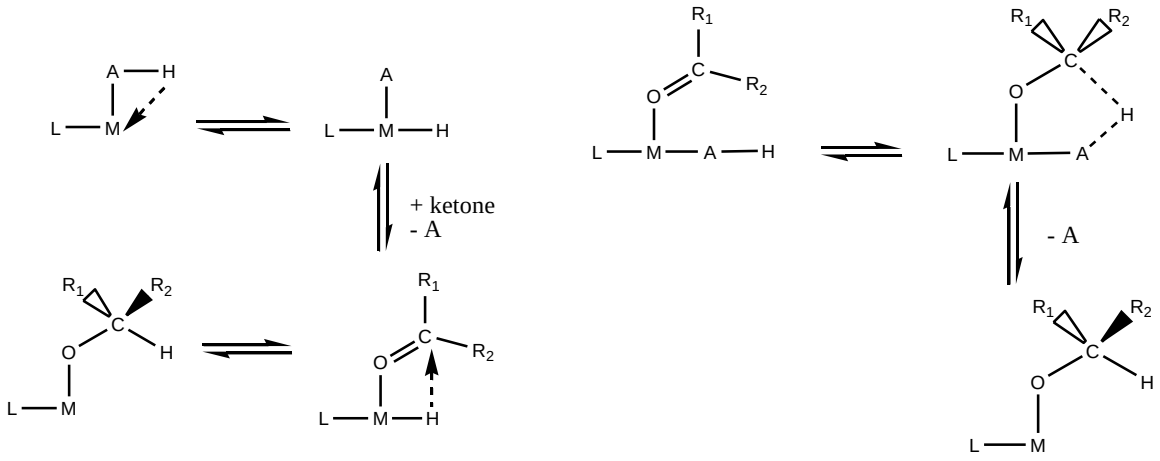

"hydridic route"

(a)

"direct hydrogen transfer"

(b)

Scheme 4.1 Possible paths for the hydrogen-transfer reactions. M = metal; L = ligand; A = hydrogen-donor.

The *"hydridic route"* involves the formation of a metal hydride intermediate by interaction of the catalyst with the hydrogen donor, followed by hydride transfer from the metal to the substrate (Scheme 4.1 (a)).[10] The "*direct hydrogen transfer*" implies that hydrogen is transferred to the substrate in a concerted process where both the H-donor and the H-acceptor are held together in close proximity by the catalyst (Scheme 4.1 (b)).

In particular, the hydrogen transfer activity of Ir complexes is well established.[11] Moreover, the introduction of N-heterocyclic carbene ligands (NHC) greatly improves the catalytic

performances of different iridium complexes. As, we have previously mentioned, indeed, NHCs impart high thermal robustness and stability to the organometallic intermediates during multi-turnover catalysis.[12] An example of a transfer hydrogenation catalysis by an Ir-NHC complex is reported in Scheme 4.2.

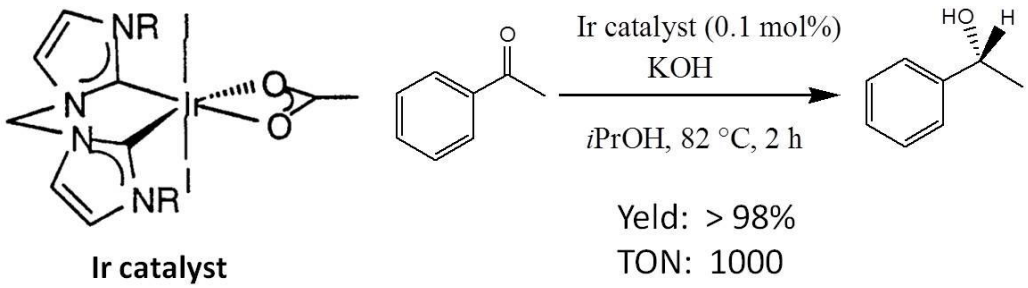

Scheme 4.2 Catalytic transfer Hydrogenation of acetophenone catalyzed by a chelated Iridium(III) bis-NHC complex (R = *i*Pr); conditions: 0.2 M substrate solution, molar ratio catalyst/base 1:5. Product yields determined by ^{1}H NMR.[11(i)]

A polymer-supported, carbon dioxide protected Ir(I)-NHC complex, was also successfully used to promote hydrogen transfer from isopropanol to benzaldehyde.[13]

Finally, the presence of a strong base and an appropriate activation procedure are required to achieve a high catalytic activity; the addition of a base, however, often may hamper the hydrogenation of base-sensitive ketones and aldehydes. New catalytic strategies are thus expected to address this issue.

In the following paragraphs, our strategy, based on the synthesis of molecular hybrid POM-appended NHC iridium complex will be described, together with its application in TH catalysis.

4.2 Results and discussion

As we have seen in the *Introduction* part of this chapter, the design of novel ligands for transition metals is a major goal in catalysis, to obtain better performances in terms of yields, selectivities and sustainability of the reaction. Molecular hybrids are of particular interest in catalysis, due to the interplay of joint organic-inorganic domains with very diverse functional environments. Such hybrid up-grade of the catalytic system can be readily accessed, through the covalent functionalization of molecular polyoxometalates.[4,14]

4.2.1 Synthesis of a POM-appended N-heterocyclic carbene (NHC) iridium complex

We present herein the synthesis, characterization, and catalytic applications of a POM-appended N-heterocyclic carbene (NHC) iridium complex and its activity in catalyzing hydrogen transfer reactions.

To this end, imidazolium moieties have been successfully grafted on the defect site of the divacant Keggin polyanion $[\gamma\text{-}SiW_{10}O_{36}]^{8-}$.

In particular the synthesis of the complex has been achieved by two steps:

(i) synthesis of an iridium organometallic complex containing an unsaturated heterocycle with a trialkoxysilyl substituent on the nitrogen atom in position 3;

(ii) grafting of the iridium organometallic complex on the polyanionic scaffold $[\gamma\text{-}SiW_{10}O_{36}]^{8-}$.

The synthetic strategy is described in the next paragraphs.

4.2.1.1 Synthesis of [(1,2,5,6-*η*)-1,5-cyclooctadiene][1-butyl-3-(3-triethoxysilylpropyl)-imidazol-2-ylidene]chloroiridium *((NHC)Ir)*

First, a monomeric imidazolium derivative has been prepared following a procedure, optimized in our research group, depicted in Scheme 4.3.[4]

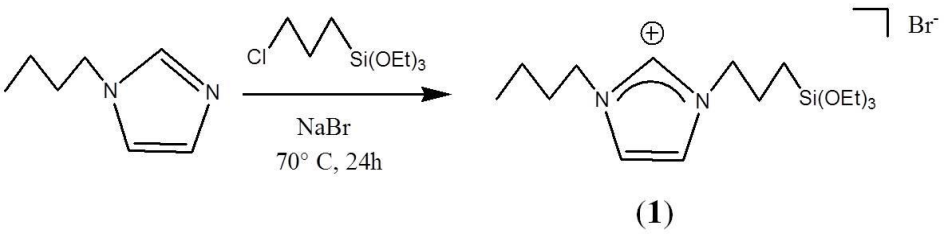

(1)

Scheme 4.3

The trialkoxysilyl-tagged unsaturated heterocycle containing a less hindered *n*-butyl substituent at the nitrogen atom (**1**), was synthesized under strictly anhydrous conditions, from (3-chloropropyl)-triethoxysilane and 1-butylimidazole. The ligand was characterized by ^{1}H NMR and ESI-MS analyses. Both techniques gave results in agreement with the expected structure.[3]

Afterwards, the intermediate (**1**) was reacted with Ag_2O (*"silver-route"*), and the reaction was followed by transmetallation with $[Ir(COD)Cl]_2$, to afford the (NHC)Ir complex [(1,2,5,6-η)-1,5-cyclooctadiene][1-butyl-3-(3-triethoxysilylpropyl)-imidazol-2-ylidene]chloroiridium (**2**), with 78% yield (Scheme 4.4).[15]

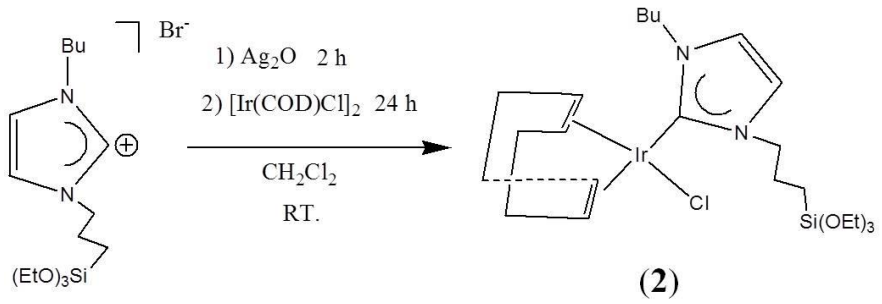

Scheme 4.4

Complex (**2**) was characterized by ^{1}H NMR and ^{13}C NMR analyses. In the ^{1}H NMR spectrum, the signal of the proton at position 2 of the imidazolium ring (δ = 10.6 ppm) disappeared, thus suggesting the formation of the carbene (see Figure 4.4 for a comparison between the spectrum of the product (**2**) and of the starting material (**1**)).

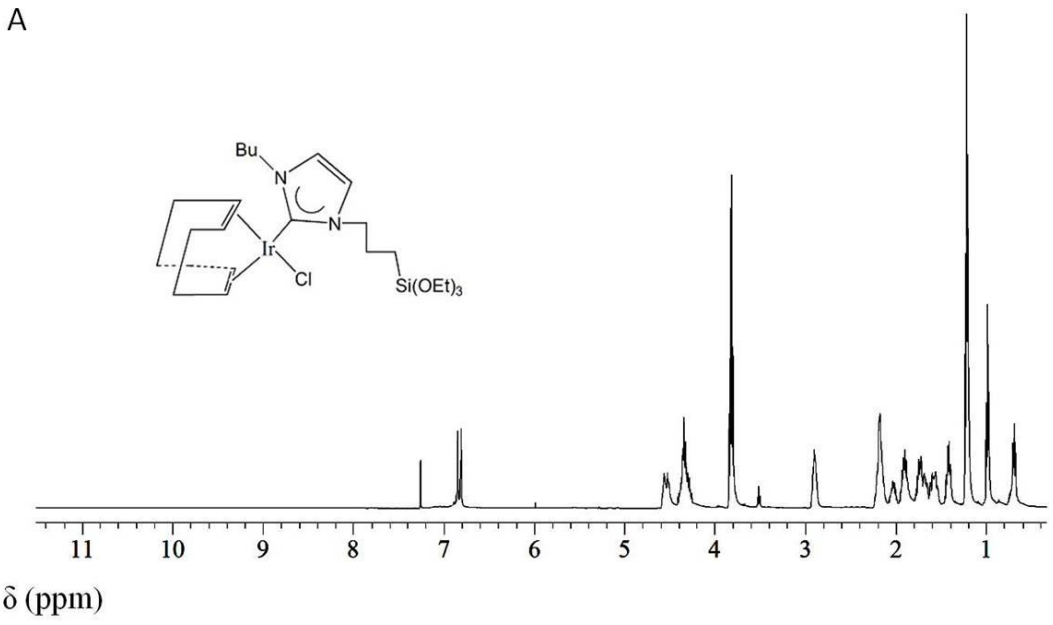

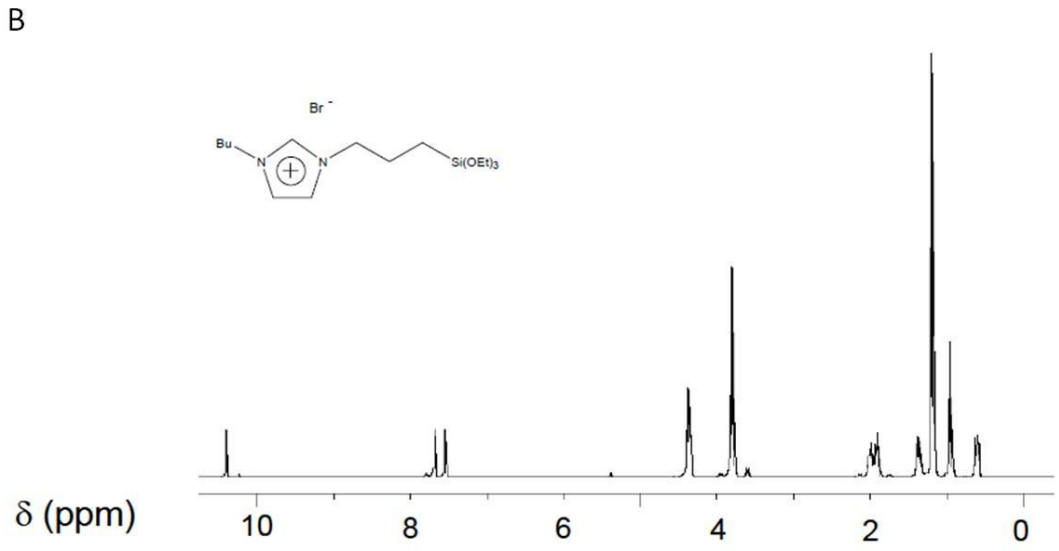

Figure 4.4 ^{1}H NMR of the complex (**2**) (**A**) and of the starting material (**1**) (**B**) in $CDCl_3$.

^{13}C NMR of the complex (**2**) reveals the presence of a weak signal at 178.70 ppm, as expected for the resonance of **C**(-Ir), and confirms the formation of the complex (Figure 4.5).

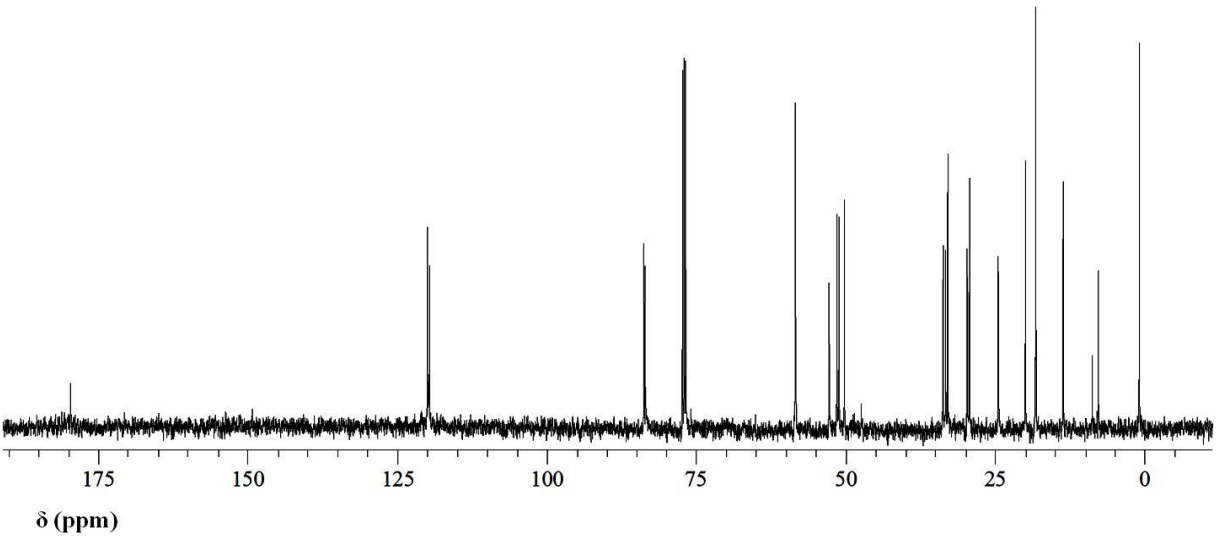

Figure 4.5 ^{13}C NMR of the complex (**2**) in $CDCl_3$.

Moreover, a single ^{29}Si NMR signal at - 48.2 ppm is indicative of a pure product. The ESI-MS (positive mode) analysis confirms the formation of the desired iridium complex, bearing

NHC and cyclooctadiene (COD) as ligands, showing signals centered at m/z = 628.9 and 670.6, corresponding to $[(C_8H_{12})\{C_{10}H_{17}N_2Si(OEt)_3\}Ir]^+$ and $[(C_8H_{12})\{C_{10}H_{17}N_2(OEt)\}Ir(CH_3CN)]^+$, respectively (Appendix; A35). Attempts to crystallize the complex (**2**) are still in progress.

4.2.1.2 Synthesis of $(n\mathbf{Bu_4N})_4[\{ClIr(C_8H_{12})(C_{10}H_{17}N_2Si)\}_2O(\gamma\text{-}SiW_{10}O_{36})]$ *((NHC)Ir-SiW$_{10}$)*

The synthetic route to obtain the Keggin-type hybrid **(NHC)Ir-SiW$_{10}$** involves the reaction of the iridium organosilane complex (**2**) with the nucleophilic oxygen atoms that border a defect site on the divacant Keggin POM $[\gamma\text{-}SiW_{10}O_{36}]^{8-}$ (see *Chapter 2*: paragraph 2.1.1.1). As already described for the complex **APTES-SiW$_{10}$** (*Chapter 2*, paragraph 2.2.2.1), the bis-substitution of the divacant POM yields hybrids with two surface-anchored organosilyl (RSi-) groups, each one linked to two oxygen atoms of two edge-shared WO_6 octahedra. Grafting occurs in acetonitrile, in which nBu$_4$NBr promotes the solubilization of the POM by counterion metathesis (Scheme 4.5), leading to the functionalized hybrid POM $(n\text{Bu}_4\text{N})_4[\{ClIr(C_8H_{12})(C_{10}H_{17}N_2Si)\}_2O(\gamma\text{-}SiW_{10}O_{36})]$ (**3**) in 54% yield.

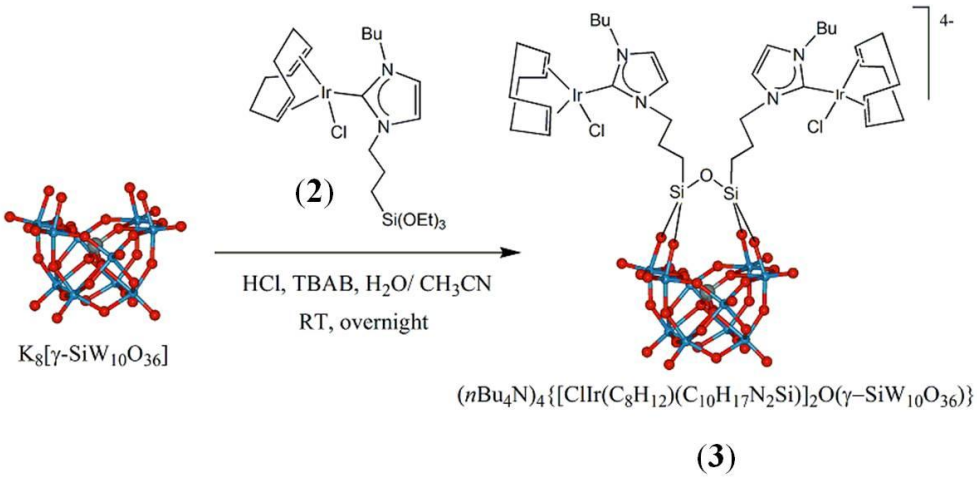

Scheme 4.5 Synthetic routes to Keggin-type decatungstate functionalized with the (NHC)Ir complex (**3**).

The product was characterized both in the solid state (by FT-IR spectroscopy and CHN elemental analysis) and in solution (^{1}H, ^{13}C, ^{29}Si and ^{183}W NMR, ESI-MS and cyclic voltammetry).[16] The ^{183}W NMR spectrum shows three resonances at -107.4, -135.8, and -142.1 ppm in 2:1:2 ratio, in agreement with a C_{2v} symmetry of the product. The ^{29}Si NMR

spectrum reveals two signals at -62.8 (organosilane resonance) and -88.4 (silicotungstate resonance) ppm with integration ratio 2:1.

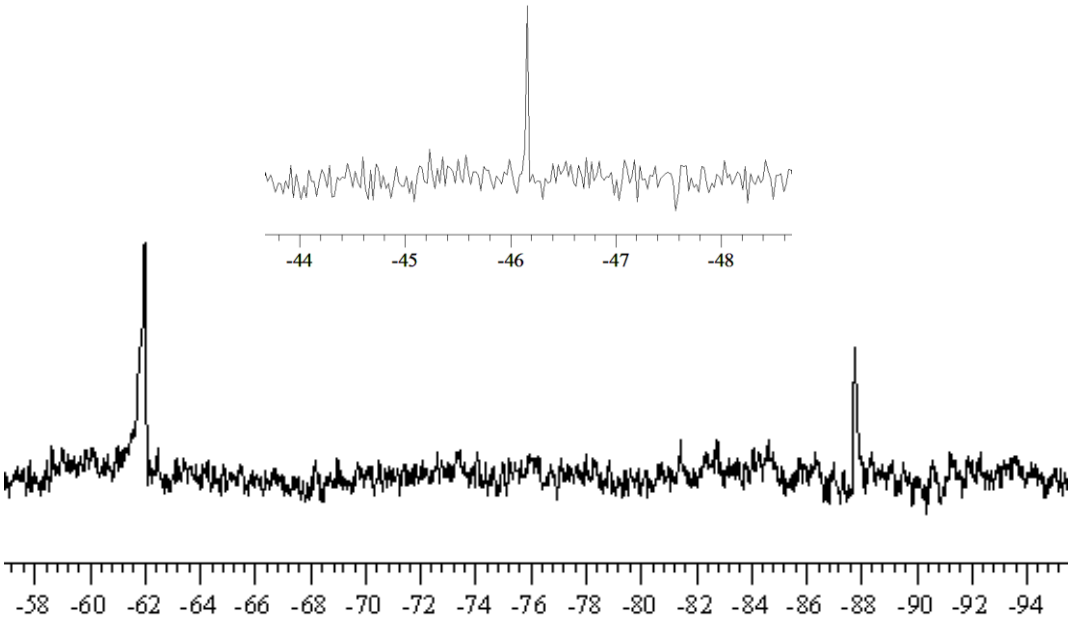

Figure 4.6 ^{29}Si NMR (79.5 MHz, 25°C) of (**3**) in CD_3CN and of (**2**) in $CHCl_3$ (inset).

These results are consistent with a double substitution of the POM surface, while a 16.6 ppm upfield shift can be observed for the organosilicon signal after grafting (Figure 4.6).

The FT-IR spectroscopy is also in agreement with the expected bis-functionalization, as shown by the RSi-O vibrational band at 1102 cm^{-1} and by the diagnostic spectral pattern due to W-O bonds vibrations, observed between 1000 and 700 cm^{-1}.

ESI-MS spectrum of (**3**), registered in negative mode, shows a dominant cluster centred at *m*/*z* = 1723, ascribable to $[\{(C_8H_{12})Ir(C_{10}H_{17}N_2Si)\}_2O(\gamma\text{-}SiW_{10}O_{36})]^{2-}$ (Figure 4.7).

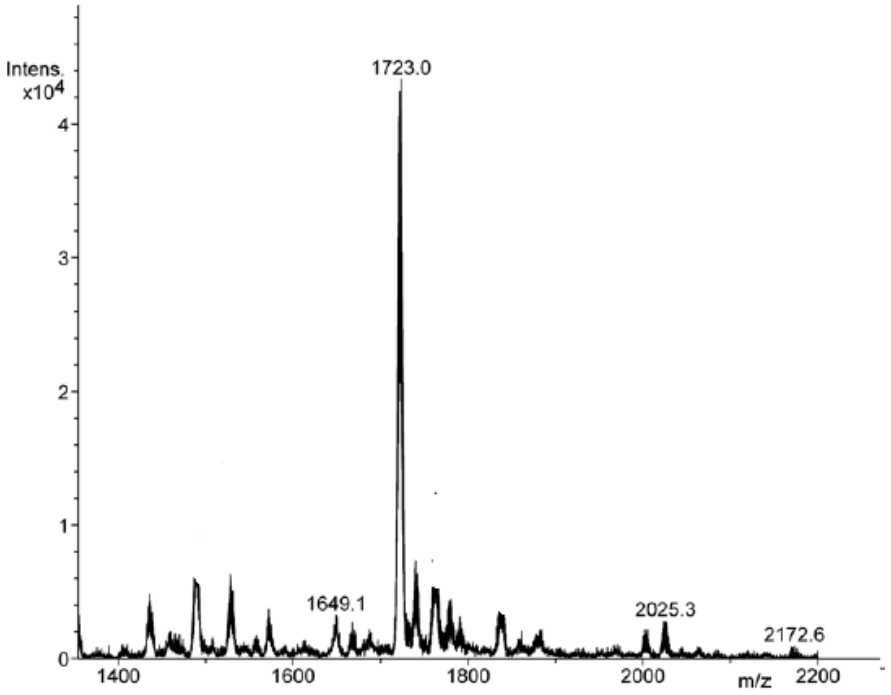

Figure 4.7 ESI-MS of (**3**) in CH_3CN (negative mode).

Finally, the cyclic voltammetry measurements rule out the occurrence of any undesired reduction pathway during the anchoring process; the $Ir^{(I)}$ center show a good stability upon attachment on the polyoxometalate, and present an irreversible anodic wave at 0.64 V (vs Ag/AgCl). In comparison to the POM-free complex (**2**), the oxidation of the complex is anticipated by 0.07 V. Furthermore, the cathodic scan in CH_3CN is dominated by a quasi reversible wave at $E_{1/2}$=0.76 V (vs Ag/AgCl), due to the formation of $Ir^{(0)}$, that occurs at less negative potential than the $W^{(VI)}$ reduction (Appendix; A24, A25).

4.2.1.3 Transfer hydrogenation (TH) activity

A catalytic screening has been performed with the catalyst (**3**) to test the activity of the (NHC)Ir complex in the hydrogen transfer reaction. The reduction of benzophenone to diphenyl methanol in *i*PrOH was used as a model reaction for probing the catalytic activity of the Iridium(I) complex (Scheme 4.6 and Table 4.1).

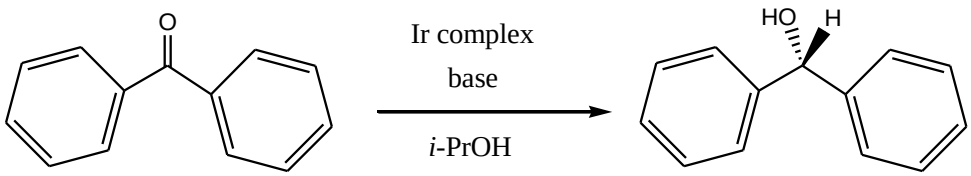

Scheme 4.6 Hydrogen transfer reaction of benzophenone.

Catalyst manipulation does not need particular precautions, and transfer hydrogenations were generally performed in air. Product conversion was monitored by ^{1}H NMR: the results are collected in Table 4.1.

In a typical reaction, the active catalyst was formed by heating a mixture of catalyst in alkaline *i*PrOH for 10 min prior to substrate addition. The base KOH was added from a concentrated aqueous solution. The complex [Ir(COD)Cl(NHC)] (**4**) has been used as a reference.[15] This is inactive in the absence of a base, while 90% conversion, in 2 h, can be achieved in the presence of KOH (entry 1). The parent $[\gamma\text{-}SiW_{10}O_{36}]^{8-}$ (**SiW_{10}**) is essentially inactive (entry 2). Combining the reference complex with the vacant POM did not affect catalytic activity of (**4**) (entry 3). Under analogue conditions, the compound (**3**) is active, but less than (**4**) (entry 4). (**3**) is also inactive in the absence of KOH (entry 5). To improve the solubility of (**3**) under the catalytic conditions, we performed a reaction with a minimum amount of DMF (entry 6), but the DMF appear to be detrimental for the catalysis.[17] Identical conversions were obtained in a comparative experiment using *t*BuOK dissolved in *i*PrOH, to avoid the addition of water (entries 7, 8). The use of *t*BuOK as base gave full conversion after 120 min (entry 7). This base is also expected to improve POM hydrolytic stability. Lowering the Ir-POM concentration from 1 mol% to 0.1 mol% still provided 70% conversion after 5h (entry 8). On the contrary, the use of $n\text{Bu}_4\text{NOH}$ substantially lowered the activity (entry 9).

Table 4.1 TH reactions obtained with Ir(I) complexes.

Entry	pre-catalyst	Base	Conv. (10 min)	Conv. (2 h)	Conv. (5 h)
1	(**4**)	KOH	40	90	
2	**SiW_{10}**	-	0.1	1.6	
3	(**4**) + **SiW_{10}**	KOH	33	87	
4	(**3**)	KOH	16	57	
5	(**3**)	-	0	0	
6[a]	(**3**)	KOH	1.7	13	
7	(**3**)	*t*BuOK	60 (30‘)	99	
8[b]	(**3**)	*t*BuOK		45	70
9	(**3**)	*n*Bu_4NOH		14	23

[a] with DMF; [b] 0.1% catalyst loading.

Finally, Figure 4.8 compares the activity over time during hydrogenation of benzophenone with the POM-based catalyst in presence of different bases.

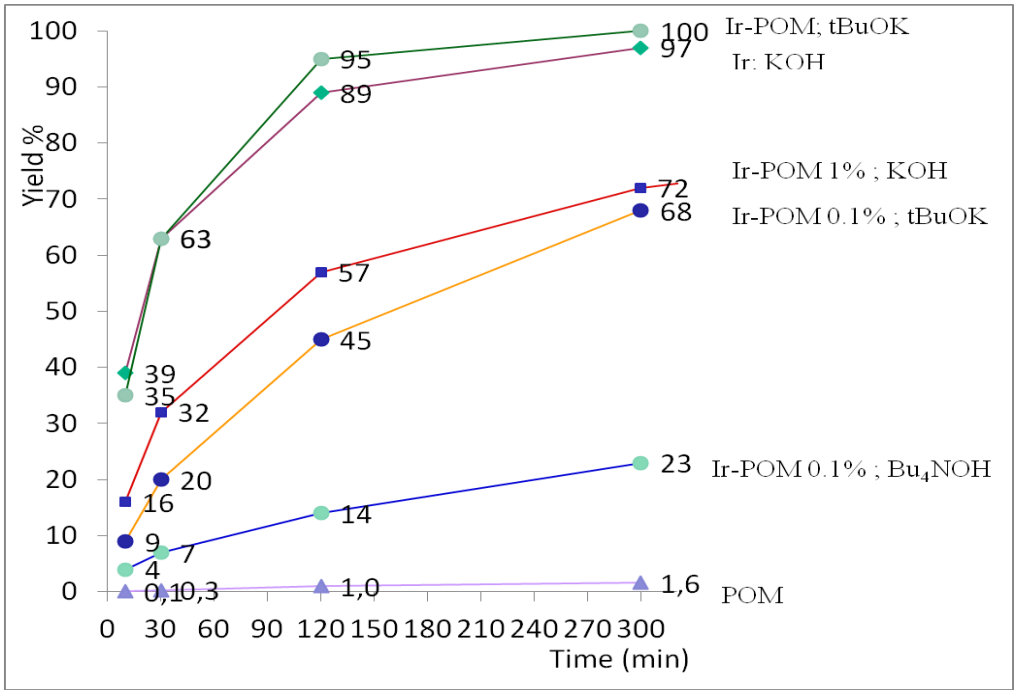

Figure 4.8 Kinetic behaviour for some of the TH reported in table 4.1.

4.3 Conclusion and future perspectives

In summary, we have described a novel POM-supported $Ir^{(I)}$ catalyst, capable of TH to carbonyls. A preliminary optimization has demonstrated that we can tune the activity of the supported catalyst up to the level of the unsupported one. In particular, the interplay of the Ir binding domains with the inorganic POM scaffold provides new opportunities to access multi-turnover catalysis while preserving good performance. Recovery strategies for the catalyst will thus be implemented.

The covalent functionalization of POM vacant sites with other M-NHC complexes will be also evaluated (e.g. Ru-NHC)

4.4 References and notes

[1] I. Bar-Nahum, H. Cohen and R. Neumann, *Inorg. Chem.* **2003**, *42*, 3677.

[2] a) I. Bar-Nahum and R. Neumann, *Chem. Commun*. **2003**, 2690.

[3] S. Berardi, M. Carraro, M. Iglesias, A. Sartorel, G. Scorrano, M. Albrecht and M. Bonchio, *Chem. Eur. J.* **2010**, *16*, 10662.

[4] S. Berardi, M. Bonchio, M. Carraro, V. Conte, A. Sartorel, G. Scorrano, *J. Org. Chem.*, **2007**, *72*, 8954.

[5] a) W. A. Herrmann *Angew. Chem. Int. Ed.* **2002**, *41*, 1290; b) O. Schuster, L. Yang, H. G. Raubenheimer, M. Albrecht *Chem. Rev.* **2009**, *109*, 3445; c) S. Nolan, in *N-Heterocyclic Carbenes in Synthesis*, Wiley-VCH Verlag GmbH & Co. KGaA, Weinheim, Federal Republic of Germany, **2006**; d) D. Bourissou, O. Guerret, F. P. Gabbaï, G. Bertrand *Chem. Rev.* **2000**, *100*, 39; e) K. J. Cavell, D. S. McGuinness *Coord. Chem. Rev.* **2004**, *248*, 671.

[6] a) O. Navarro, N. Marion, J. Mei, S. P. Nolan *Chem. Eur. J.* **2006**, *12*, 5142; b) A. J. Arduengo III, R. L. Harlow, M. Kline *J. Am. Chem. Soc.* **1991**, *113*, 361; c) E. A. B. Kantchev, C. J. O'Brien, M. G. Organ *Angew. Chem. Int. Ed.* **2007**, *46*, 2768.

[7] M.-T. Lee, C.-H. Hu *Organometallics* **2004**, *23*, 976.

[8]) J. Huang, H.-J. Schanz, E. D. Stevens, S. P. Nolan *Organometallics* **1999**, *18*, 5375; b) M. Scholl, T. M. Trnka, J. P. Morgan, R. H. Grubbs *Tetrahedron Lett.* **1999**, *40*, 2247; c) M. Heckenroth, E. Kluser, A. Neels, M. Albrecht *Angew. Chem. Int. Ed.* **2007**, *46*, 6293.

[9] Gonell, S.; Poyatos, M.; Mata, J. A.; Peris, E. *Organometallics* **2012**, *31*, 5606.

[10] a) G. Zassinovich, G. Mestroni *Chem. Rev.* **1992**, *92*, 1051; b) J. S. M. **S**amec, J.-E. Backvall, P. G. Andersson, P. Brandt, *Chem. Soc. Rev.* **2006**, *35*, 237; c) R. Corberan, E. Peris *Organometallics* **2008**, *27*, 1954.

[11] a) S. H. Oakley, M. P. Coogan, R J. Arthur *Organometallics* **2007**, *26*, 2285; b) A. Azua, J. A. Mata, E. Peris *Organometallics* **2011**, *30*, 5532; c) X. Wu, X. Li, A. Zanotti-Gerosa, A. Pettman, J. Liu, A. James Mills, J. Xiao *Chem. Eur. J.* **2008**, *14*, 2209; d) R. ter Halle, A. Bréhéret, E. Schulz, C. Pinel, M. Lemaire *Tetrahedron: Asymm.* **1997**, *8*, 2101; e) T. Abura, S. Ogo, Y. Watanabe, S. Fukuzumi *J. Am. Chem. Soc.* **2003**, *125*, 4149; f) X. Wu, J. Liu, X. Li, A. Zanotti-Gerosa, F. Hancock, D. Vinci, J. Ruan, J. Xiao *Angew. Chem. Int. Ed.* **2006**, *45*, 6718; g) F. E. Hahn, C. Holtgrewe, T. Pape, M. Martin, E. Sola, L. A. Oro *Organometallics* **2005,** *24*, 2203; h) J. R. Miecznikowski, R. H. Crabtree *Organometallics* **2004,** *23*, 629; i) M. Albrecht, J. R. Miecznikowski, A. Samuel, J. W. Faller, R. H. Crabtree *Organometallics* **2002**, *21*, 3596; l) W. He, B.-L. Zhang, R. Jiang, P. Liu, X.-L. Suna, S.-Y. Zhanga *Tetrahedron Lett.* **2006**, *47*, 5367; m) X. Gong, H. Zhang, X. Li, *Tetrahedron Lett.* **2011**, *52*, 5596.

[12] a) G. Mestroni, G. Zassinovich, G, A. Camus, F.J. Martinelli *Organomet. Chem.***1980**, *198*, 87; b) S. J. M.. Nordin, P. Roth, T. Tarnai, D. A. Alonso, P. Brandt, P. G. Andersson *Chem. Eur. J.* **2001**, *7*, 1431; c) P. Dani, T. Karlen, R. A. Gossage, S. Gladiali, G. van Koten *Angew. Chem. Int. Ed.* **2000**, *39*, 743; d) A. C. Hillier, H.M. Lee, E. D. Stevens, S. P. Nolan *Organometallics* **2001**, *20*, 4246.

[13] G. M. Pawara, M. R. Buchmeisera, *Adv. Synth. Catal.* **2010**, *352*, 917.

[14] a) M. T. Pope, A. Müller, in *Heteropoly and Isopoly Oxometalates*, Springer Verlag, New York, **1983**; b) M. T. Pope, A. Müller *Angew. Chem. Int. Ed.* **1991**, *30*, 34; c) C. L. Hill *Polyoxometalates*, *Chem. Rev.* (Special Issue) **1998**, *98*, 1. d) M. Carraro, A. Sartorel, G. Scorrano, C. Maccato, M. H. Dickman, U. Kortz, M. Bonchio *Angew. Chem. Int. Ed.* **2008**, *47*, 7275. e) M. Carraro, L. Sandei, A.

Sartorel, G. Scorrano, M. Bonchio, *Org. Lett.* **2006**, *8*, 3671; f) M. Carraro, G. Modugno, A. Sartorel G. Scorrano, M. Bonchio *Eur. J. Inorg. Chem.* **2009**, 5164.

[15] A. R. Chianese , X. Li , M. C. Janzen , J. W. Faller , and R. H. Crabtree *Organometallics* **2003,** *22,* 1663.

[16] A different synthetic approach consisting in the covalent attachment of the trialkoxysilyl-tagged imidazolium precursor (**1**) to the divacant decatungstosilicate, followed by transmetalation with the iridium complex, through the silver route, has also been investigated. However, no transmetalation occurred using Ag_2O: the inorganic polyanionic domain may indeed electrostatically interact with Ag^+, as well as with the imidazolyl moieties, thus reducing its availability for the reaction.

[17] We estimated that about 50% of the Ir-functionalized POM is soluble in *i*PrOH

Chapter 5

Experimental section

5.1 General remarks

5.1.1 Solvents and chemicals

All commercially available reagents and solvents were used as received, without further purification.

MilliQ-deionized water (Millipore) was used as solvent for the reactions and for spectrometric measurements.

Sigma-Aldrich: ethylic ether, hexane, pentane, tetrahydrofuran, methanol, ethanol, chloroform, dichloromethane, acetonitile, deuterated chloroform, deuterated acetonitrile, D_2O; Fluka: anhydrous dichloromethane, anhydrous ethylic ether; Prolabo: acetonitrile, 2-propanol, N,N-dimethylformamide, dichloromethane, P_2O_5; Lab Scan: dimethylsulfoxide.

Sigma-Aldrich: sodium tungstate dihydrate, KBr, KCl, K_2CO_3, Na_2SiO_3, *(R)*-(−)-1-aminoethylphosphonic acid, *(S)*-(+)-1-aminoethylphosphonic, tetrabutylammonium bromide, tetramethylammonium bromide, sulfonic acid, pyrene, dansyl chloride, fluorescein isothiocyanate, biotin, 1-hydroxy-1,2,3-benzotriazole (HOBt), N,N'-dicyclohexylcarbodiimide (DCC), N-hydroxysuccinimide (NHS), acetophenone, silver oxide, HABA/avidin reagent; Fluka: 1-methylimidazole; Prolabo: $MgSO_4$, NaOH; Acros Organics: 1-ethyl-3-(3-dimethylaminopropyl)carbodimmide (EDC); Carlo Erba: HCl 37%, HNO_3 65%, Na_2CO_3, $KHCO_3$, triethylamine; Merck: celite.

$K_8[\gamma\text{-}SiW_{10}O_{36}]$,[1] $\beta\text{-A-}Na_8[HPW_9O_{34}]*24H_2O$,[2] 3-(dansylamido) propyl triethoxysilane,[3] pyrene-1-sulfonyl-chloride,[4] triethoxysilyl-functionalized 4,5-dihydro-imidazolium bromide,[5] $[Ir(COD)Cl]_2$ and [Ir(COD)Cl(NHC)][6] were prepared as described in the literature.

HEK-293 cell culture was maintained in Dulbecco's modified Eagle' s medium (DMEM, Sigma–Aldrich) containing glucose (4500 mgL^{-1}), l-glutamine (5 mM), sodium pyruvate (1 mM) and sodium bicarbonate (1 mM), supplemented with heat-inactivated FCS (foetal calf serum, 10%, Sigma–Aldrich) in a humidified atmosphere (5% CO_2) at 37 °C.

5.1.2 Instruments and apparatus

^1H NMR spectra have been recorded with Bruker AV300 instruments operating at 300.13 MHz; for protonic spectra, the following symbolism has been used: s: singlet; d: doublet; t: triplet; q: quartet; m: multiplet. ^{13}C NMR spectra have been recorded with Bruker AV300 operating at 75.4 MHz; $Si(CH_3)_4$ was used as reference. ^{183}W NMR and ^{29}Si NMR spectra have been recorded with a Bruker Avance DRX 400 instrument operating at 16.67 MHz and 79.50 MHz, respectively, using 2M Na_2WO_4 in D_2O and $Si(CH_3)_4$ in $CDCl_3$ as external

references; ^{31}P NMR spectra were recorded with a Bruker Avance DRX 300 spectrometer operating at 121.49 MHz with H_3PO_4 85% as external reference. FT-IR (KBr) spectra were collected on a Thermo Quest Nicolet 5700 instrument. For FT-IR spectra the following symbolism has been used: w: weak signal; s: strong signal; b: broad band signal. ESI-MS spectra have been obtained with a Agilent LC/MSD Trap SL spectrometer, by using a capillary potential of 1500V. UV-Vis spectra were recorded with Lambda 45 Perkin-Elmer and Cary 5000 Varian spectrophotometers (the spectra were collected in the range 200-800 nm using a 1 cm quartz cell). Molar extinction coefficients ε are expressed in M^{-1} x cm^{-1}. Fluorimetric analysis have been performed on a Perkin Elmer LS50B instrument 1 cm quartz cell. Circular dichroism (CD) spectra were recorded with a Jasco J-715 polarimeter with 1 cm UV quartz cells. Dynamic light scattering (DLS) was performed on a Malvern Zetasizer Nano-S instrument. Field emission-scanning electron microscopy (FESEM) measurements were carried out at acceleration voltages between 5 and 20 kV by means of a Zeiss SUPRA 40VP instrument. Transmission Electronic Microscopy (TEM) measurements were obtained using a FEI Tecnai G2 transmission electron microscope at Biology Department, University of Padova. Cyclic voltammograms were recorded with a BAS (Bio Analytical Systems) Epsilon workstation at scan rates of 200 mV s^{-1} in a conventional electrochemical cell containing a three-electrode system; experiments were performed in CH_3CN (0.1 M $n$$Bu_4ClO_4$), using a Ag/AgCl reference. Elemental Analysis were performed at Microanalysis Laboratory of Chemical Science Department, University of Padova. Thin Layer Cromatography (TLC) were performed using DC *Fertigplatten-Durasil-25* UV_{254} sheets (Machery-Nagel). Chromatography Column purifications were performed on gravity column using Sigma Aldrich silica gel, mesh grade 10184, granulometry 70-230 mesh, 100 Angstrom. pH meter: pH lab 827, Metroohm – Swiss.

The imaging microscopy experiments and biological analysis were performed at Center for Biomedical Science and Engineering, University of Nova Gorica: HEK cells were plated in glass bottom optical imaging petri dishes and exposed to different compounds for the indicated time; samples were analyzed using a Axiovert Zeiss microscope with the following filter sets: EX BP 470/40, BS FT 495, EM BP 525/50 for the analysis of POMs: FITC-SiW_{10}, FITC-PW_9 and of the ligand FITC-AEPA; EX G 365, BS FT 395, EM BP 445/50 for the analysis of POMs: Dans-SiW_{10}, Pyr-SiW_{10} and for the detection of nuclear probe Hoechst 333423 (Invitrogen). For mitochondrial staining, cells were incubated for 15 min with MitoTracker probe (Molecular Probes, 250 nM) and observed with following filter set: EX BP 587/25, BS FT 605, EM BP 647/70. Images were acquired simultaneously using a 10x and

40x oil-immersion objective in transmitted light and fluorescence mode with the Axiovision software (Zeiss). For proliferation tests, after exposure with different compounds, cells were washed and incubated with Cell Proliferation Reagent WST-1 (Roche), following manufacturer instructions, and absorbance was measured at different time points during an interval of 6 h. For citotoxicity, cells were incubated for Thiazolyl Blue Tetrazolium Bromide (MTT, 0.025mg/ml Sigma) for 1.5 h at the cell incubator. Reaction was blocked with DMSO and absorbance was analysed with a Tecan Infinite Reader at 560 nm.

5.2 Synthesis and characterization

5.2.1 Synthesis of hybrid POMs

Synthesis of (nBu$_4$N)$_4$[(NH$_2$(CH$_2$)$_3$Si)$_2$O(γ-SiW$_{10}$O$_{36}$)] *(APTES-SiW$_{10}$)*

600 mg (0.20 mmol) of $K_8[\gamma\text{-}SiW_{10}O_{36}]$ were suspended in 10 mL of a mixture CH_3CN/H_2O 10:1, and 262 mg (0.80 mmol, 4 equiv.) of nBu$_4$NBr, were added. Then 95 µl (0.40 mmol, 2 equiv.) of 3 amminopropyl triethoxysilane and 293 µL (6 equiv.) of HCl 4M were added in rapid sequence. Upon addition of acid, immediate clearing of the solution was observed. The mixture was kept under vigorous stirring overnight at r.t., then filtered to remove the insoluble material. The mixture was concentrated to about 1 mL volume, and the product was precipitated by adding deionized water (20 mL). The product was collected by filtration, in a fritted funnel, washed with portions of deionized water and diethyl ether, and dried in vacuo. 257 mg (76.5 µmol) of 2 were obtained (38% yield).

FT-IR (KBr): ν= 2964 (m), 2932 (m), 2872 (m), 1626 (m, b), 1485 (m), 1381 (w), 1105 (m), 1043 (m, b), 965 (m), 904 (s), 874 (s), 823 (s), 792 (s), 740 (s, b) cm^{-1}. ^{1}H NMR: δ_H (300.13 MHz, CD_3CN, 301 K) 0.70 (m, 4H, N(CH$_2$)$_2$C*H$_2$*Si), 0.99 (t, 48 H, (C*H$_3$*CH$_2$CH$_2$CH$_2$)$_4$N); 1.39 (m, 32 H, (CH$_3$C*H$_2$*CH$_2$CH$_2$)$_4$N), 1.62 (m, 32 H, (CH$_3$CH$_2$C*H$_2$*CH$_2$)$_4$N), 1.86 (m, 4H, N CH$_2$C*H$_2$*CH$_2$Si), 3.18 (t, 32 H, (CH$_3$CH$_2$CH$_2$C*H$_2$*)$_4$N), 3.50 (m, 4H, NC*H$_2$*CH$_2$CH$_2$Si), 7.39 (m, broad, 4 H, *H$_2$*N(CH$_2$)$_3$Si). ^{13}C NMR: δ_C (75.47 MHz, CD3CN, 301 K) 58.97 (16C, (CH$_2$CH$_2$CH$_2$*C*H$_2$)$_4$N), 38.03 (2C, SiCH$_2$CH$_2$*C*H$_2$N), 29.02 (2C, SiCH$_2$*C*H$_2$CH$_2$N), 24.10 (16C, (CH$_2$CH$_2$*C*H$_2$CH$_2$)$_4$N), 20.04 (16C, (CH$_2$*C*H$_2$CH$_2$CH$_2$)4N), 15.13 (Si*C*H$_2$CH$_2$CH$_2$N), 13.64 (16C, (*C*H$_2$CH$_2$CH$_2$CH$_2$)$_4$N). ^{29}Si NMR (79.49 MHz, CD_3CN/CH_3CN, 298 K): δ = –62.45 (2 Si), –88.36 (1 Si) ppm.^{183} W NMR (16.67 MHz, CD_3CN/CH_3CN, 298 K): δ = –107.8 (4 W), –135.3 (2 W), –142.1 (4 W) ppm.

(nBu$_4$N)$_4$[{{(CH$_3$)$_2$N}C$_{10}$H$_6$SO$_2$NH(CH$_2$)$_3$Si}$_2$O(γ-SiW$_{10}$O$_{36}$)] ***(Dans-SiW$_{10}$)***

In a round-bottomed flask, **APTES-SiW$_{10}$** (400 mg, 0.12 mmol) was suspended in acetonitrile (3 mL). Triethylamine (58 μL, 0.42 mmol) was slowly added under vigorous stirring. After 5 min, dansyl chloride (112 mg, 0.415 mmol) was dissolved in acetonitrile (4 mL) and added to the solution whilst stirring. The mixture was heated at 40 °C under reflux for 2.5 h and then centrifuged to remove insoluble reagents and byproducts. The volume of the solution was reduced to 1 mL by evaporation under vacuum, then diethyl ether was added to precipitate the product. The solid was washed with water and diethyl ether on a fritted funnel and dried for several hours under vacuum. Yield: 69% (366 mg, 0.09 mmol). $C_{94}H_{182}N_8O_{41}S_2Si_3W_{10}$ (4067.38): calcd. C 27.75, H 4.51, N 2.75, S 1.58; found C 26.87, H 4.45, N 2.82, S 1.06. FTIR (KBr): ν = 2961 (m), 2938 (m), 2873 (m), 634 (w,b), 1476 (m), 1394 (w), 1316 (w), 1146 (m), 1102 (m), 1043 (m,b), 967 (m), 906 (s), 885 (s), 821 (s), 792 (s), 741 (s, m), 684 (m), 625 (m), 569 (m), 544 (m), 508 (m) cm^{-1}. ^{1}H NMR (300 MHz, CD_3CN, 301 K): δ = 0.24 (m, 4 H, $NCH_2CH_2CH_2Si$), 0.97 [t, ^3J = 8.7 Hz, 48 H, $N(CH_2CH_2CH_2CH3)_4$], 1.31 [m, 36 H, $N(CH_2CH_2CH_2CH_3)_4$ and $SiCH_2CH_2CH_2N$], 1.62 [m, 32 H, $N(CH_2CH_2CH_2CH_3)_4$], 2.84 [m, 16 H, $N(CH3)_2$ and $SiCH_2CH_2CH_2N$], 3.14 [m, 32 H, $N(CH_2CH_2CH_2CH_3)_4$], 5.95 (t, ^3J = 6.0 Hz, 2 H, $NHCH_2CH_2CH_2Si$), 7.22 (m, 2 H, Ar-H), 7.58 (m, 4 H, Ar-H), 8.16 (m, 2 H, Ar-H), 8.30 (d, ^3J = 8.7 Hz, 2 H, Ar-H), 8.48 (d, ^3J = 8.4 Hz, 2 H, Ar-H) ppm. ^{13}C{1H} NMR (75.47 MHz, CD_3CN, 301 K): δ = 13.01 (2 C, $SiCH_2CH_2CH_2N$), 14.07 [16 C, $N(CH_2CH_2CH_2CH_3)_4$], 20.47 [16 C, $N(CH_2CH_2CH_2CH_3)_4$], 24.51[16 C, $N(CH_2CH_2CH_2CH_3)_4$], 24.73 (2 C, $SiCH_2CH_2CH_2N$), 45.83 [4 C, $N(CH_3)_2$], 46.83 (2 C, $SiCH_2CH_2CH_2N$), 59.40 [16 C, $N(CH_2CH_2CH_2CH_3)_4$], 124.53, 129.27, 129.99, 130.50, 130.70, 136.82, 152.87 (20 C, Ar) ppm. ^{183} W NMR (16.67 MHz, CD_3CN/CH_3CN, 298 K): δ = –107.9 (4 W), –136.2 (2 W), –142.1 (4 W) ppm. ^{29}Si NMR (79.49 MHz, CD_3CN/CH_3CN, 298 K): δ = –62.5 (2 Si), –88.4 (1 Si) ppm. ESI-MS (–, CH_3CN): calcd. for $[C_{30}H_{36}N_4O_{41}S_2Si_3W_{10}]^{4-}$ 773.3; found 773.9. UV: λ (log ε) = 251 (4.7), 211 (5.1) nm.

Synthesis of (nBu$_4$N)$_4$[{C$_{16}$H$_9$SO$_2$NH(CH$_2$)$_3$Si}$_2$O(γ-SiW$_{10}$O$_{36}$)] ***(Pyr-SiW$_{10}$)***

In a round bottomed flask, **APTES-SiW$_{10}$** (450 mg, 0.14 mmol) was suspended in CH_3CN (3 mL). After stirring for 5 min, triethylamine (49 μl, 0.35 mmol) was slowly added under vigorous stirring. 1-Pyrensulfonyl chloride (105 mg, 0.35 mmol) was dissolved in CH_3CN (6 ml) and added dropwise in solution whilst stirring. The mixture was heated at 50°C under reflux for 3 h and then centrifuged to remove insoluble reagents and byproducts. The volume of the solution was reduced to 1 mL, upon evaporation under vacuum, than diethylether was

added to precipitate the product. The solid was finally washed with diethyl ether (2 times), water (2 times) and a small amount of CH_2Cl_2 (2 times) on a fritted funnel, and dried several hours under vacuum. 410 mg (0.1 mmol) of product were obtained (71% yield).

Elemental analysis: Calcd. for $C_{102}H_{176}N_6O_{41}S_2Si_3W_{10}$ C 29.65 H 4.26; N 2.03; S 1.55; Found: C 28.87; H 3.57; N 1.94; S 1.03. FTIR (KBr): ν = 2961 (m), 2923 (m), 2873 (m), 1483 (m, b), 1385 (m), 1318 (w, b), 1159 (w), 1143 (w), 1132 (w), 1100 (m, b), 964 (m), 949 (m), 902 (s), 885 (s), 839 (s), 819 (s), 742 (s, b), 650 (w) cm^{-1}. ^1H NMR (300 MHz, CD_3CN, 301 K) δ = 0.57 (4H, m, $NCH_2CH_2CH_2Si$), 0.94 [48H, t, $N(CH_2CH_2CH_2CH_3)_4$], 1.27 (4H, m, $NCH_2CH_2CH_2Si$), 1.34 [32H, m, $N(CH_2CH_2CH_2CH_3)_4$], 1.59 [32H, m, $N(CH_2CH_2CH_2CH_3)_4$], 3.09 [32 H, m, $N(CH_2CH_2CH_2CH_3)_4$], 3.54 (4H, m, $NCH_2CH_2CH_2Si$), 6.14 (2H, t, ^3J = 5.6 Hz, $NHCH_2CH_2CH_2Si$), 8.86 - 8.02 (18 H, m, Ar-H), ppm. $^{13}C\{^1H\}$NMR (75.47 MHz, CD_3CN, 301 K): δ = 12.35 (2C, $SiCH_2CH_2CH_2N$), 13.86 [16C, $N(CH_2CH_2CH_2CH_3)_4$], 20.29 [16C, $N(CH_2CH_2CH_2CH_3)_4$] 22.99 (2C, $SiCH_2CH_2CH_2N$), 24.32 [16C, $N(CH_2CH_2CH_2CH_3)_4$], 46.50 (2C, $SiCH_2CH_2CH_2N$), 59.24 [16C, $N(CH_2CH_2CH_2CH_3)_4$], 135.25-124.42 (32 C, Ar-*C*) ppm. ^{29}Si NMR (79.5 MHz, CD_3CN/*d*-DMSO, 25°C): δ = -62.61 (2 Si), -88.34 (1 Si) ppm. ^{183}W NMR (16.7 MHz, CD_3CN, 25°C): -107.51 (4 W), -136.03 (2W), - 141.52 (4 W) ppm. ESI-MS (–, CH_3CN): *m*/*z* = 789.5, 1053.1 expected for $[C_{38}H_{32}N_2O_{41}S_2Si_3W_{10}]^{4-}$ = 789.9; $[C_{38}H_{33}N_2O_{41}S_2Si_3W_{10}]^{3-}$ = 1053.5.

Synthesis of $(n\mathbf{Bu_4N})_4[\{(C_{20}H_{11}O_5)NHCSNH(CH_2)_3Si\}_2O(\gamma\text{-}SiW_{10}O_{36})]$ *(FITC-SiW$_{10}$)*

In a round bottomed flask, **APTES-SiW$_{10}$** (400 mg, 0.12 mmol) was suspended in CH_3CN (7 mL). Triethylamine (42 μl, 0.30 mmol) was slowly added under vigorous stirring. After stirring for 5 min, fluoresceine isothiocyanate (116 mg, 0.30 mmol) was dissolved in CH_3CN (5 ml) and added in solution whilst stirring. The mixture was heated at 50°C under reflux for 3 h and then centrifuged to remove insoluble reagents and byproducts. The volume of the solution was reduced to 1 mL, upon evaporation under vacuum, than diethylether was added to precipitate the product. The solid was finally washed with water (3 times), diethyl ether (3 times), and finally Et_2O/MeOH (5:1, 5 times) on a fritted funnel and dried several hours under vacuum. 276 mg (0.06 mmol) of product were obtained (53% yield).

Elemental analysis: Calcd. for $C_{112}H_{182}N_8O_{47}S_2Si_3W_{10}$ C 30.72; H 4.19; N 2.56; S 1.46; Found: C 28.80; H 3.94; N 2.09; S 1.04. FT-IR (KBr): ν = 2960 (m), 2927 (m), 2872 (m), 1751 (m),1616 (m), 1457 (m), 1107 (w), 966 (m), 888 (s), 820 (s), 778 (s,br), 541 (w) cm^{-1}. ^1H NMR (300 MHz, CD_3CN, 301 K) δ = 9.14-6.56 (fluoresceine protons), 3.32 (4H, $SiCH_2CH_2CH_2N$), 3.14 [32 H, m, $N(CH_2CH_2CH_2CH_3)_4$], 2.14 (4H, $SiCH_2CH_2CH_2N$), 1.63 [32H, m, $N(CH_2CH_2CH_2CH_3)_4$], 1.38 [32 H, m, $N(CH_2CH_2CH_2CH_3)_4$], 0.97 [48 H, m,

$N(CH_2CH_2CH_2C\mathit{H}_3)_4$], 0.76 (4H, $SiC\mathit{H}_2CH_2CH_2N$). $^{13}C\{^1H\}$ NMR (75.47 MHz, CD_3CN, 301 K): δ = 181.78 (2C, C=S), 169.93 (2C, C=O), 160.24, 153.34, 148.63, 142.79, 137.40, 130.23, 127.76, 124.73, 113.39, 111.55, 103.42, 84.25 (fluoresceine carbons), 65.48 (2C, $SiCH_2CH_2\mathit{C}H_2N$), 59.23 [16C, $N(\mathit{C}H_2CH_2CH_2CH_3)_4$], 47.87 (2C, $SiCH_2\mathit{C}H_2CH_2N$), 24.35 [16C, $N(CH_2\mathit{C}H_2CH_2CH_3)_4$], 20.32 [16C, $N(CH_2CH_2\mathit{C}H_2CH_3)_4$], 13.94 [16C, $N(CH_2CH_2CH_2\mathit{C}H_3)_4$], 9.54 (2C, $Si\mathit{C}H_2CH_2CH_2N$). ^{29}Si NMR (79.5 MHz, CD_3CN/[D_6]DMSO, 25°C): δ = -61.34 (2 Si), -88.26 (1 Si) ppm. ^{183}W NMR (16.7 MHz, CD_3CN, 25°C): - 108.32 (4 W), -132.87 (2W), - 143.32 (4 W) ppm. ESI-MS (–, CH_3CN): *m*/*z* = 852.5, expected for $[C_{48}H_{38}N_4O_{47}S_2Si_3W_{10}]^{4-}$ = 852.4; m/*z* = 1217.5, expected for $[C_{64}H_{74}N_5O_{47}S_2Si_3W_{10}]^{4-}$ = 1217.3.

Synthesis of $(n\mathrm{Bu_4N})_3Na_2[((C_{20}H_{11}O_5)NHCSNHCH(CH_3)PO)_2(\alpha\text{-A-}PW_9O_{34})]$ *(FITC-PW_9)*

In a round-bottomed flask, β-A-$Na_8[HPW_9O_{34}]$ (187 mg, 0.06 mmol) was suspended in CH_3CN (3 mL), with $n\mathrm{Bu_4NBr}$ (99 mg, 0.30 mmol). **FITC-AEPA** (70 mg, 0.13 mmol) was dissolved in DMSO (0.4 mL) and added to the solution, followed by the slow addition of HCl (70 µl, 4 M) under vigorous stirring. The mixture was heated at reflux overnight and filtered to remove insoluble reagents and byproducts. The volume of the solution was reduced to 1 mL, upon evaporation under vacuum, than water was added to precipitate the product. The solid was washed with water (3 times), diethyl ether (3 times), and finally Et_2O/MeOH (5:1, 5 times) on a fritted funnel. 112 mg (0.03 mmol) of product were obtained (50% yield).

Elemental analysis: Calcd. for $C_{94}H_{142}Na_2N_7O_{46}P_3S_2W_9$ C 28.48; H 3.61; N 2.47; S 1.62; Found: C 29.63; H 3.07; N 2.32; S 1.12. FTIR (KBr): ν = 2962 (m), 2934 (m), 2873 (m), 1755 (m, b), 1620 (m, b), 1461 (w, b), 1383 (w), 1341 (w), 1258 (w), 1182 (m, b), 1086 (m), 1034 (m), 962 (s), 881 (s), 850 (s), 785 (s), 750 (s), 640 (w) cm^{-1}. ^1H NMR (300 MHz, [D_6]DMSO, 301 K) δ = 10.42 – 6.59 (m, O*H* and Ar-*H*), 3.55 (2H, m, C*H* hidden by the water peak) 3.17 [m, 24 H, $N(C\mathit{H}_2CH_2CH_2CH_3)_4$], 1.57 [m, 24 H, $N(CH_2C\mathit{H}_2CH_2CH_3)_4$], 1.33 [m, 30 H, $N(CH_2CH_2C\mathit{H}_2CH_3)_4$; $C\mathit{H}_3$], 0.93 [m, 36 H, $N(CH_2CH_2CH_2C\mathit{H}_3)_4$] ppm. $^{13}C\{1H\}$ NMR (75.47 MHz, [D_6]DMSO, 28 °C): δ = 179.76, 168.56, 159.31, 151.81, 148.08, 145.74, 140.92, 128.95, 126.51, 125.40, 112.51, 110.08, 109.53, 102.14, 83.08 (fluoresceine carbons), 57.52 [12 C, $N(\mathit{C}H_2CH_2CH_2CH_3)_4$], 56.41 (2 C) 23.04 [12 C, $N(CH_2\mathit{C}H_2CH_2CH_3)_4$], 19.16 [12 C, $N(CH_2CH_2\mathit{C}H_2CH_3)_4$], 13.30 [12 C, $N(CH_2CH_2CH_2\mathit{C}H_3)_4$], 7.98 (2C, $\mathit{C}H_3$) ppm. $^{31}P\{1H\}$ NMR (121.50 MHz, [D_6]DMSO, 28 °C): *δ* = 20.18 (s, 2 P), - 12.02 (s, 1 P) ppm.

Synthesis of (nBu$_4$N)$_4$[{($C_5H_7N_2OS$)(CH_2)$_4$CONH(CH_2)$_3$Si}$_2$O(γ-SiW$_{10}$O$_{36}$)] *(Biot-SiW$_{10}$)*

Biotin (37 mg, 151 µmol) was introduced in a well dried Schlenk with magnetic stirring and connected to the line of nitrogen. Anhydrous DMF (0.5 mL), anhydrous CH_3CN (1 mL), N,N'-dicyclohexylcarbodiimide DCC (33 mg, 160 µmol) and N-hydroxysuccinimide NHS (19 mg, 164 µmol) were then added. The reaction mixture, vigorously stirred, was allowed to react for one night at 50 ° C, under nitrogen. After one night, **APTES-SiW$_{10}$** (200 mg, 59.4 µmol) and TEA (21.3 µL, 149 µmol) were dissolved in 2 ml of anhydrous CH_3CN and added to the reaction mixture. The mixture was stirred for one day at room temperature. Finally, the reaction mixture was centrifuged to remove insoluble reagents and byproducts. The volume of the solution was reduced to 1 mL, upon evaporation under vacuum, than water was added to precipitate the product. The solid was washed with water (3 times), diethyl ether (3 times) on a fritted funnel. 154 mg of product were obtained (64% yield).

Elemental analysis: Calcd. for C: 23.3; H: 4.0; N: 3.3; S: 1.7. Found: C: 23.1; H: 4.2; N: 2.7; S: 0.9. FT-IR (KBr): ν = 2961 (m), 2934 (m), 2873 (m), 1662 (m), 1469 (m), 1387 (w), 1099 (w), 948 (m), 901 (s), 820 (s), 734 (s), 544 (w) cm^{-1}. ^{1}H NMR (CD_3CN) δ: 0.55 (4 H, m), 0.99 (48 H, m), 1.39 (32 H, m), 1.64 (32 H, m), 2.63 (2 H, m), 3.15 (32 H, m), 4.33 (2 H, m), 4.49 (2 H, m), 5.09 (2 H, s, br), 5.85 (2H, s, br), 6.89 (2 H, s, br).^{13}C NMR (75.5 MHz, CD_3CN, 301 K) δ: 14.08 (32 C), 20.42 (32 C), 21.96 (2 C), 24.47 (32 C), 25.92 (2 C), 26.67 (2 C), 29.21 (2 C), 36.77 (2 C), 41.89 (2 C), 42.90 (2 C), 56.56 (2 C), 61.24 (2 C), 62.77 (2 C), 164.69 (2 C), 174.18 (2 C). ^{29}Si NMR (CH3CN\CD3CN, 301 K) δ: - 62.01 (2 Si, s), - 88.43 (1 Si, s). ^{183}W NMR (16.67 MHz, CH3CN/CD3CN, 301 K) δ: - 107.55 (4 W, s), - 136.09 (2W, s), -142.08 (4 W, s). ESI-MS (–, CH_3CN): m/z = 768.0, calc. for $[C_{26}H_{44}N_6O_{41}S_2Si_3W_{10}]^{4-}$ = 770.5.

Synthesis of (nBu$_4$N)$_4$[{ClIr(COD)($C_{10}H_{17}N_2Si$)}$_2$O(γ-SiW$_{10}$O$_{36}$)] *((NHC)Ir-SiW$_{10}$)*

380 mg (0.13 mmol) of $K_8[\gamma\text{-}SiW_{10}O_{36}]$ were suspended in 500 µL of H_2O under nitrogen. 206 mg (65 mmol, 5 equiv.) of nBu$_4$NBr, and CH_3CN (5 mL) were added and the mixture was stirred at room temperature for 20 minutes. The ligand [(1,2,5,6-η)-1,5-cyclooctadiene][1-butyl-3-(3-triethoxysilylpropyl)-imidazol-2-ylidene]chloroiridium ***((NHC)Ir)*** (170 mg, 0.26 mmol) was dissolved in 3 mL of solution CH_2Cl_2/CH_3CN 1/2 under nitrogen. Then the solution of **(NHC)Ir** and 190 µl of HCl 4.05 M were added in rapid sequence to the reaction mixture. Upon addition of acid, immediate clearing of the solution was observed. The mixture was kept under vigorous stirring overnight at r.t., then filtered to remove the insoluble material. The mixture was concentrated to about 1 mL volume, and the

product was precipitated by adding deionized water (20 mL). The product was collected by filtration, in a frittel funnel, washed with portions of deionized water and diethyl ether, and dried *in vacuo*. 298 mg (0.07 mmol) of product were obtained (54% yield).

Elemental analysis calcd (%) for $C_{100}N_8Si_3Ir_2Cl_2W_{10}O_{37}$: C 26.75, H 4.50, N 2.50; found: C 25.25, H 4.00, N 2.54. FTIR (KBr): ν= 2960 (m), 2932 (m), 2872 (m), 1660 (m), 1482 (m), 1463 (m), 1418 (m), 1380 (m), 1105 (m), 964 (s), 902 (s), 886 (s), 820 (s), 733 (s), 544 (m), 508 (m) cm-1. ^{1}H NMR (300 MHz, CD_3CN, 301 K) δ = 7.22 (2H, s, C*H* imidazol-2-ylidene), 7.04 (2H, s, C*H* imidazol-2-ylidene), 4.44-4.16 [24H, m, CH_{COD}, $Si(CH_2)_2CH_2N$, $NCH_2(CH_2)_2CH_3$, CH_3CH_2O], 3.16 [32H, m, $(CH_3CH_2CH_2CH_2)_4N$], 2.79-2.13 (28H, m, CH_{cod}, $NCH_2CH_2CH_2CH_3$, $SiCH_2CH_2CH_2N$, $NCH_2CH_2CH_2CH_3$), 1.65 [32H, m, $N(CH_2CH_2CH_2CH_3)_4$], 1.40 [50H, $N(CH_2CH_2CH_2CH_3)_4$, OCH_2CH_3], 0.98 [54H, $N(CH_2CH_2CH_2CH_3]$ $N(CH_2)_3CH_3$], 0.60 (4H, m, $SiCH_2$) ppm. $^{13}C\{^1H\}$ NMR (75.47 MHz, *d*-DMF, 301 K): δ = 178.7 (2C, C-Ir), 122.16, 121.40 (4C, C4 and C5, imidazol-2-ylidene), 82.75 (2C, CH_{COD}), 82.57 (2C, CH_{COD}), 59.27 [16C, $N(CH_2CH_2CH_2CH_3)_4$], 58.93, 58.54, 58.17, 50.77 [8C, $CH_3(CH_2)_2CH_2N$, $SiCH_2CH_2CH_2N$ and CH_{COD}], 34.06, 33.89, 33.48, 30.46, 26.31 (14C, methylene groups and CH_{COD}), 24.36 [16C, $N(CH_2CH_2CH_2CH_3)_4$], 20.6 (6C, OCH_2CH_3), 20.33 [16C, $N(CH_2CH_2CH_2CH_3)_4$], 13.90 [16C, $N(CH_2CH_2CH_2CH_3)_4$], 13.16 [2C, $CH_3(CH_2)_2CH_2N$] ^{29}Si NMR (79.5 MHz, CD_3CN, 25°C): δ = -62.0 (2 Si), -87.8 (1 Si) ppm. ^{183}W-NMR (16.7 MHz, CD_3CN, 25°C): - 105.8 (4 W), -135.6 (2W), - 141.8 (4 W) ppm. ESI-MS (–, CH_3CN) m/z = 1723.0, calcd. For $\{[(C_8H_{12})Ir(C_{10}H_{17}N_2Si)]_2O(\gamma\text{-}SiW_{10}O_{36})\}^{2-}$ = 1723.

5.2.2 General procedure for the cationic exchange

In around-bottomed flask with magnetic stirring 100.0 mg of **Dans-SiW$_{10}$** (24.8 µmol) were dissolved in 3 ml of acetonitrile. Then 26.7 mg of tetramethylammonium (173 µmol) dissolved in 2 ml of water were added. The reaction mixture, vigorously stirred, was allowed to react at room temperature, for one night. The solution obtained was poured into EtOH (15 mL). The white precipitate obtained was filtered, dried under vacuum and, finally, eluted in a resin (Amberlyst 15) loaded with sodium ions, using a gradient eluent of a mixture water / acetonitrile (1:1 to 1:0). Finally, the solution was lyophilized to remove water.

5.2.3 Synthesis of organic ligands

Synthesis of 1-Pyrensulfonyl Chloride *($PyrSO_2$-Cl)*

Sodium 1-Pyrene Sulfonate. To a vigorously stirred solution of pyrene (9.2 g, 47.1 mmol) in CH_2Cl_2 (60 mL) at 0 °C under nitrogen, chlorosulfonic acid (3.2 mL, 48 mmol), previously dissolved in CH_2Cl_2 (10 mL), was added dropwise. This solution was stirred at 0 °C for 3 h, then at room temperature for 16 h. The resulting dark green solution was poured onto ice (100 g), and the CH_2Cl_2 was removed by rotary evaporation. The remaining solution was filtered twice through celite to remove particulates, and washed with water (2 x 30 ml) each time. Solid NaOH (2 g) was added, followed by addition of an aqueous solution of 5% NaCl (20 ml). The resulting yellow solid was filtered off, washed with water and air-dried. Yield 10.2 g (71%).

1-Pyrenesulfonyl Chloride. In CH_2Cl_2 (95 ml) sodium pyrene sulfonate (1.8 g, 5.9 mmol) and phosphorus pentachloride (4 g, 13.9 mmol) were dispersed, and then heated at 40 °C for 1 h. The resulting solution was filtered and the filtrate was washed with water (2 x 200 ml), then dried ($MgSO_4$) and concentrated by rotary evaporation to give pyrene sulfonyl chloride, that was purified by silica gel column chromatography, using CH_2Cl_2:hexane (2:3) as eluent. The yield of the orange product was 1.65 g (92.7%); m.p. 172-173 °C (lit. 172).

FT-IR (KBr): ν = 2921 (m, aromatic CH stretch); 1588 (m, S-Cl stretch); 1384 (m), 1373 (m), 1362 (s, asymmetric S=O), 1172 (s, asymmetric S=O), 1146 (m), 1134 (m), 849 (m) cm^{-1}; ^1H NMR δ_H (300 MHz, d_6-DMSO, 301 K) all aromatic resonances; ^{13}C-NMR: δ_C (75.47 MHz, d_6-DMSO, 301 K) 143.04, 132.82, 132.15, 131.56, 129.13, 128.67, 128.31, 128.11, 127.65, 126.75, 126.74, 126.24, 125.67, 125.16.

Synthesis of $(C_{20}H_{11}O_5)NHCSNHCH(CH_3)PO(OH)_2$ *(FITC-AEPA)*

In around-bottomed flask, R or S 1-aminoethylphosphonic acid (**AEPA**) (70 mg, 0.56 mmol) was dissolved in H_2O (12 mL) buffered with a solution of CO_3^{2-}/HCO_3^- (1M) at pH 9. Separately, FITC (200 mg, 0.51 mmol) was dissolved in DMSO (1 mL). This latter solution was added dropwise to the solution of **AEPA**, and the resulting mixture was stirred overnight. The solution was acidified with aqueous $KHSO_4$ solution (pH 2) to obtain a neutral species. Then the product was collected upon centrifugation and washing with acidic water (3 times) and finally with AcOEt (5 times). 123 mg (0.24 mmol) of product were obtained (yield 47%). FTIR (KBr): ν= 3090-2850 (w), 1636 (m), 1603 (m), 1539 (m), 1459 (m), 1389 (m), 1318 (m), 1277 (m), 1209 (m), 1174 (m), 1118 (m), 1024 (m), 950 (m), 850 (m) cm^{-1}. ^1H NMR (300 MHz, CD_3OH, 28°C): δ = 8.41 – 6.73 (m, 11 H, Ar-*H*), 3.60 (1H, m, C*H* hidden by the

ethanol peak), 1.44 (m, 3H, C*H*$_3$). ppm. ^{13}C{^{1}H} NMR (75.47 MHz, CD_3OH, 301 K): δ = 183.12, 182.99, 182.56, 169.92, 165.66, 156.70, 156.38, 143.26, 142.78, 132.70, 131.88, 131.68, 130.20, 127.69, 116.45, 114.16, 113.75, 103.49 (fluoresceine carbons), 15.88 (1C, *C*H$_3$) ppm ^{31}P{^{1}H} NMR (121.50 MHz, [D$_6$]DMSO, 28 °C): *δ* = 21.05 (s, 1 P) ppm. ESI-MS (–, CH_3OH): *m*/*z* = 513.1, expected for $[C_{23}H_{18}N_2O_8PS]^-$= 513.4.

Synthesis of [(1,2,5,6-*η*)-1,5-cyclooctadiene][1-butyl-3-(3-triethoxysilylpropyl)-imidazol-2-ylidene]chloroiridium *((NHC)Ir)*

1-butyl-3-(3-triethoxysilylpropyl)-imidazolium bromide (0.5 g, 1.22 mmol) was introduced in a well dried schlenk tube. Anhydrous CH_2Cl_2 (40 mL) and Ag_2O (0.142 g, 0.61 mmol) were then added. The reaction mixture, vigorously stirred, was allowed to react at room temperature, under nitrogen. After 5 h $[Ir(cod)Cl]_2$ (0.410 g, 0.61 mmol) was added and the mixture was stirred for one night, then filtered through celite. Evaporation of the solvent gives the desired product as a yellow oil. Yield: 85% (0.69 g).

Elemental analysis calcd (%) for $C_{24}H_{44}ClIrN_2O_3Si$: C 43.39, H 6.68 N 4.22; found: C 42.39, H 5.75 N 4.13; FT-IR (KBr). ν = 3163 (w), 3126 (w), 3103 (w), 2961 (s), 2927 (s), 2876 (s), 2013 (w, b), 1456 (m), 1420 (m), 1257 (m), 1226 (m), 1201 (m), 1167 (m), 1102 (s), 1077 (s), 956 (m), 883 (w), 798 (m), 777(m), 703 (m), 690k (m) cm-1. ^{29}Si-NMR (79.5 MHz, CD_3CN, 25°C): δ = - 48.2 ppm. ^{1}H NMR (360 MHz, CD_2Cl_2, 25°C) 6.87 (1H, s, CH imidazol-2-ylidene), 6.82 (1H, s, CH imidazol-2-ylidene), 4.58 (2H, s, b, CH_{cod}) 4.36 [4H, m, $Si(CH_2)_2CH_2N$, $NCH_2(CH_2)_2CH_3$], 3.84 (6H, q, CH_3CH_2O), 2.92 (2H, s, b, CH_{cod}), 2.20 (4H, s, b, CH_{cod}), 2.06-1.38 (10H, m, CH_{cod}, $NCH_2CH_2CH_2CH_3$, $SiCH_2CH_2CH_2N$, $NCH_2CH_2CH_2CH_3$), 1.24 (9H, t, CH_3CH_2O), 1.00 [3H, t, $N(CH_2)_3CH_3$], 0.71 (2H, m, $SiCH_2$) ppm**.** ^{13}C{^{1}H} NMR (62.5 MHz, CD_2Cl_2, 25°C): 179.65 (C-Ir), 119.99, 119.68 (C4 and C5, imidazol-2-ylidene), 83.83 (1C, CH_{cod}), 83.52 (1C, CH_{cod}), 58.44 (3C, OCH_2), 52.79, 51.46, 51.14, 50.23 (4C, $CH_3(CH_2)_2CH_2N$, $SiCH_2CH_2CH_2N$ and CH_{cod}), 33.73, 33.35, 32.94, 29.69, 29.33, 24.50, 19.98 (7C, methylene groups and CH_{cod}), 18.27 (3C, OCH_2CH_3), 13.70 [1C, $CH_3(CH_2)_2CH_2N$], 7.77 (1C, $SiCH_2$) ppm. ESI-MS(+, CH_3CN) m/z = 628.9 and 670.6, calcd. For $[(C_8H_{12})\{C_{10}H_{17}N_2Si(OEt)_3\}Ir]^+$ and $[(C_8H_{12})\{C_{10}H_{17}N_2(OEt)_3\}Ir(CH_3CN)]^+$.

5.3 Analysis methods

5.3.1 Spectrophotometric titrations

Fluorimetric titrations of Dans-SiW_{10}

$CuSO_4 \cdot 5H_2O$, $Zn(NO_3)_2 \cdot {}_6H_2O$, $HgSO_4$, $PbSO_4$, $NiSO_4 \cdot 6H_2O$, $FeSO_4$, $CdSO_4 \cdot H_2O$, and $CoSO_4 \cdot 6H_2O$ were analytical-grade products and were used to prepare 1.6 mM aqueous solutions. 2 mL of a 10 μM CH_3CN solution of **Dans-SiW_{10}** were placed in a fluorescence quartz cell. A variable volume of concentrated metal ion solution (up to 40 μL) was added, and water was added to provide a fixed 2.5% water content. The resulting solutions were allowed to equilibrate until stable emission spectra were obtained (less than 5 min were usually required, except for Pb^{2+}).

Fluorimetric titrations of Pyr-SiW_{10}

C_{60} titration: 3 mg of **Pyr-SiW_{10}** were dispersed in 10 mL of DMF (solution A); at the same time, 7.2 mg of C_{60} was dissolved into 2 mL of *o*-DCB (solution B). Both the solutions were stirred for 5 minutes for a complete and homogeneous dispersion of the molecules in solution. Afterwards, solution A and B were dilute for having UV signals under Abs value of 1; so, 0.45 ml of solution A were added to 2.25 mL of DMF (solution C, dilution of 1/6), and 0,4 ml of solution B were added to 2 ml of *o*-DCB (solution D, dilution of 1/6).

UV-Vis-NIR and fluor. titrations were performed with stepwise addition of 4 μl of solution D to solution C, except for the very last add (+ 50 μl). About fluor. experiments, excitation wavelength was set at 335 nm.

The inner filter effect correction was carried out as follows: in our system, C_{60} shows absorption at the excitation wavelength (335 nm) of **Pyr-SiW_{10}**. As a consequence, with the gradual addition of C_{60}, the excitation light is absorbed by both of the entities. This phenomenon is called inner filter effect. Thus it is very important to subtract such an effect from the raw quenching data. At the position of emission, which is in the half of the cell length, the absorption of the excitation light by the C_{60} can be calculated by the following set of equations :

$$OD = Log\frac{I_0}{I} = \frac{1}{2}\varepsilon_{295}CL$$

$$F = F_1\frac{I_0}{I}$$

where ε_{295} is the molar absorption coefficient constant of the C_{60} at 335 nm, F is the real fluorescence intensity after deduction of the inner filter effect, and F_1 is the original fluorescence intensity measured from the spectra.

Carbon nanotubes (CNTs) titration: 3 mg of **Pyr-SiW$_{10}$** were dispersed in 3 ml of DMF/MeOH 1:1 solution; after stirring the mixture for 5 minutes for increasing solubilisation, 3 mg of **CNT**s were added. The solution was sonicated for 30 minutes, and then was stirred for further 30 minutes. The mixture was centrifugated for 1 h at 3000 rpm, and after this the supernatant solution was collected. UV-Vis-NIR and fluor. experiments were performed directly on the supernatant solutions without any dilutions; excitation wavelength was set at 335 nm.

Binding study between Biot-SiW$_{10}$ and avidin

The binding between **Biot-SiW$_{10}$** and avidin has been monitored by means of UV-Vis spectrophotometry. The solution avidin/HABA acid was commercially available product (Sigma-Aldrich) and suitable for the spectrophotometric determination of biotin levels. The commercial reagent was diluted 1/10 (0.68 µM in H_2O; solution A). 2 mL of solution A were placed in a fluorescence quartz cell. 5 µL of a concentrated **Biot-SiW$_{10}$** solution (70 µM; solution B in DMF) were added to the solution A up to 20 µL, and then 5 µL of a concentrated **Biot-SiW$_{10}$** solution (140 µM; solution C in DMF) up to 50 µL.

5.3.2 DFT Calculations

Computational resources and assistance were provided by the Laboratorio Interdipartimentale di Chimica Computazionale (LICC) at the Department of Chemical Sciences of the University of Padova. DFT calculations were carried out using the Amsterdam density functional (ADF) code;[7] scalar relativistic effects were taken into account by means of the two-component zeroorder regular approximation (ZORA) method,[8] adopting the Becke 88 exchange plus the Perdew 86 correlation (BP) functional.[9] The basis functions for describing the valence electrons are triple-zeta quality, doubly polarized (TZ2P), specially optimizedfor ZORA calculations. Due to the large size of the molecules under investigation, the internal or core electrons (C, N and O: 1s; Si: 1s to 2sp; W: 1s to 4spdf) were kept frozen. Geometries were optimized without symmetry constraints. The solvent effect was modeled by means of the ADF implementation[10] of the COSMO method.[11]

5.3.3 Typical procedure for catalytic transfer hydrogenation

Typically, the transfer hydrogen of benzophenone to diphenyl methanol in *i*PrOH was performed in a glass reactor. Catalyst manipulation does not need particular precautions, and transfer hydrogenations were generally performed in air.

In a typical reaction, the catalyst (0.01 mmol, 1 mol%) was stirred, together with KOH (0.05 mL of 2 M solution in H_2O, 0.1 mmol) and *i*PrOH (5.0 mL) at reflux for 10 min. Then the ketone (1.0 mmol) was added at once. Aliquots (0.2 mL) were taken at fixed times, quenched in hexane (2 mL), and filtered through a plug of silica, then the silica was washed with diethyl ether or *tert*-butyl methyl ether. The combined organic filtrates were evaporated and analyzed by ^{1}H NMR spectroscopy.

5.4 References and notes

[1] J. Canny, A. Tézé, R. Thouvenot, G. Hervé, *Inorg. Chem.* **1986**, *25*, 2114. a) A. Tézé, G. Hervé, Inorg. Synth. **1990**, *27*, 85. b) A. Tezè, G. Hervè, J. Inorg. Nucl. Chem. **1977**, *39*, 999. c) J. Canny, A. Tezè, R. Thouvenot, G. Hervè, Inorg. Chem. **1986**, *25*, 2114. d) see also M. Carraro, Ph. D. Thesis, Università degli studi di Padova, 2001 and A. Sartorel, Ph. D. Thesis, Università degli Studi di Padova, 2002 in the Experimental Parts.

[2] R. Massart, R. Contant, J.-M. Fruchart, J.-P. Ciabrini. M. Fournier, *Inorg. Chem.* **1977**, *16*, 2916.

[3] E. Rampazzo, E. Brasola, S. Marcuz, F. Mancin, P. Tecilla, U. Tonellato, *J. Mater. Chem.* **2005**, *15*, 2687.

[4] J. B. Issa, A. S. Salameh, E. W. Castner, Jr. J. F. Wishart, S. S. Isied, *J. Phys. Chem. B* **2007**, *111*, 6878.

[5] S. Berardi, M. Carraro, M. Iglesias, A. Sartorel, G. Scorrano, M. Albrecht, M. Bonchio *Chem. Eur. J.* **2010**, *16*, 10662 .

[6] A. R. Chianese , X. Li , M. C. Janzen , J. W. Faller , and R. H. Crabtree *Organometallics* **2003,** *22*, 1663.

[7] G. te Velde, F. M. Bickelhaupt, E. J. Baerends, C. Fonseca Guerra, S. J. A. van Gisbergen, J. G. Snijders, T. Ziegler, *J. Comput. Chem.* **2001**, *22*, 931.

[8] a) J. Autschbach, in: *Calculation of NMR and EPR Parameters: Theory and Applications* (Eds.: M. Kaupp, M. Bühl, V. G. Malkin), Wiley-VCH, Weinheim, Germany, **2004**, Chapter 14; b) E. van Lenthe, E. J. Baerends, J. G. Snijders, *J. Chem. Phys.* **1993**, *99*, 4597; c) E. van Lenthe, *Ph. D. Thesis*, Vrije Universiteit, Amsterdam, The Netherlands, **1996**; d) S.K. Wolff, T. Ziegler, E. van Lenthe, E. J. Baerends, *J. Chem. Phys.* **1999**, *110*, 7689.

[9] a) J. P. Perdew, *Phys. Rev. B* **1986**, *33*, 8822; b) A. D. Becke, *Phys. Rev. A* **1988**, *38*, 3098.

[10] C. C. Pye, T. Ziegler, *Theor. Chem. Acc.* **1999**, *101*, 396.

[11] a) A. Klamt, G. Schürmann, *J. Chem. Soc. Perkin Trans.* **1993**, *2*, 799; b) A. Klamt, V. Jones, *J. Chem. Phys.* **1996**, *105*, 9972; c) A. Klamt, *J. Phys. Chem.* **1995**, *99*, 2224.

Appendix

Acronyms and abbreviations

AcOH: Acetic Acid (CH_3COOH)

AcONa: Sodium Acetate (CH_3COONa)

AEPA: 1-aminoethylphosphonic acid

ADF: Amsterdam Density Functional code

aFtn: apoferritin

Ftn: Ferritin

APTES-SiW_{10} = $(n Bu_4N)_4[(NH_2(CH_2)_3Si)_2O(\gamma\text{-}SiW_{10}O_{36})]$

Biot-SiW_{10}: $(n Bu_4N)_4[\{(C_5H_7N_2OS)(CH_2)_4CONH(CH_2)_3Si\}_2O(\gamma\text{-}SiW_{10}O_{36})]$

COD: Cyclooctadiene

Dans-SiW_{10}: $(n Bu_4N)_4[\{\{(CH_3)_2N\}C_{10}H_6SO_2NH(CH_2)_3Si\}_2O(\gamma\text{-}SiW_{10}O_{36})]$

DCC: N.N'-Dicyclohexylcarbodiimide

DCU: N,N'-Dicyclohexylurea

DFT: Density Functional Theory

DLS: Dynamic Light Scattering

DMF: Dimethylformamide

DMSO: Dimethylsulfoxide

EDC: 1-ethyl-3-(3-dimethylaminopropyl)carbodiimide

ESI-MS: Electrospray Ionsation Mass Spectroscopy

EtOH: Ethanol

EuPOM: $[EuW_{10}O_{36}]^{9-}$

FID: Flame Ionisation Detector

FITC: Fluorescein Isothiocyanate

FITC-AEPA: $(C_{20}H_{11}O_5)NHCSNHCH(CH_3)PO(OH)_2$

FITC-PW_9: $(n Bu_4N)_3Na_2[((C_{20}H_{11}O_5)NHCSNHCH(CH_3)PO)_2(\alpha\text{-}A\text{-}PW_9O_{34})]$

FITC-SiW_{10}: $(n Bu_4N)_4[\{(C_{20}H_{11}O_5)NHCSNH(CH_2)_3Si\}_2O(\gamma\text{-}SiW_{10}O_{36})]$

FT-IR: Fourier Transform - Infrared spectroscopy

Gly: Glycine

HABA: 4'-hydroxyazobenzene-2-carboxylic acid

HEK293: Human Embryonic Kidney 293 cells

HOBt: 1-hydroxy-1,2,3-benzotriazole

HPAs: Heteropolyacids

HSA: Human Serum Albumin

IC_{50}: median inhibitory concentration (in µM)

ITC: Isothiocyanate

ITC: Isothermal Titration Calorimetry

LICC: Laboratorio Interdipartimentale di Chimica Computazionale

LUMO: Lowest Unoccupied Molecular Orbital

MTT: (3-(4,5-Dimethylthiazol-2-yl)-2,5-diphenyltetrazolium bromide

MW: Microwave radiation

$n Bu_4N^+$: Tetrabutylammonium cation

NMR: Nuclear Magnetic Resonance

NHC: N-Heterocyclic Carbene

(NHC)Ir: [(1,2,5,6-η)-1,5-cyclooctadiene][1-butyl-3-(3-triethoxysilylpropyl)-imidazol-2 ylidene]chloroiridium

(NHC)Ir-SiW_{10}: $(nBu_4N)_4[\{ClIr(COD)(C_{10}H_{17}N_2Si)\}_2O(\gamma\text{-}SiW_{10}O_{36})]$

NHS: N-hydroxysuccinimide

o-DCB: *ortho*-dichlorobenzene

Pyr-SiW_{10}: $(nBu_4N)_4[\{C_{16}H_9SO_2NH(CH_2)_3Si\}_2O(\gamma\text{-}SiW_{10}O_{36})]$

PyrSO_2-Cl: 1-Pyrensulfonyl Chloride

POM: Polyoxometalate

RuPOM: $[Ru^{IV}_4(\mu\text{-}OH)_2(\mu\text{-}O)_4(H_2O)_4(\gamma\text{-}SiW_{10}O_{36})_2]^{10-}$

SEM: Scansion Electron Microscopy

TEA: Triethylamine

TEM: Transmission Electron Microscopy

TH: Transfer Hydrogenation

THF: Tetrahydrofuran

TLC: Thin Layer Cromatography

TMA: Tetramethylammonium

TMSP: Transition Metals Substituted Polyoxometalates

TOF: Turnover Frequency

TON: Turnover Number

TRIS: tris(hydroxymethyl)aminomethane ($(HOCH_2)_3CNH_2$)

TZ2P: Triple-Zeta quality, doubly Polarized

UV-Vis: Ultraviolet-Visible spectroscopy

WST-1: Water Soluble Tetrazolium salts

ZORA: two-component ZeroOrder Regular Approximation

SPECTRA

Hybrid POMs

(nBu$_4$N)$_4$[(NH$_2$(CH$_2$)$_3$Si)$_2$O(γ-SiW$_{10}$O$_{36}$)] (*APTES-SiW$_{10}$*)

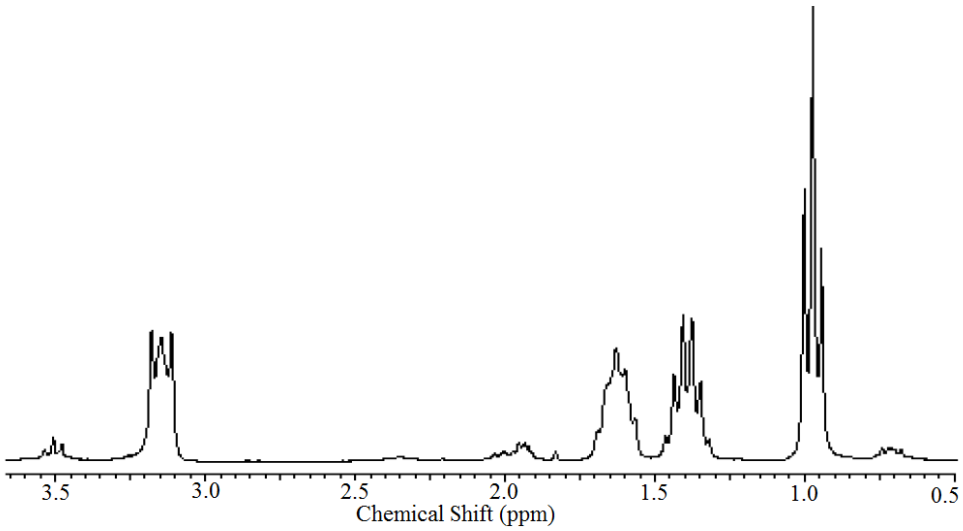

A1 ^{1}H NMR (CD_3CN) of **APTES-SiW$_{10}$.**

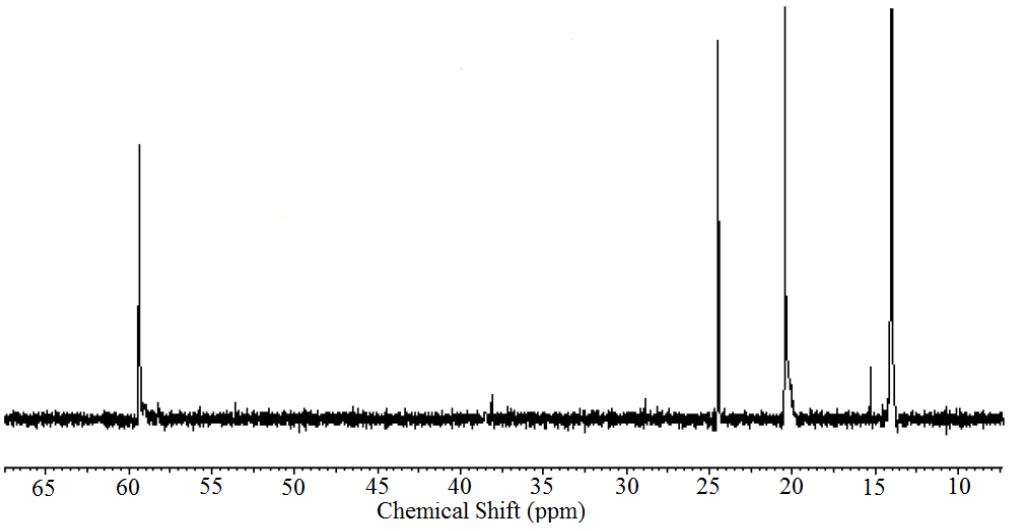

A2 ^{13}C NMR (CD_3CN) of **APTES-SiW10.**

(nBu$_4$N)$_4$[{{(CH$_3$)$_2$N}C$_{10}$H$_6$SO$_2$NH(CH$_2$)$_3$Si}$_2$O(γ-SiW$_{10}$O$_{36}$)] (*Dans-SiW$_{10}$*)

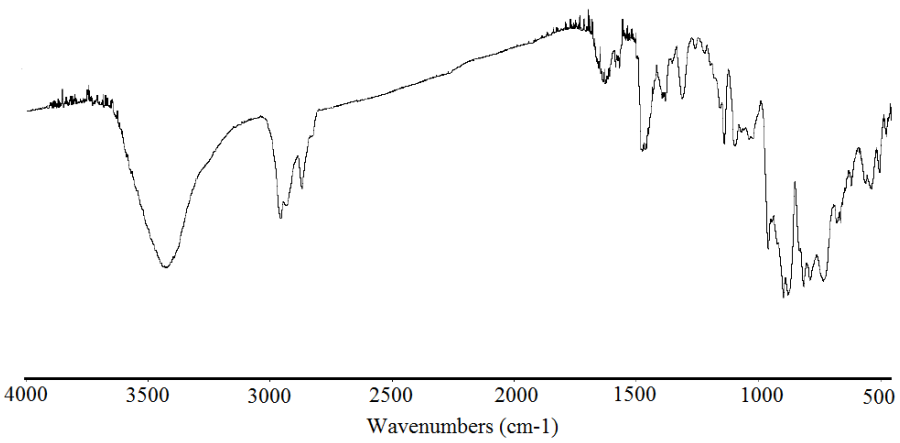

A3 FT-IR of **APTES-SiW$_{10}$**.

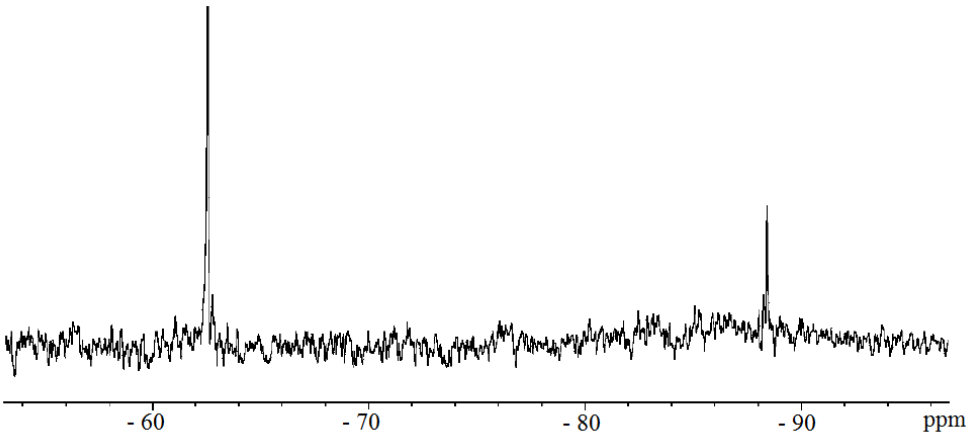

A4 ^{29}Si NMR (CD$_3$CN) of **Dans-SiW$_{10}$**.

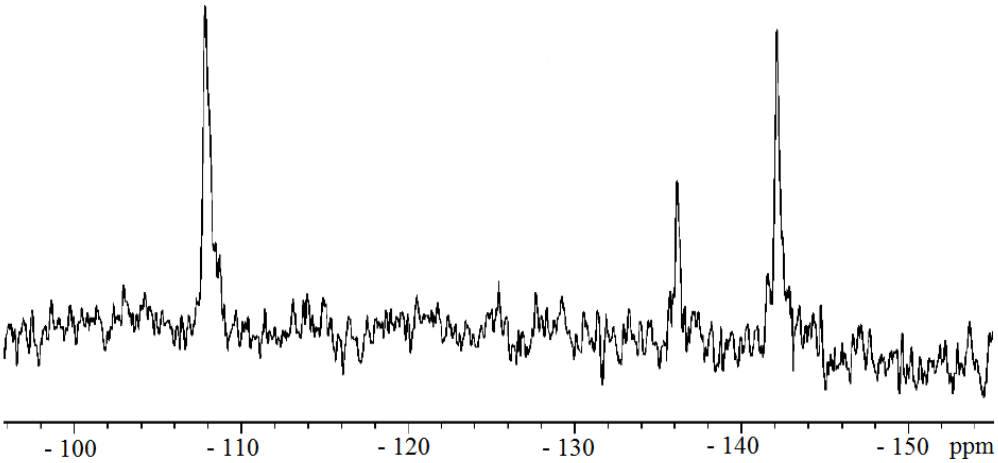

A5 ^{183}W NMR (CD$_3$CN) of **Dans-SiW$_{10}$**.

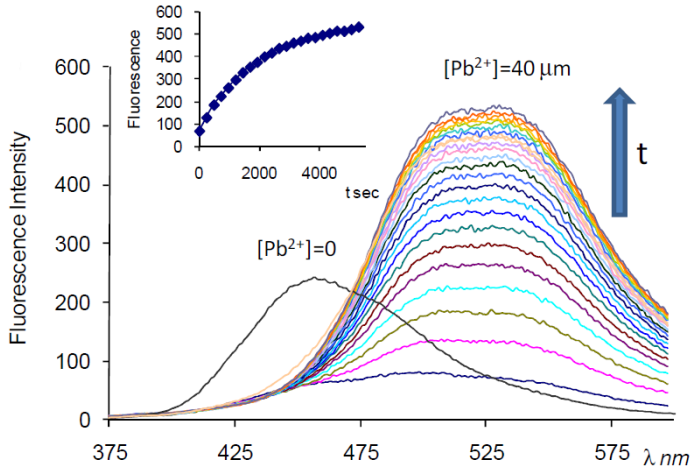

A6 Emission of **Dans-SiW$_{10}$** ($1x10^{-5}$M in CH_3CN with 2.5% v/v H_2O, λ_{ex} = 293 nm) after addition of $Pb(NO_3)_2$ (40 μM).

(nBu$_4$N)$_4$[{C$_{16}$H$_9$SO$_2$NH(CH$_2$)$_3$Si}$_2$O(γ-SiW$_{10}$O$_{36}$)] (***Pyr-SiW$_{10}$***)

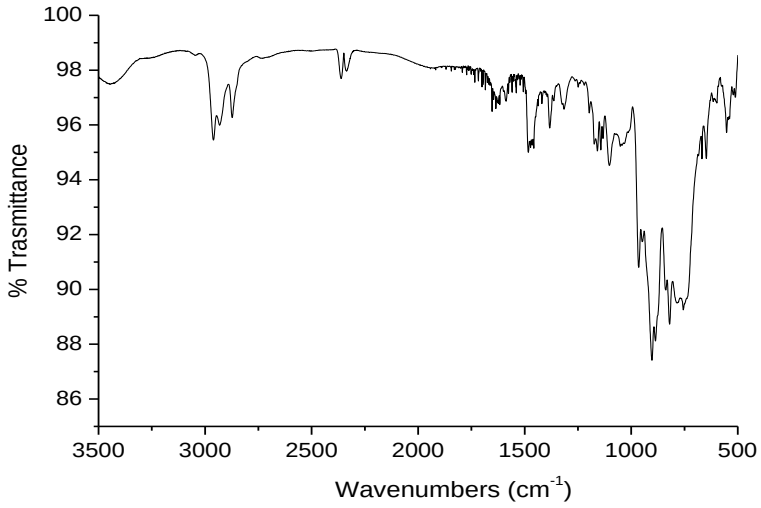

A7 FT-IR (KBr) of **Pyr-SiW$_{10}$**.

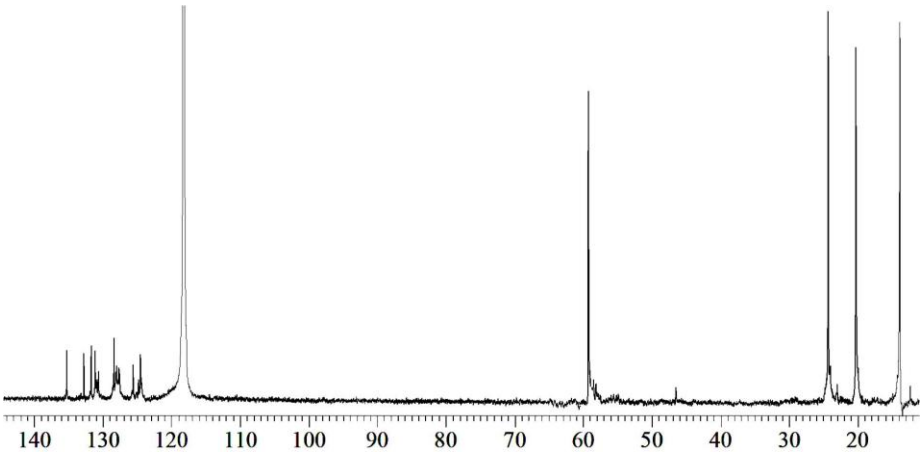

A8 ^{13}C NMR (CD_3CN) of **Pyr-SiW$_{10}$**.

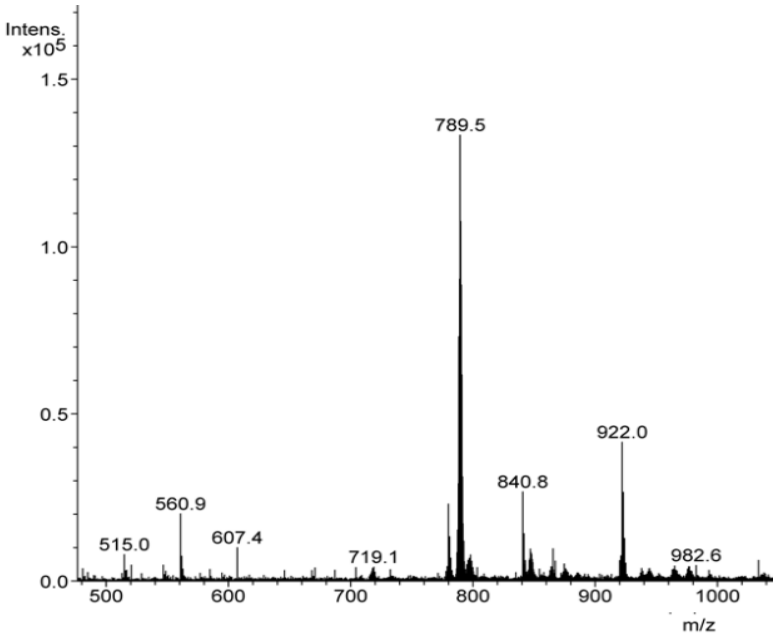

A9 ESI-MS ((-),CH_3CN) of **Pyr-SiW$_{10}$**.

(nBu$_4$N)$_4$[{($C_{20}H_{11}O_5$)NHCSNH(CH_2)$_3$Si}$_2$O(γ-SiW$_{10}$O$_{36}$)] (***FITC-SiW$_{10}$***)

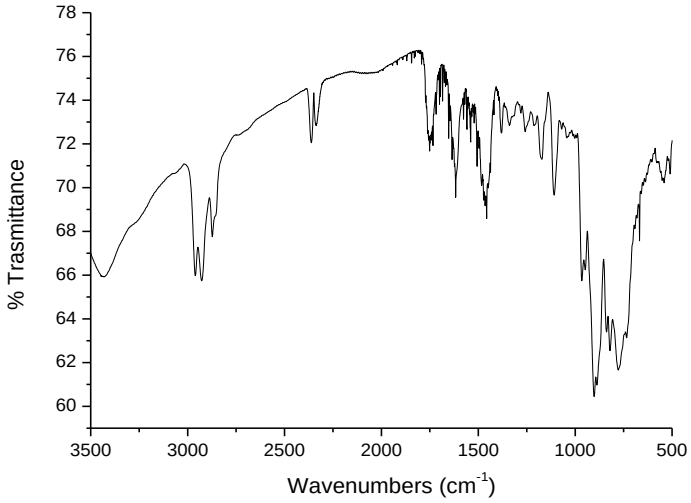

A10 FT-IR (KBr) of **FITC-SiW$_{10}$**.

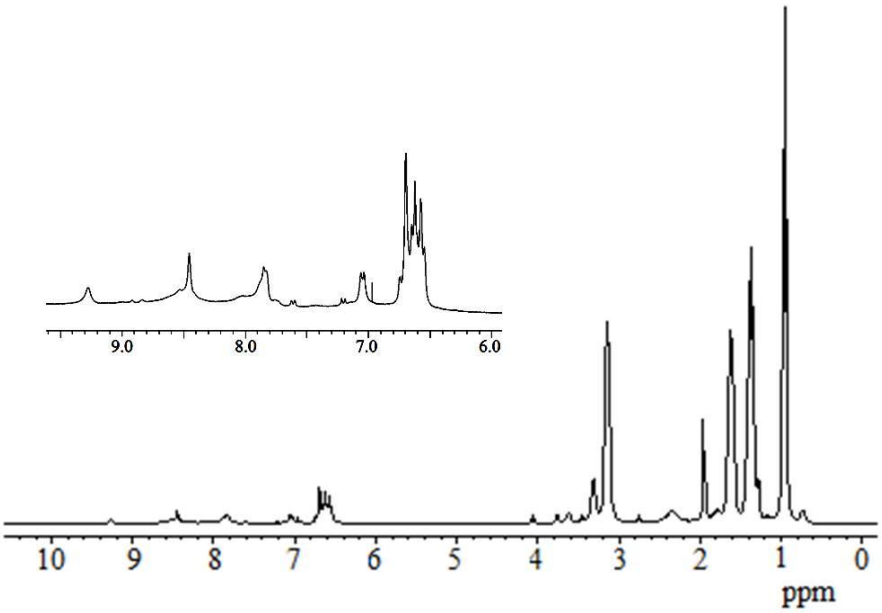

A11 ^{1}H NMR (CD_3CN) spectrum of **FITC-SiW$_{10}$**.

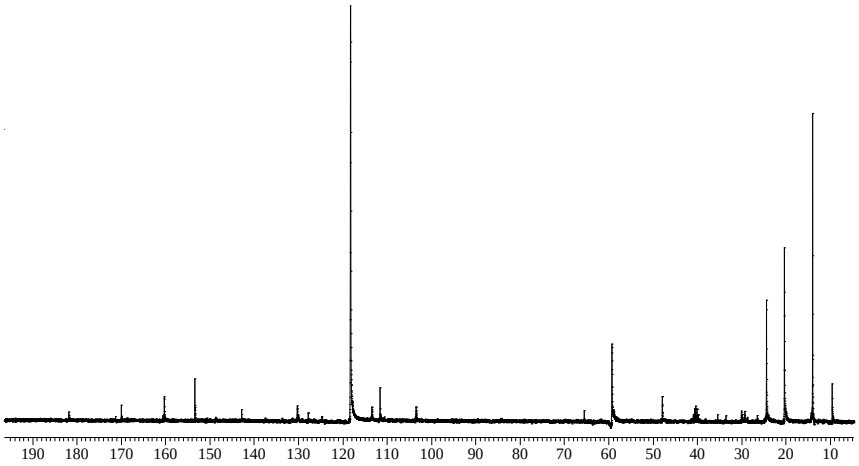

A12 ^{13}C NMR (CD_3CN) spectrum of **FITC-SiW$_{10}$**.

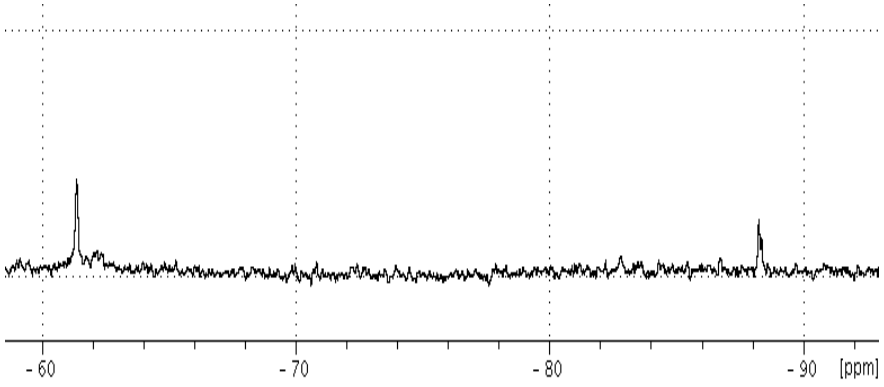

A13 ^{29}Si NMR (CD_3CN) spectrum of **FITC-SiW$_{10}$**.

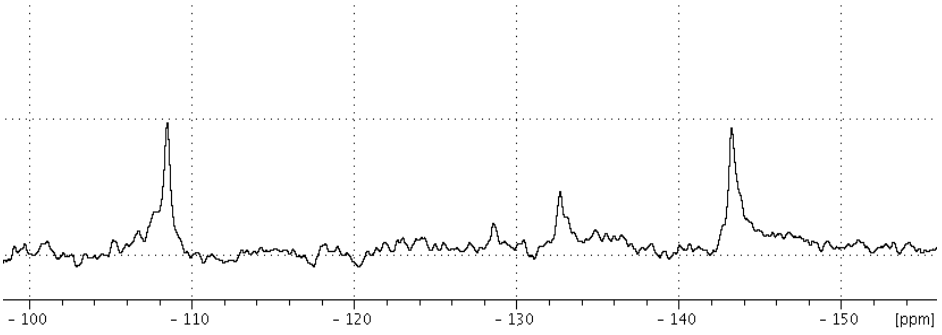

A14 ^{183}W NMR (CD_3CN) spectrum of **FITC-SiW$_{10}$**.

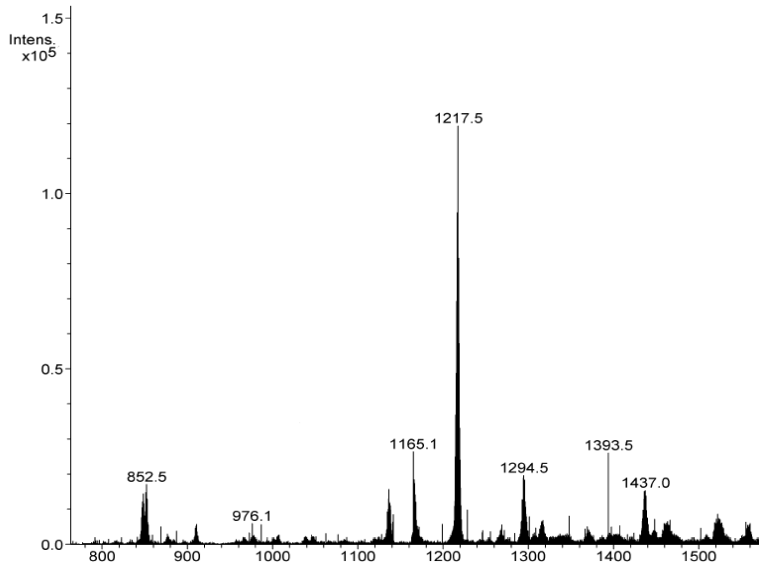

A15 ESI-MS ((-),CH_3CN) of **FITC-SiW$_{10}$.**

(*n*Bu$_4$N)$_3$Na$_2$[(C$_{20}$H$_{11}$O$_5$)NHCSNHCH(CH$_3$)PO)$_2$(α-A-PW$_9$O$_{34}$)] (***FITC-PW$_9$***)

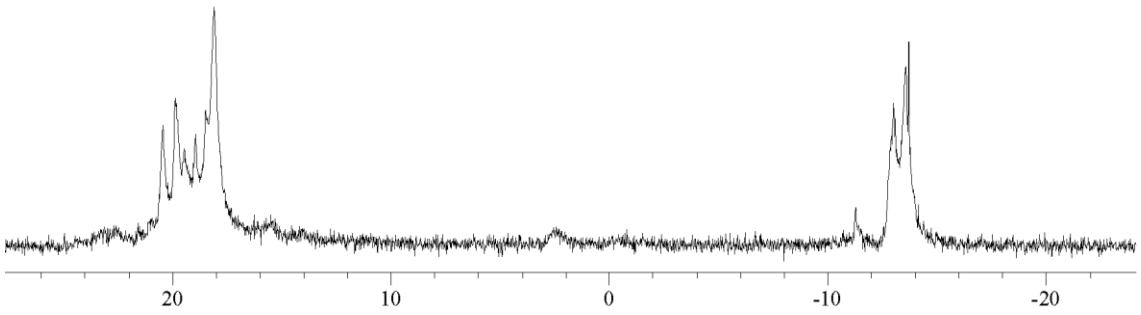

A16 ^{31}P NMR (CD_3CN/[D]$_6$DMSO) recorded at -32 °C of **FITC-PW$_9$.**

$(n\mathrm{Bu_4N})_4[(C_5H_7N_2OS(CH_2)_4CONH(CH_2)_3Si)_2(\gamma OSiW_{10}O_{36})]$ ***(Biot-SiW$_{10}$)***

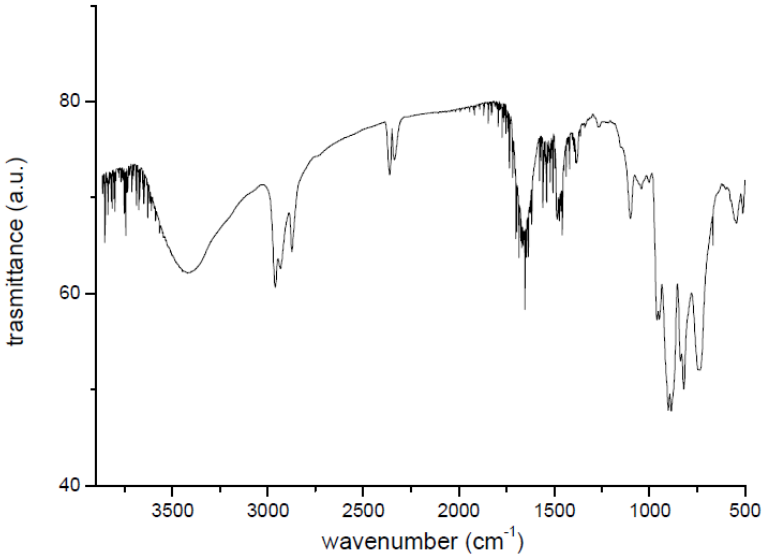

A17 FT-IR (KBr) of **Biot-SiW$_{10}$**.

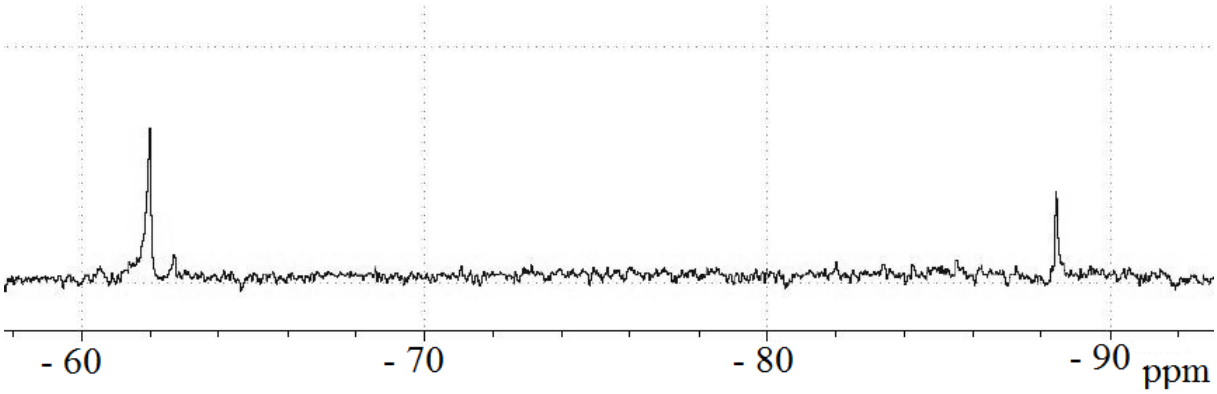

A18 ^{29}Si NMR (CD_3CN) spectrum of **Biot-SiW$_{10}$**.

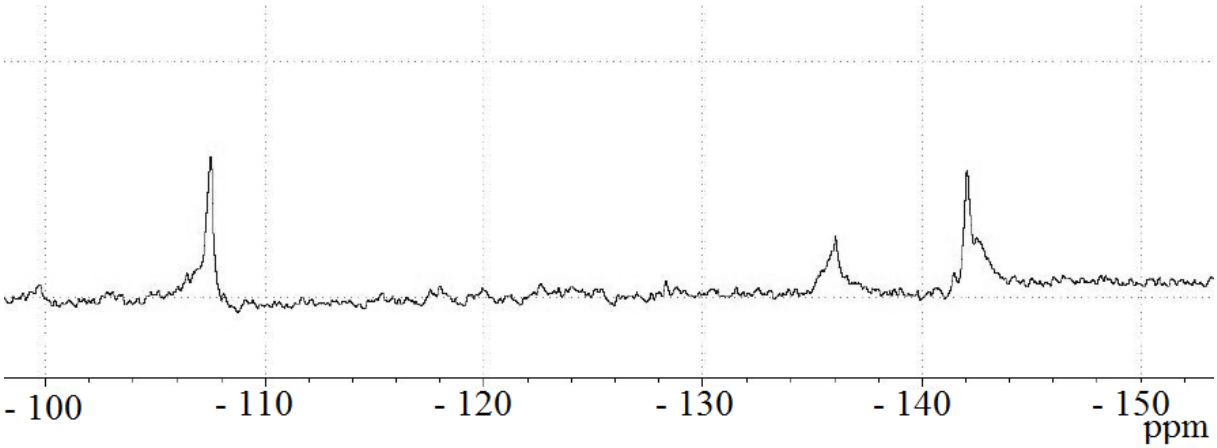

A19 ^{183}W NMR (CD_3CN) spectrum of **Biot-SiW$_{10}$**.

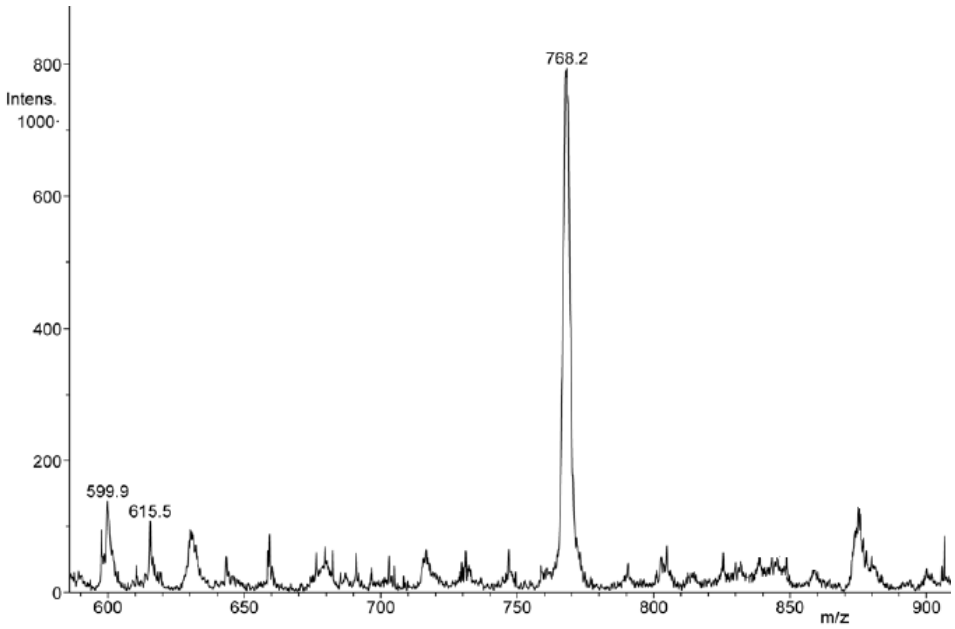

A20 ESI-MS ((-),CH_3CN) of **Biot-SiW$_{10}$**.

(n*Bu$_4$N)$_4${[ClIr(COD)(C$_{10}$H$_{17}$N$_2$Si)]$_2$O(γ-SiW$_{10}$O$_{36}$)}** ((NHC)Ir-SiW$_{10}$***)

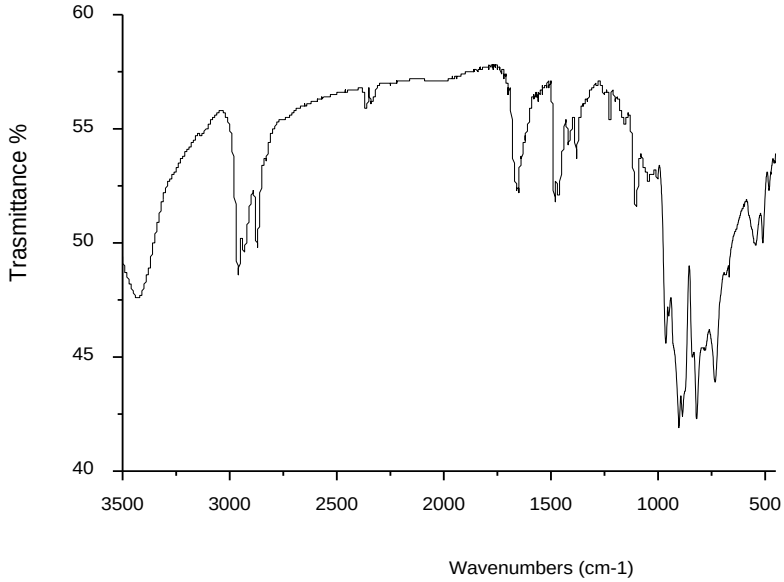

A21 FT-IR (KBr) of **(NHC)Ir-SiW$_{10}$**.

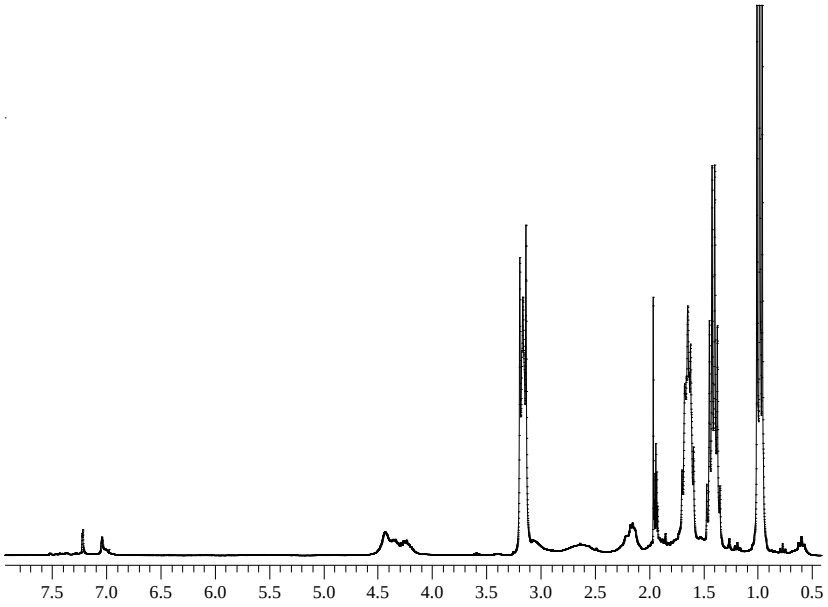

A22 ^{1}H NMR (CD_3CN) of **(NHC)Ir-SiW$_{10}$.**

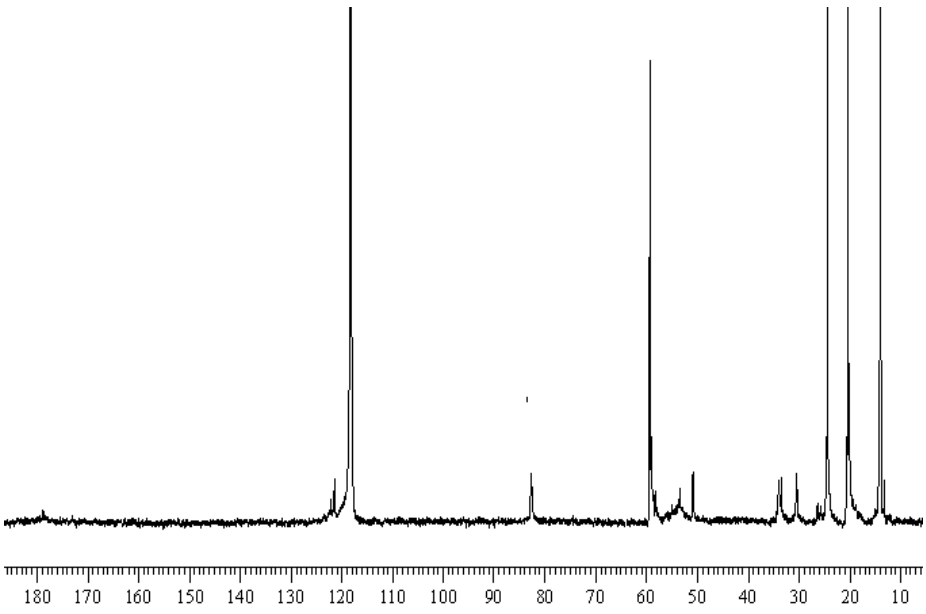

A23 ^{13}C NMR (CD_3CN) of **(NHC)Ir-SiW$_{10}$**

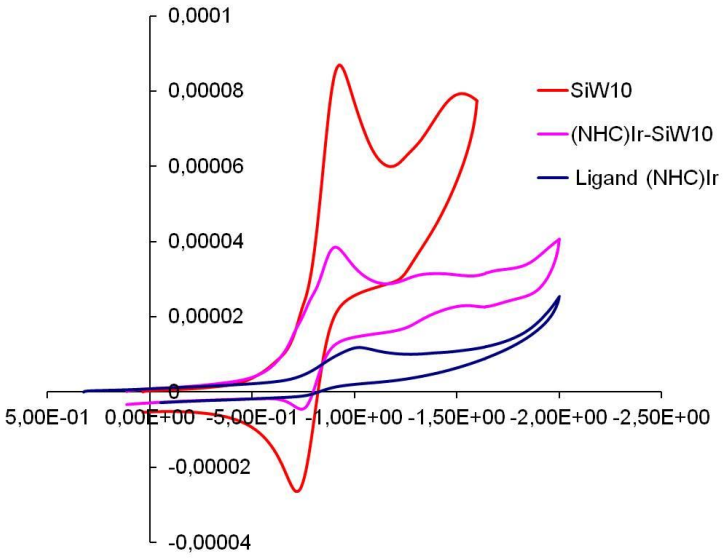

A24 Cyclic voltammetry; cathodic scan: 0.5 mM; CH_3CN (nBu_4ClO_4; 0.1M); 200 mV/sec.

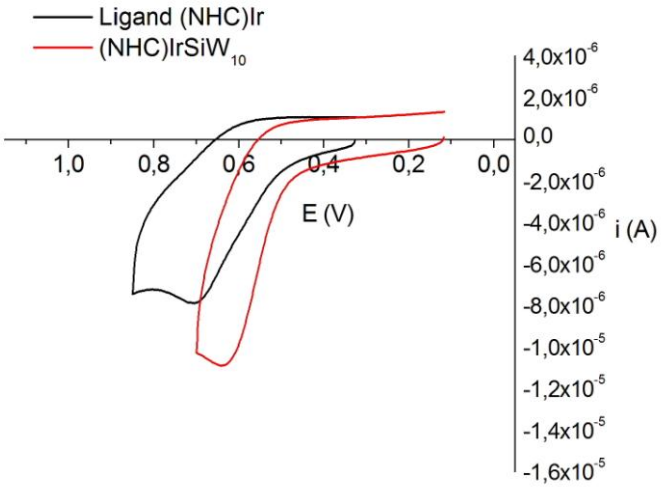

A25 Cyclic voltammetry; anodic scan: 0.05 mM; CH_3CN (nBu_4ClO_4; 0.1M); 200 mV/sec.

Ligands

Synthesis of 1-Pyrensulfonyl Chloride *($PyrSO_2$-Cl)*

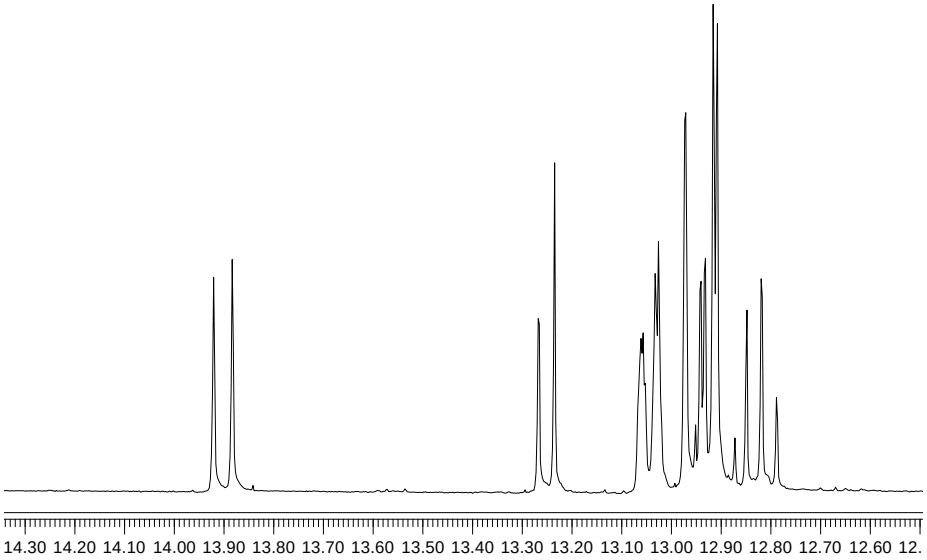

A26 ^{1}H NMR (CD_3CN) of **$PyrSO_2$-Cl**.

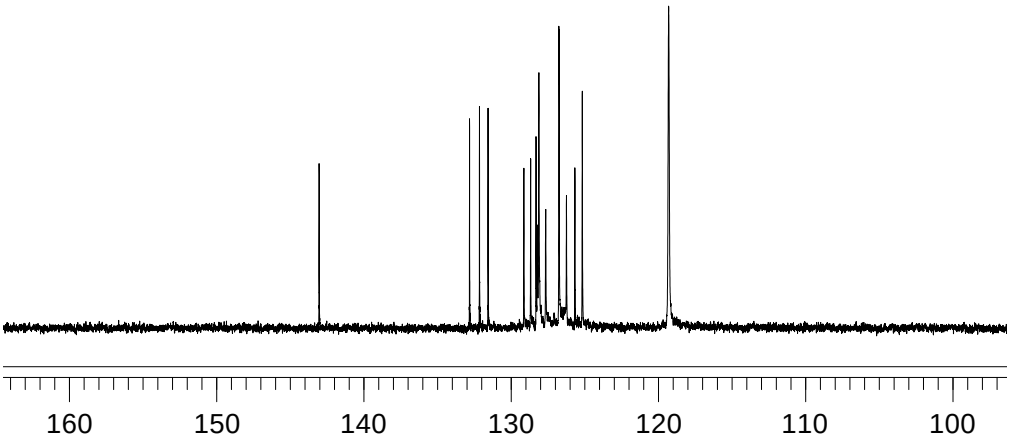

A27 ^{13}C NMR (CD_3CN) of **$PyrSO_2$-Cl**.

$(C_{20}H_{11}O_5)NHCSNHCH(CH_3)PO(OH)_2$ *(FITC-AEPA)*

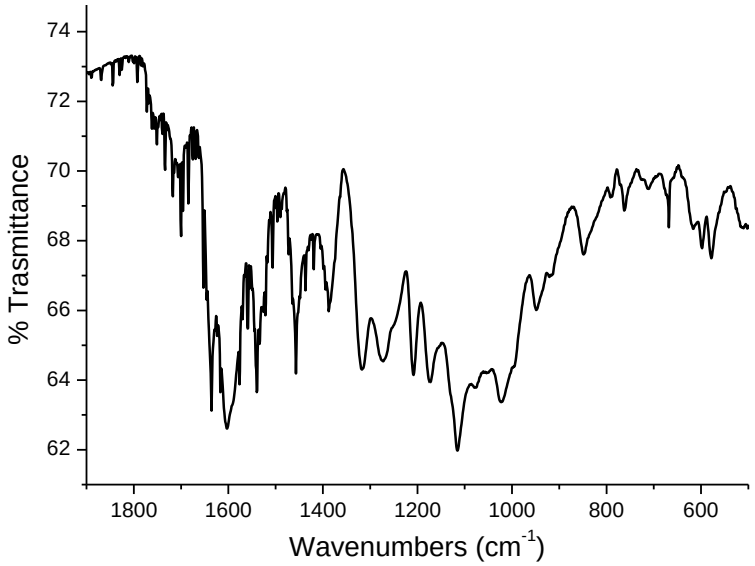

A28 FT-IR (KBr) of **FITC-AEPA**.

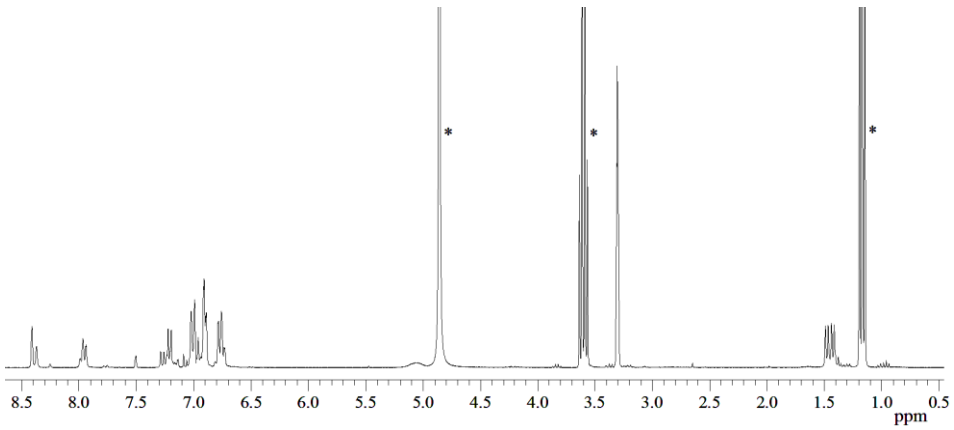

A29 ^{13}H NMR spectrum of **FITC-AEPA** in CD_3OH.*Residual peaks (ethanol and water).

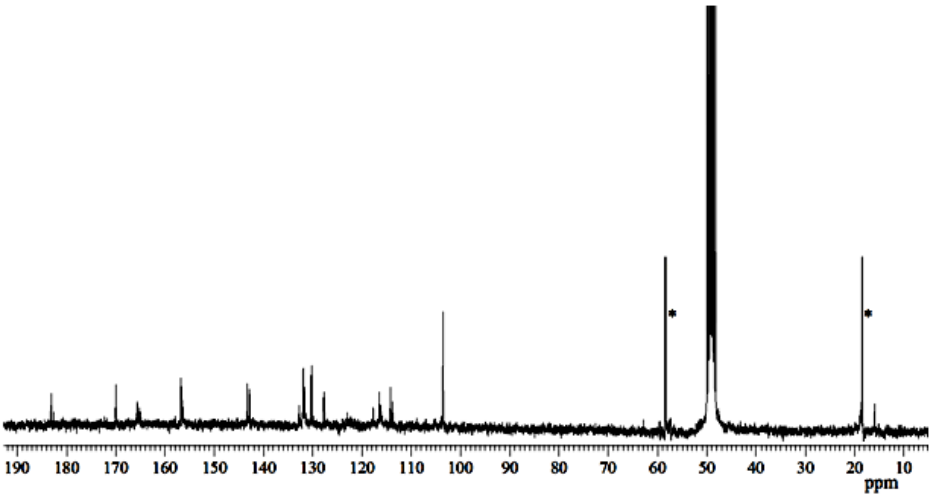

A30 ^{13}C NMR spectrum of **FITC-AEPA** in CD_3OH. *Residual ethanol peaks.

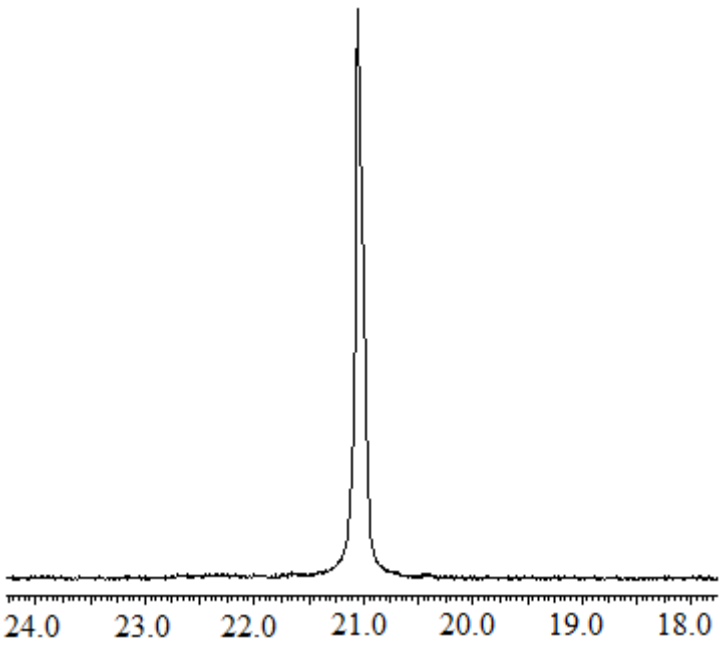

A31 ^{31}P NMR spectrum of **FITC-AEPA** in $[D_6]DMSO$.

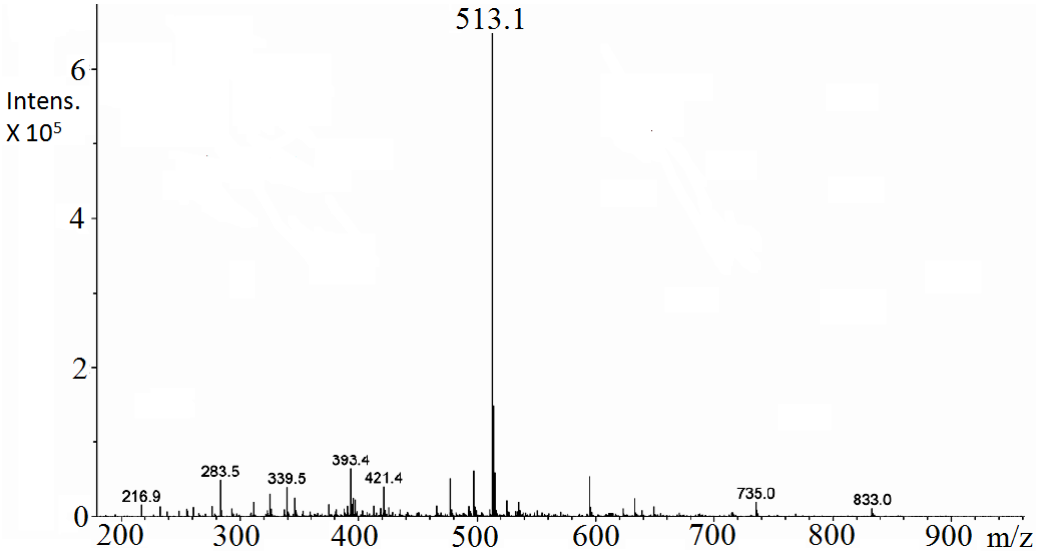

A32 ESI-MS ((+),CH_3OH) of **FITC-AEPA.**

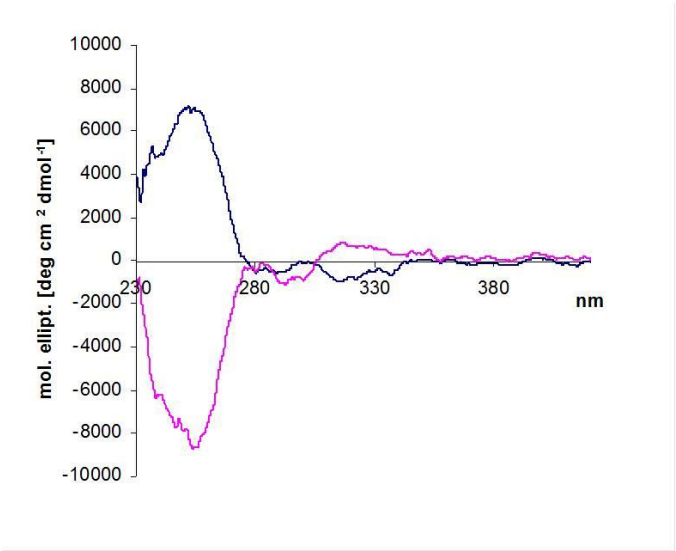

A33 Circular dichroic spectrum (CH_3CO) of **FITC-AEPA**.

[(1,2,5,6-*η*)-1,5-cyclooctadiene][1-butyl-3-(3-triethoxysilylpropyl)-imidazol-2 ylidene]chloroiridium *((NHC)Ir)*

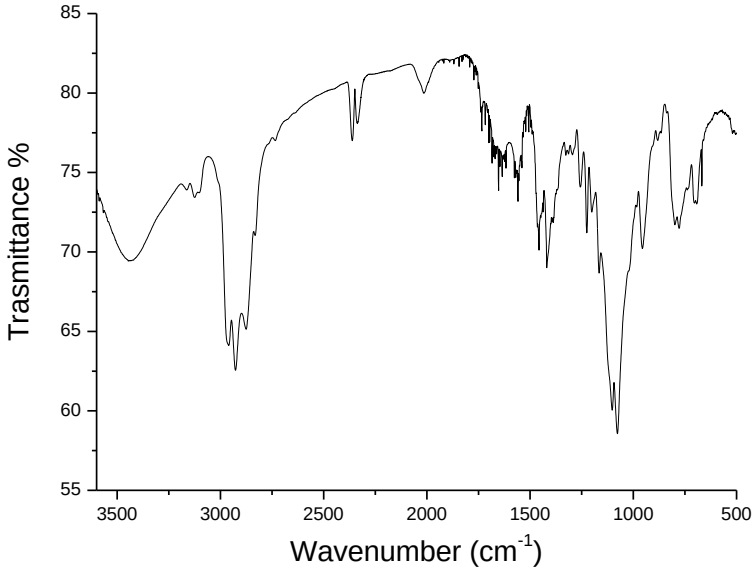

A34 FT-IR (KBr) of **(NHC)Ir**

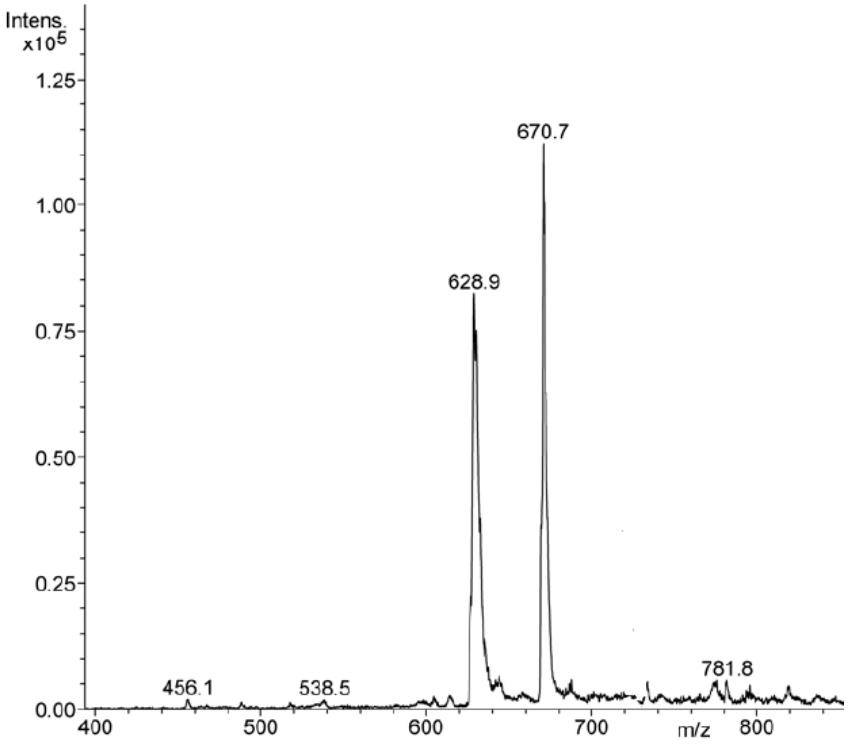

A35 ESI-MS ((+),CH_3CN) of **(NHC)Ir**.

ζ-potential measurements of luminescent hybrid POMs

Dans-SiW_{10}

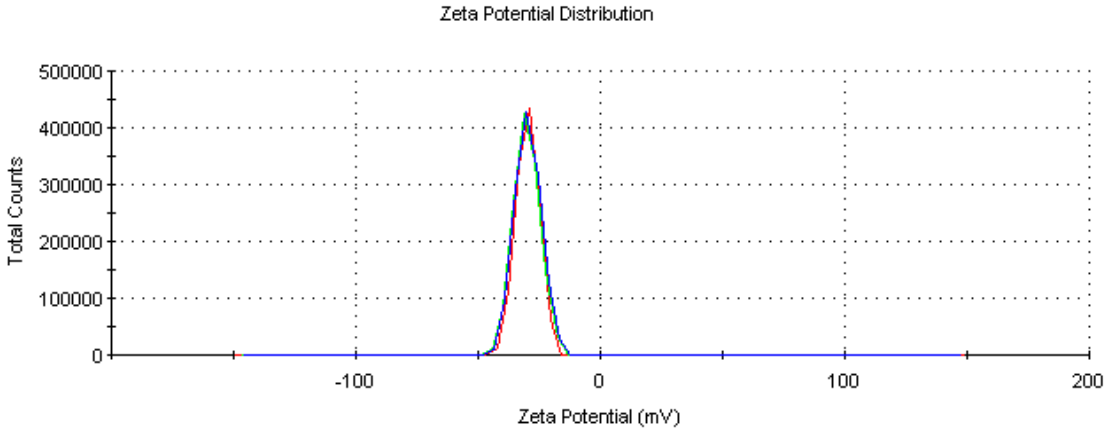

Pyr-SiW_{10}

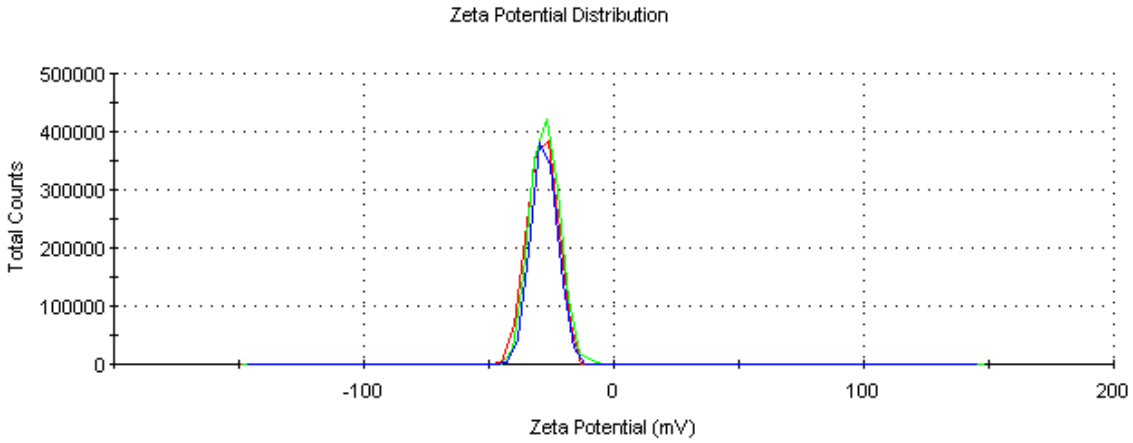

FITC-SiW_{10}

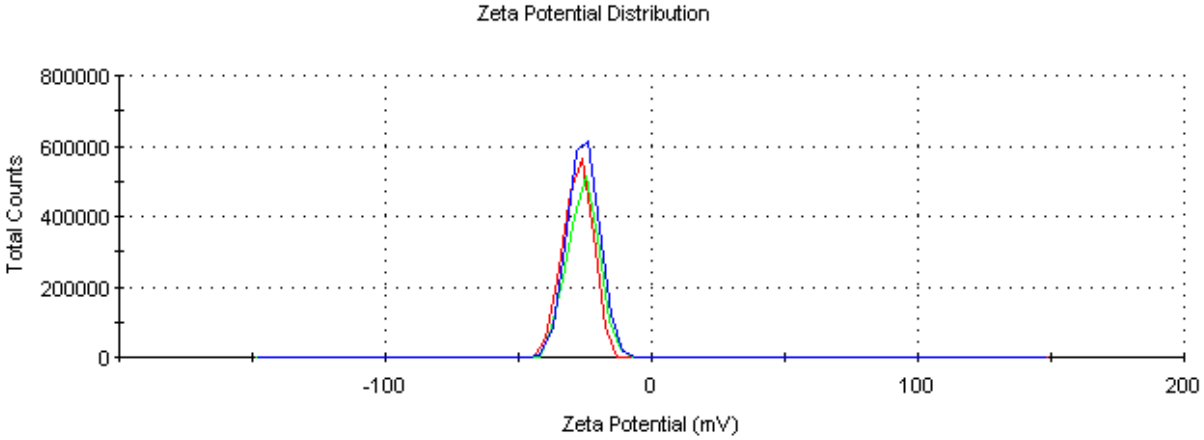

FITC-PW_9

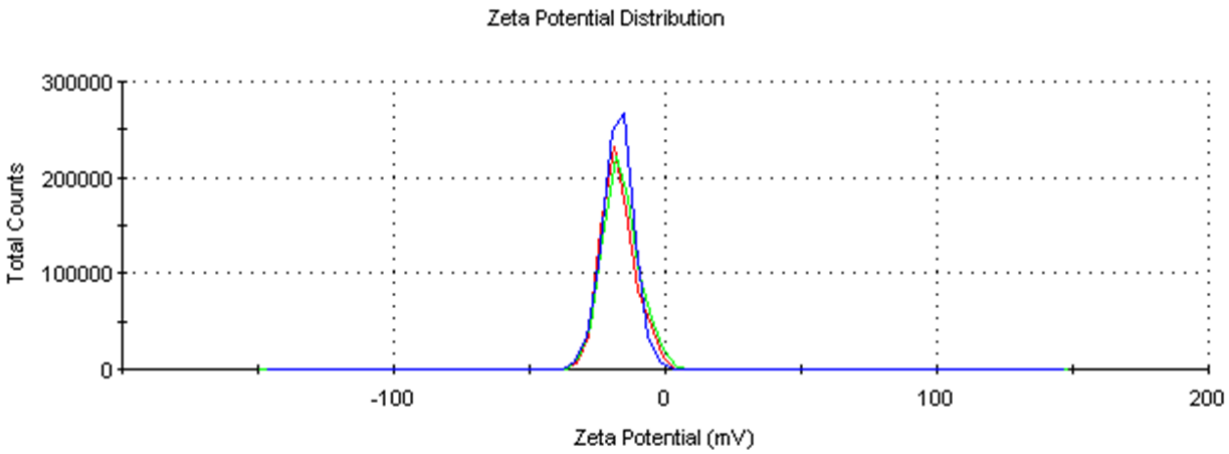

A36 ζ-potential of hybrid POMs: Dans-SiW_{10}, Pyr-SiW_{10}, FITC-SiW_{10}, FITC-PW_9 in in H_2O/0.05 % DMSO.

Dynamic light Scattering of luminescent hybrid POMs

Dans-SiW_{10}

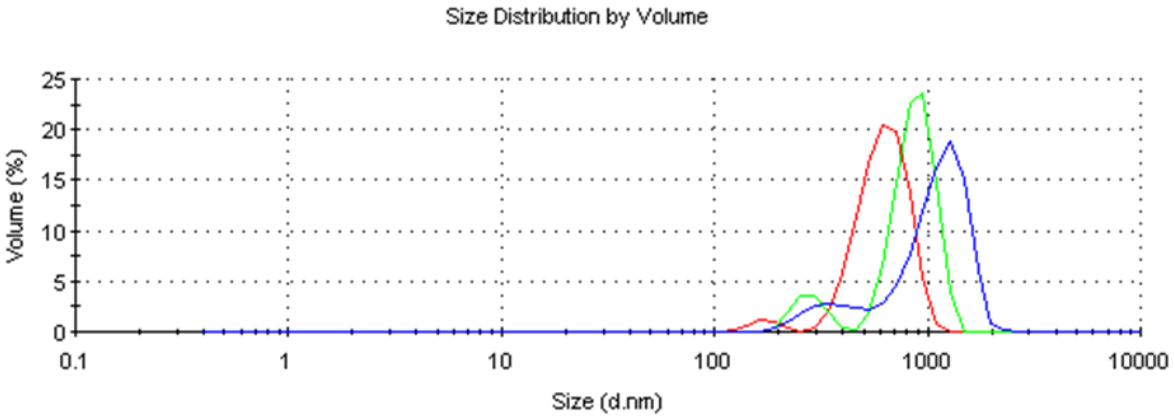

Pyr-SiW_{10}

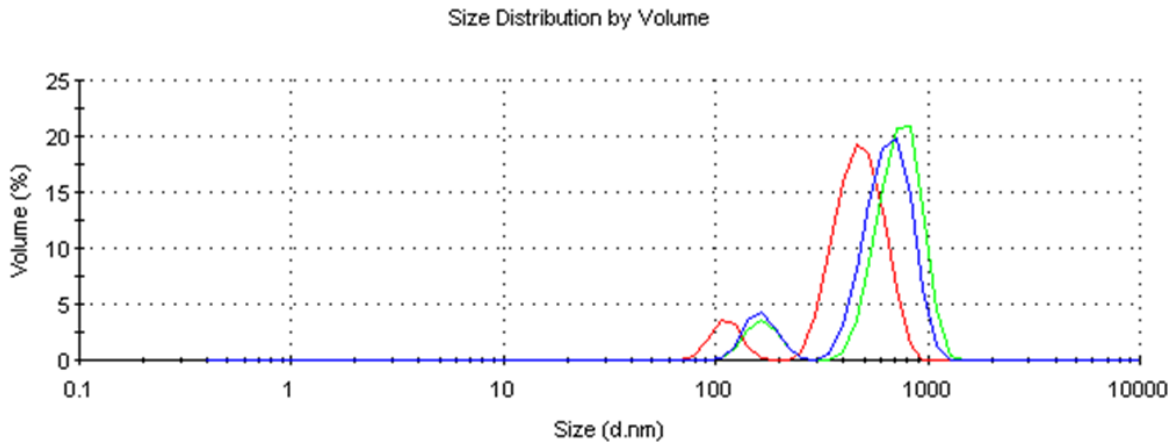

FITC-SiW_{10}

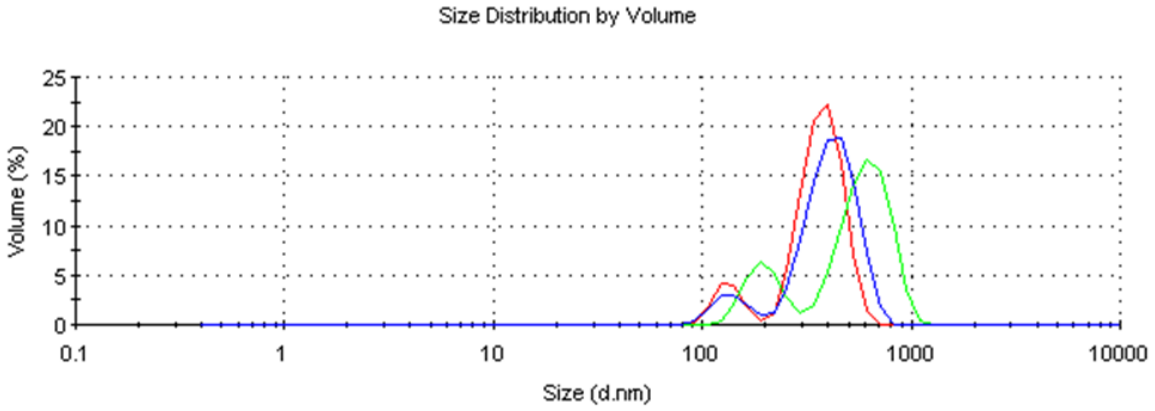

FITC-PW_9

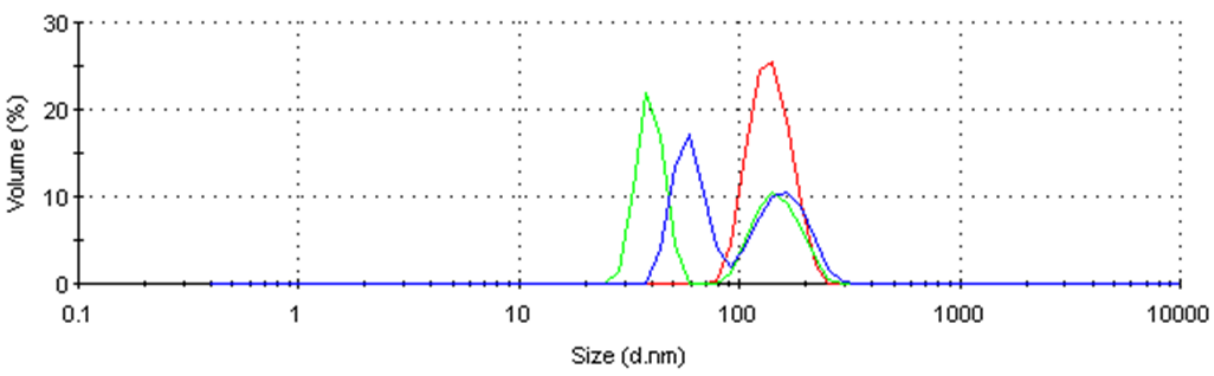

A37 Dynamic Light Scattering (DLS) of Dans-SiW_{10}, Pyr-SiW_{10}, FITC-SiW_{10}, FITC-PW_9 in H_2O/0.05 % DMSO.

Electronic microscopy imaging of luminescent hybrid POMs

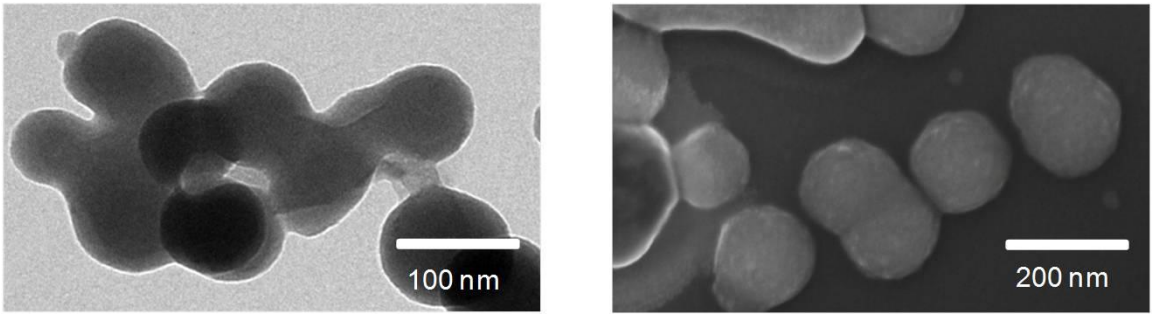

A38 Left: transmission electronic microscopy (TEM) images of POM **Pyr-SiW$_{10}$** (**2**) in physiological-like solution containing 0.05% v/v of DMSO. Right: scanning electronic microscopy (SEM) images of POM **Pyr-SiW$_{10}$** in physiological-like solution containing 0.05% v/v of DMSO

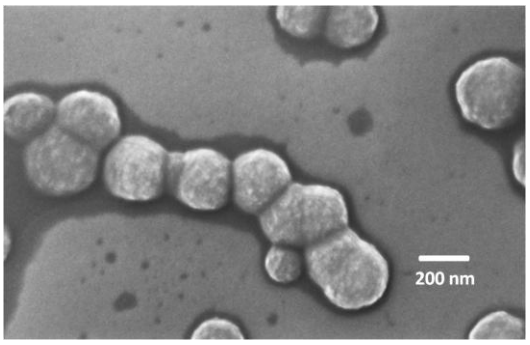

A39 Scanning electronic microscopy (SEM) images of POM **FITC-PW$_9$** in physiological-like solution containing 0.05% v/v of DMSO.

Optical microscopy imaging of cells incubated with luminescent hybrid POMs

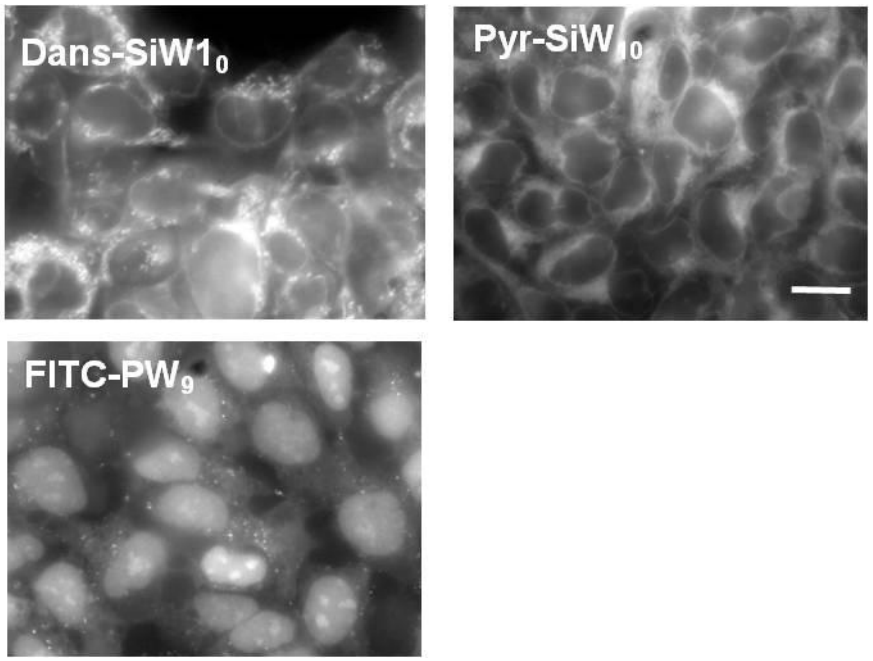

A40 Subcellular localisation In *vitro* fluorescent large magnification microscopy imaging of HEK cells exposed to FITC-PW9 and Pyr-SiW10 (18 μM, at 37°C) for longer time (>15h). Note different preferential localisation of the two compounds. Scale bar : 10 μm.

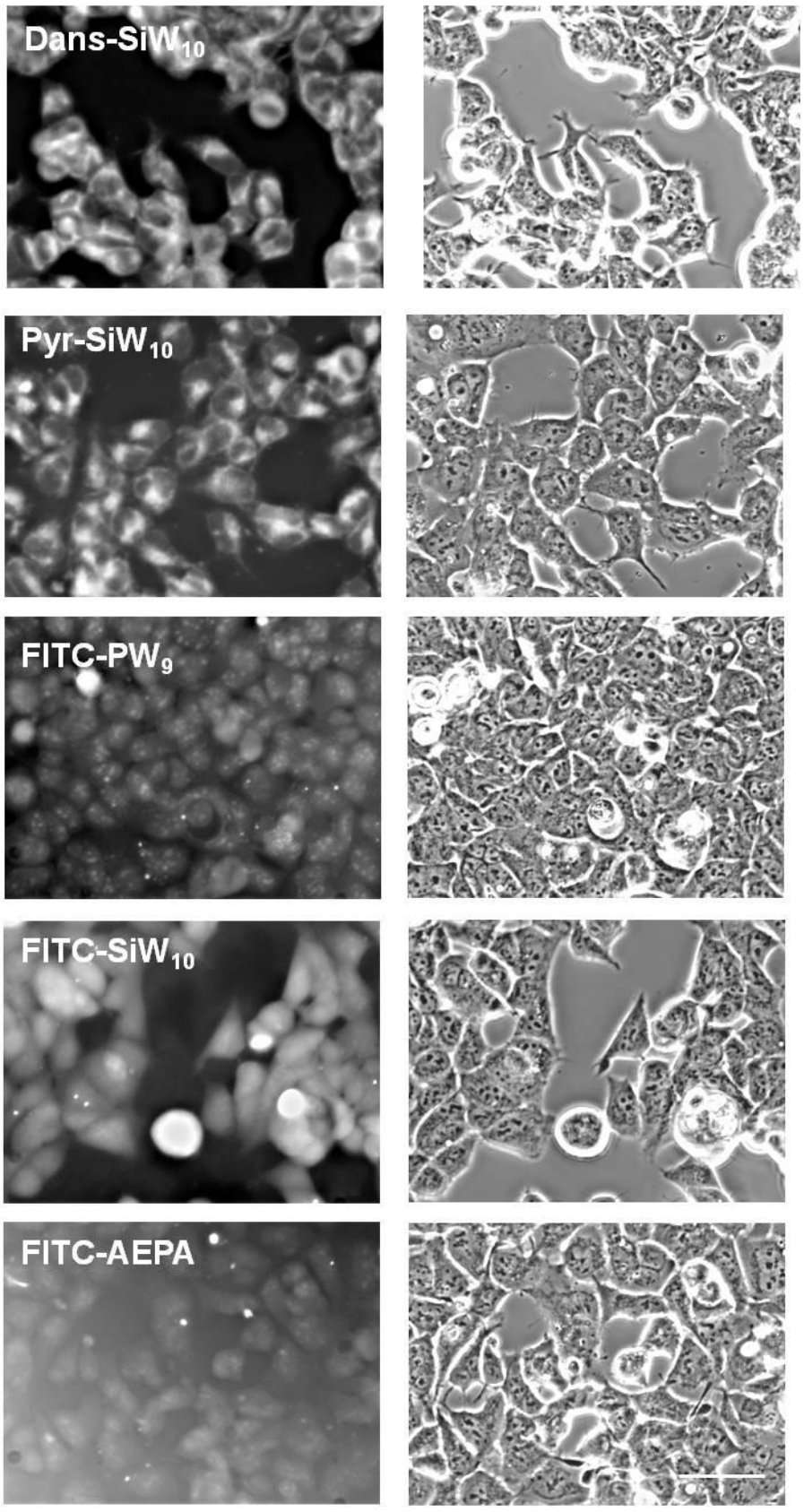

A41 Representative images of cells exposed to different POMs (18 µM, 15 h, 37°C) and visualised with appropriate fluorescence filters and transmitted light to appreciate cell morphology. Note dense cell monolyer induced by FITC-PW_9. Bar = 50 µm.

Biological activity of luminescent hybrid POMs

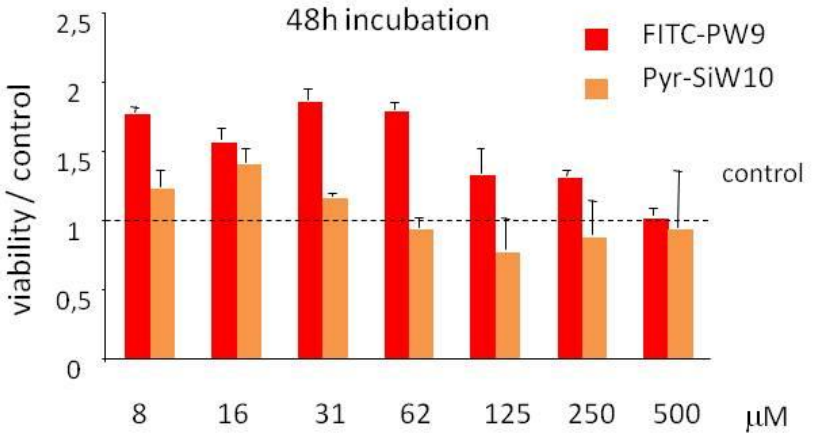

A42 Cells viability studies of HEK cells incubated with different concentrations of POMs **Pyr-SiW$_{10}$** and **FITC-PW$_9$** at 37°C for 48 h.

ζ-potential measurements of aFtn/POMs system

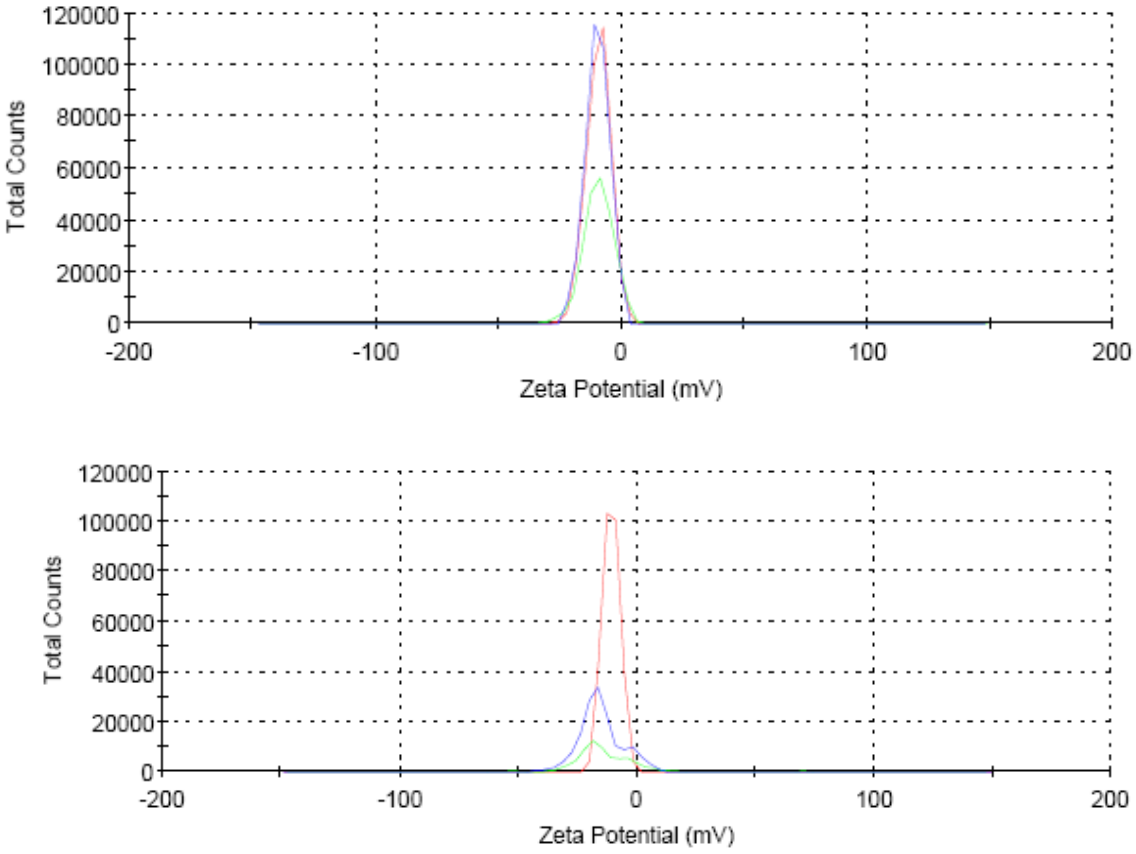

A43 ζ-potential of aFtn (0.245 µM) (up) and in the presence of **RuPOM** (below), at pH 3.5 with HCl.

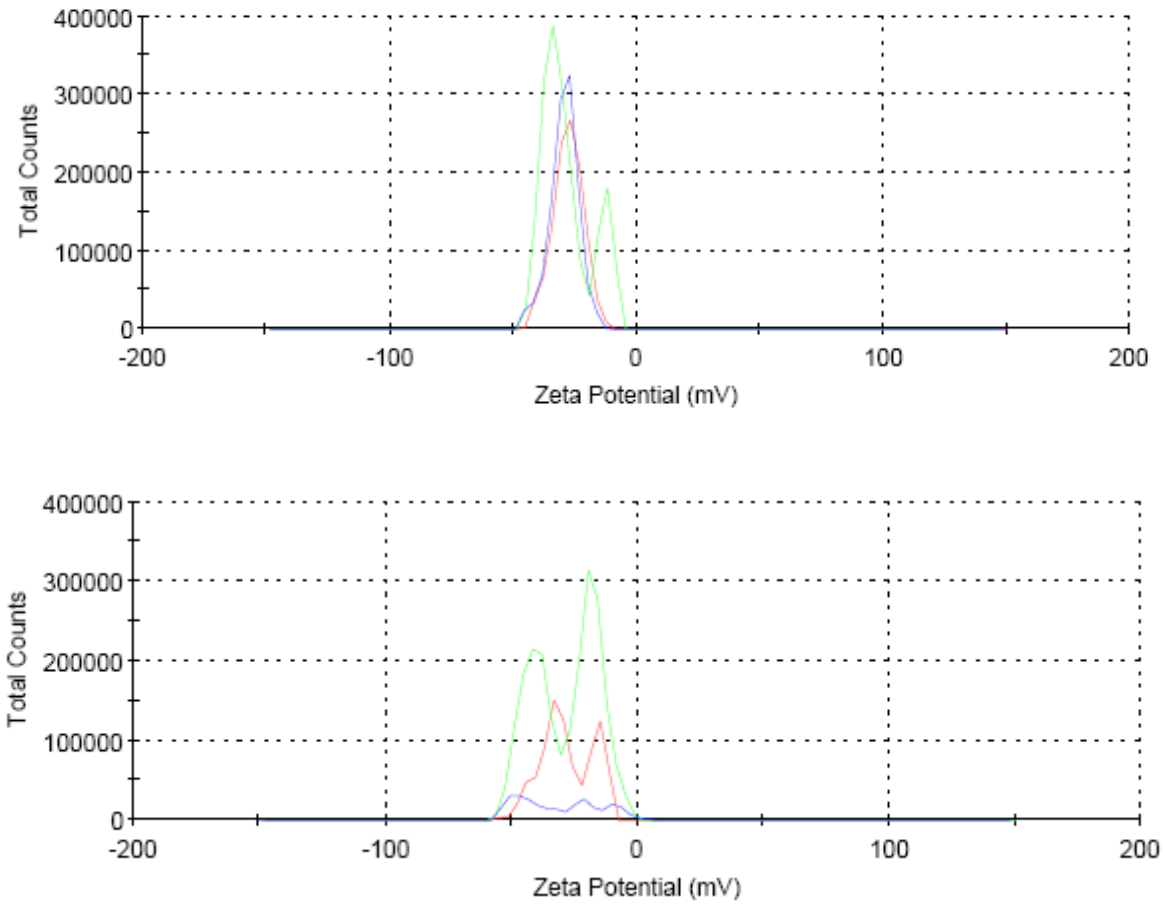

A44 Ftn (0.245 µM), in the absence (top) and in the presence (bottom) of **RuPOM** (24 eqs), after addition of NaOH, to solutions at pH 2.5 (final pH 7.8).

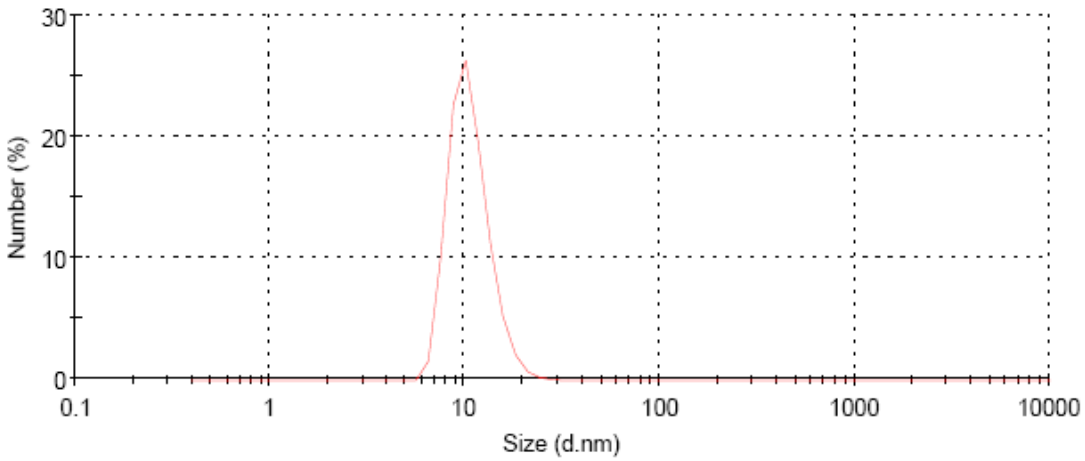

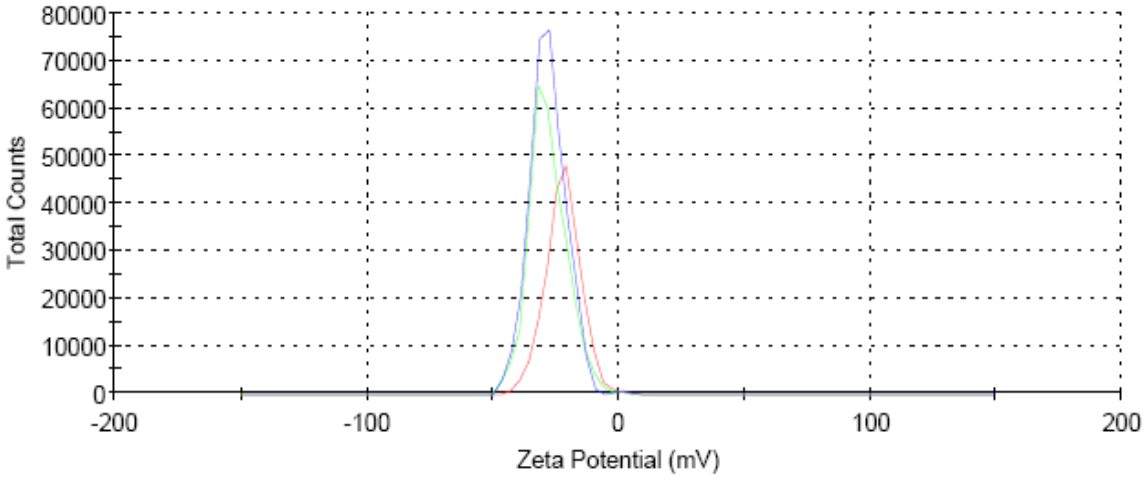

A45 DLS (above) and ζ-potential (below) of aFtn (0.245 µM) and **EuPOM** (12.25 µM), back to pH 7.8, by dialysis against TRIS/AcOH buffer.

Ringraziamenti

Al termine di questo meraviglioso e tortuoso percorso, desidero ringraziare tutte le persone che hanno collaborato con me e che mi sono state vicine durante questi tre anni.

Davanti a tutti ringrazio il Dott. Mauro Carraro. Lo ringrazio come Supervisore per la pazienza, disponibilità ed entusiasmo con le quali mi ha seguito passo per passo nello svolgimento di questo lavoro. Lo ringrazio per avere condiviso con me idee sempre nuove e stimolanti che mi hanno insegnato che solo da una grande passione e dedizione può nascere un lavoro di qualità e per avere sempre dato una risposta semplice ma altrettanto efficace ad ogni mio dubbio o difficoltà. Lo ringrazio come amico per avermi spesso ascoltato e incoraggiato, e per tutti i momenti trascorsi insieme.

Desidero, inoltre, ringraziare la Dott. Marcella Bonchio, per aver seguito con interesse ed entusiasmo l' avanzamento di questo lavoro, per i preziosissimi consigli e per il suo sguardo critico e lungimirante che hanno, spesso, reso possibile trasformare idee e progetti in lavori importanti.

Ringrazio il Dott. Andrea Sartorel per la sua gentilezza, pazienza, infinita disponibilità e per il suo importante apporto per la parte di calcolo computazionale.

I wish to thank Prof. Martin Albrecth and all nice people that I have met during the short term scientific mission in Dublin for the research experience and for all the things I have learned about (but not only) chemistry.

Desidero, inoltre, ringraziare: la Dott. Chiara Maccato per le analisi SEM; il Dott. Federico Caicci per le analisi TEM; la Dott. Elsa Fabbretti (Università di Nova Gorica (Slovenia)) per le analisi biologiche e le immagini di microscopia ottica; il Dott. Zois Syrgiannis (Università di Trieste) per gli studi di interazione con i nanotubi.

Ringrazio i miei compagni di laboratorio e "dintorni" per essere diventati anche amici e parte della mia vita ...

... in maniera speciale, ringrazio Serena, Irene, Francesca Di Sarra e Giulia Fiorani per avermi aiutata nel lavoro e per avere condiviso con me momenti importanti: pause pranzo, cene, chiacchiere e tante avventure. Ringrazio tutti gli altri ragazzi del lab. 106 e dell'ufficio: Rommel, Valeria e Ajeandro, Giulia Beltrame, Massimo, Marta e Andrea ... Grazie per le serate in compagnia e le tante risate ...
Ringrazio tutti gli altri ragazzi del mio gruppo: Antonio, Debora, Omar, Angela, Andrea, Francesca, Erika, Matteo e i troppi laureandi ...

Un ringraziamento specialissimo alle mie amiche del lab. 108: compagne di ufficio e di vita... Grazie a Sara, Rosalia, Aga, e specialmente Grazie a Blerina (per il suo carico di pazzie e di verità)... Grazie ragazze per: aperitivi, spettegolezzi, serate, pause caffè ... Grazie per avere condiviso con me arrivi, partenze, scherzi, tante risate, ma anche pianti ... Grazie soprattutto per essere amiche importanti!!

Un ringraziamento doveroso ai miei cari amici e compagni di corso ("I Cortinas"): Edoardo, Enrica, Chiara e Ketty e Grazie a Diego ... Ringrazio, poi, le mie amiche Rita, Daniela e Chiara G. insieme al suo papà per avermi dato importanti consigli ...

Grazie alla mamma e al papà di Elena per essermi molto vicini ...

Ringrazio la mia famiglia per l'affetto, per avermi sempre supportato e incoraggiato nelle mie scelte ... Soprattutto ringrazio mia mamma per tutto il suo aiuto, per essermi sempre vicina e per essere anche fonte di ispirazione ... Grazie a Stella e al suo veterinario ... Un forte ringraziamento a mia nonna per essere sempre orgogliosa e felice dei miei successi ... Ringrazio mio fratello Filippo e mia cugina Beatrice per essere una costante presenza nella mia vita ...

... Il ringraziamento più straordinario è per te Elena ... questa volta sarà così forte da arrivare fino al cielo ... Grazie per tutti i momenti felici che abbiamo trascorso insieme, Grazie per essere la Mia Migliore Amica, Grazie per essere Per Sempre parte della mia vita e ... Grazie per il Nostro Dottorato!!

Gloria